U F m G

Universidade Federal de Minas Gerais
Departamento de Física

Ph.D. Thesis

Emergent properties from first principles: d^0 magnetism and metal-insulator transitions

Walber Hugo de Brito

Belo Horizonte
2016

Walber Hugo de Brito

Emergent properties from first principles: d^0 magnetism and metal-insulator transitions

Tese apresentada ao Programa de Pós graduação em Física da Universidade Federal de Minas Gerais, como requisito parcial para a obtenção do título de Doutor em Física.

Orientador:
Prof^{o} Dr. Hélio Chacham

Co-Orientadora:
Prof^{a} Dra. Maria Carolina de Oliveira Aguiar

Belo Horizonte
2016

The ability to reduce everything to simple fundamental laws does not imply the ability to start from those laws and reconstruct the universe.

Philip Warren Anderson

Resumo

Neste trabalho empregamos diferentes métodos de estrutura eletrônica para o estudo de propriedades emergentes em materiais, em específico, para se investigar o magnetismo d^0 em materiais de carbono e transições metal-isolante em óxidos de metais de transição. Na primeira parte da tese estudamos (*i*) a estabilidade energética relativa, propriedades magnéticas e eletrônicas de nitretos de carbono com estrutura hexagonal; em seguida investigamos (*ii*) as propriedades estruturais, energéticas, eletrônicas e magnéticas de cristais de politetrafluoretileno (Teflon) com vacâncias de flúor e impurezas de oxigênio. Na segunda parte investigamos (*iii*) as transições metal-isolante nos dióxidos de vanádio e nióbio, concentrando-se nos mecanismos físicos responsáveis pela formação do *gap* de energia nas fases de baixa temperatura.

Em (*i*) obtivemos um conjunto de estruturas de nitreto de carbono de baixa energia de estrutura hexagonal com diferentes concentrações de nitrogênio. Nesse contexto, identificamos que a estabilidade relativa dessas estruturas está associada ao ganho de energia devido à dopagem eletrônica induzida pelas impurezas de nitrogênio. Adicionalmente, propomos novas estruturas semicondutoras e ferromagnéticas de nitreto de carbono.

Em (*ii*) encontramos que vacâncias de flúor e impurezas de oxigênio no *bulk* de Teflon dão origem a estruturas sem a quebra da cadeia polimérica. Nesse contexto, obtivemos que impurezas de oxigênio dão origem a configurações mais estáveis energeticamente do que as com vacâncias de flúor. Adicionalmente, encontramos que a formação de estruturas policonjugadas nas cadeias poliméricas é mais estável do que a presença das mesmas isoladas nas cadeias. Encontramos também que vacâncias de flúor e impurezas de oxigênio podem dar origem a momentos magnéticos locais. Porém, não foi observado nenhum tipo de ordenamento ferromagnético devido ao acoplamento entre os mesmos. Esses resultados, por sua vez, sugerem que as configurações investigadas em nosso trabalho não podem dar origem ao ferromagnetismo observado em fitas de Teflon com defeitos estruturais.

Por fim, em (*iii*) propusemos um novo mecanismo para a abertura do *gap* nas fases de baixa temperatura do VO_2 e NbO_2. Identificamos que a física de Mott é essencial para a descrição de todas as fases do VO_2 devido ao fato de que os elétrons nesse material estão próximos a uma transição de Mott. Em relação às fases M_1 e M_2 do VO_2, observamos que a instabilidade de Mott-Hubbard é "aprisionada" devido a dimerização dos átomos ou surgimento de um ordenamento antiferromagnético. Encontramos também que as correlações eletrônicas não locais favorecem a abertura do *gap* nas fases de baixa temperatura. Instabilidades de Hubbard só foram encontradas para os átomos de vanádio não dimerizados da fase M_2 paramagnética.Em relação ao NbO_2, encontramos que as correlações eletrônicas não locais são menos importantes do que no VO_2, embora as mesmas desempenham um papel relevante na abertura do *gap* de sua fase de baixa temperatura.

Abstract

In this thesis we employed electronic structure methods to investigate emergent properties of different materials, namely d^0 magnetism in carbon based materials and metal insulator transitions in transition-metal oxides. In the first part, we investigated (*i*) the morphology, relative energetic stability, electronic, and magnetic properties of graphene-like carbon nitride structures and (*ii*) the structural, energetics, electronic, and magnetic properties of polytetrafluoroethylene (Teflon) crystals with fluorine vacancies and oxygen impurities. In the second part we studied (*iii*) the metal-insulator transition in vanadium and niobium dioxides, with focus on the physical mechanism responsible for the gap formation in their low-temperature phases.

In (*i*) we obtained a set of low-energy graphene-like structures with distinct nitrogen concentrations. In particular, we identified that their relative stability is associated with the energy cost due to the charge doping induced by the nitrogen impurities. In addition, new semiconducting and ferromagnetic carbon nitride structures were proposed.

In (*ii*) we obtained that both fluorine vacancies and oxygen impurities in bulk Teflon lead to structural configurations without the breaking of the carbon backbone. Oxygen impurities were found to be energetically more stable than fluorine vacancies. In addition, the formation of polyconjugated structures in the polymer chain was found to be energetically favorable. The local magnetic moments associated with the point defects do not give rise to any ferromagnetic ordering, which rules out the investigated configurations as the origin of ferromagnetism in defective Teflon tapes.

Finally, in (*iii*) we proposed a new mechanism for the gap opening in the low-temperature phases of VO_2 and NbO_2. We identified that Mott physics is central for the proper description of all phases of VO_2 since its electrons are in the near vicinity of the Mott transition. In the M_1 phase and in the antiferromagnetically ordered M_2 phase, we found that the Mott-Hubbard instability is arrested due to V-atoms dimerization and antiferromagnetic ordering, respectively. In especial, we obtained that nonlocal electronic correlations support the gap opening in the low-temperature phases. Hubbard instabilities were found only in the case of undimerized V-atoms of the paramagnetic M_2 phase. In respect to NbO_2, we found that electronic correlations are less important, though they do play a role in the gap opening of its low-temperature phase.

Acknowledgements

Gostaria de agradecer ao Professor Hélio Chacham por toda orientação, discussões, paciência e por ter me dado a chance de aprender um pouco mais sobre a física dos materias de carbono.
A Professora Maria Carolina de Oliveira Aguiar pela orientação, paciência, dedicação, atenção e incentivo ao longo do doutorado. Agradeço também pelas oportunidades e por sempre estar disposta a ensinar um pouco mais sobre a física de sistemas fortemente correlacionados.

I would like to thank Professor Kristjan Haule for giving me the opportunity to work with him, for his expert guidance, and for helping me to overcome difficult problems on my research. I also appreciate his attention during my stay at Rutgers and for all the inspiring discussions.
I also would like to thank Professor Gabriel Kotliar for giving me the opportunity to work at his group at Rutgers, for the financial support during my staying in the USA, and for the insightful discussions.

Gostaria também de agradecer a minha mãe que mesmo de longe sempre me apoiou com muito amor, carinho e dedicação. Aos meus irmãos por todo incentivo e paciência ao longo de todos esses anos.

A Andreza, pelo amor, companheirismo, paciência e por toda ajuda desde que nos conhecemos. Agradeço também a sua mãe por toda ajuda conferida. Aos meus amigos: Marcos Fabrício, Arthur Alves, Wladimir ("Barcinha"), Marcelão e Anna pela amizade e boas conversas. Aos colegas de Departamento: Yuri, Raphael Longuinhos ("Longuin"), Helena, Ana Paula e Nathan pelo convívio.

I thank my friends Manuel Pino ("Manuu..."), Vanessa Sastre & Juan Pablo for spending time joyfully at Pino's and during my stay in New Jersey. Agradeço também aos colegas brasileiros que fiz em Nova Jersey: Aline Ramires e Leonardo Santana, o meu muito obrigado por toda ajuda e suporte durante minha estadia nos EUA. I also thank Turan Birol and Victor Alexandrov for their help during my stay at Rutgers.

Por fim, agradeço ao CENAPAD-SP pelo suporte computacional e ao CNPq por todo suporte financeiro.

Contents

List of Figures

List of Tables

Abbreviations

DFT	**D**ensity **F**unctional **T**heory
LDA	**L**ocal **D**ensity **A**pproximation
GGA	**G**eneralized **G**radient **A**pproximation
DMFT	**D**ynamical **M**ean **F**ield **T**heory
MT	**M**uffin **T**in
PTFE	**P**oly**T**etra**F**luoroethylen**E**
XPS	**X**-ray **P**hotoemission **S**pectroscopy
BIS	**B**remsstrahlung **I**sochromat **S**pectroscopy
cRPA	**c**onstrained **R**andom **P**hase **A**pproximation
FLL-DC	**F**ully **L**ocalized **L**imit **D**ouble **C**ounting
HF-QMC	**H**irsch-**F**ye **Q**uantum **M**onte **C**arlo
CTQMC	**C**ontinuous **T**ime **Q**uantum **M**onte **C**arlo
LAPW	**L**inearized **A**ugmented **P**lane **W**ave
APW	**A**ugmented **P**lane **W**ave
PW	**P**lane **W**ave
LCAO	**L**inear **C**ombination of **A**tomic **O**rbitals
NAO	**N**umerical **A**tomic **O**rbitals
ARPES	**A**ngle **R**esolved **P**hotoemission **E**lectron **S**pectroscopy
FET	**F**ield **E**ffect **T**ransistor
TMO	**T**ransition **M**etal **O**xide
NMR	**N**uclear **M**agnetic **R**esonance
ESR	**E**lectron **S**pin **R**esonance
IXS	**I**nelastic **X**-ray **S**cattering
UPS	**U**ltraviolet **P**hotoelectron **S**pectroscopy
PIXE	**P**roton **I**nduced **X**-ray **E**mission
XRD	**X** **R**ay **D**iffraction
bct	**b**ody-**c**entered **t**etragonal

Introduction

Since the 20th century the technological development has been driven by important achievements in condensed matter physics and materials science. In particular, the discovery, controlled production, and better understanding of the properties of semiconductors and magnetic materials have supplied the basic ingredients to electronic and magnetic devices used in information processing and storage [1]. Figure 1 illustrates the usage of each chemical element in this information technology.

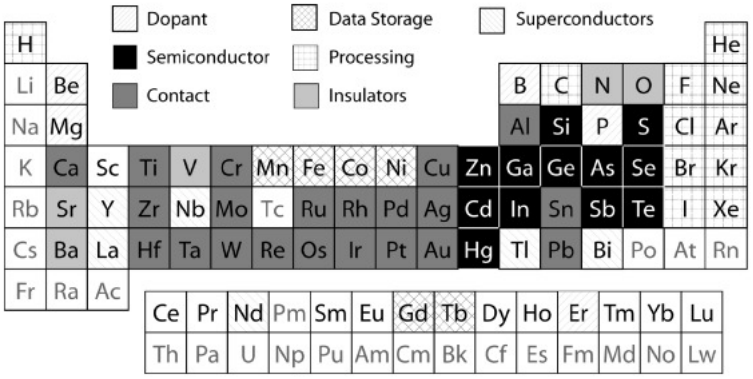

FIGURE 1: Chemical elements used in microelectronic and magnetic devices. Figure taken from Ref. [1].

At the heart of the fundamental understanding of the properties of solids lies the quantum mechanical description of many interacting electrons and nuclei. Historically, it has been a tendency of theory to reduce this complex many-body problem to a problem of many independent particles. For instance, the lattice specific heat of monoatomic solids can be understood by a simple model of many independent phonons with distinct frequencies [2]. Likewise, the electrical conductivity of metals, semiconductors, and insulators can be understood with a model of energy bands of independent electrons in a periodic structure, as in a crystal [3]. However, there are many other emergent phenomena [4], such as magnetic ordering, superconductivity, and metal-insulator transitions,

which cannot be properly addressed without considering the interactions between electrons.

Nowadays, most theoretical studies of materials properties are carried out by means of computational modeling and simulation. In fact, modern density-functional theory (DFT) calculations have allowed the microscopic understanding and prediction of their properties, and even the computational design of new materials with the desired properties [5]. In particular, such methods, within the standard approaches for the electron-electron interaction, have successfully described the electronic structure of systems known as weakly correlated materials, e.g. simple metals, organic and inorganic semiconductors, and carbon-based nanostructures, such as carbon nanotubes and graphene. By weakly correlated material we mean systems in which the valence electrons give rise to broad energy bands, thus having large values of kinetic energy. These electrons behave like delocalized particles over the entire solid, being thus highly itinerant.

It is well known that the different sorts of magnetic ordering observed in nature are the result of electron-electron interaction in a solid. Over the decades, such emergent phenomena have mainly been observed in magnetic materials containing transition metal atoms or rare earth elements, that is, in materials with d or f electrons. More recently, though, spontaneous magnetic ordering has been experimentally observed in weakly correlated materials which do not have d or f electrons in their composition. Since then, this type of magnetism has been called d^0 or sp magnetism [6]. For example, magnetic properties have been reported in carbon based materials such as organic crystals, nanographites, and fullerene-based compounds [7]. In this thesis, we investigate this property in graphitic carbon nitride structures and thin films of polytetrafluoroethylene (PTFE), known as Teflon.

Graphitic carbon nitrides have in general graphene-like layers with C_3N_4 stoichiometry and in-plane structures based on s-triazine or tri-s-triazine subunits. From a technological perspective, numerous experimental works have indicated that these materials are promissing metal-free photocatalysts for the light-driven water splitting, active layers for field effect transistors, and photoluminescent material for biomedical applications. Despite these great potentials, previous theoretical works have also proposed that these materials can present ferromagnetic properties induced by changes in its stoichiometry

and structure. In particular, the possibility of tuning the properties of graphitic carbon nitride by controling its structure and composition has motived the synthesis of graphitic structures with distinct stoichiometries and morphology. Motivated by the interest in new graphitic carbon nitride structures, we performed simulated annealing and DFT calculations aiming at the prediction of new graphene-like carbon nitride structures with distinct stoichiometries. We also investigated their energetic, electronic, and magnetic properties.

Polytetrafluoroethylene, usually known as Teflon, is a polymer with molecular chains composed by tetracoordinated carbons with fluorine atoms of molecular formula -$(CF_2)_n$ -. Due to its chemical and physical properties this material is extensively used in coating of surfaces and in fabrication of biomechanical implants, for instance. This material is also insulating and diamagnetic. However, experimental evidences of ferromagnetism in polytetrafluoroethylene samples were reported recently. Through mechanical stretching, cutting, and heat treatment the authors fabricated defective Teflon tapes with signatures of intrinsic room-temperature ferromagnetism. This ferromagnetism was then suggested to has its origin in the coupling between local magnetic moments of carbon dangling bonds, which were created by the experimental procedures mentioned above. In addition, experiments on gamma-ray irradiation of PTFE induced color and fluorescent properties in this material. As pointed out by Khatipov *et al.* [8] these properties may be explained by considering the formation of polyconjugated structures in the polymer chains. Motivated by these experiments, we performed DFT calculations to investigate the electronic properties of defective Teflon crystals, and on the possibility of inducing magnetic ordering by point defects, such as fluorine vacancies and oxygen impurities.

On the other hand, DFT calculations have failed in the description of systems known as strongly correlated materials. In these systems, the interaction energy between electrons has the same magnitude of their kinetic energy, leading to a tendency towards localization [9]. This localization is the physical mechanism responsible for the insulating nature of materials known as Mott insulators. In addition, systems in which electrons are close to this localization undergo metal-to-insulator transitions under external perturbation. Such metal-insulator transitions (MITs) can be driven by pressure, temperature, or even chemical doping. Theoretically, a successful description of this transition has been achieved through the solution of the Hubbard model, by employing

the dynamical mean field theory (DMFT) [10]. However, the neglect of materials specific information hinders quantitative comparison between theoretical calculations and experiments. In order to overcome this issue, a combination of DFT and DMFT methods has been proposed and successfully applied to the study of the electronic structure of many strongly correlated materials [11, 12]. In this thesis, we present our theoretical investigation on the metal-insulator transition of vanadium and niobium dioxide, namely VO_2 and NbO_2.

Vanadium dioxide undergoes a metal-insulator transition at 340 K while in the case of niobium dioxide it happens at around 1081 K. In both systems, the MITs are accompained by structural distortions from high-temperature rutile structures, where the transition-metal atoms are equally spaced along the rutile c axis, to low-temperature distorted structures. Fundamentally, the complex interplay between electronic correlations and structural distortions have attracted great attention. In the case of VO_2, since the establishing of the Peierls [13] and Mott pictures [14, 15] on the MIT of VO_2, numerous investigations have attempted to disclose the driving force behind this transition and to understand the insulating nature of the low-temperature phases. In respect to NbO_2, the role of electron-electron correlations in its electronic properties was in general neglected. In our investigation, we employed DFT+DMFT calculations to address the physical mechanism responsible for the gap formation in the low-temperature insulating phases of these transition-metal oxides, as well as the role of electronic correlations on the electronic structure of their high-temperature metallic phases.

The thesis is organized as it follows:

- Chapter 1 is devoted to the theoretical methodology employed in our investigations. We focused on a general formalism from which we can derive the DFT, DMFT, and DFT+DMFT approaches to the many interacting electron problem;
- In Chapter 2 we present our results on the graphitic carbon nitride structures, with focus on the low-energy graphene-like structures, and their associated electronic and magnetic properties;
- In Chapter 3 we present our *ab initio* calculations of point defects in PTFE and our investigation on the possibility of magnetic ordering in this material, having point defects as the source of unpaired electrons;

- In Chapter 4 we present a brief review of experimental and theoretical works in literature on metal-insulator transitions in VO_2 and NbO_2;
- and finally in Chapter 5 we present our investigation on the metal-insulator transitions in VO_2 and NbO_2 by employing DFT+DMFT calculations.

At the end of this thesis we present our general conclusions and perspectives for future works.

Chapter 1

Methodology

In this chapter we present the theoretical methods used in the investigations performed in this thesis. We start by introducing the effective action formalism which allows us to obtain an unified description of different electronic structure approaches. Within this theoretical framework we first present a density based method, namely the density functional theory (DFT). Additional approaches related to its standard implementation are also discussed. Next we turn to the Baym-Kadanoff theory which paves the way for a Green's function based method, namely the dynamical mean field theory (DMFT). Finally we present the DFT+DMFT theory which has enjoyed great success in the realistic modeling of strongly correlated materials. Throughout this chapter we use atomic Rydberg units, in which $\hbar = 1$, $m_e = 1/2$, and $e^2 = 2$.

1.1 Effective Action Formalism

From a microscopic viewpoint the solid state of matter can be regarded as a system of many interacting electrons and nuclei, as illustrated in figure 1.1. In particular, it is well known that the electrical properties of solids are determined by their electrons.

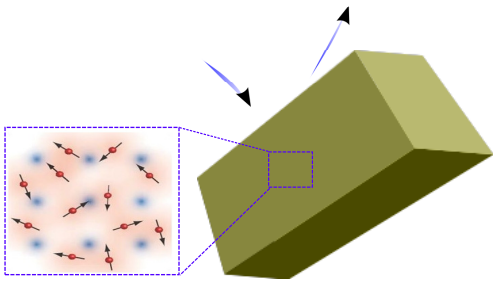

FIGURE 1.1: Microscopically a solid can be viewed as a system of many interacting electrons and nuclei, as illustrated in the zoom, in which the red spheres are the electrons with their intrinsic spin (arrows) and the blue points represent the periodic arrangement of atoms in the crystal. One can study this piece of a solid by measuring its responses to external perturbations, e.g. electromagnetic radiation (illustrated by the the curved arrows).

The quantum mechanical description of these many interacting electrons rests upon the impractical solution of the electronic Hamiltonian

$$H = \sum_{\sigma} \int d\mathbf{r} \psi^{\dagger}_{\sigma}(\mathbf{r}) \left[-\nabla^2 + V_{ext}(\mathbf{r}) \right] \psi_{\sigma}(\mathbf{r}) + \frac{1}{2} \sum_{\sigma\sigma'} \int d\mathbf{r} d\mathbf{r}' \psi^{\dagger}_{\sigma}(\mathbf{r}) \psi^{\dagger}_{\sigma'}(\mathbf{r}') V(\mathbf{r} - \mathbf{r}') \psi_{\sigma'}(\mathbf{r}') \psi_{\sigma}(\mathbf{r}), \tag{1.1}$$

where $V_{ext}(\mathbf{r}) = \sum_I v_{ext}(\mathbf{R}_I - \mathbf{r})$ is the periodic atomic potential ($\mathbf{R}_I$ denotes the atomic positions), $V(\mathbf{r} - \mathbf{r}')$ is the electron-electron interaction potential, and $\psi^{\dagger}_{\sigma}(\mathbf{r})$, $\psi_{\sigma}(\mathbf{r})$ are the field operators. It is noteworthy that we treat the ions as if they are static due to their much larger mass than the mass of electrons. This approximation is called Born-Oppenheimer approximation.

Alternatively, one can study this many-body system by its responses to external perturbations, as illustrated by the curved arrows in figure 1.1. In principle, one can investigate many of its properties by measuring how its free energy changes due to external perturbations, that is, measuring its derivatives [16]. We begin by writing the partition function, related to the free-energy, as a path integral [17]

$$Z = e^{-F} = \int D[\psi^{\dagger}\psi] e^{-S}, \tag{1.2}$$

where $\psi^{\dagger}$ and ψ are the Grassman variables [17, 18] (see appendix A), F is the free energy, and S is the action determined by the Hamiltonian 1.1.

Let us now select an observable quantity of interest A which will be coupled to

the source field J. This results in a modified action[1] $S' = S + JA$, with the resulting partition function given by

$$Z[J] = e^{-F[J]} = \int D[\psi^\dagger \psi] e^{-(S+JA)}, \tag{1.3}$$

showing that, in this case, the free energy becomes a functional of J. It is important to mention that changes in J give us the correlation functions, e.g. the Green's function, of our system.

In order to eliminate the J-dependence of the free energy, we perform a Legendre transform in favor of our observable A,

$$\Gamma = F[J] - pJ, \tag{1.4}$$

where

$$p = \frac{\delta F[J]}{\delta J} = A, \tag{1.5}$$

by using equation 1.3. Therefore, we obtain a new functional of the observable A written as

$$\Gamma[A] = F[J[A]] - AJ[A]. \tag{1.6}$$

This functional $\Gamma[A]$, called effective action functional,[2] allows us to study the response of our many-body system by means of changes in A.

When we set the source field $J = 0$, the observable A turns into the physical observable A_r. In this case $J[A_r] = 0$, allowing us to obtain the physical free energy of our system by evaluating the effective action functional at A_r [19], that is

$$F_r = \Gamma[A_r]. \tag{1.7}$$

Further, if we take the variational derivative of $\Gamma[A]$ with respect to A we obtain

$$\frac{\delta \Gamma}{\delta A} = \frac{\delta F}{\delta J}\frac{\delta J}{\delta A} - J - A\frac{\delta J}{\delta A} = -J. \tag{1.8}$$

Since $J[A_r] = 0$, we get $\frac{\delta \Gamma}{\delta A}\Big|_{A=A_r} = 0$, which means that $\Gamma[A]$ is extremized at the physical observable A_r, or, in other words, in the absence of external source fields.

[1] It is noteworthy that JA denotes $\mathrm{Tr}(JA) = \int dx J(x)A(x)$ [11].

[2] The effective action $\Gamma[A]$ is an analog of the Gibbs free energy.

We now extend our formalism carrying out an expansion of $\Gamma[A]$ to some order in a parameter λ [11], which yields

$$\Gamma[A] = \Gamma_0[A] + \lambda_1\Gamma_1[A] + \ldots, \tag{1.9}$$

$$J[A] = J_0[A] + \lambda_1 J_1[A] + \ldots, \tag{1.10}$$

in which the index 0 in the equations above is associated to a reference system described by $S_0 + AJ_0$, which, in turn, gives the correct value of A. $J_0[A]$ in this equation is a functional called constrained field, which will be used in our derivation. This functional plays the role of an additional term which needs to be added to the reference action S_0 in order to obtain A from the reference system [11]. Also, when the observable is properly chosen the other observables of our many-body system can be obtained perturbatively from their values in this reference system. By using the effective action of the reference system Γ_0, which is given by

$$\Gamma_0[A] = F_0[J_0] - AJ_0, \tag{1.11}$$

we can split $\Gamma[A]$ as follows

$$\Gamma[A] = \Gamma_0[A] + \Delta\Gamma[A]. \tag{1.12}$$

As a result, the effective action functional now becomes a functional of A and J_0

$$\Gamma[A, J_0] = F_0[J_0] - AJ_0 + \Delta\Gamma[A]. \tag{1.13}$$

The variational derivatives of this functional with respect to A and J_0 lead to the following [3]

$$\left(\frac{\delta\Gamma[A, J_0]}{\delta A}\right)_{J_0} = -J_0 + \frac{\delta\Delta\Gamma[A]}{\delta A}, \tag{1.14}$$

and

$$\left(\frac{\delta\Gamma[A, J_0]}{\delta J_0}\right)_{A} = \frac{\delta F_0[J_0]}{\delta J_0} - A. \tag{1.15}$$

As demonstrated previously the functional Γ is extremized at A_r. Therefore, from equation 1.14 we obtain

$$J_0[A_r] = \frac{\delta\Delta\Gamma[A]}{\delta A}\Big|_{A_r}. \tag{1.16}$$

[3] In our notation $(\frac{\delta f(a,b,\ldots)}{\delta b})_a$ denotes the derivative of f with respect to b, with a as a constant; while $\frac{\delta f(a,b,\ldots)}{\delta b}|_{a_r}$ denotes the derivative of f with respect to b applying a_r.

In addition, from the Legendre transform used to obtain equation 1.11 we know that $A = \frac{\delta F_0[J_0]}{\delta J_0}$. Therefore, from equation 1.15 we obtain that Γ is also stationary in J_0. Equation 1.16 and the definition of $J_0[A]$ determine exactly the constrained field of the problem. It is important to mention that the observable A and the reference system determine the structure of the theoretical approach used.

In the following we apply this formalism to derive the main equations of density functional theory (DFT) (section 1.2), Baym-Kadanoff functional (section 1.3), dynamical mean field theory (DMFT) (section 1.4), and the combination DFT+DMFT (section 1.5).

1.2 Density Functional Theory

Density Functional Theory (DFT) is in principle an exact theory of many-body systems. In fact, it provides an alternative solution of the electronic Hamiltonian 1.1 focusing on the electron density of the interacting electron system. To date electronic structure methods based on DFT have been successfully applied in the understanding and predictions of the ground-state properties of many materials known as weakly-correlated materials, such as conventional metals, insulators, and semiconductors. Such accomplishment encouraged the usage of DFT-based computational simulations as a guide to design materials with desired properties [20].

Fundamentally DFT is based upon the assumption that any ground-state property of a system of many interacting electrons is a functional of the ground-state electron density. This leads to an enormous simplification when solving the electronic Hamiltonian. Indeed, instead of solving a problem of $3N$ variables to obtain the many-body wave function $\Psi(\mathbf{r}_1, \mathbf{r}_2, \ldots, \mathbf{r}_N)$, one can solve a problem of three variables to obtain the ground-state electron density. This assumption is established on two fundamental theorems known as Hohenberg-Kohn theorems [21], which are presented below.

1.2.1 Hohenberg-Kohn Theorems

Theorem 1.2.1. *For any system of interacting electrons the ground-state electron density* $\rho_o(\mathbf{r})$ *uniquely determines the external potential* $V_{ext}(\mathbf{r})$*, that is,*

$$V_{ext}(\mathbf{r}) = V_{ext}[\rho_o](\mathbf{r}). \tag{1.17}$$

Since the Hamiltonian is uniquely determined by the external potential $V_{ext}(\mathbf{r})$, it follows that the many-body wave function of the system is also determined if we know the ground-state electron density. Hence, one can state that ρ_o contains all the information about the system of interacting electrons, as the many-body wave function. From this the many-body wave function can be viewed as a functional of ρ_o, $\Psi[\rho_o]$. We emphasize that this theorem gives to the density ρ_o the status of a key quantity from which the physical properties of the many-body system can be obtained.

Theorem 1.2.2. *There exists an universal functional for the energy* $E[\rho]$ *which can be defined for any external potential* V_{ext}*. The energy functional* $E[\rho]$ *is minimum for the exact ground-state electron density* $\rho_o(\mathbf{r})$*.*

The proofs of these theorems are presented in appendix B. Overall, this reformulation of the many-body problem proposed by Hohenberg and Kohn introduces the concept of functionals of the electron density, which are unknown in principle. Although the first work by Hohenberg and Kohn establishes the fundamental theorems of a theory of density functionals, the forms of these functionals were unknown until the work by Kohn and Sham [22], where they presented further approximations for the functionals and the so-called Kohn-Sham equations.

1.2.2 Kohn-Sham equations

In this section we derive the Kohn-Sham formulation of DFT starting from the effective action formalism. For this purpose we consider the observable A as being the electron density $\rho(\mathbf{r})$ of an interacting electron system under an external potential $V_{ext}(\mathbf{r})$. By using the interacting Green's function one can express the electron density as a sum over

Matsubara frequencies[4] ω as it follows

$$\rho(\mathbf{r}) = T\sum_{i\omega} G(\mathbf{r},\mathbf{r},i\omega)e^{i\omega 0^+}, \tag{1.18}$$

where T is the temperature and $G(\mathbf{r},\mathbf{r},i\omega)$ is the interacting Green's function on the imaginary frequency axis.

To construct the DFT effective action we couple the electron density to a source field J such that the action becomes a functional

$$S'[J] = S + \int dx J(x)\psi^\dagger(x)\psi(x), \tag{1.19}$$

where $x = (\mathbf{r},\tau)$ is the space-imaginary time coordinate. To obtain this equation we used the density operator written in terms of the field operators, that is, $\hat{\rho}(x) = \psi^\dagger(x)\psi(x)$. Then the DFT effective action is obtained by a Legendre transform in favor of the electron density

$$\Gamma[\rho] = F[J] - \int dx J(x)\rho(x), \tag{1.20}$$

where

$$\rho(x) = \frac{\delta F[J]}{\delta J} \tag{1.21}$$

is the electron density in the presence of J. In the following we restrict ourselves to time independent source field and electron density.

Likewise in the Kohn-Sham formulation of DFT, we introduce a reference system of noninteracting electrons moving in an effective potential denoted by V_{KS}, which results from the external potential V_{ext} due to the ions and from an effective potential due to the remaining electron-electron interactions, described by V_{aux},

$$V_{KS}(\mathbf{r}) = V_{ext}(\mathbf{r}) + V_{aux}(\mathbf{r}). \tag{1.22}$$

With this potential, the electron density of the interacting system is obtained as the electron density of the reference system. This mapping, denoted by Kohn-Sham *ansatz* [23],

[4] At finite temperature, the single-particle Green's function is derived in the imaginary time formalism, resulting in $G(\tau)$, whose Fourier transform corresponds to $G(i\omega_n)$, where ω_n are the Matsubara frequencies. For fermions these frequencies are given by $\omega_n = (2n+1)\pi T$, where T is the temperature. In this chapter we omitted the subindex n associated with ω_n.

is illustrated in figure 1.2. Accordingly, the DFT constrained field is the auxiliary potential $J_0 \equiv V_{aux}[\rho]$ (see appendix C).

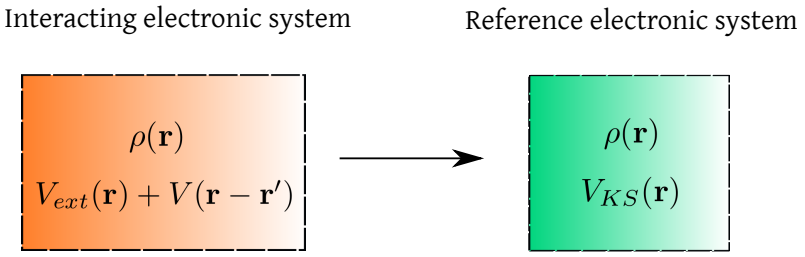

FIGURE 1.2: Ilustration of the mapping of the interacting electronic system into a reference system of noninteracting electrons under an effective potential V_{KS}.

Hence the Hamiltonian of the reference system reads

$$H = -\nabla^2 + V_{ext}(\mathbf{r}) + V_{aux}(\mathbf{r}). \tag{1.23}$$

We also write the noninteracting Green's function

$$G_0^{-1}(\mathbf{r}, \mathbf{r}', i\omega) = \delta(\mathbf{r} - \mathbf{r}')[i\omega + \mu + \nabla^2 - V_{ext}(\mathbf{r})], \tag{1.24}$$

and the full Green's function as it follows

$$\begin{aligned} G^{-1}(\mathbf{r}, \mathbf{r}', i\omega) =& \delta(\mathbf{r} - \mathbf{r}')[i\omega + \mu + \nabla^2 - V_{ext}(\mathbf{r}) - V_{aux}(\mathbf{r})] \\ =& G_0^{-1}(\mathbf{r}, \mathbf{r}', i\omega) - V_{aux}(\mathbf{r})\delta(\mathbf{r} - \mathbf{r}'). \end{aligned} \tag{1.25}$$

Notice that G determines the electron density $\rho(\mathbf{r})$ of the interacting electronic system, as can be seen from equation 1.18.

Using the Green's function of the reference system, we then write the DFT effective action as a functional of ρ and V_{aux},[5]

$$\begin{aligned} \Gamma_{DFT}[\rho, V_{aux}] &= F_0[V_{aux}] - \int \rho(\mathbf{r}) V_{aux}(\mathbf{r}) d\mathbf{r} + \Delta\Gamma[\rho] \\ &= -T \sum_{i\omega} \mathrm{Tr} \ln(i\omega + \mu + \nabla^2 - V_{ext}(\mathbf{r}) - V_{aux}(\mathbf{r})) - \int \rho(\mathbf{r}) V_{aux}(\mathbf{r}) d\mathbf{r} + \Delta\Gamma[\rho]. \end{aligned} \tag{1.26}$$

In addition, the interaction energy functional $\Delta\Gamma[\rho]$, which corresponds to what has been left out from the effective action of the reference system, can be written in terms of the

[5]The Free energy functional can be written in terms of the Green's function as $F[V_{aux}] = -\mathrm{Tr} \ln[G_0^{-1} - V_{aux}]$ [11].

Hartree and the resulting exchange-correlation energy functional at finite temperature,

$$\Delta\Gamma[\rho] = \Phi_H[\rho] + \Phi_{xc}[\rho], \tag{1.27}$$

with $\Phi_H[\rho](\mathbf{r}) = \int \frac{\rho(\mathbf{r})\rho(\mathbf{r}')}{|\mathbf{r}-\mathbf{r}'|} d\mathbf{r}d\mathbf{r}'$. At zero temperature Φ_{xc} becomes the standard exchange correlation functional energy of DFT, which can be written as $\Phi_{xc}[\rho] = T_c[\rho] + \Phi_x[\rho] + \Phi_c[\rho]$, where $\Phi_x[\rho]$ and $\Phi_c[\rho]$ are the exchange and correlation energy functionals, respectively. It is noteworthy that in this case the functional $T_c[\rho]$ corresponds to the amount of the kinetic energy due to correlations between the interacting electrons. That is, one can decompose the kinetic-energy functional $T[\rho]$ of interacting electrons as $T[\rho] = T_s[\rho] + T_c[\rho]$, where $T_s[\rho]$ is the kinetic-energy functional of noninteracting particles [24]. Therefore, the DFT effective action reads

$$\begin{aligned}\Gamma_{DFT}[\rho, V_{aux}] = -T\sum_{i\omega} \mathrm{Tr}\ln(i\omega + \mu + \nabla^2 - V_{ext}(\mathbf{r}) - V_{aux}(\mathbf{r})) - \int \rho(\mathbf{r})V_{aux}(\mathbf{r})d\mathbf{r} \\ + \int \frac{\rho(\mathbf{r})\rho(\mathbf{r}')}{|\mathbf{r}-\mathbf{r}'|} d\mathbf{r}d\mathbf{r}' + \Phi_{xc}[\rho].\end{aligned} \tag{1.28}$$

As we pointed out before, this functional must be stationary at the physical electron density ρ_r, which yields

$$\left.\frac{\delta\Gamma}{\delta\rho}\right|_{\rho_r} = -V_{aux}(\mathbf{r})[\rho_r] + 2\int \frac{\rho_r(\mathbf{r})}{|\mathbf{r}-\mathbf{r}'|} d\mathbf{r} + \left.\frac{\delta\Phi_{xc}[\rho]}{\delta\rho}\right|_{\rho_r} = 0, \tag{1.29}$$

resulting into

$$V_{aux}(\mathbf{r})[\rho_r] = V_H[\rho_r](\mathbf{r}) + V_{xc}[\rho_r](\mathbf{r}), \tag{1.30}$$

where

$$V_H[\rho_r](\mathbf{r}) = 2\int \frac{\rho_r(\mathbf{r})}{|\mathbf{r}-\mathbf{r}'|} d\mathbf{r} \tag{1.31}$$

is the Hartree potential.

The form of the exchange-correlation potential $V_{xc}[\rho_r]$ is not known exactly, making further approximations needed to practical calculations. Approximations for this term, at zero temperature, will be discussed in subsection 1.6.1. One can see that $V_{aux}(\mathbf{r}) = V_H(\mathbf{r}) + V_{xc}(\mathbf{r})$ is the term which must be added to the Hamiltonian $H_0 = -\nabla^2 + V_{ext}(\mathbf{r})$ to reproduce the exact electron density of the interacting system.

Once we know $V_{KS}[\rho]$, in practice, it is convenient to write the single-particle eigenvalue equation for the reference system as it follows

$$(-\nabla^2 + V_{KS}[\rho](\mathbf{r}))\psi_{\mathbf{k}j}(\mathbf{r}) = \epsilon_{\mathbf{k}j}\psi_{\mathbf{k}j}(\mathbf{r}), \tag{1.32}$$

where $\psi_{\mathbf{k}j}(\mathbf{r})$ are the Kohn-Sham states with j band index. Thus, it follows that at zero-temperature the electron density can be written in terms of these Kohn-Sham states,

$$\rho(\mathbf{r}) = \sum_{\mathbf{k}j} \psi^*_{\mathbf{k}j}(\mathbf{r})\psi_{\mathbf{k}j}(\mathbf{r}), \tag{1.33}$$

in which the sum goes over the occupied Kohn-Sham states. Equations 1.32 and 1.33, known as Kohn-Sham equations of DFT, are solved self-consistently since V_{KS} is a functional of the density, which in turn depends on the Kohn-Sham states as in equation 1.33. In figure 1.3 we illustrate a generic self-consistent cycle employed in DFT calculations.

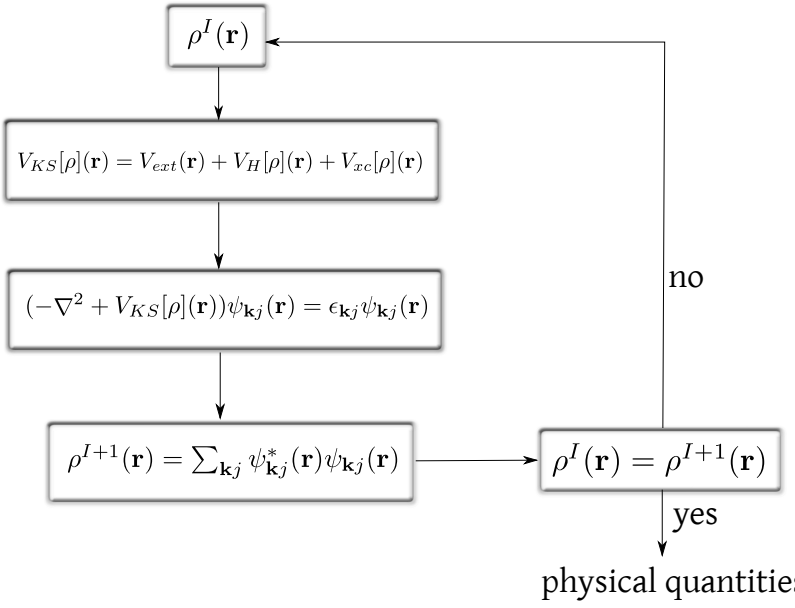

FIGURE 1.3: Schematic representation of the self-consistent cycle of DFT.

1.3 Baym-Kadanoff Functional

We now turn to a Green's function based method in which we derive the Baym-Kadanoff functional. Green's function based methods have the advantage, in comparison with

DFT,[6] that the excitation spectra of the system of many interacting electrons can be obtained from the poles of the one-particle Green's function [11]. In this section we derive the Baym-Kadanoff functional, which is constructed within the effective action framework (discussed in section 1.1) by choosing the observable A as the one-particle Green's function.

We define the one-electron Green's function by

$$G(x,x') = -\langle T_\tau \psi(x)\psi^\dagger(x')\rangle, \tag{1.34}$$

where $x = (\mathbf{r},\tau)$, T_τ is the time-ordering operator, and $\psi(x), \psi^\dagger(x)$ are the field operators. By adding a source field $J(x,x')$ to the action we obtain

$$S'[J] = S + \int dx dx' J(x,x')\psi^\dagger(x)\psi(x'), \tag{1.35}$$

with the corresponding free energy,

$$e^{-F[J]} = \int D[\psi^\dagger\psi] e^{-S'[J]}. \tag{1.36}$$

The Baym-Kadanoff functional is then obtained by the Legendre transform in favor of $G(x,x')$, as it follows

$$\Gamma_{BK}[G] = F[J] - \mathrm{Tr}(JG), \tag{1.37}$$

where the Green's function in the presence of the source field is given by

$$G(x,x') = \frac{\delta F}{\delta J(x',x)}. \tag{1.38}$$

Further, one can split $\Gamma_{BK}[G]$ into the effective action $\Gamma_0[G]$, associated with a noninteracting Hamiltonian, and the so-called Luttinger-Ward functional [11],

$$\Gamma_{BK}[G] = \Gamma_0[G] + \Phi_{LW}[G], \tag{1.39}$$

with the effective action $\Gamma_0[G]$ given by

$$\Gamma_0[G] = F_0[J_0] - \mathrm{Tr}(J_0 G). \tag{1.40}$$

[6] The Kohn-Sham eigenvalues are not the true excitation spectra of a system of many interacting electrons [23].

As the free energy associated with the noninteracting Hamiltonian is given by [17]

$$F_0[J_0] = -\operatorname{Tr}\ln(J_0 - G_0^{-1}), \tag{1.41}$$

we obtain from equation 1.38

$$J_0[G] = G_0^{-1} - G^{-1}. \tag{1.42}$$

Then the Baym-Kadanoff functional is rewritten as

$$\Gamma_{BK}[G] = \operatorname{Tr}\ln G - \operatorname{Tr}((G_0^{-1} - G^{-1})G) + \Phi_{LW}[G]. \tag{1.43}$$

As we know, this functional is extremized at the physical Green's functional G_r,

$$\left.\frac{\delta\Gamma_{BK}[G]}{\delta G}\right|_{G_r} = G_r^{-1} - G_0^{-1} + \left.\frac{\delta\Phi_{LW}}{\delta G}\right|_{G_r} = 0, \tag{1.44}$$

where G_r is the physical interacting Green's function. Using equation 1.42 we obtain the constrained field in terms of the Luttinger-Ward functional,

$$\Sigma_r[G_r] \equiv J_0[G_r] = \left.\frac{\delta\Phi_{LW}}{\delta G}\right|_{G_r}. \tag{1.45}$$

Similarly as it has been done for DFT (see equation 1.25 and remember that in that case $J_0 = V_{aux}$), we find that if Σ_r is added to the noninteracting Green's function of the reference system, the resulting Green's function becomes

$$G_r^{-1}(\mathbf{r}, \mathbf{r}', i\omega) = G_0^{-1}(\mathbf{r}, \mathbf{r}', i\omega) - \Sigma_r(\mathbf{r}, \mathbf{r}', i\omega), \tag{1.46}$$

with G_0 given by

$$G_0^{-1}(\mathbf{r}, \mathbf{r}', i\omega) = \delta(\mathbf{r} - \mathbf{r}')[i\omega + \mu + \nabla^2 - V_{ext}(\mathbf{r})]. \tag{1.47}$$

Equation 1.46 is known as the Dyson equation, which is usually written as a geometric expansion of the one-particle Green's function in terms of G_0 and $\Sigma_r(\mathbf{r}, \mathbf{r}', i\omega)$, called the self-energy [17].

Moreover, one can write down the Baym-Kadanoff functional in terms of G and Σ as it follows

$$\Gamma_{BK}[G,\Sigma] = -\operatorname{Tr}\ln(G_0^{-1}-\Sigma) - \operatorname{Tr}(\Sigma G) + \Phi_{LW}[G]. \tag{1.48}$$

Evaluating its variational derivatives with respect to G and Σ we obtain

$$\Big(\frac{\delta\Gamma_{BK}}{\delta G}\Big)_{\Sigma} = -\Sigma_r + \frac{\delta\Phi_{LW}}{\delta G}\bigg|_{Gr} = 0, \tag{1.49}$$

$$\Big(\frac{\delta\Gamma_{BK}}{\delta \Sigma}\Big)_{G} = (G_0^{-1}-\Sigma)^{-1} - G = 0, \tag{1.50}$$

which, when evaluated at physical G_r and Σ_r, lead to the equations 1.45 and 1.44.

In the next section we will obtain a functional of the *local* Green's function, instead that of the full Green's function, as considered in the Baym-Kadanoff theory. The introduction of a functional method based on the local Green's function is motivated by the assumption that this is a good quantity to describe the energetics and the excitation spectrum of strongly correlated materials [11].

1.4 Dynamical Mean Field Theory

To obtain the DMFT effective functional, we now focus on the local Green's function G_{loc} rather than on the full Green's function presented in the Baym-Kadanoff theory. To construct its effective action functional, we begin by considering an interacting system with Hamiltonian written using a general tight-binding basis set,

$$\begin{aligned} H = &\sum_{\alpha\beta}\sum_{RR'} h^{(0)}_{\alpha R\beta R'}(c^{\dagger}_{\alpha R}c_{\beta R'} + c_{\alpha R}c^{\dagger}_{\beta R'}) \\ &+ \frac{1}{2}\sum_{\alpha\beta\gamma\delta}\sum_{RR'R''R'''} V^{RR'R''R'''}_{\alpha\beta\gamma\delta}\, c^{\dagger}_{\alpha R}c^{\dagger}_{\beta R'}c_{\delta R'''}c_{\gamma R''}, \end{aligned} \tag{1.51}$$

where α, β, γ, and δ correspond to angular momentum index lm, whereas R, R', R'', and R''' are the unit cell index (for more details about the basis set see appendix D). Notice that this Hamiltonian is a full interacting Hamiltonian containing different sorts of interactions denoted by $V^{RR'R''R'''}_{\alpha\beta\gamma\delta}$. Simple-model Hamiltonians can be derived from equation 1.51, e.g. assuming short-range Coulomb interactions one gets the so-called Hubbard model.

Let us now add a local source field $J_{loc,R\alpha\beta}(\tau,\tau')$ to the action describing the Hamiltonian 1.51, resulting into the modified action

$$S'[J_{loc,R\alpha\beta}] = S + \sum_{R\alpha\beta}\int d\tau d\tau' J_{loc,R\alpha\beta}(\tau,\tau')c^{\dagger}_{R\alpha}(\tau)c_{R\beta}(\tau'), \tag{1.52}$$

with corresponding free energy,

$$e^{-F[J_{loc,R\alpha\beta}]} = \int dc^{\dagger}dc e^{-S-\sum_{R\alpha\beta}\int d\tau d\tau' J_{loc,R\alpha\beta}(\tau,\tau')c^{\dagger}_{R\alpha}(\tau)c_{R\beta}(\tau')}. \tag{1.53}$$

For simplicity, in the following we omit the $R\alpha\beta$ index of J_{loc}. The DMFT effective action functional is thus obtained through a Legendre transform in favor of G_{loc},

$$\Gamma_{DMFT}[G_{loc}] = F[J_{loc}] - \mathrm{Tr}(J_{loc}G_{loc}), \tag{1.54}$$

where

$$G_{loc,\alpha\beta}(\tau,\tau') = \frac{\delta F[J_{loc}]}{\delta J_{loc,R\beta\alpha}(\tau',\tau)} = -\langle T_{\tau}c_{R\alpha}(\tau)c^{\dagger}_{R\beta}(\tau')\rangle. \tag{1.55}$$

We now introduce a reference system of noninteracting electrons described by the simplified Hamiltonian

$$H_0 = \sum_{\alpha\beta}\sum_{RR'} h^{(0)}_{\alpha R\beta R'}(c^{\dagger}_{\alpha R}c_{\beta R'} + c_{\alpha R}c^{\dagger}_{\beta R'}), \tag{1.56}$$

with electronic bands described by $\hat{h}^{(0)}(\mathbf{k})$, which is the Fourier transform of $h^{(0)}_{\alpha R\beta R'}$. The noninteracting Green's function associated with this reference system is given by

$$G_0^{-1} = (i\omega+\mu)\hat{I} - \hat{h}^{(0)}(\mathbf{k}), \tag{1.57}$$

where $\hat{I}$ is the unitary matrix. Similarly as for the Baym-Kadanoff case, the effective action for this noninteracting system reads

$$\Gamma_0[G_{loc}] = F_0[J_{0,loc}] - \mathrm{Tr}(J_{0,loc}G_{loc}), \tag{1.58}$$

with

$$F_0[J_{0,loc}] = -\,\mathrm{Tr}\ln(J_{0,loc} - G^{-1}_{0,loc}), \tag{1.59}$$

yielding

$$J_{0,loc}[G_{loc}] = G_{0,loc}^{-1} - G_{loc}^{-1}. \tag{1.60}$$

Therefore, the DMFT effective action functional is given by

$$\begin{aligned}\Gamma_{DMFT}[G_{loc}] &= \Gamma_0[G_{loc}] + \Phi_{DMFT}[G_{loc}] \\ &= -\operatorname{Tr}\ln(J_{0,loc} - G_0^{-1}) - \operatorname{Tr}(J_{0,loc}G_{loc}) + \Phi_{DMFT}[G_{loc}],\end{aligned} \tag{1.61}$$

where $\Phi_{DMFT}[G_{loc}]$ is the local counterpart of the Lutting-Ward functional. In addition, from equations 1.60 and 1.57 we write the local Green's function in terms of the constrained field

$$G_{loc,\alpha\beta}(i\omega) = \sum_{\mathbf{k}}[(i\omega+\mu)\hat{I} - \hat{h}^0(\mathbf{k}) - J_{0,loc}(i\omega)]^{-1}_{\alpha\beta}. \tag{1.62}$$

Further, we can rewrite the DMFT functional considering that G_{loc} and $J_{0,loc}$ are independent variables,

$$\begin{aligned}\Gamma_{DMFT}[G_{loc}, J_{0,loc}] = &-\sum_{\mathbf{k}} \operatorname{Tr}\ln[(i\omega+\mu)\hat{I} - \hat{h}^0(\mathbf{k}) - J_{0,loc}(i\omega)] \\ &- \operatorname{Tr}(J_{0,loc}G_{loc}) + \Phi_{DMFT}[G_{loc}].\end{aligned} \tag{1.63}$$

This effective functional is stationary at the physical local Green's function G^r_{loc}, which yields

$$\Sigma^r_{loc} \equiv J_{0,loc}[G_{loc}] = \left.\frac{\delta\Phi_{DMFT}[G_{loc}]}{\delta G_{loc}}\right|_{G^r_{loc}}. \tag{1.64}$$

Thus we find that the constrained field is the local self-energy, which can be obtained from $\Phi_{DMFT}[G_{loc}]$. We notice that (see equation 1.62) Σ^r_{loc} plays the role of a frequency-dependent potential that has to be added to the noninteracting Hamiltonian to obtain the physical local Green's function G^r_{loc}.

One can also derive the DMFT effective action functional starting from the atomic limit, in which the auxiliary system turns into an atom embedded in a medium. In this case, the interacting Hamiltonian can be written as $H = H_0 + H_1$, where $H_0 =$

$\sum_R H_{at}[R]$ with

$$H_{at}[R] = \sum_{\alpha\beta} h^{(0)}_{\alpha R\beta R}(c^\dagger_{\alpha R}c_{\beta R} + c_{\alpha R}c^\dagger_{\beta R}) + \frac{1}{2}\sum_{\alpha\beta\gamma\delta} V^{RRRR}_{\alpha\beta\gamma\delta} c^\dagger_{\alpha R}c^\dagger_{\beta R}c_{\delta R}c_{\gamma R}, \tag{1.65}$$

and H_1 is the interaction term [11]. $H_{at}[R]$ gives rise to the following action

$$S_{at} = \int d\tau \sum_{\alpha\beta} c^\dagger_{\alpha R}(\tau)(\partial_\tau - \mu)c_{\beta R}(\tau) + \int d\tau H_{at}(\tau). \tag{1.66}$$

By adding a source field $\Delta_{\alpha\beta}(\tau,\tau')$ to this action, we obtain

$$S' = S_{at} + \sum_{\alpha\beta}\int d\tau d\tau' \Delta_{\alpha\beta}(\tau,\tau')c^\dagger_{\alpha R}(\tau)c_{\beta R}(\tau). \tag{1.67}$$

$\Delta_{\alpha\beta}(\tau,\tau')$ gives the hybridization function of the atom located in R with an effective medium. It is important to mention that this atom embedded in an effective medium constitutes a quantum impurity problem, which is an auxiliary problem that has to be solved within DMFT. Thus DMFT can be viewed as a treatment where a lattice problem is mapped into a single-impurity problem embedded in a self-consistent bath.

The free energy of this atom yields

$$e^{-F_{at}[\Delta]} = \int dc^\dagger dc e^{-S_{at} - \sum_{\alpha\beta}\int d\tau d\tau' \Delta_{\alpha\beta}(\tau,\tau')c^\dagger_\alpha(\tau)c_\beta(\tau')}. \tag{1.68}$$

The resulting free energy of the set of atoms is then given by

$$e^{-F[\Delta]} = \int dc^\dagger dc e^{-\sum_R S_{at} - \sum_{R\alpha\beta}\int d\tau d\tau' \Delta_{\alpha\beta}(\tau,\tau')c^\dagger_{\alpha R}(\tau)c_{\beta R'}(\tau')}. \tag{1.69}$$

Kotliar and Savrasov [25] showed that this free energy leads to the DMFT effective functional in terms of local Green's function, self-energy and hybridization function, which is given by

$$\Gamma_{DMFT}[G_{loc}[\Delta],\Sigma[\Delta]] = F[\Delta] - \mathrm{Tr}\ln G_{loc} - \sum_{\mathbf{k}} \mathrm{Tr}\ln[(i\omega+\mu)\hat{I} - \hat{h}^{(0)}(\mathbf{k}) - \Sigma_{loc}] - \sum_{i\omega}(\Sigma_{loc} - i\omega - \mu + E_{imp} + \Delta)G_{loc}, \tag{1.70}$$

where E_{imp} is the atom level. Since this functional is extremized at the local physical Green's function (denoted by superscript r) we obtain

$$\left.\frac{\delta\Gamma_{DMFT}}{\delta G_{loc}}\right|_{G^r_{loc}} = -G^{r-1}_{loc} - \Sigma^r_{loc} + i\omega + \mu - E_{imp} - \Delta = 0, \tag{1.71}$$

where the hybridization function becomes

$$\Delta(i\omega) = i\omega + \mu - E_{imp} - \Sigma^r_{loc}(i\omega) - G^{r-1}_{loc}(i\omega). \tag{1.72}$$

Using equations 1.62 and 1.71 we obtain the so-called DMFT self-consistent equation

$$G^r_{loc,\alpha\beta} = \sum_{\mathbf{k}}[(i\omega+\mu)\hat{I} - \hat{h}^{(0)}(\mathbf{k}) - \Sigma^r_{loc}]^{-1}_{\alpha\beta} = (i\omega + \mu - E_{imp} - \Delta - \Sigma^r_{loc})^{-1}_{\alpha\beta}, \tag{1.73}$$

where, as written in equation 1.64, Σ^r_{loc} is obtained from Φ_{DMFT}. The equation 1.73 reveals the condition of the Green's function of the quantum impurity problem to be equivalent to the local Green's function of the lattice problem. It is worth mentioning that these equations are solved using a self-consistent cycle, which will be discussed in the next section in the context of DFT+DMFT theory.

1.5 DFT+DMFT theory

Over decades most of theoretical efforts to explain the physics of strongly correlated electron systems were done using simple model Hamiltonians, such as the Hubbard, periodic and impurity Anderson models [12]. Among the many important achievements one can mention the progress made in our physical understanding of the metal-insulator transitions driven by electronic correlations and unusual transport propeties of correlated metallic phases. These achievements have shed some light in the metal-insulator transition observed in numerous transition metal oxides, e.g. V_2O_3, and in unsual transport properties of organic Mott systems, e.g. $k-(BETD-TTF)_2Cu[N(CN)_2]Cl$. It is worth mentioning that these important accomplishments were made possible mainly due to the advent of DMFT.

DFT in the local density and generalized gradient approximations fails in the description of the physical properties of strongly correlated materials, such as several vanadium

and copper oxides and solid lanthanides and actinides, e.g. α-Ce and δ-Pu. For many years this led to an absence of material specific information in the theoretical investigations of strongly correlated materials, which in turn enabled qualitative comparisons between theoretical and experimental findings for this class of systems. To overcome this issue, Anisimov *et al.* [26] proposed a new method by combining DFT with DMFT for the calculation of the electronic structure of strongly correlated materials. In this method a LDA hamiltonian, written on a tight-binding basis set, is supplemented with Coulomb interaction for d and f electrons. To solve this interacting model DMFT is employed, taking into account many-body effects *beyond* a Hartree-Fock approximation. Notice that the Hartree-Fock approximation corresponds to the LDA+U method previously proposed by Anisimov and co-workers [27] for the description of magnetically ordered phases of $3d$-transition metal monoxides. It is worth mentioning that this approach fails to describe strongly correlated materials in the paramagnetic phase and without orbital ordering [11].

In the following subsections we briefly introduce the basis set and the projection-embedding method within the DFT+DMFT implementation [28] used in the present work. Next we return to the derivation of the effective action of the DFT+DMFT method.

1.5.1 Full-potential implementation: basis set and local quantities

As can be noticed in the previous section about DMFT, the definition of local quantities such as the local Green's function and self-energy depends on the definition of the basis set. In DFT+DMFT treatment a similar issue takes place when one has to separate the Hilbert subspace of correlated electronic states, which are treated within DMFT, from the Hilbert subspace of weakly correlated electronic states treated with DFT. In particular, it is well known that the subspace of weakly correlated electronic states comprises electrons of s and p bands, which are well described with DFT, while the correlated subspace comprises the electronic states associated with d and f bands. In this respect, previous implementations have used Wannier orbitals, tight-binding linearized Muffin thin orbitals (LMTO), nonorthogonal LMTO's, and maximally localized Wannier orbitals to span the electronic states of the correlated subspace. However, all

of them suffer from several limitations, such as the computation of electronic charge self-consistently.

The DFT+DMFT method used in our studies is implemented within a full-potential method, in which the space is separated in muffin-tin (MT) spheres, centered at atomic positions, and the remaining interstitial region. For the DFT basis set (see subsection 1.6.3), inside the MT spheres the Kohn-Sham states are spanned in a linear combination of radial functions $u_l^{\tau\kappa}(r_\tau)$ times spherical harmonics $Y_{lm}(\hat{r})$, while in the interstitial region a plane wave expansion is used. Here the τ index denotes the atomic positions $\mathbf{R}_\tau$ in such a way that a vector with the origin at $\mathbf{R}_\tau$ is given by $\mathbf{r}_\tau = \mathbf{r} - \mathbf{R}_\tau$. The κ index denotes the κ-order derivative of $u_l^\tau(r_\tau)$ with respect to r_τ, i.e. $\kappa = 0$ corresponds to $u_l^\tau(r_\tau, E_l)$, $\kappa = 1$ to $\dot{u}^\tau(r_\tau, E_l)$, etc. ($E_l$ corresponds to the linearization energies presented in subsection 1.6.3). This MT basis set, by its turn, provides a suitable choice for the DFT+DMFT calculation. In particular, in the full-potential DFT+DMFT implementation used, the correlated electronic states are spanned in a local basis set of atomic-like heavy orbitals, e.g. d and f orbitals, defined as

$$\langle \mathbf{r}|\tau\kappa L\rangle = u_l^{\tau\kappa}(r_\tau)Y_L(\hat{r}), \tag{1.74}$$

where in this case $u_l^{\tau\kappa}$ is the radial solution of the Schrödinger equation, τ is the index associated with the atom containing the correlated orbitals ("correlated atom"), and Y_L are the complex spherical harmonics with index L. Hence, the local correlated orbitals are considered as being the "heads" of a (L)APW+lo basis set (see section 1.6.3). The precise definition of L depends on the crystal field and atomic spin-orbit coupling presented in the system, so that L can denote angular momentum index lm, cubic harmonics (d_{xz}, d_{xy}, d_{yz}, $d_{x^2-y^2}$, d_{z^2} for d subshell) or relativistic harmonics jm_j.

Let us now introduce the full Green's function in real space $G(\mathbf{r}, \mathbf{r}')$ from which one wants to extract the local Green's function denoted as $\mathcal{G}(\mathbf{r}, \mathbf{r}')$. This procedure is done using a projector operator $P(\mathbf{r}\mathbf{r}', \tau LL')$ which acts on $G(\mathbf{r}, \mathbf{r}')$ in such a way that the local Green's function in orbital space is given by [28]

$$\mathcal{G}_{LL'}^\tau = \int d\mathbf{r}d\mathbf{r}' P(\mathbf{r}\mathbf{r}', \tau LL')G(\mathbf{r}, \mathbf{r}'). \tag{1.75}$$

It is important to mention that this integral is performed inside the MT sphere of size

S around the correlated atom. We emphasize that this "atomic-like" Green's function is one of the local quantities in our formalism.

The inverse procedure, denoted as embedding, is done by using the same projector. For instance one can embed the local self-energy as follows

$$\Sigma(\mathbf{r},\mathbf{r}') = \sum_{\tau LL' \in H} P(\mathbf{r}'\mathbf{r},\tau L'L)\Sigma^{\tau}_{LL'}. \tag{1.76}$$

H in the equation above denotes the Hilbert subspace of the correlated orbitals. Notice also that the projector operators obey

$$\int d\mathbf{r}d\mathbf{r}' P(\mathbf{r}\mathbf{r}',\tau L_1 L_2)P(\mathbf{r}'\mathbf{r},\tau' L_3 L_4) = \delta_{L_1 L_4}\delta_{L_2 L_3}\delta_{\tau\tau'}. \tag{1.77}$$

By applying the embedding operator onto the local Green's function in orbital space we obtain the local Green's function in real space as follows

$$\mathcal{G}(\mathbf{r},\mathbf{r}') = \sum_{\tau LL' \in H} P(\mathbf{r}'\mathbf{r},\tau L'L)\mathcal{G}^{\tau}_{LL'}. \tag{1.78}$$

Hence, from equation 1.75 we obtain the local Green's function in real space,

$$\mathcal{G}(\mathbf{r},\mathbf{r}') = \sum_{\tau LL' \in H} P(\mathbf{r}'\mathbf{r},\tau L'L)\int d\mathbf{r}_1 d\mathbf{r}_2 P(\mathbf{r}_1\mathbf{r}_2,\tau LL')G(\mathbf{r}_1,\mathbf{r}_2), \tag{1.79}$$

which will be used in the following derivation of the DFT+DMFT effective action functional.

Several different forms for this projection to the correlated orbital subspace have been proposed. In real space, the two simplest forms are given by [28]

$$P^0(\mathbf{r}\mathbf{r}',\tau LL') = Y_L(\hat{\mathbf{r}}_\tau)\delta(r-r')Y^*_{L'}(\hat{\mathbf{r}}'_\tau), \tag{1.80}$$

$$P^1(\mathbf{r}\mathbf{r}',\tau LL') = Y_L(\hat{\mathbf{r}}_\tau)u^0_l(r_\tau)u^0_{l'}(r_\tau)Y^*_{L'}(\hat{\mathbf{r}}'_\tau). \tag{1.81}$$

Using the Kohn-Sham basis set, the latter projector can be rewritten as

$$P^1_{\mathbf{k}}(ij,\tau LL') = \sum_{\kappa\kappa'} \mathcal{A}^{\tau\kappa}_{Li}(\mathbf{k})\mathcal{A}^{\tau\kappa' *}_{L'j}(\mathbf{k})\langle u^{\tau\kappa}_l|u^0_l\rangle\langle u^0_{l'}|u^{\tau\kappa'}_{l'}\rangle, \tag{1.82}$$

where $\mathcal{A}_{Li}^{\tau\kappa}(\mathbf{k}) = \sum_{\mathbf{K}} A_{\mathbf{k}+\mathbf{K},L}^{\tau\kappa}(\mathbf{k}) C_{i\mathbf{K}}^{\mathbf{k}}$. The coefficients $A_{\mathbf{k}+\mathbf{K},L}$ and $C_{i\mathbf{K}}^{\mathbf{k}}$ are the coeffiecients of the expansion in the LAPW basis set. As pointed out by Haule *et al.* [28] these two forms of projection lead to non causal DMFT equations and incorrect spectral weights. Thus, the same authors proposed an alternative projector, denoted as P^2, similar to P^1 but with renormalization factor depending on the bands within an energy window around the Fermi level. Using the Kohn-Sham states $\psi_{\mathbf{k}i}(\mathbf{r})$ and the coefficients $\mathcal{A}_{Li}^{\tau\kappa}(\mathbf{k})$, the projector P^2 is written as [28]

$$P^2(\mathbf{r}\mathbf{r}', \tau LL') = \sum_{ij\mathbf{k}\kappa\kappa'} \psi_{\mathbf{k}i}(\mathbf{r}) \mathcal{A}_{Li}^{\tau\kappa}(\mathbf{k}) \langle u_l^{\tau\kappa} | u_l^{\tau 0} \rangle \langle u_{l'}^{\tau 0} | u_{l'}^{\tau\kappa'} \rangle \mathcal{A}_{L'j}^{\tau\kappa' *}(\mathbf{k}) \psi_{\mathbf{k}j}^*(\mathbf{r}')$$
$$\times \sqrt{\left(\frac{\sum_{\kappa_1\kappa_2} \mathcal{A}_{Li}^{\tau\kappa_1} \mathcal{A}_{Li}^{\tau\kappa_2 *} \langle u_l^{\tau\kappa_1} | u_l^{\tau\kappa_2} \rangle}{\sum_{\kappa_1\kappa_2} \mathcal{A}_{Li}^{\tau\kappa_1} \mathcal{A}_{Li}^{\tau\kappa_2 *} \langle u_l^{\tau\kappa_1} | u_l^{\tau 0} \rangle \langle u_l^{\tau 0} | u_l^{\tau\kappa_2} \rangle} \right) \left(\frac{\sum_{\kappa_1\kappa_2} \mathcal{A}_{L'j}^{\tau\kappa_1 *} \mathcal{A}_{L'j}^{\tau\kappa_2} \langle u_{l'}^{\tau\kappa_1} | u_{l'}^{\tau\kappa_2} \rangle}{\sum_{\kappa_1\kappa_2} \mathcal{A}_{L'j}^{\tau\kappa_1 *} \mathcal{A}_{L'j}^{\tau\kappa_2} \langle u_{l'}^{\tau\kappa_1} | u_{l'}^{\tau 0} \rangle \langle u_{l'}^{\tau 0} | u_{l'}^{\tau\kappa_2} \rangle} \right)}. \tag{1.83}$$

This projector is the one used in our calculations.

1.5.2 Effective action of DFT+DMFT

We now turn to the derivation of the effective action of DFT+DMFT method. In this respect, we construct a functional of $\rho(\mathbf{r})$ and the correlated local Green's function $\mathcal{G}(\mathbf{r}, \mathbf{r}')$. We couple these two observables to the source fields $l(\mathbf{r})$ and $J_{LL'}^a$, respectively, leading to the modified action

$$S'[l, J_{LL'}^a] = S + \sum_{aLL' \in H} \int d\tau d\tau' J_{LL'}^a(\tau, \tau') c_{aL}^\dagger(\tau) c_{aL'}(\tau') + \int l(\mathbf{r}) \rho(\mathbf{r}) d\mathbf{r}. \tag{1.84}$$

Here the index a corresponds to the index of the atomic positions in the solid, that is an atom indicated by a is centered at $\mathbf{r}_a = r - \mathbf{R}_a$. The effective action is constructed performing a Legendre transform in favor of $\rho(\mathbf{r})$ and $\mathcal{G}(\mathbf{r}, \mathbf{r}')$ as it follows

$$\begin{aligned} \Gamma_{DFT+DMFT}[\mathcal{G}, \rho] &= F[l, J_{LL'}^a] - \mathrm{Tr}(l\rho(\mathbf{r})) - \mathrm{Tr}(\mathcal{G}J) \\ &= \Gamma_0[\mathcal{G}, \rho] + \Phi[\mathcal{G}, \rho]. \end{aligned} \tag{1.85}$$

Noticed from previous sections that $\rho(\mathbf{r}) = \frac{\delta F}{\delta l(\mathbf{r})}$ and $\mathcal{G} = \frac{\delta F}{\delta J_{LL'}^a(\tau', \tau)}$. We introduce now a reference system of electrons moving in an effective dynamic potential, with effective

action given by

$$\Gamma_0[\mathcal{G},\rho] = -\operatorname{Tr}\ln(G^{-1}) - \operatorname{Tr}(V_{aux}\rho) - \operatorname{Tr}(\Sigma^{'}\mathcal{G}), \tag{1.86}$$

where $V_{aux}(\mathbf{r}) = V_H(\mathbf{r}) + V_{xc}(\mathbf{r})$ and $\Sigma^{'} = \Sigma - E_{DC}$. Σ is the self-energy associated with the correlated orbitals and E_{DC}, the so-called double counting-correction term, which is included to avoid the double-counting of interaction energy already considered in DFT. Moreover, the interacting functional $\Phi[\mathcal{G},\rho]$ is written in terms of the Hartree $\Phi_H[\rho]$ and exchange-correlation $\Phi_{xc}[\rho]$ functionals, which are functionals of the density, and the Luttinger-Ward $\Phi_{DMFT}[\mathcal{G}]$ functional of DMFT and double-counting $\Phi_{DC}[\mathcal{G}]$ functional, which in turn, are functionals of $\mathcal{G}$ [28],

$$\Phi[\mathcal{G},\rho] = \Phi_H[\rho] + \Phi_{xc}[\rho] + \Phi_{DMFT}[\mathcal{G}] - \Phi_{DC}[\mathcal{G}]. \tag{1.87}$$

Therefore, the DFT+DMFT effective action is given by

$$\begin{aligned}\Gamma_{DFT+DMFT}[\mathcal{G},\rho] = &-\operatorname{Tr}\ln(G^{-1}) - \operatorname{Tr}(V_{aux}\rho) - \operatorname{Tr}(\Sigma^{'}\mathcal{G}) + \Phi_H[\rho] + \Phi_{xc}[\rho] \\ &+ \Phi_{DMFT}[\mathcal{G}] - \Phi_{DC}[\mathcal{G}].\end{aligned} \tag{1.88}$$

The full Green's function, by its turn, can be written in terms of the Kohn-Sham potential, which is equal to $V_{ext} + V_{aux}$ according to equation 1.22, and the shifted self-energy as follows

$$G^{-1}(\mathbf{r}\mathbf{r}', i\omega) = [i\omega + \mu + \nabla^2 - V_{ext}(\mathbf{r}) - V_{aux}(\mathbf{r})]\delta(\mathbf{r}-\mathbf{r}') - \Sigma^{'}(\mathbf{r}\mathbf{r}', i\omega), \tag{1.89}$$

where

$$\Sigma^{'}(\mathbf{r}\mathbf{r}', i\omega) = \sum_{aLL'\in H} P(\mathbf{r}'\mathbf{r}, aL'L)(\Sigma - E_{DC})^a_{LL'}. \tag{1.90}$$

It is important to mention that, differently from the density obtained in DFT method, the electron density in this case is obtained in the presence of the Kohn-Sham effective potential and a frequency-dependent self-energy, taking into account the many-body effects associated with the correlated orbitals. From equation 1.89 the electron density can be written as

$$\rho(\mathbf{r}) = T\sum_{i\omega}\langle\mathbf{r}|(i\omega+\mu+\nabla^2 - V_{KS}(\mathbf{r}) - \sum_{aLL'\in H} P(\mathbf{r}'\mathbf{r}, aL'L)(\Sigma - E_{DC})^a_{LL'}|\mathbf{r}\rangle e^{i\omega 0^+}, \tag{1.91}$$

where we remind that $V_{KS}(\mathbf{r}) = V_{ext}(\mathbf{r}) + V_{aux}(\mathbf{r})$.

Finally, the DFT+DMFT effective action in terms of the density and the local Green's function is given by

$$\Gamma_{DFT+DMFT}[\mathcal{G},\rho] =$$
$$-\operatorname{Tr}\ln\left([i\omega+\mu+\nabla^2-V_{ext}(\mathbf{r})-V_{aux}(\mathbf{r})]\delta(\mathbf{r}-\mathbf{r}')-\sum_{aLL'\in H}P(\mathbf{r}'\mathbf{r},aL'L)(\Sigma-E_{DC})^a_{LL'}\right)$$
$$-\operatorname{Tr}(V_{aux}\rho)-\operatorname{Tr}(\Sigma^{'}\mathcal{G})+\Phi_H[\rho]+\Phi_{xc}[\rho]+\Phi_{DMFT}[\mathcal{G}]-\Phi_{DC}[\mathcal{G}]. \tag{1.92}$$

Since the functional 1.92 is extremized at the physical electronic density ρ_r and local Green's function $\mathcal{G}_r$, we obtain

$$\begin{aligned} V_{aux}[\rho_r](\mathbf{r}) &= \left.\frac{\delta\Phi_H}{\delta\rho}\right|_{\rho_r}+\left.\frac{\delta\Phi_{xc}}{\delta\rho}\right|_{\rho_r} \\ &= V_H[\rho_r](\mathbf{r})+V_{xc}[\rho_r](\mathbf{r}), \end{aligned} \tag{1.93}$$

and

$$\Sigma^{'}=\Sigma_r-E_{DC,r}=\left.\frac{\delta\Phi_{DMFT}}{\delta\mathcal{G}}\right|_{\mathcal{G}_r}-\left.\frac{\delta\Phi_{DC}}{\delta\mathcal{G}}\right|_{\mathcal{G}_r}. \tag{1.94}$$

Thus, the potential $V_H[\rho_r](\mathbf{r})+V_{xc}[\rho_r](\mathbf{r})$ and the self-energy $\left.\frac{\delta\Phi_{DMFT}}{\delta\mathcal{G}}\right|_{\mathcal{G}_r}-\left.\frac{\delta\Phi_{DC}}{\delta\mathcal{G}}\right|_{\mathcal{G}_r}$ are potentials which have to be added to the reference system to obtain the physical ρ_r and $\mathcal{G}_r$ of the interacting electron system.

Similarly to DMFT one can derive an effective action starting from the atomic limit [11, 25]. In this respect, one obtain that the local Green's function in orbital space can be written as

$$\mathcal{G}^a_{LL'}=[(i\omega-E^a_{imp}-\Sigma^a-\Delta^a)^{-1}]_{LL'}, \tag{1.95}$$

where E^a_{imp} are the impurity energy levels and Δ^a the hybridization function corresponding to the correlated atom at $\mathbf{r}_a$. From equations 1.75, 1.89 and 1.95 we then obtain the

DFT+DMFT self-consistency condition

$$\int d\mathbf{r}d\mathbf{r}' P(\mathbf{r}\mathbf{r}', aLL')\Big\{[i\omega + \mu + \nabla^2 - V_{KS}(\mathbf{r})]\delta(\mathbf{r} - \mathbf{r}') - \sum_{L_1L_2 \in H} P(\mathbf{r}'\mathbf{r}, aL_1L_2)(\Sigma - E_{DC})^a_{L_2L_1}\Big\}^{-1} = [(i\omega - E^a_{imp} - \Sigma^a - \Delta^a)^{-1}]_{LL'}. \quad (1.96)$$

Using the projectors written in Kohn-Sham basis-set this self-consistency condition turns into

$$\sum_{\mathbf{k}ij} P_{\mathbf{k}}(ij, aLL')[(i\omega + \mu - \epsilon_{\mathbf{k}} - \Sigma(\omega) - E_{DC})^{-1}]_{ji} = \Big[\frac{1}{i\omega - E^a_{imp} - \Sigma^a(\omega) - \Delta^a(\omega)}\Big]_{LL'}. \quad (1.97)$$

The DFT+DMFT equations are solved self-consistently, as illustrated in figure 1.4. In this figure we numbered the mainly steps in our calculations:

1. we start from a converged electron density obtained from a previous DFT calculation;

2. using the electron density the Kohn-Sham potential is evaluated;

3. by solving the Kohn-Sham equation one obtains $\epsilon_{\mathbf{k}i}$ and $\psi_{\mathbf{k}i}$;

4. a new density $\rho(\mathbf{r})$, in presence of a self-energy and Kohn-Sham potential, is then obtained. The steps (2)-(4) compose the DFT loop (shown in figure 1.4 in indigo), which can be performed more than once to obtain a better converged electron density; we emphasize that this loop is performed using a fixed-self-energy in which the electron density is obtained in the presence of the Kohn-Sham potential and the self-energy (see equation 1.91);

5. in this step: (i) by using $\epsilon_{\mathbf{k}i}$ we evaluate the local Green's function $\mathcal{G}^a_{LL'}$; (ii) from E_{DC}, projectors, and $\epsilon_{\mathbf{k}i}$ we obtain the impurity levels $(E_{imp})_{LL'}$; (iii) we evalulate the hybridization function $\Delta^a_{LL'}$;

6. using the hybridization function, impurity levels and the Coulomb interaction $\hat{U}$ (see section 1.5.3), the quantum impurity problem is solved, from which we obtain

the new local Green's function and self-energy. The steps (5) − (6) compose the DMFT loop (shown in figure 1.4 in orange), which can be performed more than once to obtain a better converged impurity Green's function and self-energy;

7. a new density is obtained, but now using the new local Green's function and self-energy (see equation 1.91).

The steps (1) to (7), denoted as charge loop, are then repeated to obtain the charge density $\rho(\mathbf{r})$, Green's function $\mathcal{G}_{LL'}(\mathbf{r})$, chemical potential μ,[7] impurity levels $(E_{imp})_{LL'}$, and self-energies $\Sigma_{LL'}$ self-consistently.

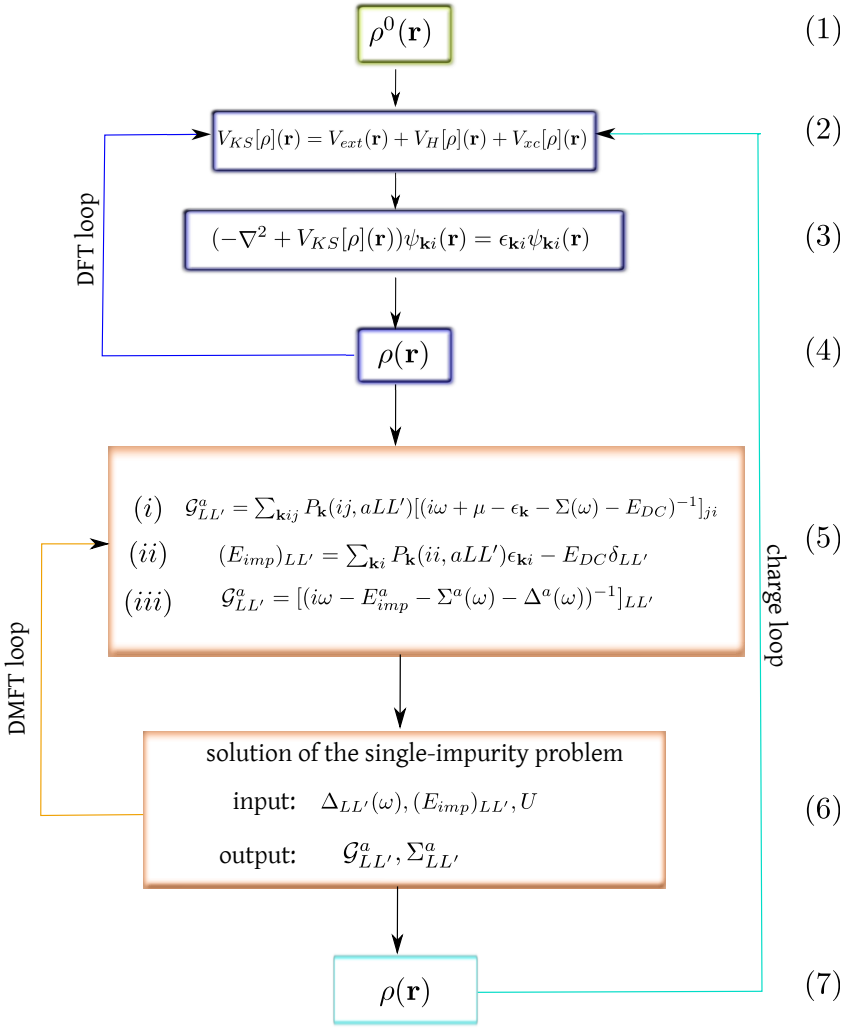

FIGURE 1.4: Schematic representation of the self-consistent cycle in DFT+DMFT calculations. We emphasize that in steps (4) and (7) the electron density is obtained in the presence of the Kohn-Sham potential and the self-energy (see equation 1.91).

[7] The steps concerning the calculation of μ can be found in Ref. [28].

1.5.3 Coulomb interaction U and double-counting correction

The Coulomb interactions between electrons in d or f bands lead to very important effects upon the electronic structure of strongly correlated materials. Due to screening effects, the local Coulomb interaction energy U is drastically reduced when going from free atomic to crystal electronic states. In fact, in the free atom $U \approx 20$ (30) eV for electrons in d shells [29] ([30]), while it takes average values between 5 and 10 eV in d bands of solids [11].

Experimentally, the effective energy[8] U_{eff} can be obtained combining x-ray photoemision spectroscopy (XPS) and bremsstrahlung isochromat spectroscopy (BIS) measurements, supplemented with theoretical calculations for a cluster model [32, 33]. For instance, Lang *et al.* [34] found values of U_{eff} ranging from 5.0 to 11.5 eV for the elements between Ce and Tm, which contain f electrons. Theoretically, different approaches have been proposed to calculate the Coulomb interactions from first-principles. We can cite first-principles self-consistent GW method [35] and constrained RPA (cRPA) within full-potential DFT [36] as examples of such methods employed to obtain and investigate the dynamical behavior of U.

If one assumes that the Coulomb interaction $\hat{U}$ has the same form in the solid as in the atom, one can parametrize it by using Slater integrals [28] (see Appendix E) as it follows

$$\hat{U} = \sum_{L_a,\ldots,L_d,q,\sigma\sigma'} \sum_{k=0}^{2l} \frac{4\pi F^k_{\{l\}}}{2k+1} < Y_{L_a}|Y_{kq}|Y_{L_c} >< Y_{L_b}|Y^*_{kq}|Y_{L_d} > f^\dagger_{L_a\sigma} f^\dagger_{L_b\sigma'} f_{L_d\sigma'} f_{L_c\sigma}, \tag{1.98}$$

where $F^k_{\{l\}}$ are the Slater integrals, Y_{L_a}, Y_{kq}, and Y_{L_c} are spherical harmonics, and $f^\dagger_{L\sigma}(f_{L\sigma})$ is the creation (annihilation) operator of one electron in orbital L (here L denotes a general angular momentum index) with spin σ. The q index runs from $-k$ to k. In particular, using the Slater integrals for $k = 0, 2$, and 4 one can define the local Coulomb interaction energy U and the Hund's coupling J [12, 37] for d orbitals ($l = 2$) as

$$U = F^0, J = \frac{(F^2 + F^4)}{14}. \tag{1.99}$$

[8] The effective energy U_{eff} is given by $U - J/2$ in some cases [31].

It is known that these Slater integrals are reduced when the correlated orbitals are embedeed in the solid. As previously shown by Kutepov *et al.* [35] the $U = F^0$ of electrons in the d states of iron is strongly screened in a solid compound in comparison with the respective value in the atom. As shown in figure 1.5 (orange line), U goes from $\approx$ 20 eV in the high-frequency region (atomic limit) to less than 6 eV when $\omega = 0$, resulting into a reduction of more than 30%. In addition, the F^2 and F^4 Slater integrals are less screened and weakly dependent on the energy.

In our calculations we consider a Coulomb interaction of the form of equation 1.98 with screened Slater integrals.

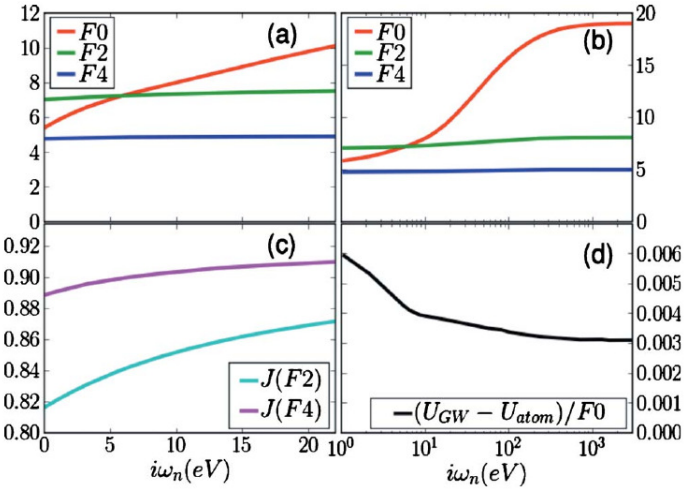

FIGURE 1.5: Screening of the on-site Coulomb interaction energy U of electrons in the d states of iron in a superconducting compound, calculated by means of first-principles self-consistent GW method. Figure taken from Ref. [35]. In (a) and (b) the Slater integrals (F^0,F^2, and F^4) are shown in a linear and logarithmic scale, respectively. For more details see Ref. [35].

We now turn to the double-counting correction term E_{DC}. The aim of this term is to subtract the electron-electron interactions of the correlated electronic states approximately taken into account within LDA or GGA, that is, to avoid the double-counting of electronic correlations. The first approximation for the E_{DC} term was introduced within the LDA+U method [38], where the double-counting functional is given by

$$\Phi_{DC}[n] = \frac{U}{2}n(n-1) - \frac{J}{2}[n^{\uparrow}(n^{\uparrow}-1) + n^{\downarrow}(n^{\downarrow}-1)], \tag{1.100}$$

where n is the number of electrons in the correlated shell. Assuming that $n^{\uparrow} = n/2$ we obtain

$$E_{DC} = \frac{\partial \Phi_{DC}}{\partial n} = U\left(n - \frac{1}{2}\right) - \frac{J}{2}(n-1), \tag{1.101}$$

which is known as the fully localized limit double-counting (FLL-DC). In this case, n is computed self-consistently throughout the charge density loop. Assuming that n does not change too much, one obtains the fixed double-counting (fixed-DC) [28] term as given by

$$E_{DC} = U\Big(n^0 - \frac{1}{2}\Big) - \frac{J}{2}(n^0 - 1), \tag{1.102}$$

where n^0 is the correlated nominal occupancy. It is worth mentioning that an exact double-counting term was recently proposed by Haule [39], which in turn shows a good agreement with the fixed-DC term in DFT+DMFT calculations for metal-transition oxides and other systems with f electrons. In our calculations we used the fixed double-counting of equation 1.102.

1.5.4 Impurity Solver: Continuous time quantum Monte Carlo

In DMFT calculations different methods have been used to solve the effective quantum impurity problem. For example, exact diagonalization, iterative perturbation theory, numerical renormalization group, and quantum monte Carlo methods have been employed as impurity solvers from which the local Green's function and self-energy are computed [10, 12].

Among these methods, the Hirsch-Fye quantum Monte Carlo (HF-QMC) was often been used as an impurity solver in DFT+DMFT calculations [11]. However, besides the fact that HF-QMC calculations can be very time-consuming, disadvantages such as systematic errors associated with time discretization and not realistic description of multiplet structure motivate distinct Monte Carlo algorithms. In this respect, the continuous time quantum Monte Carlo (CTQMC) method was introduced [40, 41]. In this method, the effective impurity partition function and the Green's function are sampled using Monte Carlo techniques (see appendix F). Since there is no time discretization, inherent shortcommings presented in HF-QMC are eliminated. Since CTQMC can be much faster for most of applications in DFT+DMFT calculations [41], during the years, its usage in DFT+DMFT calculations as an impurity solver has increased. This method is the one used to solve the effective quantum impurity problem in our DFT+DMFT calculations.

1.6 DFT: further approximations

In this section we present the further approximations considered in practice in DFT calculations. We first present the local density and generalized gradient approximations for the exchange-correlation energy functionals. Next, the pseudopotential approximation and the different basis set employed in the studies of part I of this thesis are introduced . Finally, we present the full-potential method within the (L)APW+lo basis set used in our DFT+DMFT calculations, which are presented in part II.

1.6.1 Exchange-correlation functionals

1.6.1.1 Local Density Approximation

Besides the Kohn-Sham mapping proposed in their work in 1965 [22], the authors also proposed an approximation for the exchange-correlation functional $V_{xc}[\rho](\mathbf{r})$. This approximation, denoted as Local Density Approximation (LDA), is based on the assumption that electrons in solids can be considered, under a certain limit, to form a homogeneous gas of electrons.

In a previous work by Thomas and Fermi [42] it was found that the kinetic energy per volume of a noninteracting gas of electrons (constant density) is given by

$$t_s^{homo}(\rho) = \frac{3}{5}(3\pi^2)^{\frac{2}{3}}\rho^{\frac{5}{3}}. \tag{1.103}$$

Based on this finding, Kohn and Sham proposed that for an inhomogeneous system the kinetic energy per volume can be approximated by

$$t_s(\mathbf{r}) \approx t_s^{homo}(\rho) = \frac{3}{5}(3\pi^2)^{\frac{2}{3}}(\rho(\mathbf{r}))^{\frac{5}{3}}. \tag{1.104}$$

Thus the kinetic energy turns into a functional of the density,

$$T_s^{LDA}[\rho] = \int d\mathbf{r} t_s^{homo}[\rho(\mathbf{r})] = \frac{3}{5}(3\pi^2)^{\frac{2}{3}}\int d\mathbf{r}(\rho(\mathbf{r}))^{\frac{5}{3}}. \tag{1.105}$$

The exchange energy per volume of an uniform electron gas is written as [24, 42]

$$\varepsilon_x^{homo}(\rho) = -\frac{3}{2}\Big(\frac{3}{\pi}\Big)^{\frac{1}{3}}\rho^{\frac{4}{3}}, \tag{1.106}$$

which gives rise to an exchange energy functional given by

$$E_x^{LDA}[\rho] = -\frac{3}{2}\Big(\frac{3}{\pi}\Big)^{\frac{1}{3}}\int d\mathbf{r}(\rho(\mathbf{r}))^{\frac{4}{3}}. \tag{1.107}$$

For the correlation energy per volume (ϵ_c), there is not any explicit equation. To obtain it Ceperley and Alder performed quantum Monte Carlo calculations to parametrize ϵ_c for an uniform electron gas [43]. Further, Perdew and Zunger [44, 45] proposed a parametrization for this energy in the following form

$$\epsilon_c^{PZ}[\rho] = \begin{cases} A\ln r_s + B + Cr_s\ln r_s + Dr_s, & r_s \leq 1 \\ \frac{\gamma}{1+\beta_1\sqrt{r_s}+\beta_2 r_s}, & r_s > 1, \end{cases} \tag{1.108}$$

where $r_s = \left(\frac{3}{4\pi\rho}\right)^{1/3}$. The values of the coefficientes can be found in Refs. [44, 45]. Therefore, the exchange-correlation functional within LDA is given by

$$E_{xc}^{LDA}[\rho] = \int d\mathbf{r}\varepsilon_{xc}^{homo}\Big|_{\rho\to\rho(\mathbf{r})} = \int d\mathbf{r}\varepsilon_{xc}^{homo}(\rho(\mathbf{r})), \tag{1.109}$$

with $\varepsilon_{xc}^{homo} = \varepsilon_x^{homo} + \varepsilon_c^{homo}$. Hence, the LDA exchange-correlation potential is obtained

$$V_{xc}[\rho](\mathbf{r}) = \frac{\partial\varepsilon_{xc}^{homo}(\rho)}{\partial\rho}\Big|_{\rho\to\rho(\mathbf{r})}. \tag{1.110}$$

We stress that if the electronic density $\rho(\mathbf{r})$ is strongly nonuniform, i.e. not slowly varying in space, the LDA is not a good approximation. This motivated an additional improvement in which the density variation is included in the functional by the density gradient, giving rise to the generalized gradient approximation. Over decades, the LDA has proved to be a good starting point for the description of many weakly-correlated materials, however with serious shortcomings concerning the strongly correlated materials.

1.6.1.2 Generalized Gradient Approximation

The Generalized Gradient Approximation (GGA) takes into account the inhomogeneous nature of the density by explicit inclusion of the density gradient into the functionals. By considering the Thomas-Fermi model one can approximate the kinetic energy of the non-interacting electronic system by considering the lowest order of the gradient corretion [24], which is added to take into account approximately the inhomogeneity of the electron density [42]

$$T_s[\rho] \approx T_s^{LDA}[\rho] + \frac{1}{4}\int d\mathbf{r}\frac{|\nabla\rho(\mathbf{r})|^2}{\rho(\mathbf{r})}, \tag{1.111}$$

and the exchange energy as

$$E_x^{GGA}[\rho] \approx E_x^{LDA}[\rho] - \frac{10}{216\pi(3\pi^2)^{\frac{1}{3}}}\int d\mathbf{r}\frac{|\nabla\rho(\mathbf{r})|^2}{(\rho(\mathbf{r}))^{\frac{4}{3}}}. \tag{1.112}$$

Similarly to the case of LDA the correlation function is parametrized from additional numerical calculations. To date the most used parametrization in physics is the one proposed by Perdew, Burker and Ernzerhof (PBE) [46]. Within this parametrization the correlation energy is given by

$$E_c^{GGA}[\rho] = \int d\mathbf{r}\rho(\mathbf{r})[\epsilon_c(r_s,\zeta) + H(r_s,\zeta,t)], \tag{1.113}$$

with the functions $\epsilon_c(r_s,\zeta)$ and $H(r_s,\zeta,t)$ defined in Ref. [46]. In this equation the relative spin polarization is $\zeta = \frac{\rho_\uparrow - \rho_\downarrow}{\rho}$ ($\rho = \rho_\uparrow + \rho_\downarrow$), the dimensionless density gradient is $t = \frac{|\nabla\rho|}{2k_s\rho\phi}$, the spin scaling factor is $\phi(\zeta) = \frac{[(1+\zeta)^{2/3}+(1-\zeta)^{2/3}]}{2}$, the Thomas-Fermi screening wave number is $k_s = \sqrt{\frac{4k_F}{\pi}}$, the Fermi wave number is $k_F = (\frac{\rho}{3\pi^2})^{1/3}$, and the Seitz radius is $r_s = (\frac{4\pi\rho}{3})^{1/3}$. Thus one can notice that within GGA, both exchange and correlation energy depends on the electron density and its gradient. Therefore, the GGA exchange-correlation functional is written in terms of the electron density and its gradient as in the general form

$$E_{xc}^{GGA}[\rho] = \int d\mathbf{r} f^{GGA}(\rho(\mathbf{r}), \nabla\rho(\mathbf{r})), \tag{1.114}$$

with $f^{GGA}(\rho(\mathbf{r}), \nabla\rho(\mathbf{r}))$ being parametrized as described above.

1.6.2 Pseudopotential Approximation, PW and LCAO basis set

To solve the Kohn-Sham equation (equation 1.32) in practice, one needs to take into account the effects of the residual potential arising from the ions and core electrons on the Kohn-Sham eigenstates. To this purpose we introduce the pseudopotential approximation. The central idea behind the pseudopotentials is that chemical bonds in molecules and solids are mainly ruled by the valence electrons of each atom. In fact, it is well known that most of physical properties of solids depends on the valence electrons other than the electrons of inner shells, which are usually denoted by core electrons. In this respect, the pseudopotential approximation is an approximation to the potential felt by the valence electrons within a solid or molecule. By employing the pseudopotential approximation, DFT calculations are further simplified because only the valence electrons are taken into account.

The pseudopotential is constructed in such a way that beyond a cutoff radius it turns into the real potential felt by the valence electrons. Likewise, the pseudowavefunction is constructed to be equal to the atomic wavefunction beyond the same cuttof radius. In figure 1.6 we illustrate the pseudopotential and pseudowavefunction together with the real potential and atomic wavefunction.

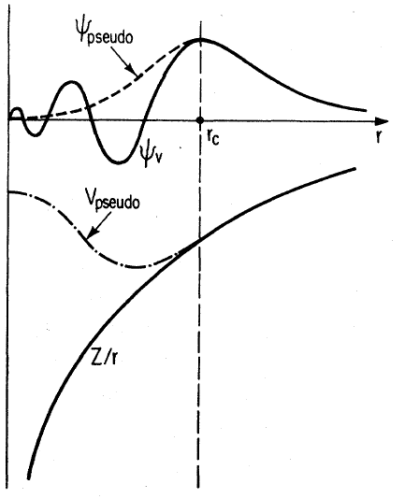

FIGURE 1.6: Illustration of the pseudowavefunction (pseudopotential) together with the real atomic wavefunction (potential). Figure taken from Ref. [47].

There exist basically two types of pseudopotentials, namely, the empirical and the

ab initio pseudopotentials. The empirical pseudopotentials are constructed from experimental results, e.g. band gap and ionization potential, which are used to fit the pseudopotential. On the other hand, the *ab initio* pseudopotentials are constructed in such a way that they provide the solution for the Schrödinger or Dirac equation for the atom. Among the *ab initio* pseudopotentials, the most used are the norm-conserving [48, 49] and ultrasoft ones [50].

To generate the *ab initio* pseudopotential an all-electron DFT calculation for the atom is performed. For atoms with closed shell configuration the radial solution[9] is obtained by solving the following equation [23]

$$\Big[-\frac{d^2}{dr^2}+\frac{l(l+1)}{r^2}+V_{KS}\Big]\phi_{nl}(r)=\epsilon_{nl}\phi_{nl}(r), \tag{1.115}$$

where the electron density is given by

$$\rho(r)=\sum_{nl}(2l+1)r^{-2}|\phi_{nl}(r)|^2. \tag{1.116}$$

To ensure transferibility the norm-conserving pseudopotentials are required to fulfill some conditions [23], such as the following:

- the pseudowavefunction should not have radial nodes, being thus a soft pseudowavefunction;
- beyond the cutoff radius r_c the pseudowavefunction should be equal to the real wavefunction;
- the charge obtained from the pseudowavefunction (inside $r < r_c$) should be equal to the charge obtained from the wavefunction;
- the eigenvalues associated with the valence, from a chosen atomic configuration, should agree if they are obtained from an all-electron or pseudopotential calculation.

In the context of pseudopotential based DFT calculations, different types of basis set have been used to expand the Kohn-Sham states. The plane-wave (PW) expansion of

[9] We emphasize that in the spherically symmetric case the atomic wavefunction is written as $\psi_{nl}(\mathbf{r}) = r^{-1}\phi_{nl}(r)Y_{ln}(\theta,\phi)$ [23].

Kohn-Sham states, for a periodic system, is performed by applying the Bloch theorem, which states that in a solid the wavefunctions can be written as product of a periodic function times a plane-wave part [47]

$$\phi_i(\mathbf{r}) = e^{i\mathbf{k}\cdot\mathbf{r}} f_i(\mathbf{r}) \tag{1.117}$$

one can span $f_i(\mathbf{r})$ using a plane-wave basis set as it follows

$$f_i(\mathbf{r}) = \sum_{\mathbf{K}} c_{i,\mathbf{K}} e^{i\mathbf{K}\cdot\mathbf{r}}. \tag{1.118}$$

Therefore, each Kohn-Sham state is spanned as a sum of plane waves

$$\phi_i(\mathbf{r}) = \sum_{\mathbf{K}} c_{i,\mathbf{k}+\mathbf{K}} e^{i(\mathbf{k}+\mathbf{K})\cdot\mathbf{r}}. \tag{1.119}$$

This summation can be truncated by using an energy cutoff E_c, in such a way that only plane waves with kinetic energy smaller than E_c compose the basis set [47], that is

$$|\mathbf{k}+\mathbf{K}|^2 < E_c. \tag{1.120}$$

Hence, the PW basis set depends only on a simple parameter E_c, which limits the size of the basis set.

In contrast, instead of using PW as a basis set one can use a linear combination of atomic orbitals (LCAO) [51]. This LCAO basis set leads to an expansion of the following form

$$\phi_i(\mathbf{r}) = \sum_{\mu} c_{i\mu}(\mathbf{k})\psi_\mu(\mathbf{r}), \tag{1.121}$$

where $\psi_\mu(\mathbf{r})$ is a linear combination of atomic-like functions, which by its turn obeys the Bloch theorem [52]

$$\psi_\mu(\mathbf{r}) = N^{-\frac{1}{2}} \sum_{\mathbf{R}} e^{i\mathbf{k}\cdot\mathbf{R}} \chi_\mu(\mathbf{r}-\mathbf{R}), \tag{1.122}$$

where $\mathbf{R}$ denotes the atom positions and N the number of unit cells in the solid. The functions $\chi_\mu(\mathbf{r})$ represent atomic orbital functions $\chi(\mathbf{r}) = R(r)Y_{lm}(\theta,\varphi)$ (lm angular momentum index; θ and ϕ are polar and azimuth angles, respectively), which have an angular dependence described by the spherical harmonics $Y_{lm}(\theta,\varphi)$, whereas $R(r)$ can be Slater-type atomic functions or Gaussian functions [53]. There exist two main types

of localized atomic orbitals basis set, namely, the Gaussian and the numerical atomic orbitals (NAO's).

The basis set of numerical atomic orbitals is characterized by its size, range and radial form. The size is related to the number of orbitals per atom in the basis set. In particular, there exist single-ζ, double-ζ, and triple-ζ basis set, including or not polarized orbitals [23]. Including polarized orbitals, by means of additional radial functions per angular momentum, one has the polarized single-ζ (SZP), double-ζ (DZP), and triple-ζ (TZP) basis set [23, 51]. The range is characterized by a cutoff radius which controls the overlap between orbitals of different atoms. In this respect, Artacho *et al.* [54] proposed a method in which the cutoff radius is defined by only one parameter, denoted by *energy-shift*. This energy-shift gives the energy gain of each orbital due to the confinement imposed by the cutoff radius [55]. This confinement is imposed in practice by using a potential of the following form [54]

$$V(r) = V_o \frac{e^{-\frac{r_c - r_i}{r - r_i}}}{r_c - r}, \tag{1.123}$$

where r_c is the cutoff radius and r_i an intern radius in the core region.

1.6.3 Full-potential method: (L)APW+lo basis set

Despite the enourmous success of pseudopotential based DFT calculations to study the physical properties of numerous *sp* materials, the disregarding of the nodal behavior of valence electron wavefunctions and the absence of core-electrons have important effects on the physical properties of a variety of materials. For example, important errors arise into the application of pseudopotentials to investigate the structural properties of materials containing alkali, alkali-earth metals, and transition metals in their compositions [56]. Thus, full-potential methods are introduced as more precise alternatives to the pseudopotential approximation.

In this subsection we introduce the full-potential (L)APW+lo method [57]. Within this method the space is divided into two regions: the non-overlapping atomic spheres (Muffin-tin spheres), which are centered on each atomic site, and the remaining interstitial region, as shown in figure 1.7.

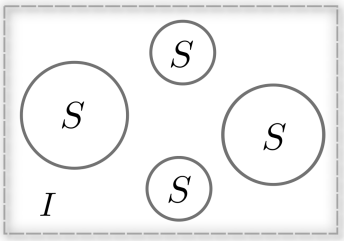

FIGURE 1.7: Illustration of the non-overlapping atomic spheres (S) and remaining interstitial region (I) which are used in the (L)APW+lo method.

Inside the atomic spheres the potential is expanded in terms of spherical harmonics $Y_{LM}(\hat{r})$, whereas in the interstitial region it is expanded in a plane-wave form [58],

$$V(\mathbf{r}) = \begin{cases} \sum_{LM} V_{LM}(r) Y_{LM}(\hat{r}), & \text{inside S,} \\ \sum_{\mathbf{K}} V_K e^{i\mathbf{K}\cdot\mathbf{r}}, & \text{in I,} \end{cases}$$

where $\mathbf{K}$ is the reciprocal lattice vector, $\mathbf{r} = r\hat{r}$, and L, M are the angular momentum index. Furthermore, the Kohn-Sham states can be spanned in different ways according to the region. In the linearized augmented plane wave (LAPW) method the basis set functions inside the atomic spheres are linear combination of radial functions times spherical harmonics, while in the interstitial region a plane wave expansion is used [57, 58],

$$\phi(\mathbf{r}) = \begin{cases} \frac{1}{\sqrt{\Omega}} e^{i(\mathbf{K}+\mathbf{k})\cdot\mathbf{r}}, & \text{in I,} \\ \sum_{lm} [A_{lm,k} u_l(r, E_l) + B_{lm,k} \dot{u}_l(r, E_l)] Y_{lm}(\hat{r}), & \text{in S,} \end{cases}$$

where Ω is the cell volume, k is the wave vector inside the first Brillouin zone, lm the angular momentum index, and u_l the solution of the radial Schrödinger equation at the energy E_l,

$$\Big[-\frac{d^2}{dr^2} + \frac{l(l+1)}{r^2} + V(r) - E_l \Big] r u_l(r, E_l) = 0, \tag{1.124}$$

while $\dot{u}_l$ is the solution of the following equation

$$\Big[-\frac{d^2}{dr^2} + \frac{l(l+1)}{r^2} + V(r) - E_l \Big] r \dot{u}_l(r, E_l) = r u_l(r, E_l). \tag{1.125}$$

In LAPW method the parameter E_l corresponds to the center of the corresponding energy band with l-like character [58].

In addition, Madsen *et al.* [59] showed that for localized orbitals, e.g. $3d$ orbitals, an augmented plane wave (APW) basis set supplemented with local orbitals (lo) leads to identical results as LAPW but with a smaller basis set. The APW+lo basis set is expressed as it follows [58]

$$\phi(\mathbf{r}) = \begin{cases} \frac{1}{\sqrt{\Omega}} e^{i(\mathbf{K}+\mathbf{k})\cdot\mathbf{r}}, & \text{in I,} \\ \sum_{lm}[A_{lm,k}u_l(r,E_l)]Y_{lm}(\hat{r}), & \text{in S,} \end{cases}$$

whereas the local orbitals are defined by

$$\phi_{lm}^{lo} = [A_{lm}u_l(r,E_l) + B_{lm}\dot{u}_l(r,E_l)]Y_{lm}(\hat{r}), \tag{1.126}$$

for the atomic spheric region (in S). It is worth mentioning that the coefficients A_{lm} and B_{lm} used in the definition of the local orbitals are not the same as the ones used in LAPW (APW), since the former do not depend on k. Notice also that the same energy E_l is used for the both APW and local orbitals.

Part I

Applications of DFT calculations

Chapter 2

Graphitic Carbon Nitrides

In this chapter we present our *ab initio* investigation on the structural, electronic and magnetic properties of graphene-like carbon nitride structures. After a general introduction about carbon nitride materials, we present two sections containing our results. In section 2.2 we present our investigation on the prediction of new graphene-like carbon nitride structures, wherein we employed a combination of model and *ab initio* calculations. From this work we found several structures with formation energies similar to those of existing tri-s-triazine and s-triazine g-C_3N_4 nanoporous structures. In particular, we obtained that the stability of carbon nitride planar structures are associated with the charge doping induced by the nitrogens. Afterwards, in section 2.3 we investigate the magnetic properties of this set of carbon nitride structures. Surprisingly, we found that 3/4 of the low-energy structures present energetically favorable magnetic phases, and that more than 3/10 are ferromagnetic, which suggests that d^0 magnetism is an usual feature in this class of materials. We also find that several structures are half-metals and one structure is half-zero-gap semiconductor.

The investigations presented in this chapter were published in the following articles: W. H. Brito, J. da Silva-Araújo, and H. Chacham, The Journal of Physical Chemistry C, **119**, 19743 (2015); and W. H. Brito, J. da Silva-Araújo, and H. Chacham, Physical Chemistry Chemical Physics , **17**, 31995 (2015).

2.1 Introduction

Nitrogen is a chemical element which can give rise not only to simple molecules but also to binary compounds with silicon, germanium, and carbon. Historically, the interest on solid compounds produced by combining nitrogen and carbon, i.e. carbon nitrides, was initially motivated by the theoretical findings of Liu and Cohen [60]. Based on *ab initio* calculations, these authors found that a hypothetical phase of carbon nitride, denoted as β-C_3N_4, would be hard as diamond. This stimulated the search for new carbon nitride phases, from which α-C_3N_4 [61], pseudocubic-C_3N_4 [62], and cubic-C_3N_4 [63] were proposed. In figure 2.1 we illustrate the crystal structures of these carbon nitride phases. Besides their hardness, their chemical [64], electronic, and optical properties are also of interest. For instance, it was pointed out that β-C_3N_4 would have a wide band gap of about 6 eV, which in turn suggests that this phase would be used as a transparent hard material [65, 66].

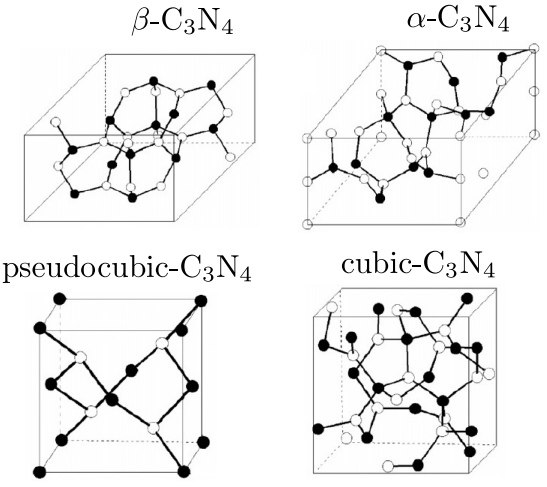

FIGURE 2.1: Dense structural phases of carbon nitride: β-C_3N_4, α-C_3N_4, pseudocubic-C_3N_4, and cubic-C_3N_4. Empty (full) circles represent nitrogen (carbon) atoms. The structures were taken from Ref. [67].

To date, the direct synthesis of such structures remains an issue, as the samples obtained provide insufficient evidences concerning their crystallization in the structures previously mentioned [68, 69]. In the case of β-C_3N_4, the synthesis of small crystallites embedded in amorphous thin films have been reported in numerous experimental works [70–73]. However, the obtained crystallites are in general nitrogen-poor [67], leading to inconclusive results about the formation of β-C_3N_4 within the samples.

Besides these dense carbon nitride structures, graphitic phases formed by graphene-like sheets with sp^2 hybridized carbon and nitrogen atoms were also considered. In the late 1980's there were some experimental works on the synthesis of graphitic carbon nitrides. In their reports the synthesis of graphitic samples with small content of nitrogen (C_5N) was achieved through high-temperature methods [74, 75]. Moreover, motivated by the fact that graphite can be used as a precursor for the high-pressure synthesis of diamond, a graphitic phase of carbon nitride with C_3N_4 composition (g-C_3N_4) was considered as a possible precursor to distinct dense structures such as β-C_3N_4 and cubic-C_3N_4. The synthesis of g-C_3N_4 was first reported by Kouvetakis *et al.* [76], where the authors obtained carbon nitride thin films with the desired stoichiometry by thermal decomposition of triazine-based precursors. We mention that g-C_3N_4 was theoretically proposed almost simultaneously with its synthesis [76] by Liu and Wentzcovitch using DFT calculations [62]. These DFT calculations also pointed out that the graphitic phase is more stable in comparison with the previous dense structures, while further calculations [63] predicted that the transition pressure from g-C_3N_4 to cubic-C_3N_4 is approximately 12 GPa.

Structurally, the graphitic phases have sheets stacked along the c axis, with graphene-like layers with in-plane void regions (nanopores) and similar linked subunits. In relation to the stacking of the sheets in g-C_3N_4, it was found that the $ABAB\ldots$ order is the most energetically favorable ordering and is the one which gives the best fit with experimental results [63, 77]. In relation to the linked subunits, the two most common subunits which have been reported experimentally are the aromatics denoted as s-triazine and tri-s-triazine [78], which are illustrated in figures 2.2(a) and (b), respectively. Since these subunits are contained in the triazine-based precursors, the final graphitic structures present a C_3N_4 composition, which motivates the common terminology g-C_3N_4 to denote graphitic carbon nitrides. It is noteworthy that the use of distinct precursors and alternative experimental methods allow for the synthesis of graphitic carbon nitrides with different subunits, stoichiometries and then in-plane structures, as illustrated in figures 2.2(c) and (d) [79, 80]. Nowadays, these graphitic carbon nitrides have been synthesized by polycondensation of organic monomers (containing the subunits) under high temperature [76, 81–83]. However, low-temperature methods have been employed by experimentalists as a cost-effective alternative [79, 84].

The nitrogen atoms adopt distinct configurations in the graphene-like layers. For

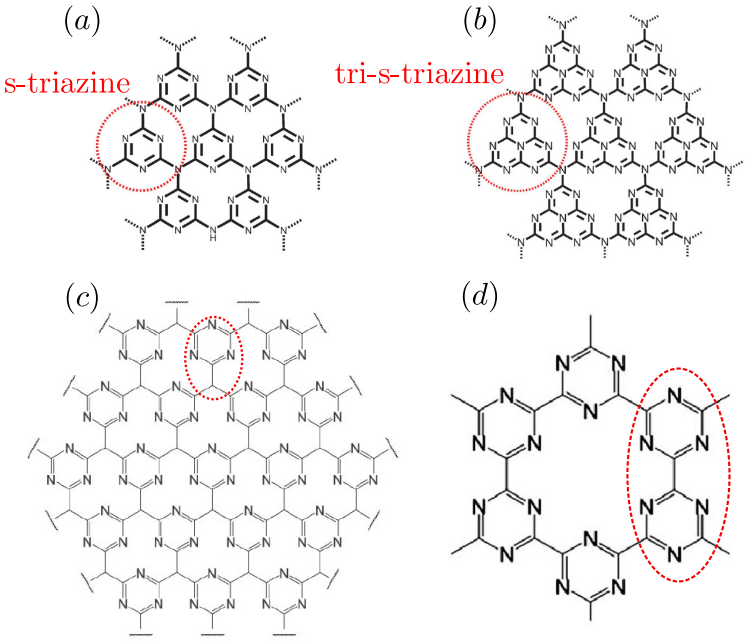

FIGURE 2.2: (a) s-triazine and (b) tri-s-triazine based g-C_3N_4. Some experimental works have obtained graphene-like structures with other subunits as shown in (c) g-C_4N_3 (Ref. [80]) and (d) g-CN (Ref. [79]). The aromatic subunits are those inside circles in red. The structures were taken from Ref. [78–80].

instance, in the structures shown in figure 2.2 there are graphitic and pyridinic nitrogens. In addition, due to the possibility of formation of pentagons in some structures containing nitrogens, the presence of pyrrolic sites should be also taken into account. These distinct configurations are shown schematically in figure 2.3. In this respect, numerous experimental and theoretical investigations have shown that these different nitrogen types can be used to tailor the properties of nitrogen-doped graphene [85–88]. For instance, graphitic nitrogens are electron donor impurities [89] and act as catalytic active centers for the redox reactions involving $[VO]^{2+}/[VO_2]^{+}$ [90]; pyridinic nitrogens are electron acceptors [89] and are able to increase the onset potential for oxygen reduction reactions [91]. These findings suggest that the properties of graphitic carbon nitrides may be tuned by controling the amount of nitrogen sites in the graphene-like structures. For example, it was recently reported that a high amount of pyridinic nitrogens can enhance the lithium storage capacity [92] of graphitic carbon nitride.

From a technological perspective graphitic carbon nitrides have been considered to be promising materials for practical applications in many cases. Numerous experimental works have indicated that these materials are promissing metal-free photocatalysts [93–96] for light-driven water splitting for hydrogen generation [97], which is of great interest in the context of renewable energy. Further, the possibility of tunning its

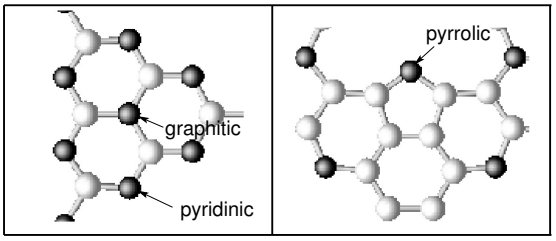

FIGURE 2.3: Scheme showing the various nitrogen sites, i.e., graphitic, pyridinic, and pyrrolic nitrogens. Carbon and nitrogen atoms are represented by white and black spheres, respectively.

band gap by controling the structure and composition motivated its use in electronic devices. For example, Mahmood *et al.* [98] fabricated field effect transistors (FETs) using graphitic carbon nitride as the active layer. Graphitic carbon nitride has also been considered in biomedical applications. As shown by Zhang *et al.* [99], ultrathin carbon nitride nanosheets have pH-dependent optical properties, with high photoluminescence response under UV-light, which make this material a nontoxic promissing candidate for bioimaging applications.

2.2 g-C_3N_4 and others: prediciting new carbon nitride structures

To date, most of experimental and theoretical works on graphitic carbon nitride have focused on graphene-like layers with C_3N_4 stoichiometry, which have more pyridinic than graphitic nitrogens. By means of total energy calculations, Kroke *et al.* [100] investigated the energetic stability of several graphitic phases with C_3N_4 stoichiometry. Their findings indicate that the graphitic structure based on tri-s-triazines (figure 2.2(b)) is more stable than the structure based on s-triazines (figure 2.2(a)). Further, Wang *et al.* [93] found that the distance between the layers in these g-C_3N_4 based on tri-s-triazines is about 0.326 nm and that these materials are semiconductors with band gap of 2.7 eV. It is worth mentioning that more recently Zhao *et al.* [101] reported the fabrication of single-layers with the same stoichiometry.

On the other hand, new graphitic structures with distinct stoichiometries have been proposed. Guo *et al.* [79] proposed a new structure based upon six-membered triazine rings with CN stoichiometry, in which there are no graphitic nitrogens (figure 2.2(c)).

In addition, Kroke *et al.* [100] proposed several possible graphitic structures with alternating arrangements and distinct subunits (for instance see figure 2.4).

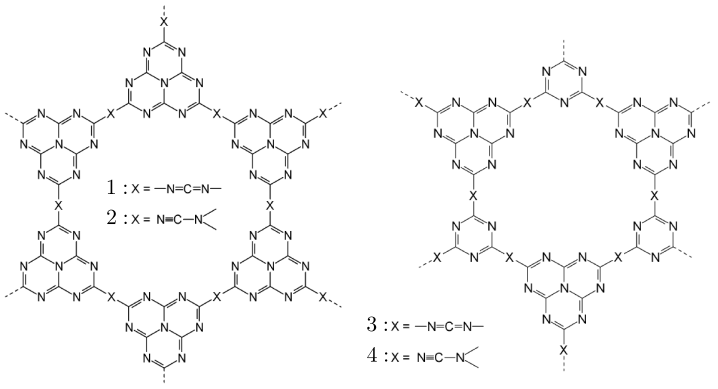

FIGURE 2.4: Tri-s-triazine and s-triazine based graphitic carbon nitride structures proposed by Kroke *et al.* [100]. The structures were taken from Ref. [100].

Motivated by the interest in new graphitic carbon nitride structures, we have carried out simulated annealing and *ab initio* calculations aiming at the prediction of new graphene-like carbon nitride structures with distinct stoichiometries. In the next section we describe the simulated annealing procedure which was used to obtain a set of low-energy carbon nitride structures.

2.2.1 Simulated Annealing

In our search for new carbon nitride structures we proposed structures with a honeycomb lattice, where each lattice site can be a carbon atom (C), a nitrogen atom (N), or a vacant site (v). These structures are denoted by the general formula $C_xN_yv_z$, where x, y, and z define the number of carbon atoms, nitrogen atoms, and vacancies, respectively, in unit cells of eighteen sites (3×3). In our investigation we considered twenty eight distinct (x, y, z) stoichiometries starting from a random configuration of sites with stoichiometry (x, y, z), we obtained a low-energy structure through the Monte Carlo simulated annealing procedure.

Our Monte Carlo simulated annealing procedure is based on the optimization method proposed by Kirpatrick *et al.* [102] and the Metropolis algorithm [103]. Different from the usual Monte Carlo Metropolis algorithm, in the simulated annealing the temperature is reduced linearly throughout the calculation, as a function of the number of Monte Carlo steps [104]. In particular, on the *nth* step, the temperature is given by $T_n = T_i \frac{(n_{MC}-n)}{n_{MC}}$,

where n_{MC} is the total number of Monte Carlo steps and T_i is the ficticious initial temperature. The main steps in the simulated annealing calculations are listed below (see also figure 2.5):

1. an initial configuration with randomly distributed C, N, and v sites with stoichiometry (x, y, z) is generated;
2. the total energy of the initial configuration is obtained;
3. by means of a perturbation in the crystal structure (atom-type exchange) a new configuration is generated;
4. the total energy of the new configuration is evaluated;
5. Metropolis criterion: if the total energy of the new configuration is smaller than the previous configuration, this new configuration is accepted; if not, a random number $r \in (0, 1)$ is generated. If $r < e^{-\beta(E_{new}-E_{old})}$ the new configuration is accepted. Finally, if none of these conditions take place the new configuration is rejected and the previous configuration is maintained;
6. the temperature is reduced and the calculation returns to step 2;

After n_{MC} steps the low-energy configuration is obtained.

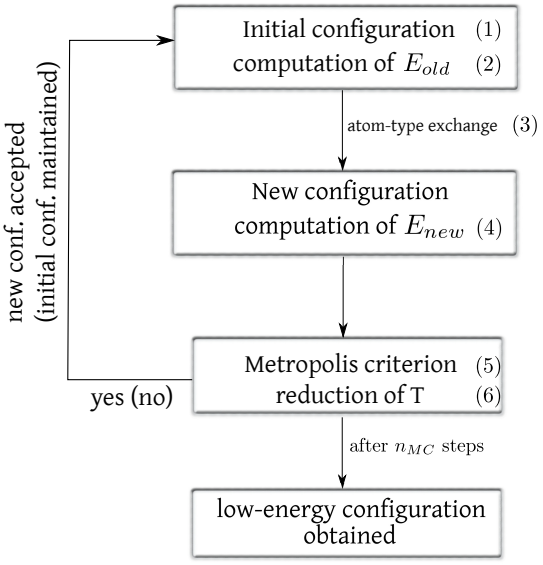

FIGURE 2.5: Fluxogram showing the steps performed in the simulated annealing calculations. The numbers indicate the steps enumarated in the text.

In our calculations we used a ficticious initial temperature of 9×10^4 K and approximately 10^5 atom-type exchanges between both first- and second-neighbors. Hence, from the annealing procedure, we obtained approximately 10^5 configurations for each distinct (x, y, z) stoichiometry, from which we selected the ones with the lowest energy by applying the Metropolis criterion. It is noteworthy that this criterion changes during the annealing since the temperature is reduced as a function of the number of Monte Carlo steps. The total energy of each configuration is evaluated by means of a bond-counting model that is described in the following section. DFT total energy calculations could be used in this step, however this would be an extremely time-consuming process.

2.2.2 Bond-counting model

For many decades, the thermodynamic properties of binary allows, e.g. the stability and phase diagram, have been addressed using the classical Ising model [105, 106]. For instance, by combining *ab initio* total energy calculations and the Ising model, Ferreira *et al.* investigated the stability of some semiconductor alloys such as $GaSb_{1-x}As_x$ [107]. In this respect, our carbon nitride structures $C_xN_yv_z$ can also be viewed as a ternary alloy, with three types of "atoms", namely carbon, nitrogen and vacancy.

Within the context of a classical Ising model, we can write the total energy of a general $C_xN_yv_z$ structure by considering a term which accounts for the nearest-neighbor interaction energy between our three types of "atoms"

$$E_0 = \sum_{\alpha,\beta} n_{\alpha,\beta}\epsilon_{\alpha,\beta}. \tag{2.1}$$

In this equation the α and β index denote the carbon and nitrogen atoms with distinct coordination, that is, carbon and nitrogens with one ($C1$, $N1$), two ($C2$, $N2$), and three ($C3$, $N3$) neighboring atoms. The $n_{\alpha,\beta}$ and $\epsilon_{\alpha,\beta}$ denote the number and bond energy of each $\alpha-\beta$ bond-type in the structure. For example, n_{C3C3} and ϵ_{C3C3} denote the number of bonds between carbons with three neighboring atoms and the bond energy of each $C3 - C3$ bond, respectively. We mention that bond-counting models with an energy functional of similar form as equation 2.1 have been successfully applied to graphene-type B-C-N structures [104, 108]. In the case of $C_xN_yv_z$ structures, we included the effects introduced by the charge doping, induced by the different types of nitrogens, by

adding the term ΔE,

$$E = \sum_{\alpha,\beta} n_{\alpha,\beta}\epsilon_{\alpha,\beta} + \Delta E. \tag{2.2}$$

Concerning the charge doping, it is well known that graphitic nitrogens are electron donors whereas pyridinic are electron-acceptors in graphene. Considering the fact that the tri-s-triazine based g-C_3N_4 is a fully compensated semiconductor, and is the most stable and synthesized structure [64, 109], we consider that ΔE must be zero for this structure. Hence, we postulate that the nitrogen-induced charge density is given by

$$\sigma = c\frac{(|2n_{C3N3} - n_{C3N2}|)}{\sum_{\alpha,\beta} n_{\alpha\beta}}, \tag{2.3}$$

where c is a constant.

Further we assume that ΔE results from the occupation (non occupation) of the conduction (valence) graphene band states induced by the nitrogens (the derivation of ΔE is presented in appendix G). As the electronic density of states in graphene is proportional to $|E|$, we obtain

$$\Delta E = k\frac{(|2n_{C3N3} - n_{C3N2}|)^{3/2}}{(\sum_{\alpha,\beta} n_{\alpha\beta})^{1/2}}, \tag{2.4}$$

where k is a constant. We mention that in our calculations we employed *ab initio* parametrized values of each bond energy in the structures. This parametrization is briefly described in appendix G.

Furthermore, the bond-counting method also allows us to analytically obtain the behavior of the formation energy of graphitic substitutional N impurities in a C_xN_y structure as a function of the nitrogen relative concentration $c_N = y/(x+y)$. To this purpose, we define the structure formation energy as

$$E_f = E - x\mu_C - y\mu_N, \tag{2.5}$$

where E is the total energy of the $(x+y)$-atom cell, and μ_C and μ_N are the chemical potentials for carbon and nitrogen atoms. Based on the equations 2.2 and 2.5, in the case of structures with graphitic N impurities that are not nearest neighbors, we obtain

that the formation energy per nitrogen atom is given by

$$\frac{E_f}{n_N} = A + Bc_N^{1/2}, \tag{2.6}$$

where $A = 3\epsilon_{C3N3} - \frac{3}{2}\epsilon_{C3C3} - \mu_N$ and $B = 12k$. In the case of structures with pyridinic N impurities, we obtain that $A = 2\epsilon_{C3N2} - \frac{81}{17}\epsilon_{C3C3} - \mu_N$ and $B = \sqrt{\frac{17}{3}}k$ (for the derivation of these formation energies see appendix G). Therefore, the bond-counting method predicts that the impurity formation energy increases linearly with $\sqrt{c_N}$.

In figure 2.6 we show the formation energies per nitrogen atoms, E_f/n_N, of C_xN_y structures that contain graphene sites ($C3$) and either substitutional graphitic N sites ($N3$) or pyridinic sites ($N2$) as a function of $\sqrt{c_N} = \sqrt{y/(x+y)}$. The formation energies are calculated with equation 2.5, wherein we considered the graphene sheet and the α-N_2 phase to obtain the carbon ($\mu_C = -154.866$ eV) and nitrogen ($\mu_N = -270.256$ eV) atomic chemical potentials, respectively. Both sets of *ab initio* results, i.e. for either $N3$ or $N2$ sites, depict a law of the type $\frac{E_f}{n_N} = A + Bc_N^{1/2}$, as predicted by equation 2.6.

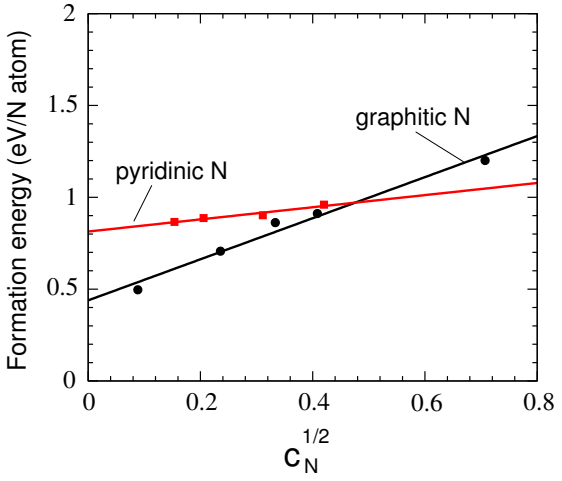

FIGURE 2.6: Formation energies per nitrogen atom of C_xN_y structures that contain $C3$ graphene sites and either substitutional graphitic N sites (black dots) or pyridinic sites (red dots), as a function of $\sqrt{c_N} = \sqrt{y/(x+y)}$.

In additon, we show in figure 2.7 the DFT Fermi energies (obtained with respect to pristine graphene) of the same set of structures, with either $N2$ or $N3$ impurity sites, as a function of $\sqrt{c_N} = \sqrt{y/(x+y)}$. Angle-resolved photoemission spectroscopy (ARPES) measurements of nitrogen-doped graphene [110] are plotted for comparison.

We first observe a good agreement between our calculated Fermi energies and the

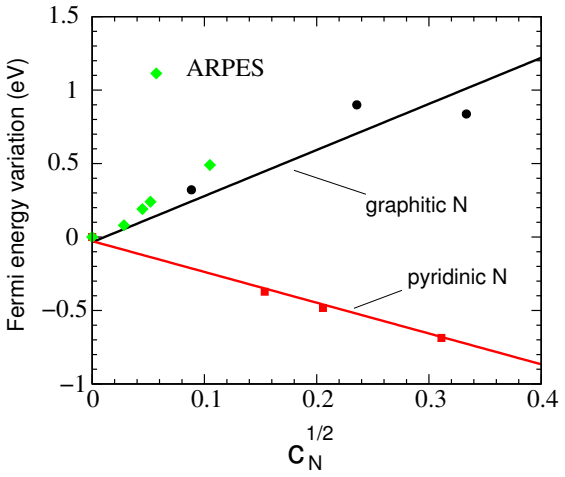

FIGURE 2.7: Fermi energies (relative to that of pristine graphene) of C_xN_y structures that contain $C3$ graphene sites and either substitutional graphitic N sites (black dots) or pyridinic sites (red dots), as a function of $\sqrt{c_N} = \sqrt{y/(x+y)}$. ARPES measurements of nitrogen-doped graphene samples [110] are plotted in green diamonds.

experimental results obtained by means of ARPES measurements. Interestingly, a behavior of the type $E_F = A + Bc_N{}^{1/2}$ is observed for both impurity types, with a positive value of B for graphitic N impurities and a negative value for pyridinic impurities. This is consistent with the donor nature of the former and the acceptor nature of the latter. These results indicate that structures presenting both graphitic and pyridinic types of nitrogen sites might have reduced formation energies due to donor-acceptor charge compensation. This will be investigated in the following.

2.2.3 New graphene-like carbon nitride structures: energetic and electronic properties

We now turn to the search of a set of low-energy structures using the Monte Carlo simulated annealing procedure. In our investigation, the range of each index (x, y, z) was fixed as $6 \leq x \leq 12$, $3 \leq y \leq 10$, and $0 \leq z \leq 6$. Starting from the $C_9N_9v_0$ structure, by adding vacancies in such a way that $z \leq 6$, we obtain a set of twenty eight different structures.

The geometries of the low-energy structures obtained through Monte Carlo calculations, in which the bond-counting model was employed, were further optimized by means of *ab initio* total energy calculations (the technical details concerning our calculations are described in appendix H.1). For clarity we organized the structures in six groups, where each structure in a group has the same number of vacancies per unit cell.

In figure 2.8(a)-(d) we show the equilibrium geometries of $C_xN_yv_1$ low-energy structures and the $C_9N_9v_0$ equilibrium geometry. The last was included in order to test our methodology. In figure 2.9(a)-(f), 2.10(a)-(g), 2.11(a)-(e), 2.12(a)-(c), and 2.13(a)-(c) we present the equilibrium geometries of $C_xN_yv_2$, $C_xN_yv_3$, $C_xN_yv_4$, $C_xN_yv_5$, and $C_xN_yv_6$ structures, respectively.

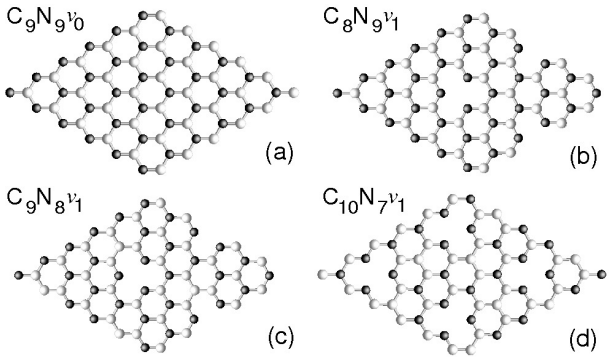

FIGURE 2.8: Equilibrium geometries, shown in (2×2) unit cells, of (a) $C_9N_9v_0$ and the $C_xN_yv_1$ structures: (b) $C_8N_9v_1$, (c) $C_9N_8v_1$, and (d) $C_{10}N_7v_1$. Carbon and nitrogen atoms are represented by white and black spheres, respectively.

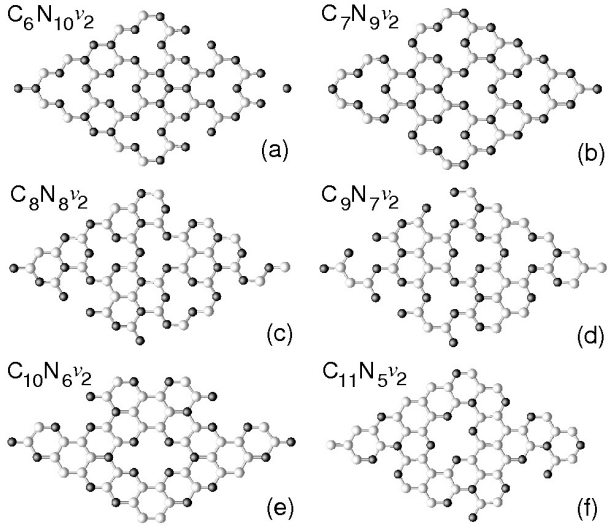

FIGURE 2.9: Equilibrium geometries, shown in (2×2) unit cells, of $C_xN_yv_2$ structures: (a) $C_6N_{10}v_2$, (b) $C_7N_9v_2$, (c) $C_8N_8v_2$, (d) $C_9N_7v_2$, (e) $C_{10}N_6v_2$, and (f) $C_{11}N_5v_2$. Carbon and nitrogen atoms are represented by white and black spheres, respectively.

The systems with formula $C_9N_9v_0$ and $C_6N_8v_4$ were used to verify the adequacy of our methodology. In this context, for the system $C_9N_9v_0$ we obtained a planar structure formed by an ideal alloying between carbon and nitrogen atoms, without C-C or N-N bonds (see figure 2.8(a)). This is in agreement with the stability trend reported in a previous theoretical work [111], since the C-N bonds are energetically more favorable than the highly energetic N-N bonds. For the system $C_6N_8v_4$ our Monte Carlo + DFT

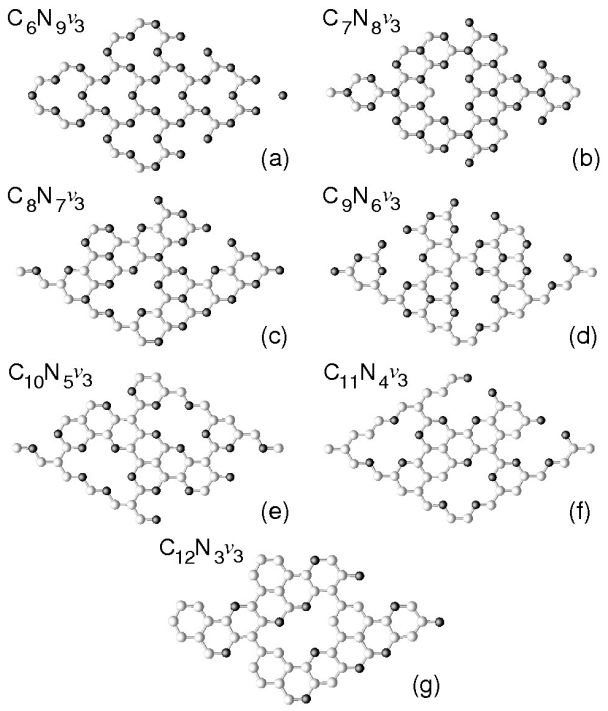

FIGURE 2.10: Equilibrium geometries, shown in (2×2) unit cells, of $C_xN_yv_3$ structures: (a) $C_6N_9v_3$, (b) $C_7N_8v_3$, (c) $C_8N_7v_3$, (d) $C_9N_6v_3$, (e) $C_{10}N_5v_3$, (f) $C_{11}N_4v_3$, and (g) $C_{12}N_3v_3$. Carbon and nitrogen atoms are represented by white and black spheres, respectively.

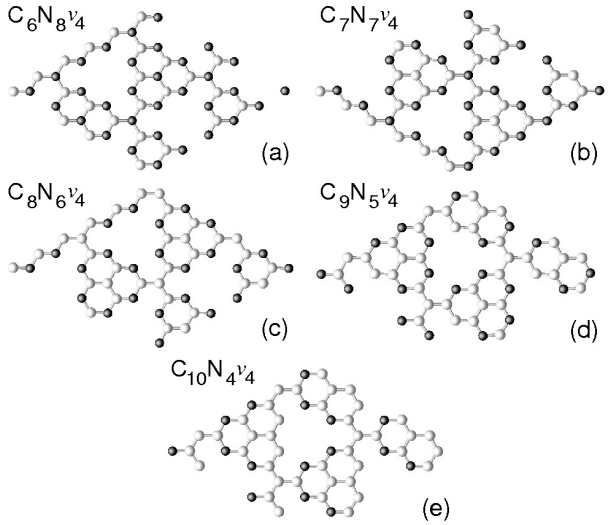

FIGURE 2.11: Equilibrium geometries, shown in (2×2) unit cells, of $C_xN_yv_4$ structures: (a) $C_6N_8v_4$, (b) $C_7N_7v_4$, (c) $C_8N_6v_4$, (d) $C_9N_5v_4$, and (e) $C_{10}N_4v_4$. Carbon and nitrogen atoms are represented by white and black spheres, respectively.

methodology resulted in a planar structure based on connected tri-s-triazine units (see figure 2.11(a)), which is in accordance with previous theoretical results [100] and with the experimentally observed structure [93, 112]. For the latter, we obtained bond lenghts of 1.34 Å, between the carbon and pyridinic nitrogens, and 1.47 Å, between carbon and

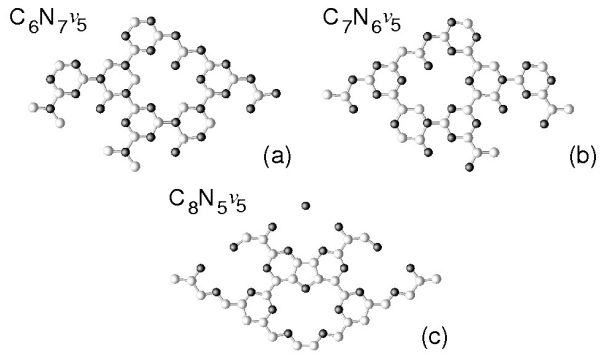

FIGURE 2.12: Equilibrium geometries, shown in (2×2) unit cells, of $C_xN_yv_5$ structures: (a) $C_6N_7v_5$, (b) $C_7N_6v_5$, and (c) $C_8N_5v_5$. Carbon and nitrogen atoms are represented by white and black spheres, respectively.

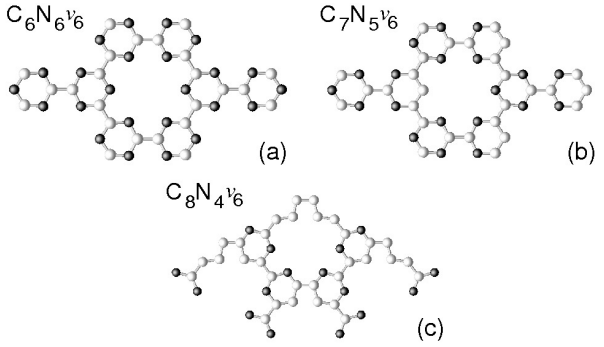

FIGURE 2.13: Equilibrium geometries, shown in (2×2) unit cells, of $C_xN_yv_6$ structures: (a) $C_6N_6v_6$, (b) $C_7N_5v_6$, and (c) $C_8N_4v_6$. Carbon and nitrogen atoms are represented by white and black spheres, respectively.

graphitic nitrogens connecting the subunits, in good agreement with previous theoretical calculations [113].

We next investigate the effects of the chemical composition on the morphology of the low-energy structures. Our equilibrium geometries indicate that, depending upon the relative concentration of atoms and vacancies, periodic structures with different nanopores should be formed. The smallest nanopore in our structures is based on a single vacancy surrounded by three pyridinic nitrogens. This type of nanopore is observed in all the equilibrium geometries of $C_xN_yv_1$ structures, $C_6N_{10}v_2$, $C_7N_9v_2$, $C_8N_8v_2$, $C_9N_7v_2$, and $C_6N_9v_3$. It is worth noticing that the same type of nanopore is found in the g-C_3N_4 structure based on condensed s-triazines [79]. The second type of nanopore is based on a double vacancy surrounded by four pyridinic nitrogens, as can be seen in the equilibrium geometries of $C_{10}N_6v_2$ and $C_{11}N_5v_2$ (see figure 2.9(e) and (f)). Other nanopore structures are the result of the coalescence of vacancies and the distinct number of defective carbon sites occupied or not by pyridinic nitrogens, see figure 2.10 and

figure 2.11 for example. Due to that, there are several structures with carbon dangling bonds, as seen in figure 2.10, figure 2.11, figure 2.12, and figure 2.13. Furthermore, due to the interplay between the chemical composition and structural relaxations, there are distorted equilibrium geometries with pyrrolic nitrogens and nitrogens that have a coordination number equal to one (see figure 2.12). Also, we can infer that in some cases the concentration of nitrogen can rule the segregation of vacancies. In particular, one should note that replacing a carbon by a nitrogen in the $C_{10}N_6v_2$ structure gives rise to a structure with chemical composition $C_9N_7v_2$, but with N-N bonds. This suggests that, depending upon the relative concentration of nitrogen and vacancy, the systems might show an energetic preference for structures with high number of smaller pores instead of structures with low number of larger pores. Finally, it is worth mentioning that the atoms in the $C_8N_8v_2$ and $C_8N_6v_4$ structures experience a maximum out of plane distortion of 0.38 and 0.11 Å, respectively, while all the other structures remain planar.

For the purpose of investigating the relative energetic stability of these structures, we calculate the formation energy per unit area, which we define as

$$\Omega = \frac{E[C_xN_yv_z] - x\mu_C - y\mu_N}{A}, \tag{2.7}$$

where $E[C_xN_yv_z]$ is the total energy of the $C_xN_yv_z$ structure obtained from the *ab initio* calculation, μ_γ (γ = C, N) the atomic chemical potentials, and A the $C_xN_yv_z$ supercell area. Table 2.1 presents our calculated formation energies and figure 2.14 shows our ternary diagram based upon these energies.

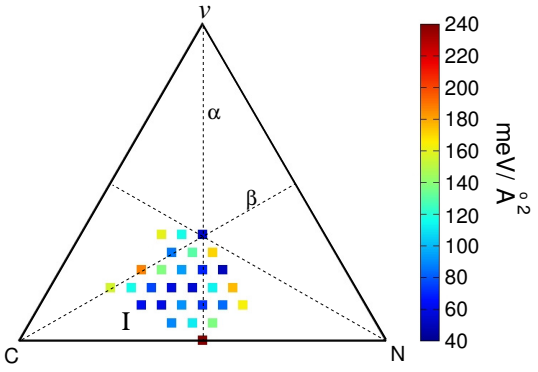

FIGURE 2.14: Formation energies per unit area (meV/Å^2) of $C_xN_yv_z$ structures. α and β lines in this figure correspond to $C_xN_yv_z$ structures with $x = y$ and $y = z$, respectively.

TABLE 2.1: Calculated formation energies per unit area, in meV/Å^2, of $C_xN_yv_z$ structures.

x y z	Ω	x y z	Ω
9 9 0	238.9		
$\underline{z=1}$		$\underline{z=2}$	
8 9 1	136.7	6 10 2	163.1
9 8 1	111.0	7 9 2	82.8
10 7 1	88.7	8 8 2	71.6
		9 7 2	90.6
		10 6 2	59.1
		11 5 2	61.8
$\underline{z=3}$		$\underline{z=4}$	
6 9 3	175.1	6 8 4	50.0
7 8 3	112.6	7 7 4	68.6
8 7 3	55.0	8 6 4	93.0
9 6 3	58.5	9 5 4	137.2
10 5 3	75.5	10 4 4	186.6
11 4 3	115.6		
12 3 3	154.7		
$\underline{z=5}$		$\underline{z=6}$	
6 7 5	170.1	6 6 6	53.0
7 6 5	129.3	7 5 6	116.1
8 5 5	85.6	8 4 6	159.4

Comparing the formation energies, we find that porous structures are more energetically stable, with a minimum energy difference of 52.3 meV/Å^2, than the structure without vacancies, i.e. $C_9N_9v_0$. These results suggest that, for graphitic carbon nitrides with chemical composition within the range we considered, the formation of graphene-like layers with periodic arrays of nanopores is an energetic favorable process. Additionally, we find that $C_6N_8v_4$ ($\Omega = 50.0$ meV/Å^2) and $C_6N_6v_6$ ($\Omega = 53.0$ meV/Å^2) are the most stable structures within the set of structures investigated in this work. The $C_6N_8v_4$ structure is the tri-s-triazine based g-C_3N_4, which has been experimentally synthesized [93, 112]. Meanwhile, the $C_6N_6v_6$ is the same structure synthesized and suggested in Ref. [79]. We also find that s-triazine (not shown) is 19 meV/Å^2 energetically less stable than the tri-s-triazine based g-C_3N_4. Interestingly, the porous structures with $z < 4$ give rise to a specific region in our ternary diagram (region I) corresponding to energetically favorable structures. Among these structures the $C_8N_7v_3$ is the most energetically stable, with formation energy difference of 5 meV/Å^2 relative to $C_6N_8v_4$.

Overall, for structures with $x = y$ (α line in figure 2.14), we note an energetic stabilization of structures upon increasing the number of vacancies per unit cell. In particular, the $C_8N_8v_2$, $C_7N_7v_4$, and $C_6N_6v_6$ structures are 167.3, 170.3, and 186 meV/Å^2 more stable than $C_9N_9v_0$, respectively. Considering now structures with $y = z$ (line β) the increase of carbon concentration makes the systems energetically less stable, which is related to the presence of carbon dangling bonds. For instance, the $C_{10}N_4v_4$ structure has two vacancies per unit cell and is 133.6 meV/Å^2 energetically less stable than $C_6N_6v_6$.

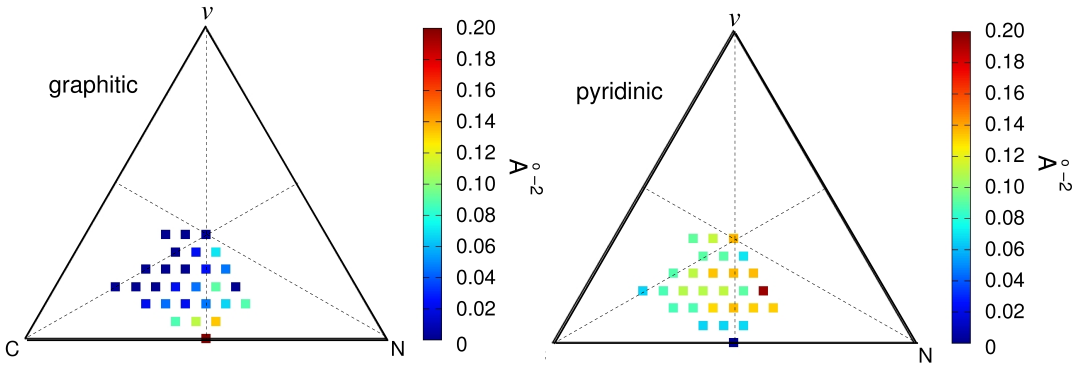

FIGURE 2.15: Density (Å^{-2}) of graphitic and pyridinic nitrogens of $C_xN_yv_z$ structures.

In figure 2.15 we present ternary diagrams showing the density of graphitic and pyridinic nitrogens of $C_xN_yv_z$ structures. From these diagrams we note that in general the low-energy structures have more pyridinic than graphitic nitrogens. This tendency can be observed in these diagrams inspecting points in region I and points associated with $C_6N_8v_4$ and $C_6N_6v_6$ structures. With the purpose of investigating the relation between the energetic stability of these structures and the relative density of different types of nitrogens, we present in figure 2.16(a) the formation energies as a function of the relative concentration of graphitic and pyridinic nitrogens. In the figure, we selected structures with $z \leq 4$ and that do not contain carbon dangling bonds nor highly energetic N-N bonds. In the figure we observe that, for the structures that only present single-vacancy nanopores, that the formation energy presents a minimum at $\rho_g/\rho_p = 0.33$, associated with $C_8N_8v_2$. In addition, one should note the same feature for the structures with $z = 4$ and 3 as presented in the inset of figure 2.16(a), with minima at 0.33 and 0.40 respectively. This gives an estimate for the range of nitrogen relative concentration in which one obtains stable carbon nitride structures.

Furthermore, as discussed previously, the non linear term in equation 2.2 takes into account the energy cost due to the charge density induced by the nitrogen sites.

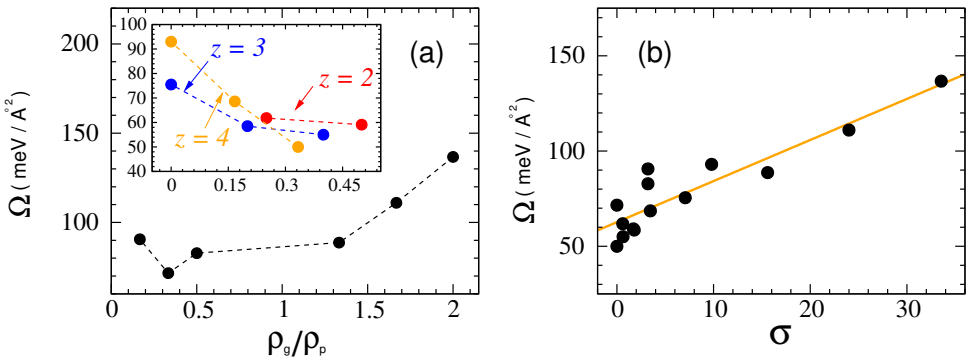

FIGURE 2.16: Formation energy per unit area (meV/Å^2) as a function of (a) relative concentration of graphitic and pyridinic nitrogens ρ_g/ρ_p and (b) $\sigma = \frac{(|2n_{C3N3}-n_{C3N2}|)^{3/2}}{(\sum_{\alpha,\beta} n_{\alpha\beta})^{1/2}}$. In (a) the points correspond to structures with $z \leq 4$, including $C_6N_8v_4$ structure and those that do not contain carbon dangling bonds nor highly energetic N-N bonds, as shown in the inset. The black dots correspond to structures that only present single-vacancy nanopores. Lines are guides to the eye.

This term was built such that it vanishes for tri-s-triazine $C_6N_8v_4$ based structure, which has the lowest formation energy and is a fully compensated semiconductor. As a result, this additional energy depends on $|2n_{C3N3} - n_{C3N2}|$, as written explicitly in equation 2.4. Focusing on the same group of structures considered in figure 2.16(a), we show in figure 2.16(b) the formation energy, given by equation 2.4, as a function of σ. In this case we observe a linear correlation between the formation energy and σ (specially for those structures with $\sigma > 7$). These findings suggest that one of the physical mechanisms that determines the relative energetic stability of several structures is the energy cost associated with additional charge density induced by nitrogens. Figure 2.16(b) suggests that the minimization of such energy cost, that is, the best charge compensation between donors and acceptors, occurs near the C_3N_4 stoichiometry. Counting rules have been suggested to favor such stoichiometry [60].

Numerous experimental results have pointed out the presence of pyrrolic nitrogens in nitrogen-doped graphene [88, 114, 115]. In order to include pyrrolic nitrogens in our structures we replaced pairs of pyridinic nitrogens by pentagons with pyrrolic nitrogens. These local structural transformations were applied to the following structures: $C_{10}N_6v_2$, $C_{11}N_5v_2$, $C_9N_6v_3$, $C_8N_7v_3$, $C_{10}N_5v_3$, $C_{11}N_4v_3$, $C_6N_6v_6$, and $C_7N_5v_6$. The calculated equilibrium geometries are shown in figure 2.17(a)-(h), while table 2.2 gives the calculated formation energies.

In figure 2.17, we observe that pyrrolic nitrogens give rise to new types of nanopores and distorted hexagons. Moreover, the calculated formation energies suggest that the

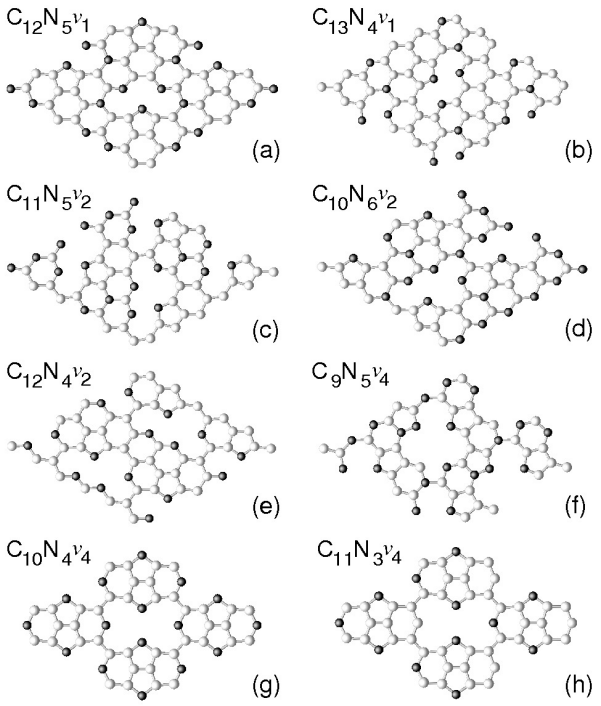

FIGURE 2.17: Equilibrium geometries, shown in (2×2) unit cells, of structures with pyrrolic nitrogens: (a) $C_{12}N_5v_1$, (b) $C_{13}N_4v_1$, (c) $C_{11}N_5v_2$, (d) $C_{10}N_6v_2$, (e) $C_{12}N_4v_2$, (f) $C_9N_5v_4$, (g) $C_{10}N_4v_4$, and (h) $C_{11}N_3v_4$. Carbon and nitrogen atoms are represented by white and black circles, respectively.

TABLE 2.2: Calculated formation energies per unit area, in meV/Å^2, of $C_xN_yv_z$ structures which have pyrrolic nitrogens.

x y z	Ω	x y z	Ω
$\underline{z=1}$		$\underline{z=2}$	
12 5 1	105.0	11 5 2	98.1
13 4 1	97.5	10 6 2	81.2
		12 4 2	117.0
$\underline{z=4}$			
9 5 4	126.9		
10 4 4	169.0		
11 3 4	229.6		

presence of pyrrolic nitrogens can lead to energetic stabilization of some structures. Indeed, the $C_{10}N_4v_4$ and $C_9N_5v_4$ structures with pyrrolic nitrogens are 17.6 and 10 meV/Å^2 energetically more stable than the equivalent structures in figure 2.11(e) and (d), respectively. In the case of $C_{10}N_4v_4$ structure, this stabilization is attributed to the reduction of carbon dangling bonds. However, pyrrolic nitrogens increase the formation energy of $C_{11}N_5v_2$ and $C_{10}N_6v_2$ structures in about 36 and 22 meV/Å^2, respectively. This can be attributed to the increase of the stress induced by the pentagons in these

structures, which leads to distorted carbon hexagons as can be seen in figure 2.17(g). Therefore, we infer that, for structures with low concentration of nitrogen and large nanopores, the formation of pentagons with pyrrolic nitrogens is an energetically favorable process, since it reduces the number of carbon dangling bonds. In contrast, the formation of pentagons with pyrrolic nitrogens in structures with smaller nanopores is energetically unfavorable due to the increase in the stress of the structure.

Next, we investigate the electronic properties of the low-energy structures. The Fermi energy values of these structures, calculated as the electronic chemical potential of the Fermi-Dirac distribution for the neutral systems at an electronic temperature of 0.001 Ry, give rise to the diagram shown in figure 2.18(a).

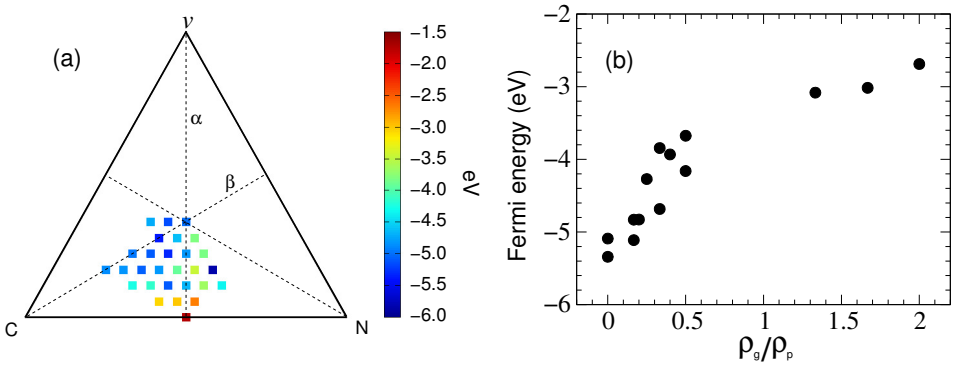

FIGURE 2.18: (a) Fermi energies (eV) of $C_xN_yv_z$ structures. (b) Fermi energy as a function of the relative concentration ρ_g/ρ_p of structures with $z \leq 4$ which have no carbon dangling bonds or N-N bonds.

Comparing the diagrams in figure 2.15 and figure 2.18(a), we notice that structures that have more pyridinic than graphitic nitrogens tend to have smaller values of Fermi energies, giving rise to a singular region, in the vicinity of the β line, that simultaneously presents low E_F values and high pyridinic concentrations. One should note an opposite trend for those structures with more graphitic nitrogens, with the bottom of α line in figures 2.15 and 2.18 presenting simultaneously high graphitic nitrogen concentrations and high E_F values. These findings can be understood from the fact that graphitic nitrogens are electron donors, while the pyridinics are acceptors. Thus, the Fermi energy reduces upon the increase of pyridinic nitrogens. In addition, we present in figure 2.18(b) the Fermi energy of the structures with $z \leq 4$, which have no carbon dangling bonds or N-N bonds. These results reveal that the Fermi energy can be tuned within an energy range of 2.65 eV depending upon the relative concentration ρ_g/ρ_p. This finding suggests that graphitic carbon nitrides can be bipolar compounds. Focusing on the structures

among the group with $\rho_g < \rho_p$ we notice the Fermi energy increases almost linearly with the relative concentration of nitrogens.

Since several of the obtained structures present carbon dangling bonds, we next investigate the possible existence of local magnetic moments due to spin polarization in the ground state of each structure. Based on our total energy calculations, we find that a set of twenty two structures present spin-polarized ground states with local magnetic moments. These structures are represented by triangles in the ternary diagram shown in figure 2.19. The remaining structures, represented by circles, do not have spin-polarized ground states. These findings are in agreement with previous theoretical calculations, which predicted that carbon dangling bonds induce electron spin polarization in the vicinity of defective sites in graphene [116].

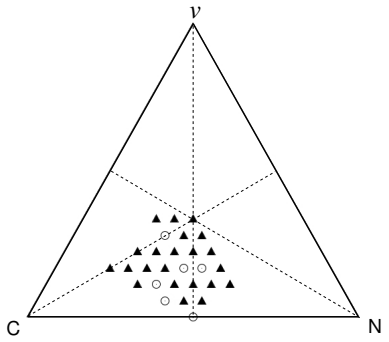

FIGURE 2.19: Spin polarization of graphene-like carbon nitride ($C_xN_yv_z$) structures. Structures with spin-polarized ground states are represented by full triangles while the structures with no spin polarization are represented by empty circles.

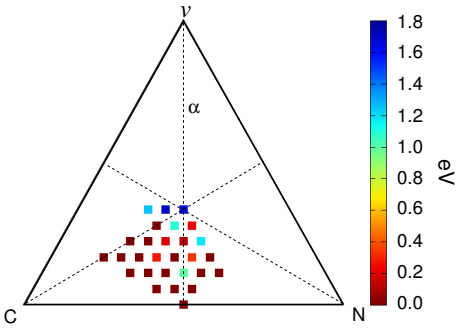

FIGURE 2.20: Energy gap (eV) of the $C_xN_yv_z$ structures.

Finally, we calculated the DFT (GGA) band gaps E_g of the structures, which give rise to the diagram shown in figure 2.20. As can be noticed in the diagram most of the structures are metallic (with zero band gap). Although DFT calculations within the GGA or LDA approximation often underestimate the band gap of semiconductors, we observe the presence of semiconductor structures near the center of the triangle and

along the α line, with the largest E_g values occurring in the vicinity of the center of the triangle. This trend correlates with the increase of the nanopore size. We obtained semiconductor structures with GGA band gaps of 0.99 eV ($C_8N_8v_2$), 0.34 eV ($C_7N_8v_3$), 0.27 eV ($C_9N_6v_3$), 0.11 eV ($C_7N_7v_4$), 0.18 eV ($C_8N_6v_4$) , 0.22 eV ($C_6N_7v_5$), 1.08 eV ($C_7N_6v_5$), and 1.69 eV ($C_7N_5v_6$); while the most stable structures $C_6N_8v_4$ and $C_6N_6v_6$ have band gaps of 1.18 and 1.62 eV, respectively. As pointed out by Xu *et al.* [113], the LDA band gap of graphitic C_3N_4 represents only 33 % of the experimental band gap, while the calculated GW band gap is in good agreement (2.88 eV) with the experimental findings. Based on this finding, there are several possible new structures, among the semicondutors listed above, that may absorb in the visible light region and might be photocatalyst candidates in the process of water-splitting.

2.2.4 Summary

In summary, we have performed Monte Carlo and *ab initio* calculations to propose and investigate the morphology, relative energetic stability, and electronic properties of graphitic carbon nitride structures. Within our set of low-energy structures, we obtained graphene-like layers with periodically distinct nanopores and different amounts of graphitic and pyridinic nitrogens. Our results indicate that the increase of nitrogen concentration leads to the coalescence of vacancies and therefore the increase in the size of nanopores. The calculated formation energies correlate with the relative concentration of pyridinic and graphitic nitrogens, with highest pyridinic concentrations leading to lower formation energies. The results for formation energies also indicate the existence of an energy cost associated with the doping due to the nitrogen impurities. We also examined the energetic stability of several systems with pyrrolic nitrogens. In this case, we find that the formation of pentagons with pyrrolic nitrogens increases the energetic stability of graphitic carbon nitrides with large nanopores and carbon dangling bonds, while it reduces the energetic stability of structures with small nanopores due to the increase in the stress induced by the pentagons. Our calculated Fermi energies correlate with the relative concentration of graphitic and pyridinic nitrogens. We observed that it is possible to tune the Fermi energies within an energy range of 2.65 eV by controling the relative concentration of nitrogens. Finally, based upon the calculated DFT (GGA) band gaps, we obtained a group of semiconductor structures that we estimate to be alternatives as photocatalyst candidates in the water splitting driven by visible light.

2.3 Magnetic properties of graphitic carbon nitride structures

Since the last decades magnetic properties have been observed in many materials in which there is no transition metal or rare earth element, that is, no d or f electrons [7]. For instance, numerous previous works have reported magnetic properties in two-dimensional carbon based materials such as graphene-based fragments, nanoribbons, and defective sheets [117], in carbon nanotubes [118], and, more recently, in graphitic carbon nitrides [80, 119]. From a fundamental viewpoint this d^0 magnetism has attracted great attention due to the interest in disclosing the physical mechanisms from which these properties emerge.

Moreover, carbon-based materials have also attracted enormous interest for applications in spintronic devices [120, 121]. For instance, the high electronic mobility and weak spin-orbit coupling of graphene [122, 123] make it a promising spin channel material. In fact, graphene spin valve devices have been fabricated, exhibiting room temperature nanosecond spin lifetimes and diffusion lengths of micrometers [124, 125]. In addition, another class of two-dimensional materials known as transition-metal dichalcogenides [126] has shown useful properties for applications in spintronics. In particular, MoS_2 monolayers exhibit direct band gap and larger spin-orbit coupling than graphene, which in turn leads to larger spin-orbit scattering lenghts [126, 127]. Despite of these spin channel candidates, carbon-based half-metals such as graphitic carbon nitrides [128, 129] have been proposed as an alternative to usual ferromagnet electrodes towards metal-free spintronics.

Despite the great potential of g-C_3N_4 as a photocatalyst [93, 96], previous theoretical works have also proposed alternatives to induce magnetic ordering in these materials. For instance, hydrogen chemisorption [130, 131], carbon doping [80, 128], periodic large pores [132, 133], and fractal morphology [129] may give rise to magnetic carbon nitride structures. From the experimental side, the synthesis of the theoretically predicted ferromagnetic g-C_4N_3 (see figure 2.2(c)) [80] and the experimental observation of room temperature ferromagnetism in g-C_3N_4 nanosheets have been recently reported [119]. In the present section, we investigate, by means of *ab initio* calculations, the magnetic

properties of the graphene-like carbon nitride structures presented in the previous section (for more details about the calculations see section H.2).

For each structure we addressed the energetic stability of the nonmagnetic, antiferromagnetic (AFM) and ferromagnetic (FM) phases. The magnetically ordered configurations were simulated starting with a spin-polarized calculation considering a predefined spin density. For those structures with stable magnetic state, we calculate the energetic stabilization driven by the formation of a magnetically ordered state, which is given by

$$\epsilon_s = E_m - E_{nm}, \tag{2.8}$$

where E_m and E_{nm} correspond to the total energies of the magnetic and nonmagnetic phases, respectively. The structures with energetically favorable magnetic phases ($\epsilon_s < 0$) are represented by triangles in the ternary diagram shown in figure 2.21. In the same diagram we represent the nonmagnetic structures by circles ($\epsilon_s > 0$). Moreover, these energies suggest a set of twenty two energetically favorable magnetic carbon nitride structures.

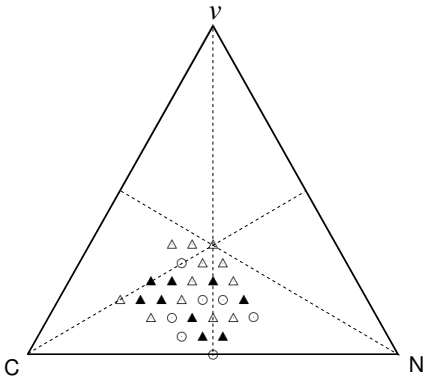

FIGURE 2.21: Magnetic phase ternary diagram of graphene-like carbon nitride ($C_xN_yv_z$) structures. Antiferromagnetic and ferromagnetic phases are represented by empty and full triangles, respectively. Nonmagnetic structures are represented by empty circles.

To investigate the energetic stability of these magnetic phases, we further calculate the energy difference between the FM and AFM configurations, for each structure, as given by

$$\epsilon_o = E_{afm} - E_{fm}, \tag{2.9}$$

where E_{afm} and E_{fm} are the total energies of the same structure, considering AFM and FM configurations, respectively. Interestingly, based upon the calculated values of

ϵ_o, we find a set of twelve structures with an energetically favorable AFM phase ($\epsilon_o < 0$): $C_7N_9v_2$, $C_8N_8v_2$, $C_{11}N_5v_2$, $C_{12}N_3v_3$, $C_9N_6v_3$, $C_6N_8v_4$, $C_8N_6v_4$, $C_6N_7v_5$, $C_7N_6v_5$, $C_6N_6v_6$, $C_7N_5v_6$, and $C_8N_4v_6$. These structures are represented by empty triangles in the ternary diagram shown in figure 2.21. In addition, we find a set of nine structures with an energetically favorable FM phase ($\epsilon_o > 0$): $C_8N_9v_1$, $C_9N_8v_1$, $C_9N_7v_2$, $C_6N_9v_3$, $C_{10}N_5v_3$, $C_{11}N_4v_3$, $C_7N_7v_4$, $C_9N_5v_4$, and $C_{10}N_4v_4$, which are represented as full triangles in the same diagram. It is important to mention that the $C_7N_7v_4$ structure obtained through our simulated annealing procedure corresponds to the same structure previously investigated in Refs. [134, 135]. Table 2.3 presents the calculated ϵ_s and ϵ_o values for the FM structures, including the g-C_4N_3 (carbon doped g-C_3N_4) proposed by Du *et al.* [128].

TABLE 2.3: Magnetic moment per supercell (m) and calculated energies (ϵ_s and ϵ_0), in meV, for structures which have energetically favorable ferromagnetic phase ($\epsilon_o > 0$). m is given in μ_B units.

x y z	y/x	m	ϵ_s	ϵ_0
8 9 1	1.13	2.35	-165.9	65.9
9 8 1	0.89	2.61	-121.2	4.2
9 7 2	0.78	4.00	-320.3	145.6
6 9 3	1.50	12.00	-1370.1	600.2
10 5 3	0.50	4.00	-233.2	61.1
11 4 3	0.36	4.00	-1069.3	136.7
7 7 4	1.00	4.00	-376.4	84.8
9 5 4	0.56	8.00	-494.5	–
10 4 4	0.40	9.98	-1467.3	248.9
g-C_4N_3	0.75	4.00	-413.1	326.9

From table 2.3 we observe that the g-C_4N_3 is found to be ferromagnetic with magnetic moment (m) equal to 1 μ_B per formula unit, in good agreement with the results of Du *et al.* [128]. For the $C_7N_7v_4$, we find m to be 1 μ_B per formula unit and that the ferromagnetic state is 84.8 meV more stable than the antiferromagnetic, in good agreement with previous results [134].

Figure 2.22 shows a plot of the magnetic moment per atom ($m/(x+y)$) of the ferromagnetic structures as a function of the N/C ratio (y/x). Two features can be observed in this figure. First, most of the $m/(x+y)$ values are in the vicinity of 0.05 μ_B/atom, suggestive of a common order of magnitude for the magnetization of C-N layers. Second, if we disregard the structure $C_6N_9v_3$, the $m/(x+y)$ values show an overall trend of decreasing magnetic moments per atom upon increasing the relative concentration

of nitrogen. We mention that a similar trend was recently observed experimentally in nitrogen-doped graphene domains [136].

Among our newly found ferromagnetic structures, $C_6N_9v_3$ and $C_{10}N_4v_4$ structures present larger energetic stabilization, as seen in table 2.3, due to the formation of magnetically ordered states. In particular, we find that the ferromagnetic state of the former is 273 meV more stable than the ferromagnetic configuration of g-C_4N_3, and that this structure presents a magnetic moment of 3 μ_B per formula unit. The ferromagnetic state of $C_{10}N_4v_4$ structure is found to be 78 meV less stable than the ferromagnetic state of g-C_4N_3, while the remaining structures present less stable ferromagnetic states. These findings indicate the possibility of a carbon nitride structure with a more stable ferromagnetic phase and high Currie temperatures as the ferromagnetic phase of g-C_4N_3.

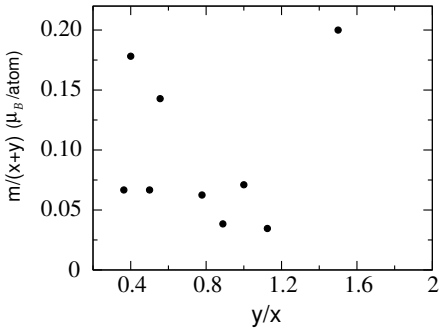

FIGURE 2.22: Magnetic moments per atom $(m/(x+y))$ as a function of relative concentration of nitrogen (y/x) of the graphene-like carbon nitride ($C_xN_yv_z$) structures which have energetically favorable FM phase ($\epsilon_o > 0$).

The calculated equilibrium geometries and spin densities of the ferromagnetic structures (excluding the $C_9N_8v_1$ structure) are shown in figure 2.23. It is important to mention that the $C_9N_8v_1$ structure will not be considered in the following investigation due to its very small value of $\epsilon_o = 4.2$ meV. From the spin density shown in figure 2.23(a) we observe the magnetic moments of g-C_4N_3 come mainly from the in-plane p_x and p_y orbitals of pyridinic nitrogens, also in good agreement with the findings of Ref. [128].

Similar to g-C_4N_3, the magnetic moments of $C_9N_7v_2$, $C_6N_9v_3$, $C_{10}N_5v_3$, and $C_7N_7v_4$ originate mainly from the p_x and p_y orbitals, as can be seen in figures 2.23(c), (d), (e) and (g), respectively. In contrast, as shown in figure 2.23(b), in the structure $C_8N_9v_1$ the magnetic moments originate mainly from p_z orbitals associated with graphitic carbon and nitrogen atoms in the "bulk" part of the structure. In figures 2.23 (f), (h), and (i) we

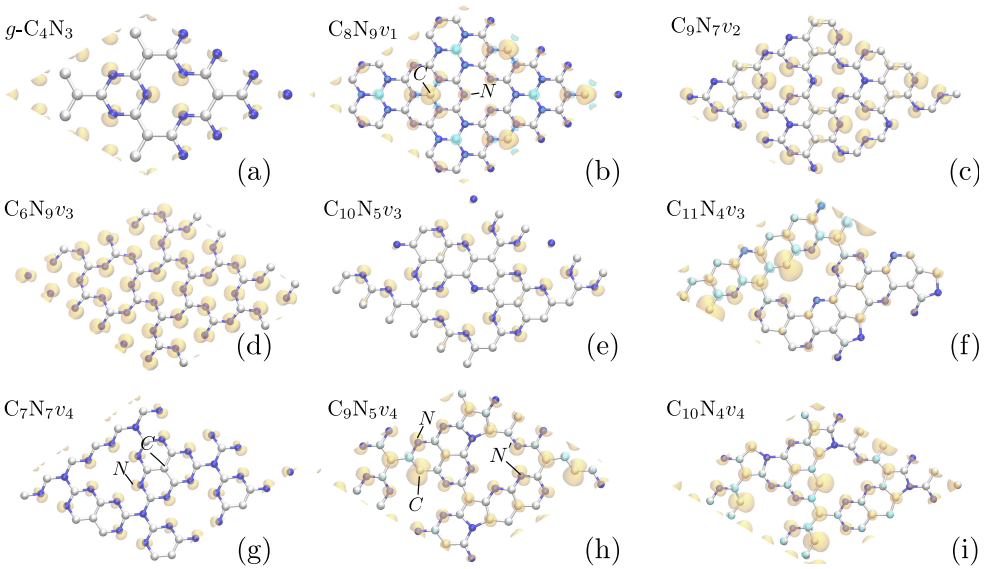

FIGURE 2.23: Equilibrium geometries (shown in 2×2 unit cells) and spin densities ($\Delta\rho = \rho_{up} - \rho_{down}$) of (a) g-$C_4N_3$, (b) $C_8N_9v_1$, (c) $C_9N_7v_2$, (d) $C_6N_9v_3$, (e) $C_{10}N_5v_3$, (f) $C_{11}N_4v_3$, (g) $C_7N_7v_4$, (h) $C_9N_5v_4$, and (i) $C_{10}N_4v_4$. Carbon and nitrogen atoms are represented by white and blue spheres. Isosurfaces, in yellow ($\Delta\rho > 0$) and cyan ($\Delta\rho < 0$), correspond to spin densities of (a) 0.02, (b) 0.002, (c)(f) 0.004, (d)(e)(g) 0.01, and (h)(i) 0.009 $e/bohr^3$.

notice a different feature. Indeed, the carbon dangling bonds in $C_{11}N_4v_3$, $C_9N_5v_4$, and $C_{10}N_4v_4$ structures give rise to local magnetic moments due to the unpaired electron.

In order to investigate the physical mechanism responsible for the instability of the nonmagnetic phases, we performed band structure calculations for the nonmagnetic states of those ferromagnetic structures. We find that the nonmagnetic state of $C_8N_9v_1$, $C_7N_7v_4$, and $C_9N_5v_4$ structures present peaked density of states at around the Fermi level, as can be seen in figure 2.24. The high density of states at around E_F reveals a Stoner-like instability of the nonmagnetic phase of these structures. In particular, in $C_8N_9v_1$ we observe that this instability is related with states which are mostly due to graphitic carbon atoms. Meanwhile, in $C_7N_7v_4$ these states are mostly due to pyridinic nitrogens. For $C_9N_5v_4$ structure, we observe that the defective carbon atoms contribute more to these states than the pyridinic nitrogens. Similarly, such high density of states was found for the other structures, although the density of states is not peaked at around the Fermi level in these cases. Overall, these findings are in accordance with the spin density features presented in figure 2.23.

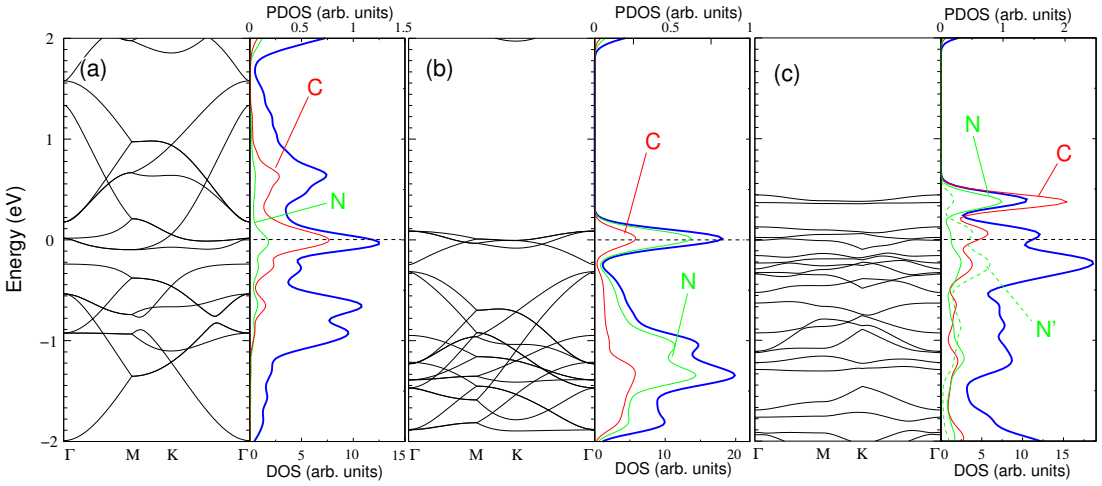

FIGURE 2.24: Calculated band structures: total (blue lines) and projected density of states of the nonmagnetic phase of (a) $C_8N_9v_1$, (b) $C_7N_7v_4$, and (c) $C_9N_5v_4$ structures. In the latter the states were projected on the carbon (red lines) and nitrogen atoms (green lines) marked in figure 2.23.

Finally, we investigate the effects of the magnetic ordering on the electronic properties of those structures. Here, we performed band structure calculations for the ferromagnetic states. A main feature in the band structures of $C_8N_9v_1$ (shown in figure 2.25), $C_{11}N_4v_3$, $C_9N_5v_4$, and $C_{10}N_4v_4$ structures, are the electronic levels with spin broken symmetry. For the $C_8N_9v_1$ structure we obtained semi-ocuppied levels, which accounts for the metallic nature of this system, while for the other structures we find band gaps of 0.25, 0.05, and 0.09 eV, respectively.

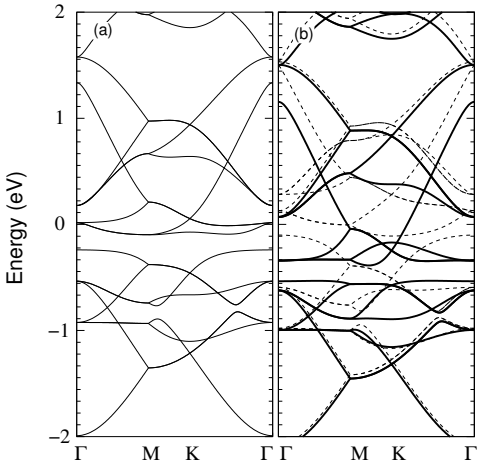

FIGURE 2.25: Calculated band structures of the (a) nonmagnetic and (b) ferromagnetic phases of $C_8N_9v_1$. In the latter solid (dashed) lines represent the spin-up (spin-down) components.

On the other hand, as shown in figure 2.26, the calculated band structures of $C_9N_7v_2$, $C_6N_9v_3$, and $C_{10}N_5v_3$ present a different feature. Interestingly, these band structures

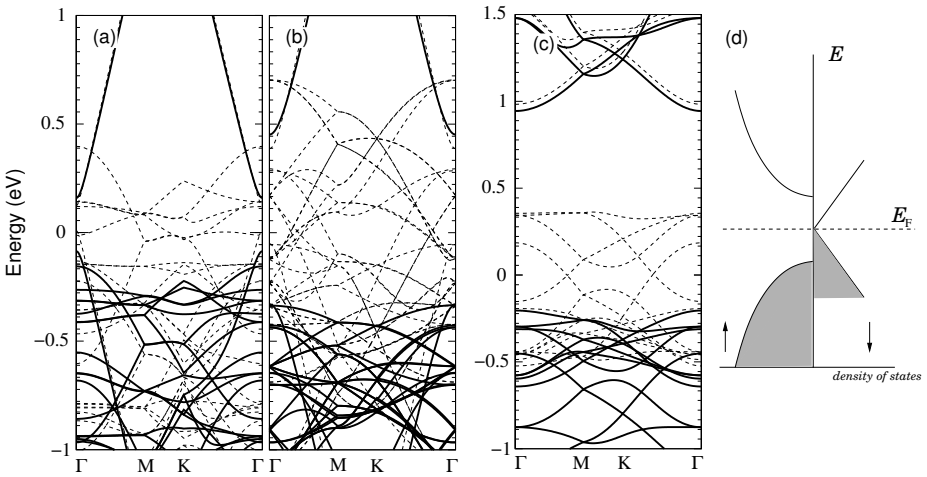

FIGURE 2.26: Calculated band structures of the ferromagnetic phases of (a) $C_9N_7v_2$, (b) $C_6N_9v_3$, and (c) $C_{10}N_5v_3$. Solid (dashed) lines represent the spin-up (spin-down) components. (d) Energy band diagrams for a half-zero-gap semiconductor.

reveal that for the spin-up component (solid lines) there are band gaps of 0.24, 0.78, and 1.14 eV for $C_9N_7v_2$, $C_6N_9v_3$, and $C_{10}N_5v_3$ respectively. Further, for the $C_9N_7v_2$ and $C_6N_9v_3$ structures, one should notice that there is no band gap for the spin-down component (dashed lines), with a considerable density of states at the Fermi level, such as in a half-metal. Such a similar feature was also found by Du *et al.* [128] for the g-C_4N_3. Surprisingly, we find that the spin-down component of the ferromagnetic state of $C_{10}N_5v_3$ presents an unusual feature. In fact, for this spin component we observe a graphene-like dispersion relation at around the Fermi level, as shown in the diagram presented in figure 2.26(d). In particular, we find two Dirac-like points along the $\Gamma - M$ and $\Gamma - K$ directions in the Brillouin zone, as can be seen in figure 2.26(c). Thus, our results indicate that this system can be considered as a half-zero-gap semiconductor.

2.3.1 Summary

In summary, by means of *ab initio* calculations we have investigated the magnetic properties of graphene-like carbon nitride structures. Among the set of structures considered, our results suggest there are twelve of them with energetically favorable antiferromagnetic phase and nine with ferromagnetic phase. Notably, within the energetically favorable ferromagnetic structures, we find that $C_{10}N_4v_4$ and $C_6N_9v_3$ may have high Currie temperatures as the previous magnetic carbon nitride structures. Our band structure calculations for the nonmagnetic phase of several structures indicate that these states

present Stoner-like instabilities. Finally, we obtained that the majority of these ferromagnetic structures remain metallic, where in special several ones may give rise to free-metal magnetic half-metals or even a half-zero-gap semiconductor.

Chapter 3

Point defects in Teflon crystals

In this chapter we present our *ab initio* investigation on the effects of point defects on the electronic structure of Teflon crystals. We first introduce some of recent experimental observations on defect-induced unsual properties in host materials, such as room-temperature ferromagentism in Teflon tapes and fluorescence properties in irradiated Teflon films. In section 3.2 we present our *ab initio* calculations on the energetic, electronic, and magnetic properties of Teflon crystals with fluorine and oxygen defects. From our calculations we obtained that oxygen substitutional impurities are energetically more stable than fluorine vacancies, and that both defects leads to the appearance of local magnetic moments in the crystals. In addition, upon increasing of the fluorine vacancy concentration, we find that the formation of polyconjugated structures in polymer chains, which may be the color centers in irradiated PTFE, is an energetically favorable process. However, our results do not support any ferromagnetic coupling between the local moments for the defective configurations considered in our work. This supports our proposal that the observed ferromagnetic ordering reported by Ma and co-workers [137] does not originate from the defective configurations addressed in this work.

3.1 Introduction

Point and extended defects are common ingredients in the atomic structure of synthetic and naturally occurring materials. Among these defects one can mention vacancies,

substitutional, and interstitial impurity atoms, which are types of point defects, and stacking faults, dislocations, and grain boundaries, which are extended defects [52].[1]

In the last several years certain types of impurities have been used to improve some of the physical properties of materials, such as the mechanical properties of metallic alloys [138] and electronic properties of semiconducting materials [1]. In contrast, structural defects have been claimed to be responsible for the detrimental of some of their properties, negatively impacting their technological applications. However, recent works have shown that defects can be beneficial to materials in order to improve some of their properties and expand their functionalities. As reviewed by Krasheninnikov and Banhart [139], the structural properties of nanostructured materials can be tailored by electron and ion-beam-induced defects. On the theoretical side, computational simulations have made valuable contributions to defect engineering of materials. For example, by means of first-principles calculations, recent theoretical works have shown the possibility of tuning the electronic properties of topological insulators through the control of stacking faults [140, 141].

Structural defects have also been used to induce magnetic ordering in different types of nonmagnetic materials. Vacancies in galium and boron nitride [142], vacancies and hydrogen impurities in graphene [116], and edges in SnO_2 [143] are examples of theoretical proposals to induce magnetic ordering in these materials. In agreement with the theoretical predictions, numerous experimental studies have observed magnetic ordering in defective samples of nonmagnetic materials. For instance, magnetic ordering has been observed in defective BN samples [144], in He irradiated GaN [145], in neutron and proton irradiated SiC single crystals (6H- and 4H-SiC structural phases) [146, 147], in defective InN films grown on Al_2O_3 [148], in proton irradiated graphite samples [149], and in defective graphene [150]. In figure 3.1 we reproduce the experimental magnetization loops reported in Refs. [144, 145, 147, 150]. It is noteworthy that in almost all the other curves shown in figure 3.1 the magnetization hystheresis were observed, which are signatures of defect-induced ferromagnetic ordering.

Also of interest are the carbon-based magnets, which have been considered as promissing candidates to biomedical and information storage applications. However, for pratical applications their Curie temperature should be improved to obtain room-temperature

[1] By extended defect we mean structural defects which extend over several nanometers in the crystalline structure.

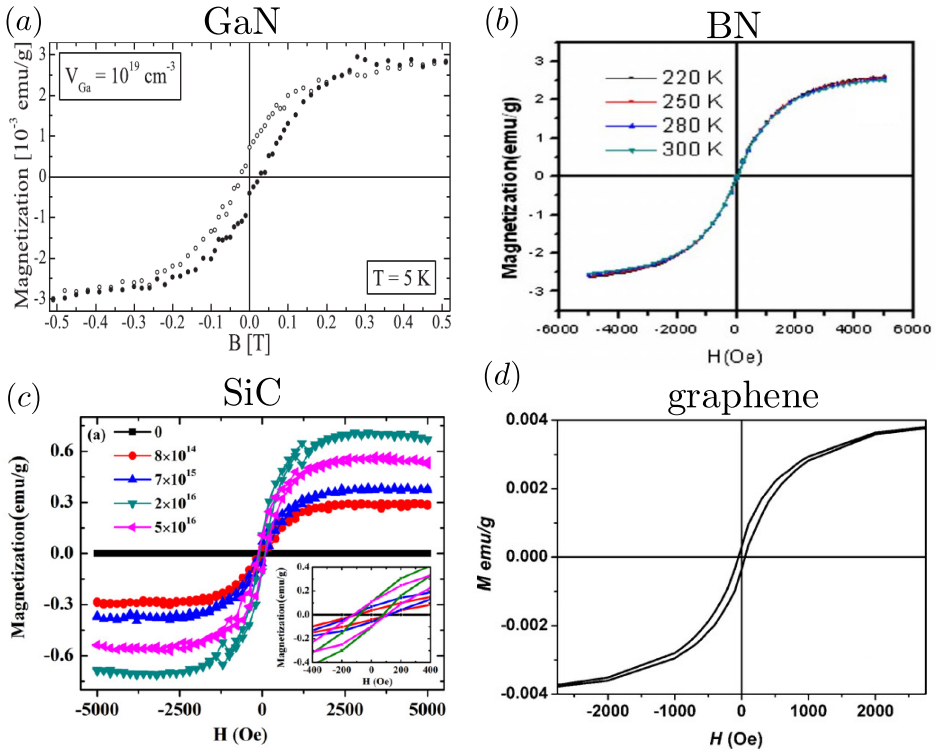

FIGURE 3.1: Magnetization loops of defective nonmagnetic materials: (a) He irradiated GaN [145], (b) defective BN [144], (c) proton irradiated 4H-SiC [147], and (d) defective graphene [150].

ferromagnets. In this respect, in a recent experimental work by Ma *et al.* [137], the authors reported on defect-induced room-temperature ferromagnetism in Teflon tapes. Polytetrafluoroethylene (PTFE), usually known as Teflon,[2] is a polymer with molecular chains composed by tetracoordinated carbons with fluorine atoms of molecular formula -$(CF_2)_n$-,[3] as illustrated in figure 3.2. Due to its chemical and physical properties, this material is used extensively in coating of surfaces, in fabrication of biomechanical implants and bullet-resistant vests.

The molecular chains of PTFE can give rise to disordered or crystalline solids. Due to the variety of molecular chain conformation and arrangement of these chains in the crystal cell, several distinct crystalline phases have been observed [151, 152]. As the energy difference between distinct conformations are small, the coexistance of segments with different conformations may be present within a crystalline film [153]. Crystalline films of PTFE are also insulating and diamagnetic. However, as suggested by Ma *et al.* [137], mechanically induced defects in PTFE can give rise to spontaneous magnetization in

[2]Teflon is the brand name of PTFE-based products by The Chermous company, which was a spin-off from DuPont Corporation, where the PTFE compound was discovered.

[3]n denotes the degree of polymerization.

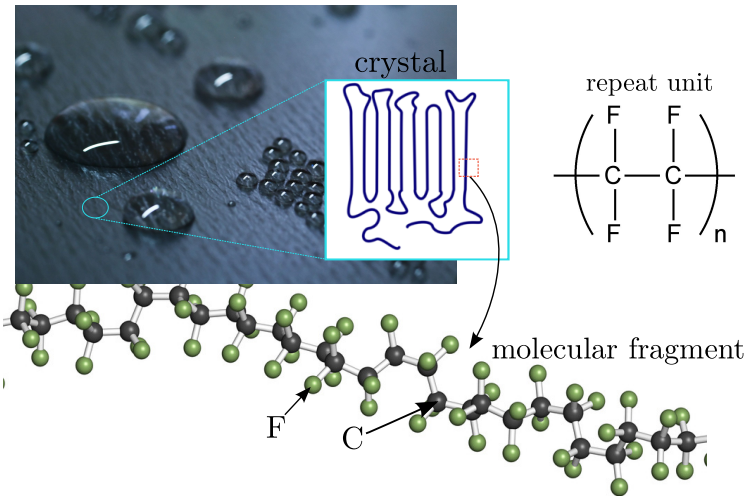

FIGURE 3.2: Illustration of the crystal, formula, and molecular fragment of the PTFE, usually known as Teflon.

the samples. In particular, the authors applied mechanical stretching, cutting, and heat treatment on Teflon tapes in order to create structural defects. As shown in figure 3.3, the stretching procedure performed in the experiment (illustrated in panel 3.3(a)) leads to the appearance of ferromagnetic ordering in the Teflon tapes, wherein the magnetization increases with the strain, as shown in panel 3.3(b). In figure 3.3(c), the obtained saturation magnetization of each segment indicates that higher values are achieved in more stretched parts of the tape. Figure 3.3(d) shows the magnetization hystheresis observed in both pure Ar and air atmospheres. These findings support the authors proposal of defect-induced ferromagnetism, where the local magnetic moments are claimed to have origin in carbon dangling bonds.

This type of d^0 magnetism has attracted great attention of the scientific community. On one hand, skeptical researchers have argued that magnetic contaminants, e.g. Fe, Co, Ni, etc., are the responsible for originating the magnetic ordering in defective samples of nonmagnetic materials. However, as reported by Ma and co-workers, X-ray photoelectron spectroscopy (XPS) measurements rule out the possibility of any contamination by magnetic impurities in Teflon tapes. In spite of the theoretical proposal of ferromagnetism induced by carbon dangling bonds, the role played by other types of point defects was not investigated.

Defective PTFE films have also shown valuable mechanical and optical properties. In especial, electron beam irradiation of PTFE films leads to an improvement of their mechanical resistance to gamma-ray radiation [154]. Gamma-ray radiation, by its turn,

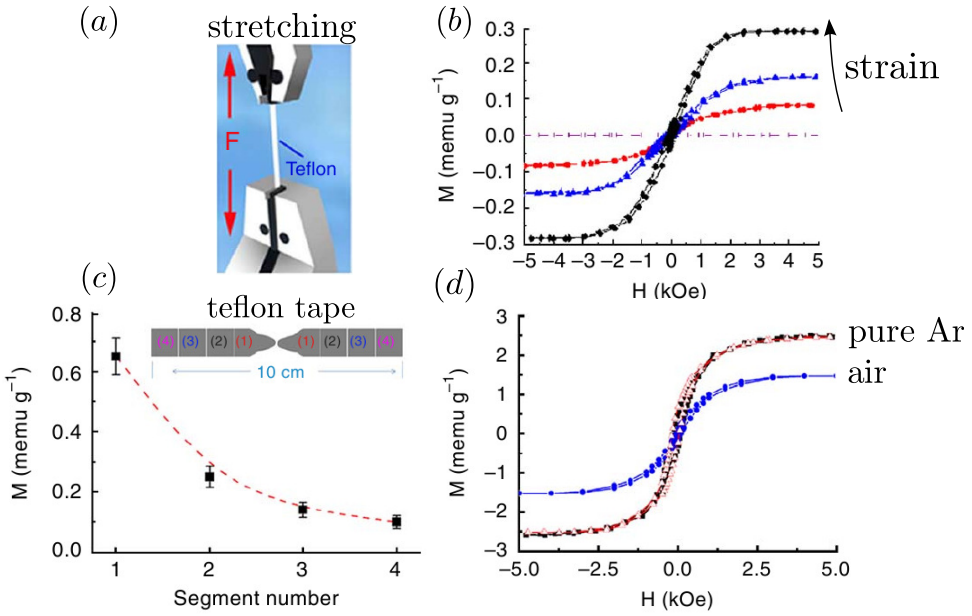

FIGURE 3.3: (a) Illustration of the stretching experimental procedure from which defective Teflon tapes were obtained. (b) Magnetization loops as a function of strain, obtained by mechanical stretching. (c) Saturation magnetization in different segments of a stretched tape. (d) Magnetization loops of Teflon tapes after annealing in pure Ar and air. Figures taken from Ref. [137].

gives rise to defective PTFE colorful[4] films with fluorescent properties in the visible spectral region [8]. Since then, numerous works have attempted to identify the physical origin of these unusual optical properties. In the work by Khatipov *et al.* [8], the authors pointed out the formation of polyconjugated structures (with π-bonds), (-CF_2-(CF=CF)$_n$-CF_2-), due to abstraction of fluorine atoms, as the physical mechanism responsible for the fluorescent properties of defective PTFE films. These findings were further supported by semiempirical calculations, which in turn suggested that the coloration of defective PTFE films have the origin in polyconjugated structures with $n = 2 - 6$ and fragments contanining terminal CFO (carbon-fluorine-oxygen) groups [155]. In this respect, more recent studies reported on experimental evidences of the formation of polyconjugated structures with $n = 4 - 7$, and on suppression of fluorescence with increase of the amount of oxygen in vacuum chamber atmosphere [156, 157].

Motivated by the above experimental results, in this work, we performed *ab initio* calculations to investigate the effects of point defects on the electronic structure of PTFE crystals. In the following sections we present our results on the pristine PTFE

[4]Pristine PTFE films have a milky color.

crystals and on the energetic, electronic, and magnetic properties of fluorine vacancies and oxygen impurities in molecular crystals of PTFE.

3.2 Results and Discussions

3.2.1 PTFE structural models

Initially we address the structural and energetic properties of two structural phases of PTFE. Technical details concerning our DFT calculations are described in appendix H.3. In figure 3.4 we present the equilibrium geometries obtained from our calculations. As can be seen, in both phases the molecular chains are packed in a hexagonal arrangement. In the structural phase shown in figures 3.4(a)-(b), denoted by 2_I, the molecular chains have planar conformation, whereas in the phase shown in figures 3.4(c)-(d), namely 15_7, the chains present helical conformation, which can be expressed as 15 units per 7 turns around the molecular axis. A similar nomenclature is adopted in Ref. [153].

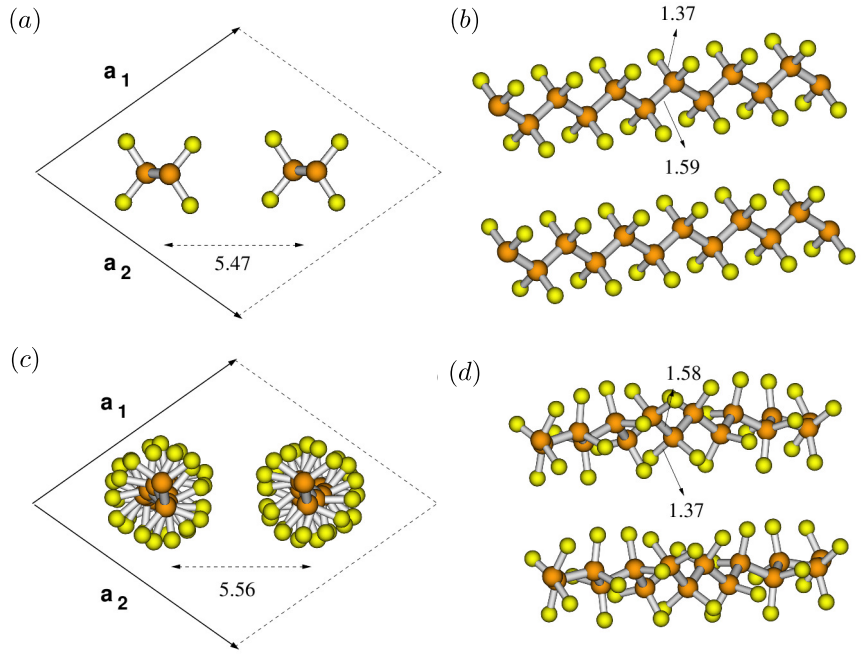

FIGURE 3.4: Equilibrium geometries of the two distinct structural phases of PTFE considered in our work. (a) Front and (b) side view of 2_I phase. (c) Front and (d) side view of 15_7 phase. Carbon and fluorine atoms are represented by orange and yellow spheres, respectively.

In the 2_I phase we obtain an average spacing between molecular chains of 5.47 Å, while in the 15_7 phase we find 5.56 Å, which are in good agreement with the value of 5.66

Å obtained by Ma *et al.* [137] through X-ray diffraction measurements (XRD). For the 2_I and 15_7 phases we obtain bond lenghts of 1.59 and 1.58 Å between the carbon atoms, respectively. Fluorine-carbon bond lenghts of 1.37 Å are obtained for both phases, which is in good agreement with the theoretical findings of Ref. [158].

For the purpose of investigating the relative energetic stability of both structural phases of PTFE, we calculated the formation energy per atom, which we define as

$$\Omega_\beta = \frac{E_\beta - n_C\mu_C - n_F\mu_F}{n_C + n_F}, \tag{3.1}$$

where E_β is the total energy of the β phase ($\beta = 2_I$ or 15_7), n_C (n_F) is the number of carbon (fluorine) atoms in the structure, and μ_C (μ_F) is the atomic chemical potential of carbon (fluorine) obtained from graphene (F_2 molecule) total energy. From our calculations we obtain that $\Delta\Omega = \Omega_{2_I} - \Omega_{15_7} = 7.3$ meV/atom, which indicates that the 15_7 is energetically more stable, suggesting that helical conformation of molecular chains increase the stability of the structure.

3.2.2 V_F and O_F defects in PTFE

We now turn to the inclusion of point defects in our structures, namely, fluorine vacancies (V_F) and oxygen substitutional impurities (O_F). We considered oxygen impurities due to its usual presence in chemical groups used in polymer synthesis as well as in polymeric films. For instance, it has been reported that oxygen substitutional impurities, denoted by keto-defects, is a common impurity found in poly(p-phenylene vinylene)(PPV) films [159]. In our investigations we only considered two distinct concentrations, i.e. one and two point defects per supercell. As we shall see these two distinct defects give rise to stable configurations without the breaking of the carbon backbone of PTFE. Figure 3.5 depicted our calculated equilibrium geometries with fluorine vacancies and oxygen impurities in 2_I and 15_7 crystals.

From our equilibrium geometries we notice that the C-C bond lengths decrease by around 0.1 Å near the fluorine vacancies, in both 2_I and 15_7 phases. The F-C bond length also decreases in the presence of the vacancy fluorine, by 0.03 Å. The angles between carbons, which were 114.45° in 2_I and 113.42° in 15_7, turn into 121.69° in 2_I and 121.32° in 15_7. This increase of $\approx 7°$ and 8° indicates the change of hybridization

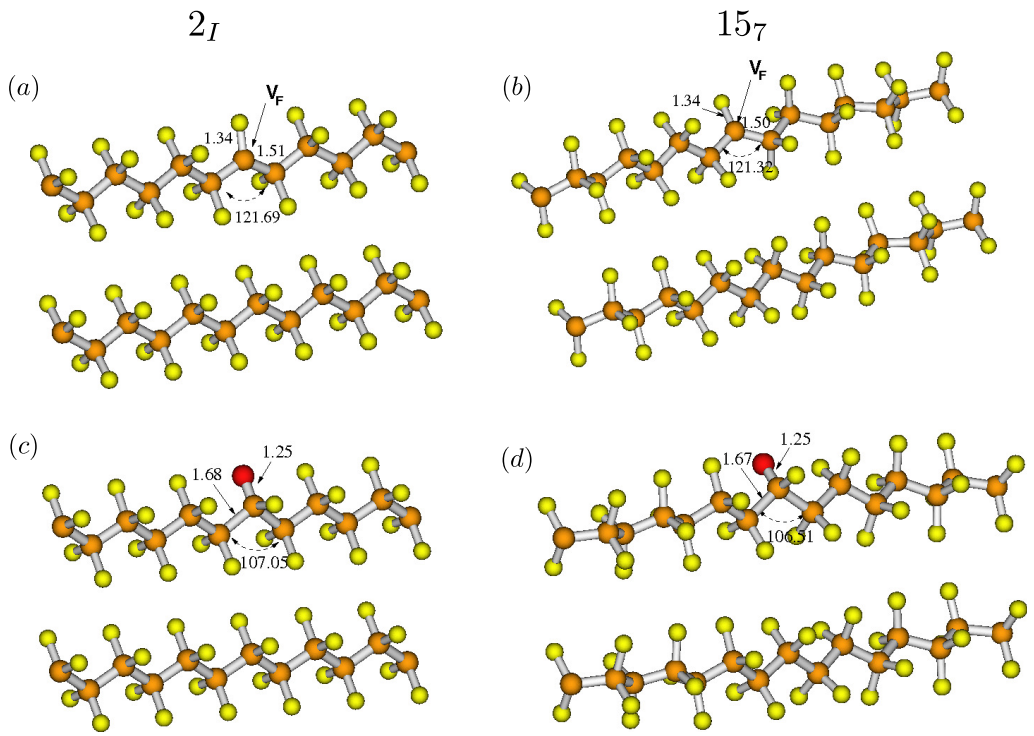

FIGURE 3.5: Equilibrium geometries of 2_I and 15_7 PTFE phases with fluorine vacancies [panels (a) and (b)] and oxygen substitutional impurities [panels (c) and (d)]. Carbon, fluorine, and oxygen atoms are represented by orange, yellow, and red spheres, respectively.

of the defective carbon site, from sp^3 to sp^2, in the presence of fluorine vacancies. By considering that oxygen impurities substitute fluorine atoms, we obtain the equilibrium geometries shown in figures 3.5(c) and (d). In this case, the C-C bond lengths increase by 0.09 Å, while the angle between carbons of the backbone chain decreases by around 7° in both 2_I and 15_7 phases, in contrast to the effect induced by the fluorine vacancies.

Furthermore, we increase the defect concentration by considering two defects per supercell. We propose different configurations as shown schematically in figure 3.6.

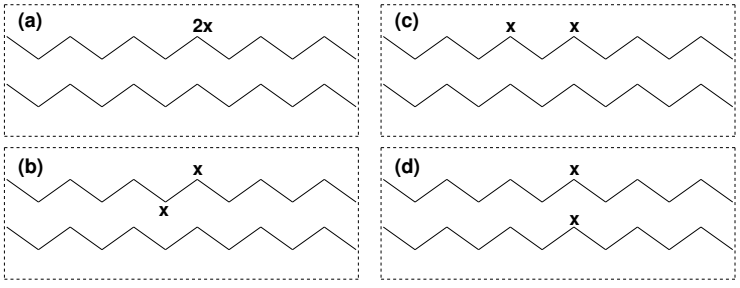

FIGURE 3.6: Scheme showing the distinct configurations considered in case of two point defects per supercell. In (a) the defects are located in the same site, in (b) nearest-neighbor sites, in (c) next-nearest-neighbor sites, and in (d) in distinct molecular chains.

The effects of the increase in the concentration of fluorine vacancies on the equilibrium geometries are shown in figure 3.7. We denote each configuration in this figure by: (a) 2_I-2V$_F$, (b) 2_I-2V$_F$N, (c) 2_I-2V$_F$NN, (d) 2_I-2V$_F$C, (e) 15_7-2V$_F$, (f) 15_7-2V$_F$N, (g) 15_7-2V$_F$NN, and (h) 15_7-2V$_F$C.

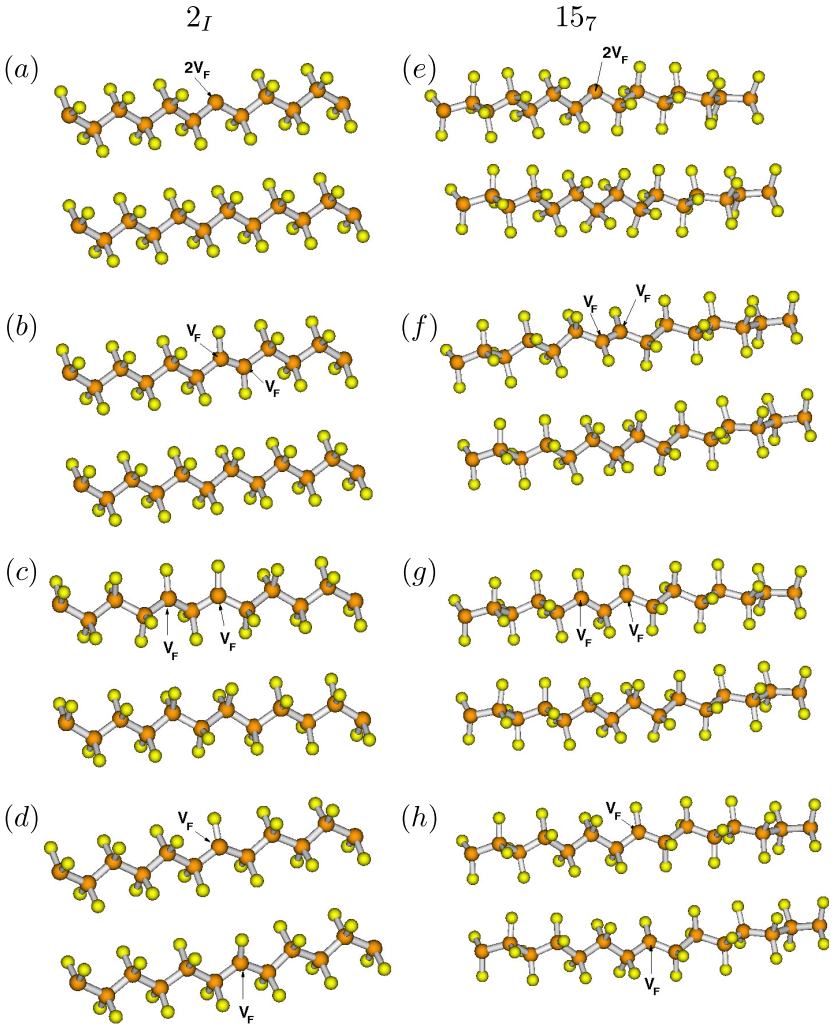

FIGURE 3.7: Equilibrium geometries of PTFE structures with two fluorine vacancies per supercell. From (a)-(d) and (e)-(h) we show the equilibrium geometries of 2_I and 15_7 phases with fluorine vacancies in configurations shown schematically in figure 3.6. Configurations are denoted by (a) 2_I-2V$_F$, (b) 2_I-2V$_F$N, (c) 2_I-2V$_F$NN, (d) 2_I-2V$_F$C, (e) 15_7-2V$_F$, (f) 15_7-2V$_F$N, (g) 15_7-2V$_F$NN, and (h) 15_7-2V$_F$C. Carbon and fluorine atoms are represented by orange and yellow spheres, respectively.

These findings suggest that under increase of fluorine vacancies the molecular chains do not break apart, and do not undergo any dramatic structural reconstruction. In particular, for fluorine vacancies in the nearest-neighbor sites, figures 3.7(b) and (f), we observe that neighboring carbon atoms adopt sp^2 hybridization. We further considered similar configurations for the oxygen impurities. However, several of these configurations

induce the rupture of the carbon backbone. In figure 3.8 we present the stable equilibrium geometries with two oxygen impurities per supercell. We denote these equilibrium geometries by: (a) 2_I-2O$_F$NN, (b) 2_I-2O$_F$C, and (c) 15_7-2O$_F$C.

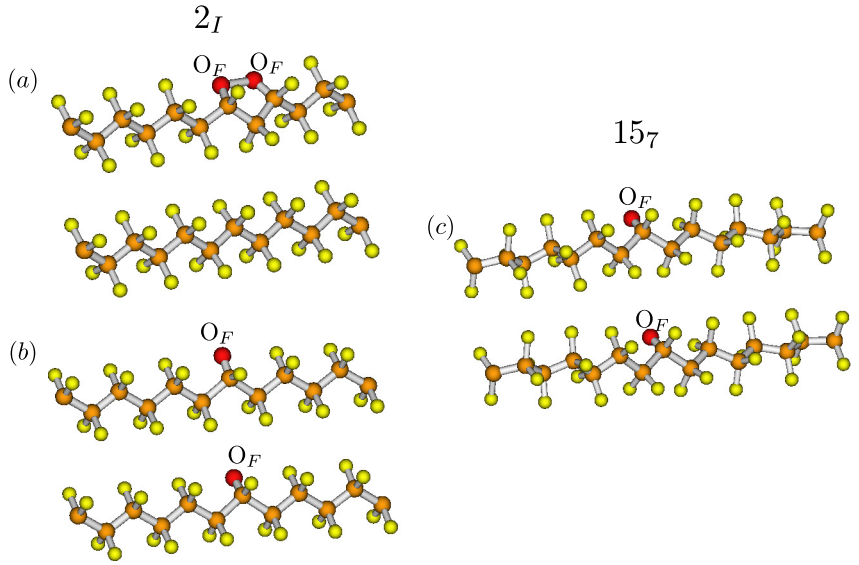

FIGURE 3.8: Equilibrium geometries of PTFE structures with two oxygen substitutional impurities per supercell. In (a) and (b) we show the equilibrium geometries of 2_I with oxygen impurities in configurations shown schematically in figure 3.6(c) and (d). Configuration in (a) is denoted by 2_I-2O$_F$NN whereas that in (b) by 2_I-2O$_F$C. In (c) the equilibrium geometry of 15_7 with oxygen impurities denoted by 15_7-2O$_F$C. Carbon, fluorine, and oxygen atoms are represented by orange, yellow, and red spheres, respectively.

Let us now investigate the relative energetic stability of the point defects considered above. With this purpose, we calculated the formation energy of each configuration as follows [160]

$$\Omega^f[X^q] = E_{tot}[X^q] - E_{tot}[bulk] - \sum_i n_i\mu_i + q[E_f + E_v + \Delta V], \tag{3.2}$$

where $E_{tot}[X^q]$ is the total energy obtained from our DFT calculations with a defect $X = (V_F, O_F)$ in the supercell, $E_{tot}[bulk]$ the total energy of pristine PTFE, n_i the number of atoms of the same atomic specie i that have been added ($n_i > 0$) or removed ($n_i < 0$) from the supercell, and μ_i the corresponding atomic chemical potentials. We remind that the chemical potential of carbon was obtained from the total energy of graphene whereas that of the fluorine from the total energy of F_2 molecule. Likewise, the chemical potential of oxygen is obtained from the total energy of O_2 molecule.[5] E_F

[5]For instance the chemical potential of oxygen is given by $\mu_O = E_{total}[O_2]/2$, where $E_{total}[O_2]$ is the total energy of a O_2 molecule.

is the Fermi level, q the charge state of the defect, E_v the valence-band maximum in the PTFE bulk, and ΔV a correction term to align the reference potential.

Further, we also calculated the total and absolute magnetization for each configuration. These quantities are defined as

$$M_T = \int (\rho_\uparrow - \rho_\downarrow) d^3r, \tag{3.3}$$

$$M_A = \int |\rho_\uparrow - \rho_\downarrow| d^3r, \tag{3.4}$$

where ρ is the charge density.[6] Our obtained formation energies and the total and absolute magnetization are listed in table 3.1.

TABLE 3.1: Calculated formation energies per point defect X ($X = V_F, O_F$) of defective 2_I and 15_7 phases of PTFE. The corresponding total (M_T) and absolute magnetization (M_A) are also listed. In these calculations we considered $q = 0$.

Config.	$\Omega^f[X^0]$ (eV/X)	M_T (μ_B/X)	M_A (μ_B/X)
2_I-V_F	3.64	1.00	1.09
2_I-O_F	2.18	1.00	1.11
2_I-$2V_F$	4.05	-1.00	1.04
2_I-$2V_F$N	2.56	0	0
2_I-$2V_F$NN	3.64	0	0.91
2_I-$2V_F$C	3.66	0	1.09
2_I-$2O_F$NN	1.80	0	0
2_I-$2O_F$C	2.16	0	1.10
15_7-V_F	3.74	1.00	1.10
15_7-O_F	2.23	1.00	1.10
15_7-$2V_F$	4.14	1.00	1.03
15_7-$2V_F$N	2.69	0	0
15_7-$2V_F$NN	3.80	0	0.93
15_7-$2V_F$C	3.74	0	1.09
15_7-$2O_F$C	2.23	0	1.11

Comparing the formation energies, we observe that oxygen impurities are energetically more stable than fluorine vacancies. In particular, for the 2_I phase we observe that configuration 2_I-O_F is 1.46 eV more stable per defect than configuration 2_I-V_F. Likewise, in 15_7 phase, the configuration 15_7-O_F is 1.51 eV per defect more stable than configuration 15_7-V_F. These findings reveal an energetic preference for oxygen substitutional impurities in PTFE crystals. Further, we find that fluorine vacancies present

[6] For ferromagnetic materials $M_T = M_A$ whereas for antiferromagnetic materials $M_T = 0$ and M_A is twice the magnetization of each atom.

an energetic preference to be located at neighboring sites, such as in configuration 2_I-$2V_F$N shown in figure 3.7(b), which is 1.08 eV/V_F energetically more stable than the 2_I structure with only one fluorine vacancy. This finding indicates that the formation of polyconjugated structures (with π-bonds) in molecular chains is an energetically favorable process, in agreement with the experimental reports on γ-irradiated PTFE films [8, 156, 157]. The same feature is observed for oxygen impurities, wherein the configuration 2_I-O_FNN is 0.38 eV/O_F energetically more stable than configuration 2_I-O_F, which corresponds to the 2_I structure with only one oxygen substitutional impurity. As expected, the fluorine vacancies as well as oxygen impurities in distinct molecular chains present similar formation energies per defect as those of isolated defects in just one chain. It is noteworthy that the energetically most stable configuration, namely 2_I-O_FNN, is characterized by oxygen impurities on next-nearest-neighbor sites mimicking an adsorbed O_2 molecule, in which O-O bond length is 0.49 Å longer than in a free O_2 molecule. Overall, the molecular chain conformation in 15_7 phase has minor effects on the energetic properties of configurations listed in table 3.1.

From the calculated magnetizations we observe that both fluorine vacancies and oxygen impurities are sources of local moments, with 1.0 μ_B per defect, signaling one unpaired electron per defect. Upon increasing the number of defects in the supercell, the total magnetization is supressed in some configurations such as 2_I-$2V_F$(15_7-$2V_F$)N and 2_I-O_F(15_7-$2V_F$)NN. For some configurations, e.g. 15_7-$2V_F$NN and 2_I-$2V_F$NN, our calculated magnetization suggests antiferromagnetic coupling between the local moments. We mention that for configurations 2_I-$2V_F$C, 2_I-O_FC, 15_7-$2V_F$C, and 15_7-$2O_F$C, our results do not suggest any ferromagnetic coupling between defects in different molecular chains. Due to the similarity between our findings for the 2_I and 15_7 phases, from this point forward, we restrict our investigation to the defective 2_I phase.

As expressed in equation 3.2, the formation energy of the point defects also depends on the Fermi level of the host material (PTFE bulk). In this respect, we also calculated the formation energy of 2_I-V_F and 2_I-O_F configurations as a function of the Fermi level. In particular, we considered the following charge states: $q = -1$ (one additional electron), $q = +1$ (removal of one electron), and $q = 0$ as previously considered. In figures 3.9(a)-(b) we show the calculated formation energies of 2_I-V_F and 2_I-O_F defects as a function of the Fermi level. In addition, we evaluated the transition levels which

are determined by the formation energy difference, as follows

$$\epsilon(q/q') = \frac{\Omega^f(X^q, E_F = 0) - \Omega^f(X^{q'}, E_F = 0)}{q' - q}, \tag{3.5}$$

where $\Omega^f(X^q, E_F = 0)$ is the formation energy of defect X in the charge state q, as defined in equation 3.2, for the Fermi level on the top of the valence band, $E_F = 0$ [161]. Our results for the 2_I-V_F configuration show that the fluorine vacancy with $q = +1$ charge state is more stable if the Fermi level is located between 0 and 0.02 eV within the energy gap. Above the transition level $\epsilon(+/0) = 0.02$ eV, the defect with $q = 0$ becomes the most stable configuration. The next transition level obtained is at $\epsilon(0/-) = 4.08$ eV, above which the V_F with $q = -1$ becomes more stable. For the 2_I-O_F configuration, we find that impurity with charge state $q = +1$ is the most stable when the Fermi level is between the valence band maximum ($E_F = 0$) and the first transition level $\epsilon(+/0) = 0.11$ eV. Above this value, the impurity with $q = 0$ becomes more stable, until the Fermi level approaches the value of $\epsilon(0/-) = 2.48$ eV, above which the $q = -1$ state turns into the energetically favorable configuration. An energy band diagram of bulk PTFE is shown in figure 3.9(c), in which the obtained transition levels are depicted. We mention that we used the 2_I phase DFT(GGA) band gap of 4.86 eV as the upper limit of E_F.

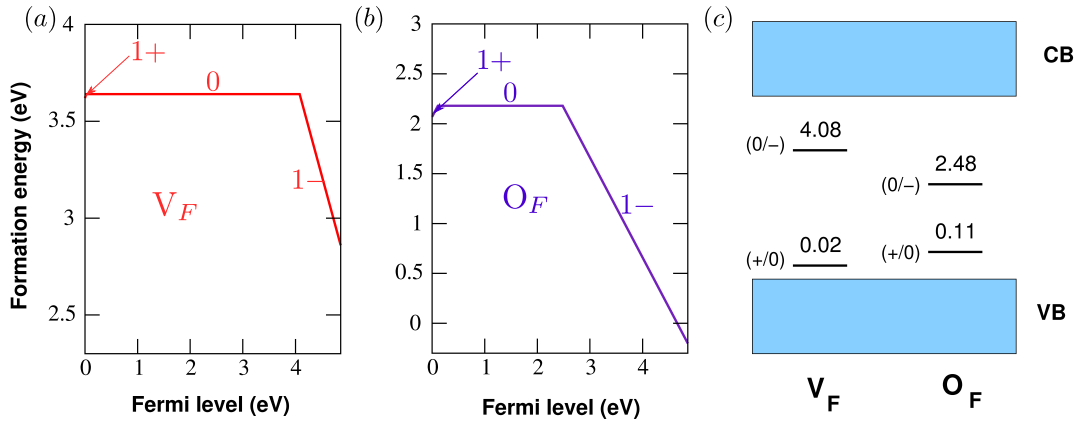

FIGURE 3.9: Formation energies of configurations (a) 2_I-V_F and (b) 2_I-O_F, as a function of 2_I PTFE Fermi level. (c) Energy band diagram and transition levels of corresponding configurations. In (c) VB and CB denote the valence and conduction bands, respectively.

To investigate the magnetic stability of defective 2_I configurations, we calculated the energetic stabilization due to the appearance of magnetic moments, defined by

$$\epsilon_s = E_m - E_{nm}, \tag{3.6}$$

where E_m is the total energy of the most stable magnetic ground state and E_{nm} the total energy of the corresponding nonmagnetic configuration. We also calculated the energy difference between the FM and AFM configurations for those configurations with stable magnetic phases. Our results are shown in table 3.2.

TABLE 3.2: Calculated magnetic stabilization energies per point defect X ($X = V_F, O_F$) of defective 2_I phase of PTFE. The corresponding energy differences between antiferromagnetic (AF) and ferromagnetic (FM) configurations are also listed. In these calculations we considered $q = 0$.

Config.	ϵ_s (meV/X)	$E_{AF} - E_{FM}$ (meV)
2_I-2V_F	-186.5	same carbon
2_I-2V_FN	-2.6	nonmagnetic
2_I-2V_FNN	-123.6	-304.1
2_I-2V_FC	-526.1	-1.2
2_I-2O_FNN	-2.1	nonmagnetic
2_I-2O_FC	-241.65	0

These results indicate that some of the investigated configurations are stabilized by the formation of local magnetic moments, with maximum energy gain of about -526.1 meV per defect. Except for configuration 2_I-2V_FNN, for the configurations with $M_A \neq 0$, the unpaired electrons do not couple as can be noticed from our calculated $E_{AF} - E_{FM}$. In contrast, configuration 2_I-2V_FNN (see figure 3.7(c)) has an energetically favorable antiferromagnetic coupling between unpaired electrons of -304.1 meV. Therefore, our calculations indicate that defect-induced local magnetic moments in PTFE are energetically favorable, however with no effective ferromagnetic coupling between them. These findings suggest that the defective configurations addressed in this section do not induce any long-range ferromagnetic ordering in PTFE films, but instead give rise to a paramagnetic response under application of an external magnetic field. Once the Fermi level of the host material can be shifted due to charge doping, we further calculated the total magnetization of 2_I-V_F and 2_I-O_F configurations for the distinct charge states previously considered. The obtained values are listed in table 3.3.

Moreover, the obtained values of total magnetization indicate that upon charge doping the local magnetic moments of V_F and O_F defects can be suppressed. In special, we find that once E_F approaches the conduction band, the impurities with charge state $q = -1$ become more stable, and their local magnetic moment are suppressed by the additional charge doping. This result suggests that the paramagnetic response of defective PTFE films is controled by physical charge doping.

TABLE 3.3: Calculated total magnetization of configurations 2_I-V_F and 2_I-O_F with distinct charge states, namely $q = -1$, 0, and +1. Magnetizations are given in units of μ_B/X, where $X = V_F$ or O_F.

Config.	q	M_T
	+1	0.75
2_I-V_F	0	1.00
	-1	0
	+1	0.50
2_I-O_F	0	1.00
	-1	0

From our calculated band structures, presented in figure 3.10, we observe that fluorine vacancies and oxygen impurities give rise to dispersionless defective levels (v_1 and c_1) with broken spin degeneracy. In addition, for fluorine vacancies in the nearest-neighbor sites (configuration 2_I-$2V_F$N), we observe defective levels near the band edges of pristine PTFE. Since this configuration can be viewed as the minimum polyconjugated structure (with π-bonds) within the polymer chain, our results suggest that upon increasing the conjugation of the polyconjugated structure, defective bands will appear within the PTFE band gap. This finding, by its turn, is in agreement with previous works [8, 155] which claimed that the color of irradiated PTFE films may be explained by the formation of polyconjugated structures in the polymer chains.

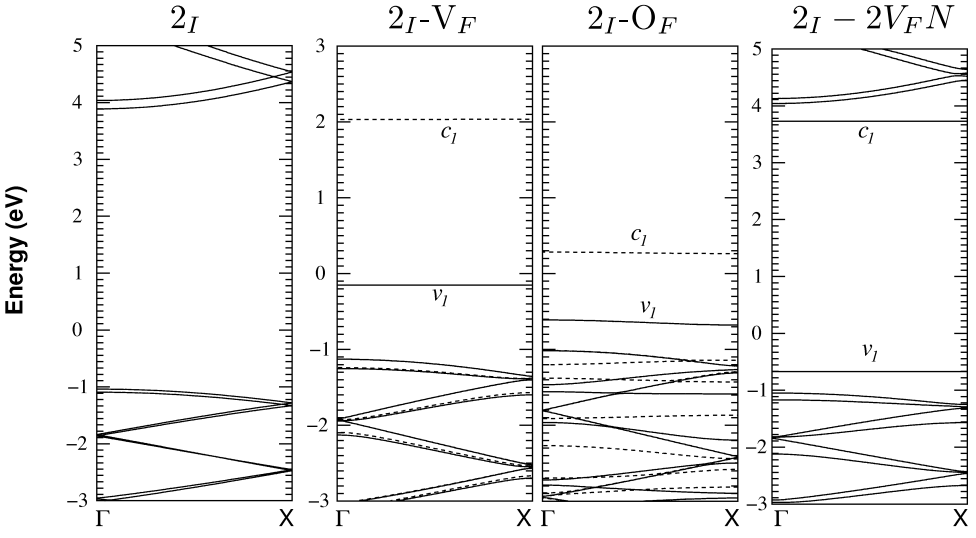

FIGURE 3.10: Calculated band structures of pristine 2_I phase, 2_I-V_F, 2_I-O_F, and 2_I-$2V_F$N configurations. Solid (dashed) lines represent the spin-up (spin-down) components.

As can be seen in the projected density of states shown in figure 3.11, these dispersionless levels originate mainly from the $2p$ electronic states of defective carbon and oxygen impurity in 2_I-V_F and 2_I-O_F configurations, respectively. In addition, we calculated

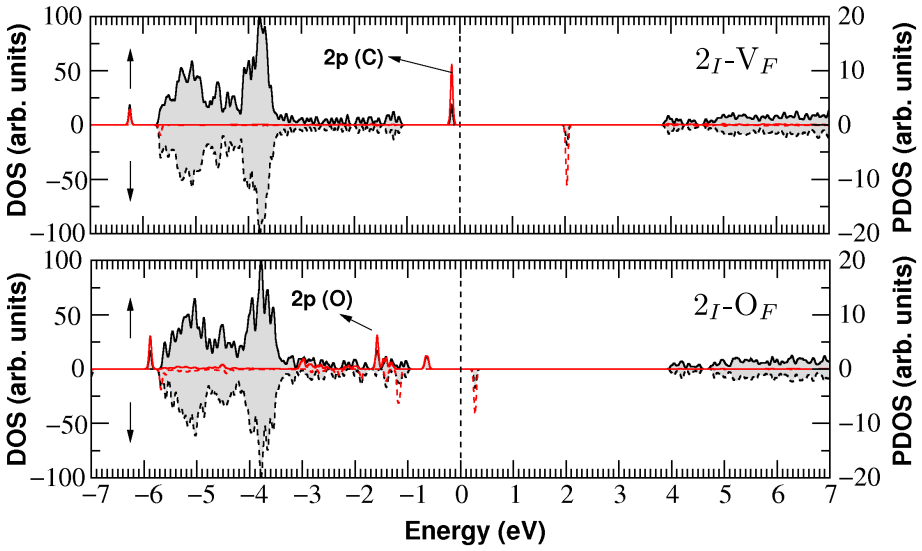

FIGURE 3.11: Calculated total (black) and projected density of states (red). In 2_I-V_F configuration the projection is on the defective carbon and in the case of 2_I-O_F configuration it is on the oxygen impurity.

the local density of states, considering an energy window which includes only the dispersionless electronic states. The corresponding isosurfaces are shown in figures 3.12(a)-(b). These isosurfaces are in agreement with our projected density of states, from which we obtain that the defect electronic states come mainly from $2p$ levels of defective carbon and the oxygen impurity. Residual contribution of fluorine atoms near the defective site can be observed for both defects. The localized character is also emphasized.

3.2.3 Magnetic ordering from defects in distintic chains

Since fluorine vacancies and oxygen impurities give rise to local magnetic moments, we next investigate whether defects in distinct molecular chains can be the source of any magnetic ordering. With this purpose we focused on configuration 2_I-$2V_F$C shown in figure 3.7(d). From our calculations we find that local moments in this configuration do not couple, as indicated by the negligible energy difference between the ferromagnetic and antiferromangetic configuration, $E_{AF} - E_{FM} = 0$. By considering that this energy difference can be a function of the relative distance between the molecular chains, we performed additional calculations for relative distances of 5.04, 4.84, 4.53, and 3.82 Å (in our calculations presented in the previous section this distance was 5.61 Å). However, our findings do not indicate any difference between the energy of FM and AF configurations, signaling the absence of magnetic coupling.

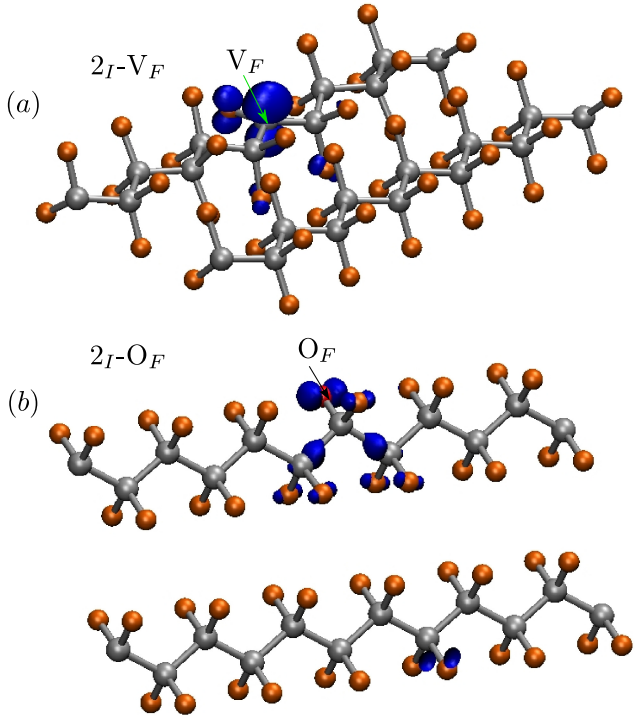

FIGURE 3.12: Isosurfaces (0.01 electrons/bohr^3) obtained from the local density of states considering only the dispersionless electronic states in (a) 2_I-V_F and (b) 2_I-O_F. Carbon, fluorine, and oxygen atoms are represented by grey, orange, and red spheres, respectively.

As previously mentioned, in Ref. [137] the authors argued that local moments originated from carbon dangling bonds, on distinct molecular chains, would be responsible for the long range magnetic ordering observed in the stretched Teflon tapes. Based on this assumption, the authors proposed a theoretical model formed by polymeric segments packed along the same direction, from which a ferromagnetic coupling was suggested based on first-principles calculations. In order to investigate the ferromagnetic coupling between carbon dangling bonds proposed by Ma and co-workes, we adopt the structural models reported in Ref. [137], which are illustrated in figure 3.13. Notice that each molecular PTFE segment has a carbon dangling bond, which, according to the authors are the source of local magnetic moments.

At first we calculated the energy difference $E_{AF} - E_{FM}$ for the distances of 4.8 Å in $1D$ and 4.95 Å in $2D$ models, as performed in Ref. [137]. In this case, we find $E_{AF} - E_{FM} = -0.8$ meV for the $1D$ model and -1.14 meV for the $2D$ case, which rules out any ferromagnetic ordering, in contrast to what was proposed by the authors. In particular, they found 59 meV for the $1D$ model and 82 meV for the $2D$ one. In

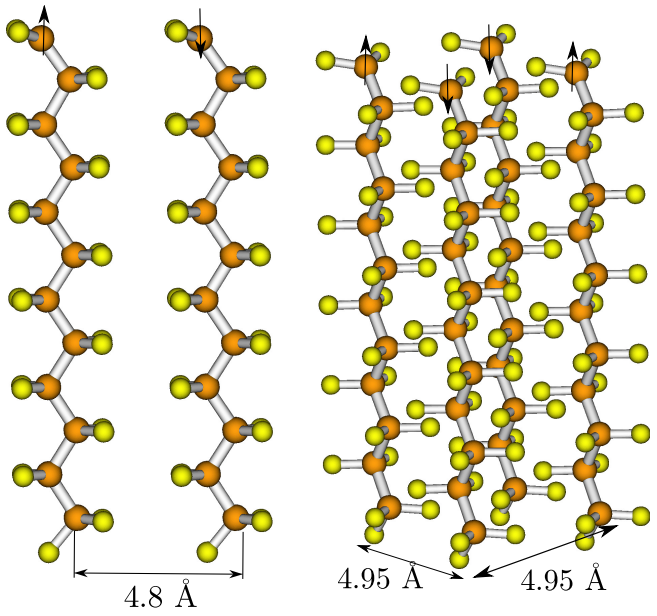

FIGURE 3.13: 1D and 2D structural models of PTFE segments considered by Ma *et al.* [137] to investigate the magnetic coupling between carbon dangling bonds. The up and down arrows represent the local magnetic moments associated with each carbon dangling bond. In particular, an antiferromagnetic configuration is depicted. Carbon and fluorine atoms are represented by orange and yellow spheres, respectively.

addition, our results indicate an energetic preference for an antiferromagnetic ordering, which is also in contrast with the findings reported in Ref. [137].

3.3 Summary

In summary, our calculations indicate that oxygen substitutional impurities are energetically more favorable than fluorine vacancies in PTFE films. In addition, upon increasing of the fluorine vacancy concentration, we find that the formation of polyconjugated structures in polymer chains is an energetically favorable process. In particular, our calculations are in agreement with previous works which suggested that these polyconjugated structures may be responsible for the color and fluorescent properties of irradiated PTFE films. We also find that fluorine vacancies and oxygen impurities can give rise to local magnetic moments without the breaking of the polymer carbon backbone. However, the corresponding local magnetic moments can be suppressed by charge doping. Importantly, we do not observe any ferromagnetic coupling among the configurations considered. This indicates that the observed ferromagnetic ordering reported by Ma and co-workers [137] does not originate from the defective configurations addressed in this work. Finally, we mention that, even for the structural models proposed by the

authors, our calculations do not suggest any ferromagnetic coupling between the PTFE fragments.

Part II

Applications of DFT+DMFT calculations

Chapter 4

Metal-Insulator transitions in VO_2 and NbO_2: a brief review

In this chapter we present a brief introduction to emergent phenomena in transition-metal oxides, focusing on metal-insulator transitions. Experiments and theoretical proposals on the metal-insulator transitions in vanadium and niobium dioxides, namely VO_2 and NbO_2, are reviewed. In particular, we present the results of previous works which attempted to disclose the driving force of these MITs and the physical mechanisms responsible for the gap formation in the low-temperature phases of both materials.

4.1 Introduction

Transition-metal oxides (TMOs) constitute a vast class of materials which exhibits a wide range of structural, electronic, and magnetic properties. Structurally, these materials can crystallize into a variety of structures, whose names are taken from the corresponding oxide minerals, as illustrated in figure 4.1. Meanwhile, in addition to the s and p electrons, the presence of transition-metal d electrons gives rise to a rich variety of electronic and magnetic properties. For instance, there exist oxides with metallic (e.g. ReO_3), insulating (e.g. $BaTiO_3$), semiconducting (e.g. TiO_2), ferromagnetic (e.g. CrO_2), antiferromagnetic (e.g. Cr_2O_3), and paramagnetic (e.g. MoO_2) properties [162].

Different from conventional metals and semiconductors, the macroscopic physical properties of TMOs emerge due to the interplay or competition of various mechanisms

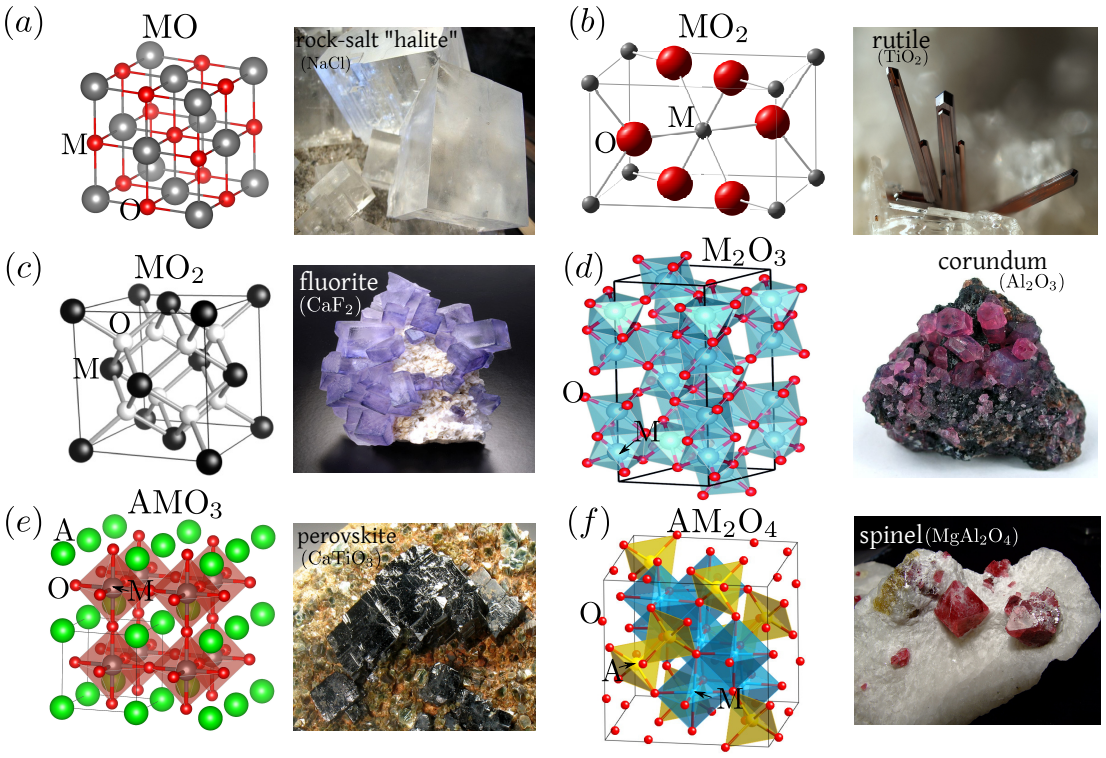

FIGURE 4.1: Common crystalline structures of transition-metal oxides: (a) rock-salt (MO), (b) rutile (MO_2), (c) fluorite (MO_2), (d) corundum (M_2O_3), (e) perovskite (AMO_3), and (f) spinel (AM_2O_4). "A" denotes cationic elements, "M" transition-metals, and "O" oxygens. The photos illustrate the respective minerals from which the structure names were given.

with similar energy scales. In particular, strong electron-electron interactions, lattice-electron, electron-spin, and spin-orbit couplings lead to competing phases with enhanced sensitivity to small external perturbations such as temperature, pressure, and applied fields [163]. For example, in systems wherein the interaction energy between electrons dominates their kinetic energy, the electrons localize giving rise to an insulating phase, denoted as Mott insulator (for an introduction about Mott insulators see appendix I). Interestingly, the variety of interactions leads to additional exotic physical properties in TMOs. Transitions to states with vanishing electrical resistivity, i.e. superconducting states, are observed in some copper and iron-based oxides when these materials are cooled down below their respective critical temperatures (see figure 4.2(a)).[1] It is noteworthy that the highest known critical temperatures achieved by cuprates and iron-based superconductors are 164 K [164] and 56.3 K [165], respectively.[2] For comparison, the highest critical temperature reported in the literature is of 203 K, obtained

[1]The critical temperature is defined as the temperature below which the material turns into a superconductor.

[2]Cuprates are commonly denoted as high-T_c superconductors due to the fact that some of these materials possess critical temperatures above the temperature of liquid nitrogen, 77 K.

for H_3S superconductors under pressure [166]. We mention that superconductivity in these compounds is one of the major problems in condensed matter physics. Another type of abrupt change of transport properties is observed in manganites, in which a dramatic change in the electrical resistivity is induced by an external magnetic field (see figure 4.2(b)) [167]. Orbital ordering [168] (see figure 4.2(c)) and multiferroicity [169] have also been observed in manganites. Finally, we mention the abrupt transitions between insulating and metallic phases in numerous transition metal oxides, which we explore in more detail below.

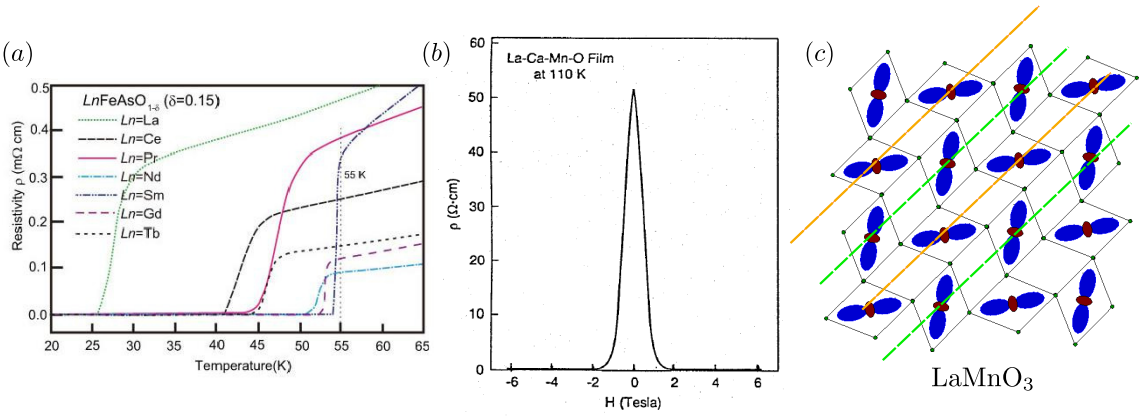

FIGURE 4.2: Examples of emergent phenomena in transition-metal oxides. (a) Electrical resistivity of iron-based superconductors as a function of temperature [170], (b) electrical resistivity as a function of external magnetic field of manganite thin films [171], and (c) illustration of orbital ordering in layers of $LaMnO_3$.

Historically, metal-insulator transitions (MITs) in transition-metal oxides were first reported by Foëx *et al.* in a couple of works in the late forties [172] and early fifties [173], in which the authors addressed the temperature dependence of the resistivity of Ti_2O_3 and V_2O_3 samples. Few years later, in the Bell laboratories, Morin observed similar MITs in polycristalline samples of Ti_2O_3, V_2O_3 [174], and single crystals of the same oxides, including VO and VO_2 [175]. As shown in figure 4.3(a), Morin observed abrupt changes of conductivity over several orders of magnitude, with hysteresis about the transition temperatures, in single crystals of Ti_2O_3, V_2O_3, VO, and VO_2.

From a technological perspective, these abrupt changes of conductivity within a short range of few kelvins, accompained by the ultrafast switching between metallic and insulating phases, have motived the realization of novel devices, denoted as phase transition electronic devices. In particular, one can mention electronic switches, field effect transistors, optical detectors, memristors [176, 177], and solid-state sensors as devices in which TMOs presenting metal-insulator transitions are promissing candidates [178].

On the other hand, the physical mechanisms responsible for the MITs in these oxides have attracted great attention of condensed matter physicists [179].

In this chapter we discuss the MIT in vanadium and niobium dioxides which are rutile-based d^1 systems. In particular, the MIT in VO_2 has been under debate for many years mainly due to the complex interplay between lattice distortions and electronic correlations. In respect to NbO_2, its MIT has been less investigated due to reasons which will be commented on the following.

4.2 Metal-insulator transitions in VO_2 and NbO_2

4.3 Experiments and first theoretical models

Vanadium dioxide undergoes a MIT at a temperature of 340 K [175] while in the case of niobium dioxide it happens at around 1081 K [180–182], as can be seen in the measurements of their conductivity as a function of temperature shown in figure 4.3.

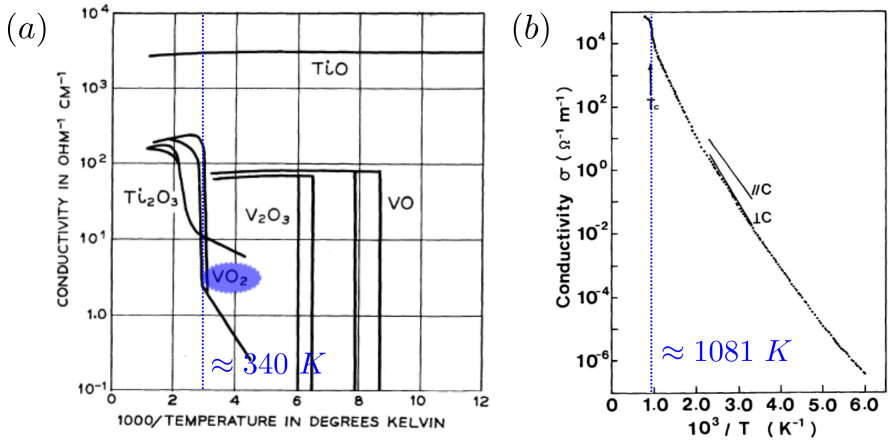

FIGURE 4.3: Conductivity of (a) VO_2 and (b) NbO_2 as a function of reciprocal temperature obtained by Morin [175] and Jannick *et al.* [180], respectively. In the graphics the transition temperatures of VO_2 (340 K) and NbO_2 (1081 K) are indicated by dotted lines.

In both systems, the MIT is accompained by structural distortions from a high-temperature rutile structure (R) [183, 184], where the transition-metal atoms are equally spaced along the rutile c axis (see figures 4.4(a) and 4.5(a)), to low-temperature distorted structures. In the case of VO_2, under ambient pressure, the vanadium atoms dimerize and tilt with respect to the rutile c axis, giving rise to the M_1 phase [185] illustrated in

figure 4.4(b). In addition, previous experimental works have shown a distinct monoclinic phase, denoted as M_2, which can be stabilized at ambient conditions by stress along the $[001]_R$ axis or by doping with 3+ ions, such as Cr^{3+}, Al^{3+}, Fe^{3+}, or Ga^{3+} [186, 187]. As can be seen in figure 4.4(c), in this phase half of vanadium atoms dimerize, without tilting, whereas the other half experiences a zigzag-like distortion along the c axis. In the case of NbO_2, the low-temperature structure is a body-centered tetragonal (bct) structure [184] (see figure 4.5(b)) which presents similar structural distortions as the M_1 phase of VO_2.

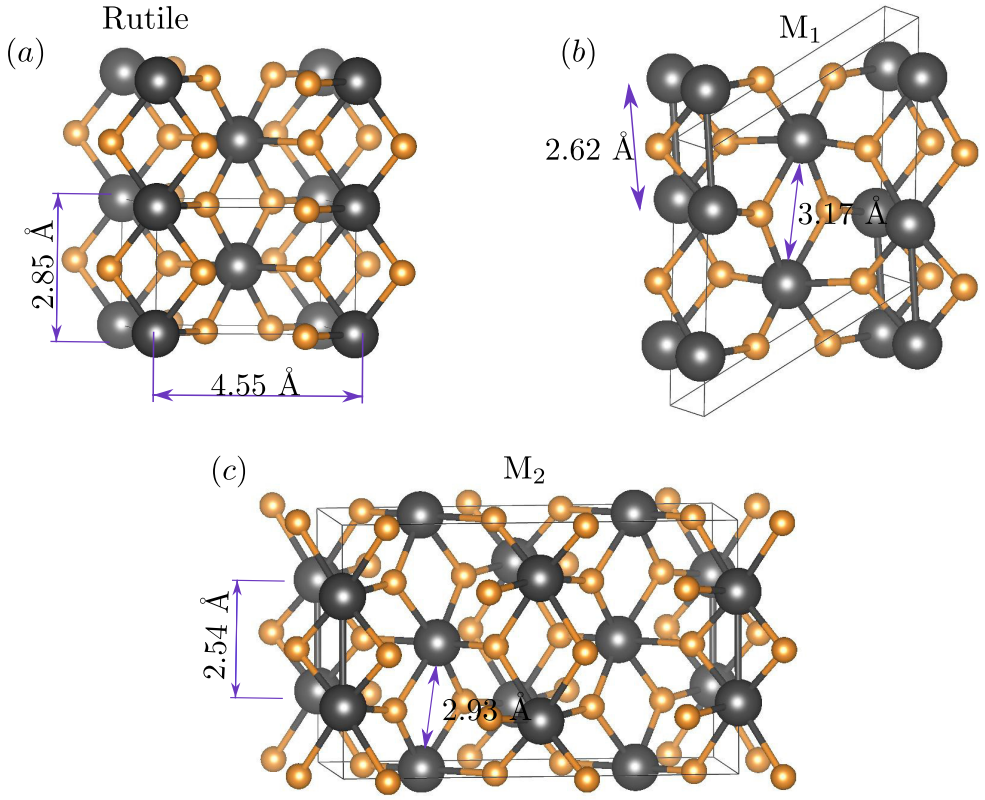

FIGURE 4.4: Crystal structures of (a) rutile (R) (space group $P4_2/mnm$), (b) monoclinic M_1 (space group $P2_1/c$), and (c) monoclinic M_2 (space group $C2/m$) phases of VO_2. Vanadium atoms are represented by the black spheres while the oxygens by the orange ones.

In the rutile structures, the vanadium or niobium atoms are located inside oxygen distorted edge-sharing octahedra. In particular, these octahedra are trigonal distorted, which in turn gives rise to a crystal field responsible to the splitting of the t_{2g} manifold into an a_{1g} state and an e_g^π douplet, *viz.*, $t_{2g} = a_{1g} \oplus e_g^\pi$, as illustrated in figure 4.6(a). Employing the local coordinate system shown in figure 4.6(b) [188], we observe that the a_{1g} level corresponds to the $d_{x^2-y^2}$, which mediates the σ-type $d-d$ overlap along the rutile c axis. Further, the e_g^π douplet corresponds to the d_{xz} and d_{yz}, where the

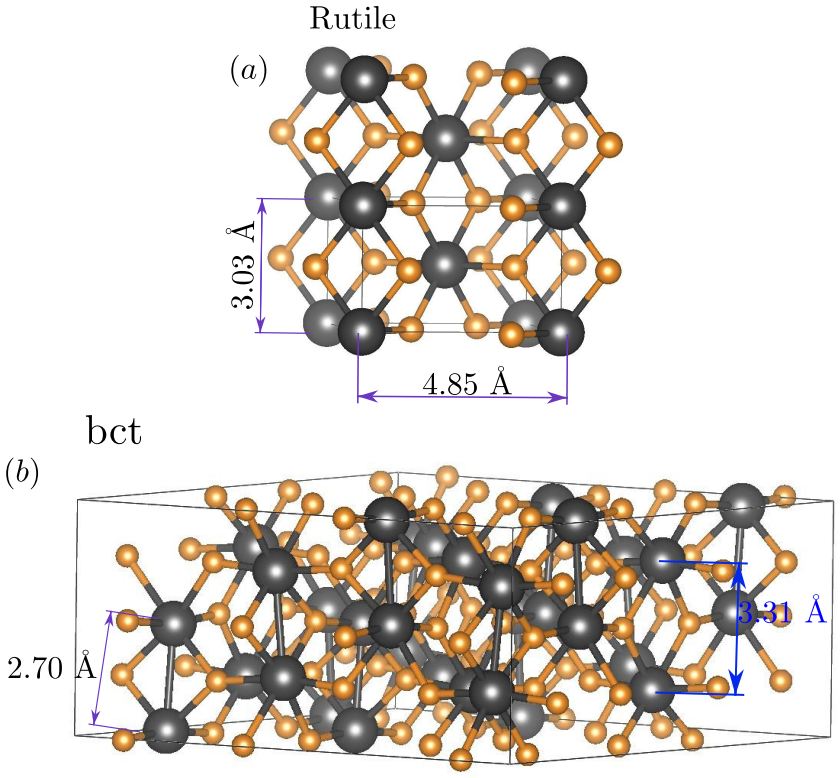

FIGURE 4.5: Crystal structures of (a) rutile (R) (space group $P4_2/mnm$) and (b) body-centered tetragonal (bct) (space group $I4_1/a$) phases of NbO_2. Niobium atoms are represented by the black spheres while the oxygens by the orange ones.

former mediates the π-type overlap along the rutile c axis while the latter mediates a smaller σ-type overlap along the a axis, as depicted in figure 4.6(b). Since the d_{z^2} and d_{xy} orbitals point toward the oxygen ions these states (e_g^σ manifold) are higher in energy than the previous levels.

Based on the d^1 configuration of each transition-metal ion and the structural distortions concerning the transition-metal atoms, the first theoretical description of the MIT in VO_2 (R$\rightarrow$ M_1) pointed out a structurally-driven MIT. According to Goodenough [189], the covalent-type cation-cation bond formation in the M_1 phase would support a phase transition with the appearance of a band gap at low temperatures. In fact, in a band-like picture, the same author showed [13] that in the rutile phase both a_{1g} and e_g^π states give rise to semi-occupied states accounting for the metallic character (figure 4.7). Further, as a result of structural distortions in M_1 phase, the a_{1g} band splits into an occupied bonding and empty antibonding subbands. In addition, the tilting of the vanadium atoms, commonly denoted as antiferroelectric displacement,[3] leads to an

[3]This distortion is characterized by the displacement of vanadium atoms perpendicular to the rutile c axis, in such a way that two first-neighbors are displaced in opposite directions.

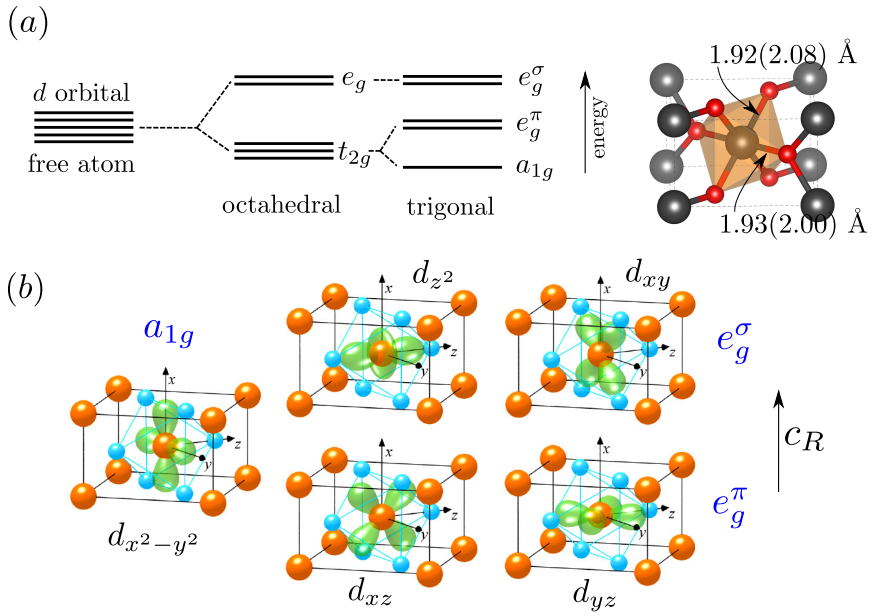

FIGURE 4.6: (a) Splitting of d-subshell in rutiles due to the crystal field, wherein the t_{2g} manifold on an octahedral symmetry field is further splitted due to the octahedral distortion (trigonal), resulting into $t_{2g} = a_{1g} \oplus e_g^\pi$. The distortion on the oxygen octahedral can be noticed by examining the transition metal-oxygen bond lenghts. In R VO_2 (NbO_2), one can notice that the distance between the vanadium (niobium) and the apical oxygen is 1.93 (2.00) Å, while the distance between the vanadium (niobium) and the basal oxygens is 1.92 (2.08) Å. This shows that the octahedron in R VO_2 (NbO_2) is elongated (compressed). In (b) the local coordinate system introduced by Eyert [188] is shown with the d orbitals. The structures were taken from Ref. [188].

upshift of the e_g^π subband with respect to the occupied a_{1g} subband, resulting in the gap formation between these two subbands (figure 4.7), suggesting thus that VO_2 undergoes a Peierls-type transition. Hence, in Goodenough's picture the M_1 phase of VO_2 is a Peierls insulator (for an introduction about a Peierls insulator see appendix I).

However, the experimental findings on the M_2 phase reported by Pouget and co-workers established the importance of electronic correlations in the electronic structure of VO_2 [190, 191]. By means of nuclear magnetic and electron spin resonance (NMR and ESR) measurements they observed the existence of two types of vanadium sites in the M_2 phase: one type related to the dimerized vanadium atoms and the other to the vanadium undimerized atoms. In particular, they found that d electrons are localized in the vanadium sites of the undimerized chain, which in turn implies that these electrons may be on the localized side of a Mott transition [190, 191]. In particular, Pouget *et al.* interpreted the obtained magnetic susceptibility of M_2 phase by considering local moments on the vanadium sites of the undimerized chain (coupled antiferromagnetically), using a set of independent spin-1/2 Heisenberg chains [190]. These findings motived

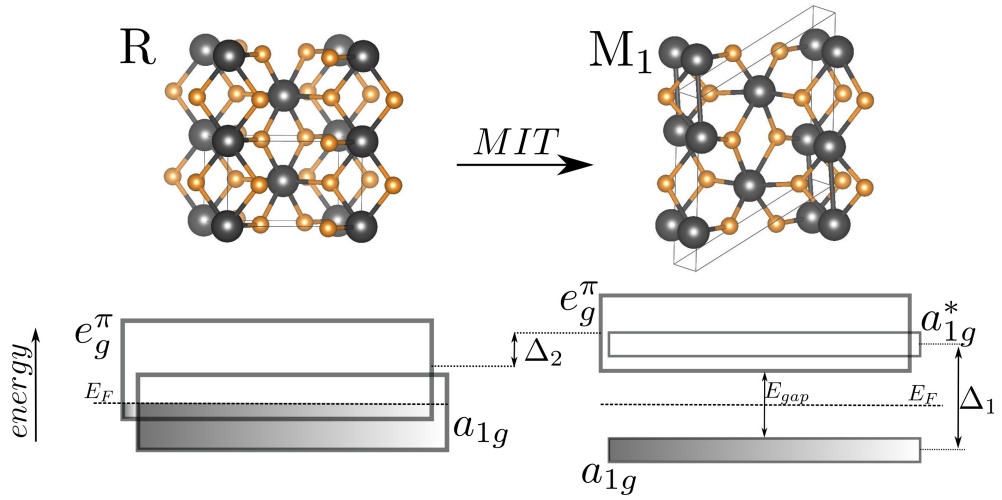

FIGURE 4.7: Energy bands of R and M_1 phases of VO_2 as proposed by Goodenough [13]. Within a band picture, Goodenough proposed that the band gap (E_{gap}) between the a_{1g} and e_g^π subbands appears in M_1 phase due to the vanadium dimerization (Δ_1) and antiferroelectric displacement (Δ_2). Differently, in Mott's picture the splitting Δ_1 is caused by Coulomb repulsion between electrons in the a_{1g} subband.

Zylbersztejn and Mott [14] to investigate the role played by electronic correlations on the gap formation of the insulating phases of VO_2. In contrast to the Peierls mechanism proposed by Goodenough, Zylbersztejn and Mott pointed out that the lattice distortions in VO_2 can only create a small gap, if any, between the a_{1g} and e_g^π subbands. In particular, they argued that the antiferroelectric displacement induces the upshift of the e_g^π subband, which, in combination with the dimerization, gives rise to an a_{1g} subband completely filled. According to them, it is a result of the Coulomb repulsion between electrons in the a_{1g} subband that this subband splits in bonding and antibonding subbands, leading to the gap formation. Therefore, in Mott's picture the role played by the distortions is to provide empty (completely filled) e_g^π (a_{1g}) subbands, but not to determine the energy band gap.

Since the establishement of the Peierls and Mott pictures on the MIT in VO_2, numerous investigations have attempted to disclose the driving force behind the MIT in VO_2, and to understand the insulating nature of the low-temperature phases of this material. Experimentally, phonon-mediated instabilities of rutile phase have supported a structurally-driven MIT. By means of inelastic X-ray scattering (IXS) measurements, Budai *et al.* [192] obtained the phonon dispersion of R phase of VO_2, which shows acoustic phonon softening along $\Gamma - R - A - M$ in the respective Brillouin zone (see figures 4.8(a) and (b)). We mention that these findings are in agreement with the previously reported softening of transverse modes near the R point in rutile phase,

as observed experimentally by Terauchi and Cohen [193] and theoretically predicted by Gervais and Kress [194]. These soft modes in the R phase of VO_2 indicate the rutile instability under cooling, towards a structural phase transition. In particular, the phonon eigenvectors of the lowest-frequency mode near the R point correspond to the structural distortions presented in the M_1 phase [194], as illustrated in figure 4.8(c).

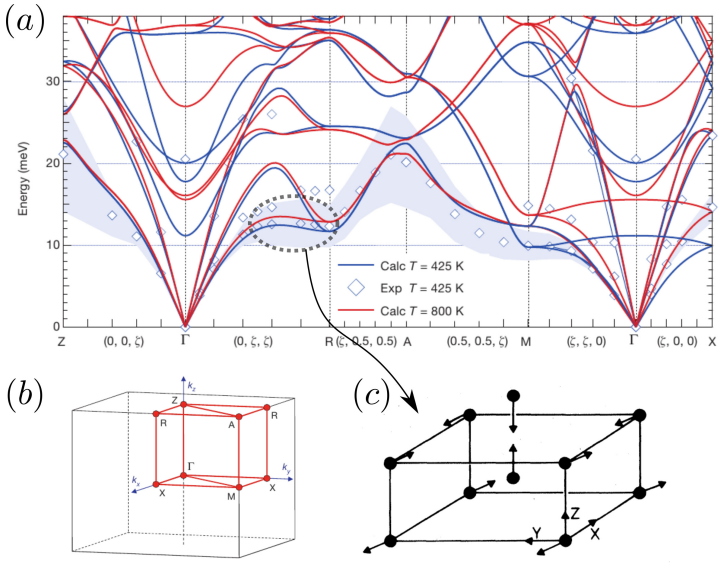

FIGURE 4.8: (a) Phonon dispersion of R phase of VO_2. Diamond points represent the experimental obtained data while the continuous lines are *ab initio* anharmonic lattice dynamics at distinct temperatures [192]. (b) Brillouin zone of R structure, with high-symmetry directions (red lines). Figures in (a) and (b) were taken from Ref. [192]. (c) Phonon eigenvectors at the R point of rutile VO_2 [194].

Other experiments on the rutile phase of VO_2 indicate signatures of strong electronic correlations effects on its electronic properties. In the work by Pouget and coworkers [195], by doping VO_2 with niobium atoms ($V_{1-x}Nb_xO_2$), the authors found that the rutile structure turns into an insulating state for a concentration $x \geq 0.15$. Since the niobium atoms have a bigger covalent radius than vanadium atoms, the doping induces a lattice expansion, which suggests that under lattice expansion the R phase undergoes a Mott-Hubbard transition (see appendix I). More recently, it was also reported that VO_2 thin films doped with tungsten ($V_{1-x}W_xO_2$) present metal-insulator transitions, without vanadium dimerization for $x \geq 0.11$, with characteristics of a Mott-Anderson transition [196]. In addition, from XPS experiments on $VO_2/TiO_2(001)$ thin films, Okazaki *et al.* [197] obtained a quasi-particle weight of about $Z \approx 1/3 = 0.33$ for the rutile phase. It is noteworthy that this quasi-particle weight can be interpreted as the inverse of the effective mass enhancement due to electron-electron interactions.

As described in the Landau Fermi liquid theory, the excitations of an interacting electron system can be mapped onto the excitations of a noninteracting electron system; where these excitations can be thought as quasiparticles with enhanced (renormalized) effective mass m^* [17]. This mass renormalization is associated with the quasi-particle weight as $m^*/m_{band} \sim 1/Z$ (see equation J.11), where m_{band} is the bare band mass of noninteracting Bloch electrons.[4]

X-ray spectroscopy and photoemission measurements have provided valuable information about the changes of the t_{2g} subbands through the metal-insulator transition in VO_2. For instance, x-ray absorption measurements obtained by Haverkort *et al.* [198], showed that the R$\rightarrow$ M_1 transition is accompained by a strong orbital polarization in favor of the a_{1g} subband. In particular, they found that the t_{2g} occupation goes from an almost isotropic occupation concerning the a_{1g} and e_g^π subbands in R phase, to an almost completely occupied a_{1g} subband in M_1 phase. These findings pointed out a feature of a Peierls-like transition (system becomes more one dimensional), though the observed strong orbital polarization is only possible in the presence of strong correlations. Furthermore, the x-ray absorption spectra obtained by Koethe *et al.* [199] indicates that the bottom of the conduction band of M_1 phase is mainly composed by e_g^π states. They observed that when the MIT takes place, the peak with a_{1g} symmetry (at around 530 eV) vanishes in the R phase, as indicated by the down arrow in figure 4.9(b). This is in agreement with the proposed a_{1g} subband splitting in the M_1 phase. With respect to the semi-occupied states in R phase, the experimental data indicates a more isotropic situation wherein both a_{1g} and e_g^π subbands contribute to the electronic states around the Fermi level. The photoemission spectra by its turn shows an occupied V-3d peak at around 0.8 eV below the Fermi level for the M_1 phase, and a shoulder at -1.3 eV for the R phase, as can be seen in figure 4.9(a). As we will mention in the next section, the latter is not captured in DFT calculations, which may signal the presence of strong correlations in the R phase of VO_2.

More recently, the fabrication of VO_2 nanostructures has allowed the precise control of the stress applied to the samples. In the experiment performed by Park *et al.* [200], the authors studied the MIT in single crystal VO_2 nanobeams by using uniaxial stress. Interestingly, they found that a triple point of R, M_1, and M_2 structural phases is at the

[4]For noninteracting systems the quasiparticle weigth is equal to unity, while in a strongly correlated system, as in a Mott insulator, Z goes to zero.

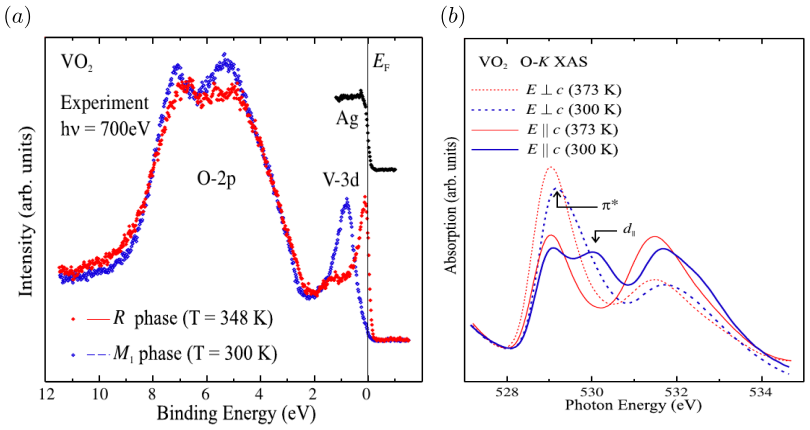

FIGURE 4.9: (a) Photoemission and (b) x-ray spectroscopy spectra of R and M_1 phases of VO_2 obtained by Koethe *et al.* [199].

transition temperature associated with the metal-insulator transition (see figure 4.10), suggesting that domains with distinct structural phases should coexist near the MIT. In fact, as shown by Qazilbash *et al.* [201] insulating and metallic phases coexist in the vicinity of the metal-insulator transition in VO_2 films, as can be seen in the images of near-field scattering amplitude measurements shown in figure 4.11. In these images the metallic regions are shown in light blue, green, and red colors whereas the insulating regions in dark blue colors. Other experiments on VO_2 nanorods [202] revealed a mixed phase of M_2 and R strucutres with antiferromagnetic properties, which indicate an antiferromagnetic ordering between unpaired vanadium atoms.

With the purpose of decoupling the relation between the structural phase transition and the MIT in VO_2, a recent experimental work has induced this transition by the application of femtosecond laser pulses on insulating VO_2 films. As reported by Wegkamp *et al.* [203], the gap of the insulating phase collapses upon photoexcitation on ultrafast time scales, giving rise to a monoclinic metallic phase. In particular, the authors pointed out that the photoexcitation gives rise to hot carriers, which have an associated temperature much higher than the lattice temperature. As a consequence, the lattice does not contribute to the fast response of VO_2 to ultrashort pulses. We mention that more recently numerous experimental works have reported on the existence of monoclinic-like metallic phases of VO_2 [204–207].

The metal-insulator transition in NbO_2 has not received so much attention. As mentioned by Seta and Naito [208] this MIT has been experimentally less studied in comparison to the MIT in VO_2, in part due to the higher temperature needed to induce

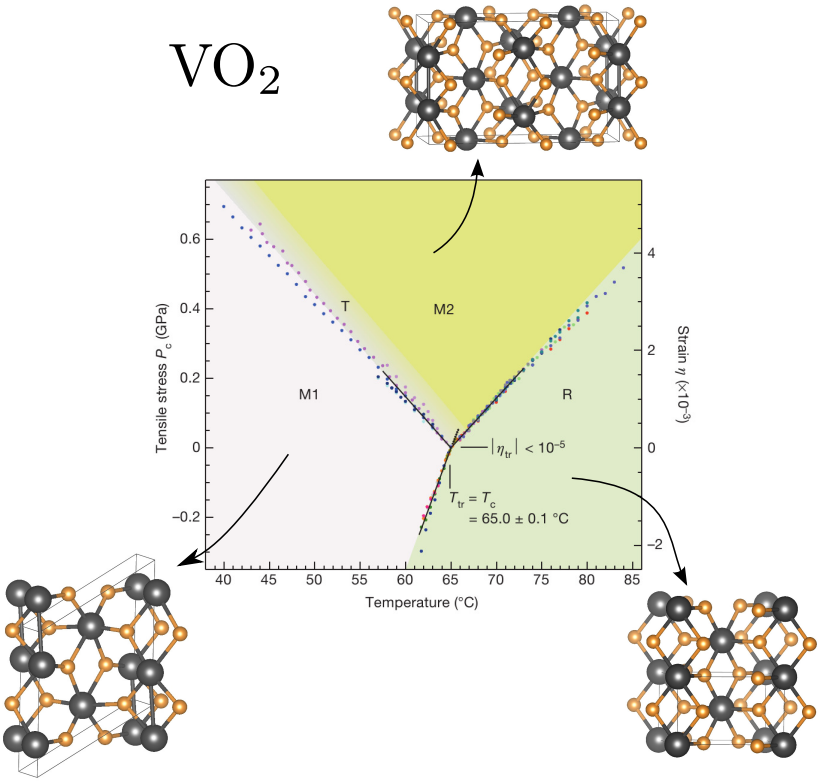

FIGURE 4.10: Phase diagram of VO_2 illustrating the solid state structural triple point near the MIT, as reported by Park *et al.* [200].

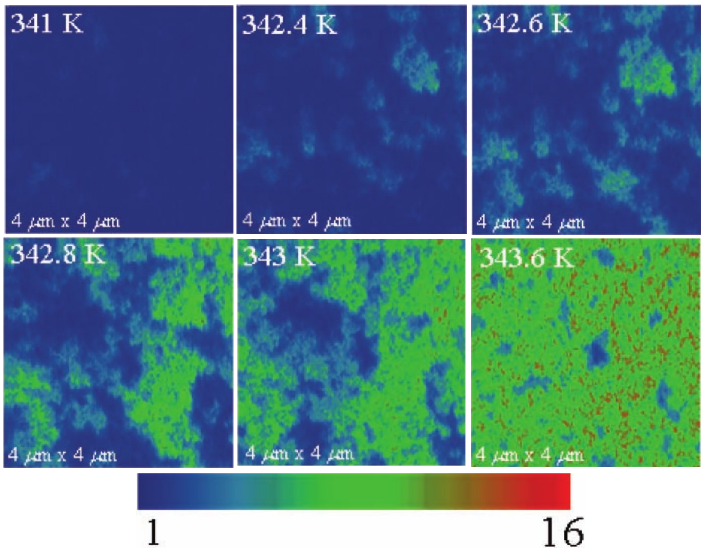

FIGURE 4.11: Images of near-field scattering amplitude measurements reported by Qazilbash *et al.* [201] of VO_2 films in the vicinity of the MIT. The metallic regions are shown in light blue, green, and red colors whereas the insulating regions in dark blue colors.

the transition in NbO_2. Since the early works on the MIT in NbO_2, it was suggested that it is a structurally-driven transition and is of second-order in contrast to the first-order MIT in VO_2 [208, 209]. As we will discuss in the following, DFT calculations support a structurally-driven MIT in NbO_2. In respect to the instability of the rutile phase of NbO_2, the experimental observation of soft mode phonons remains inconclusive. In particular, Shapiro *et al.* investigated the phase structure transition in single crystals of NbO_2, by means of neutron scattering. From their findings they suggested the existence of soft phonon mode at the P point, with wavevector $q_p = (1/4, 1/4, 1/2)$ [210]. However a few years later, Pynn and co-workers [211] reported inelastic neutron scattering measurements on NbO_2 with no clear evidence of soft phonon modes in the rutile phase. Finally, we mention that a recent theoretical work [212] emphasizes a structurally-driven MIT in NbO_2 due to soft modes at the P point of the rutile Brillouin zone, which in turn supports that the bct phase of NbO_2 is a Peierls-type insulator.

In the experimental literature the precise value of the energy gap of the bct phase remains inconclusive. In particular, previous experimental works have reported a wide range of values, ranging from 0.5 eV to 1.20 eV [182, 213]. In the work by Posadas *et al.* [214], the authors obtained a band gap of at least 1.0 eV through x-ray photoelectron spectroscopy and inverse photoelectron spectroscopy measurements for NbO_2 films on various oxide substrates. From ellipsometric measurements for NbO_2 films on (111)-oriented LSAT[5] single crystal, O'Hara and co-workers [215] found an indirect gap of 0.7 eV. As we shall see in chapter 5 this latter value is in good agreement with our obtained gap.

4.4 First principles investigations

DFT calculations have been employed to investigate the electronic structure of VO_2 and NbO_2. With respect to the rutile phase, DFT calculations, based on LDA or GGA, were able to describe the metallic nature of this phase [188, 216–219]. In figure 4.12(a), we show the DFT (LDA) band structure of rutile VO_2 obtained by Eyert [188], in which the bands between -7.6 and -2.2 eV are mainly due to $O-2p$ states, those from -0.6 to 2.0 eV are mainly due to t_{2g} states, and those from 2.0 to 5.5 eV correspond to e_g states. For the rutile NbO_2 the same author obtained the same group of bands [219], wherein the

[5] $(LaAlO_3)_{0.3}(Sr_2AlTaO_6)_{0.7}$.

bands between -9 and -3 eV are mainly due to $O-2p$ states and those from -1 to 3 eV are mainly due to t_{2g} states. From the a_{1g}-character[6] bands shown in figure 4.12(b) one can see that the a_{1g} ($d_{x^2-y^2}$) subband in R VO_2 is a little bit downshifted in relation to the remaining e_g^π douplet (d_{xz},d_{yz}) due to the small distortion on the oxygen octahedrons. The difference between the electronic dispersion of the a_{1g} subband along the $\Gamma - Z$ (parallel to the rutile c axis) and along the $Z - X$ (perpendicular to the rutile c axis) emphasizes the overlap between the $d_{x^2-y^2}$ orbitals along the rutile c axis. By comparing these results with photemission spectra obtained by Koethe *et al.* [199] (red continuous line in figure 4.9(b)), one notices a good agreement with the position of the $O-2p$ band; however the shoulder located at -1.3 eV is not captured in the total density of states (figure 4.12(c)). In addition, the DFT t_{2g} bandwidth is overestimated in comparison with experimental results.

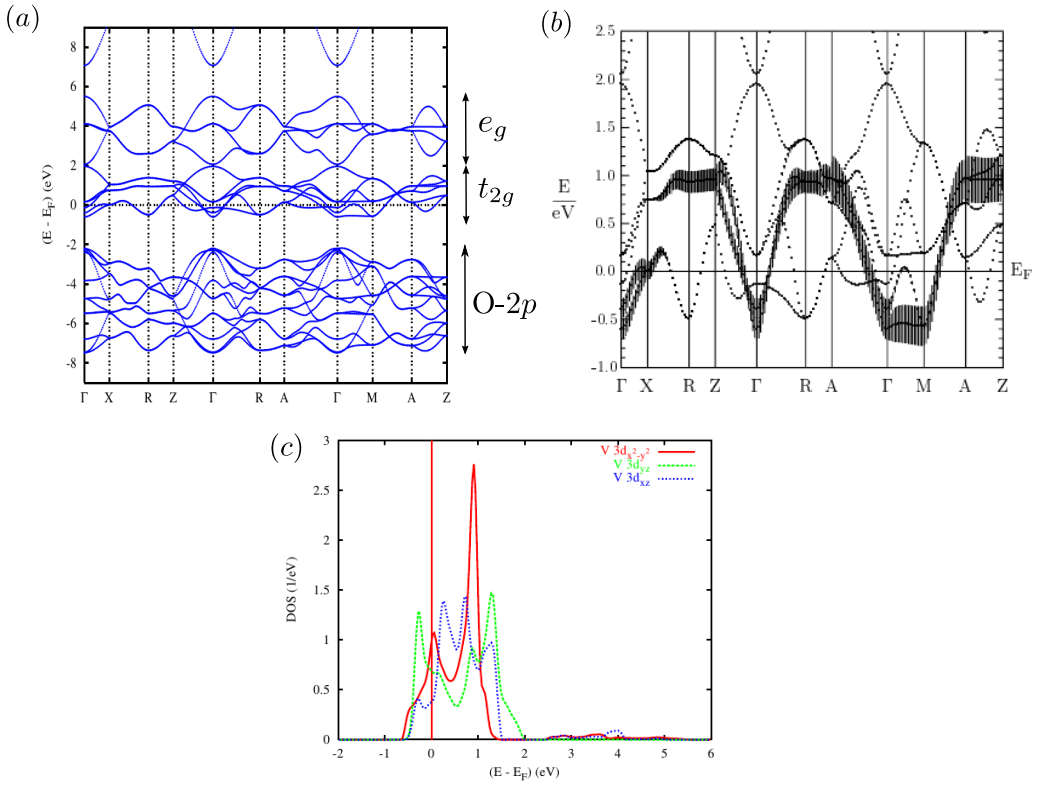

FIGURE 4.12: (a) DFT (LDA) band structure of rutile VO_2 and (b) corresponding a_{1g}-character bands obtained by Eyert [188]. (c) Total density of states corresponding to the band structure shown in (a).

In contrast to the theoretical findings for the rutile phase, similar calculations fail to describe the insulating nature of the monoclinic phases of VO_2. In part these findings suggest that the associated structural distortions cannot give rise to band gaps in the M_1

[6]The contribution of $d_{x^2-y^2}$ orbital of V atom for each band is given by the height of the bars.

and M_2 phases [188, 217]. From the DFT (LDA) calculations performed by Eyert [188], it was shown that the dimerization of vanadium atoms leads to strong effects on the a_{1g} subband. Due to dimerization the a_{1g} subband splits, giving rise to an occupied (empty) bonding (antibonding) a_{1g} subband, as shown in figure 4.13(a) and (b). More recent DFT calculations attempted to take into account the electronic correlation effects beyond LDA/GGA approximation by employing hybrid functionals, such as the Heyd-Scuseria-Ernzerhof (HSE) and modified Becke-Johnson exchange and LDA correlation (mBJLDA). As reported by Eyert [218] DFT calculations within HSE functionals were able to take into account the insulating nature of both monoclic phases of VO_2. However, as pointed out by Grau-Crespo *et al.* [220] these calculations predicted wrong magnetic ground states for the phases of VO_2. In the work by Zhu *et al.* [221] the authors properly described the gap and the magnetic ground states by employing mBJLDA functionals, though the incoherent bands observed in photoemission measurements are not described within this band picture.

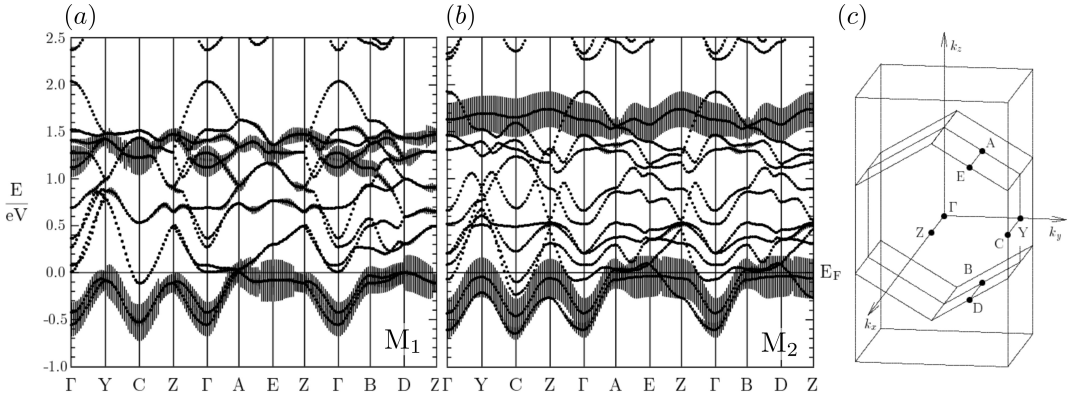

FIGURE 4.13: DFT (LDA) a_{1g}-character band structures of (a) M_1 and (b) M_2 phases of VO_2 obtained by Eyert [188]. In (c) the Brillouin zone of monoclinic is shown.

GW and quantum Monte Carlo calculations (QMC) were also performed to investigate the M_1 and R phases of VO_2. GW calculations were reported to describe the insulating nature of the M_1 phase, with gap of 0.6 eV in good agreement with experiments, and the metallic nature of the R phase [222, 223]. However, as observed by Sakuma *et al.* [223], the R phase was found less correlated than in experiment ($Z \approx 0.5$ while $Z_{exp} \approx 0.33$), with no satellite structure below the Fermi level, in contrast to photoemission spectra shown in figure 4.9. The authors pointed out that this disagreement is due to the absence of important electronic correlations neglected in their GW calculations. Diffusion QMC calculations also described the R→M_1 metal-insulator transition [224].

However, for both R and M_1 phases it was predicted antiferromagnetic configurations in disagreement with experiments.

DFT calculations have also been applied to the bct phase of NbO_2. As shown in figure 4.14(a), the band structure obtained by Eyert [219] takes into account the insulating nature of this phase, with a band gap of 0.1 eV. As in the M_1 phase of VO_2, the dimerization of niobium atoms leads to the splitting of the a_{1g} subband, giving rise to an occupied (empty) bonding (antibonding) a_{1g} subband, as can be noticed from the a_{1g}-character band structure presented in figure 4.14(a). Therefore, DFT calculations describe the MIT in NbO_2, supporting a Peierls-type MIT, as expected from the Goodenough picture. However, we stress that the DFT (LDA) band gap is underestimated in comparison with experimental findings. By means of ultraviolet photoelectron spectroscopy (UPS), Weibin *et al.* [225] reported an energy gap of 0.70 eV while Posadas *et al.* [214] found that the band gap of NbO_2 thin films on STO(111) is at least 1.0 eV. Recent ellipsometric measurements reported by O'Hara *et al.* [215] indicate an indirect gap of 0.7 eV.

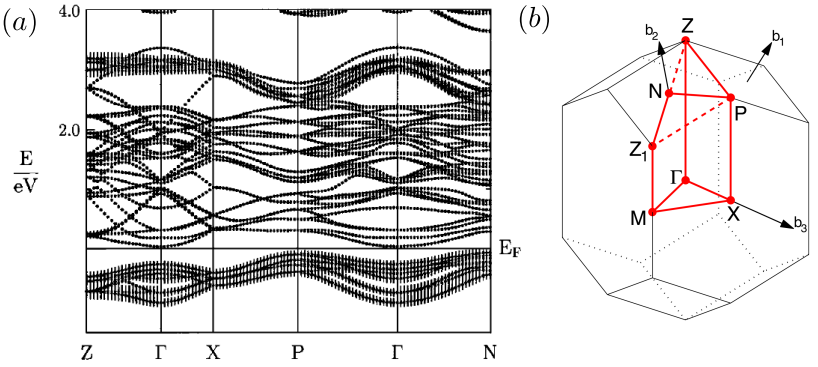

FIGURE 4.14: (a) DFT (LDA) a_{1g}-character band structure of bct phase of NbO_2 obtained by Eyert [219]. (b) Brillouin zone of the bct structure.

4.5 DFT+DMFT investigations

More recent calculations have employed dynamical mean field theory to describe several aspects of the physics of VO_2, but some discrepancies between different implementations remain. In the work by Biermann *et al.* [226] the authors applied the so-called down-folding procedure to obtain a multiband Hubbard Hamiltonian for VO_2 of the following

form [227]

$$H = H^{LDA} + \frac{1}{2}\sum_{imm'\sigma} U_{mm'} n_{im\sigma} n_{im'-\sigma} + \frac{1}{2}\sum_{im(\neq m')\sigma} (U_{mm'} - J_{mm'}) n_{im\sigma} n_{im'\sigma}, \quad (4.1)$$

where $n_{im\sigma} = a^{\dagger}_{im\sigma} a_{im\sigma}$ ($a^{\dagger}_{im\sigma}$ creates an electron with spin σ in a localized orbital m at site i) and H^{LDA} is the DFT part containing the material specific informations. By choosing a set of isolated correlated bands (correlated subspace), e.g. t_{2g} bands, one can obtain Wannier functions, which in turn can be used as the basis set of H^{LDA}. The screened on-site Coulomb interaction is parametrized as $U_{mm} = U$, $U_{mm'} = U - 2J$, with $J_{mm'(\neq m)} = J$. The Hamiltonian in equation 4.1 is then solved by cluster-DMFT.[7] As depicted in figure 4.15, the authors obtained a R metallic phase, with renormalized t_{2g} bands ($Z \approx 0.66$), and an insulating M_1 phase with gap of 0.6 eV in agreement with experimental findings [199].

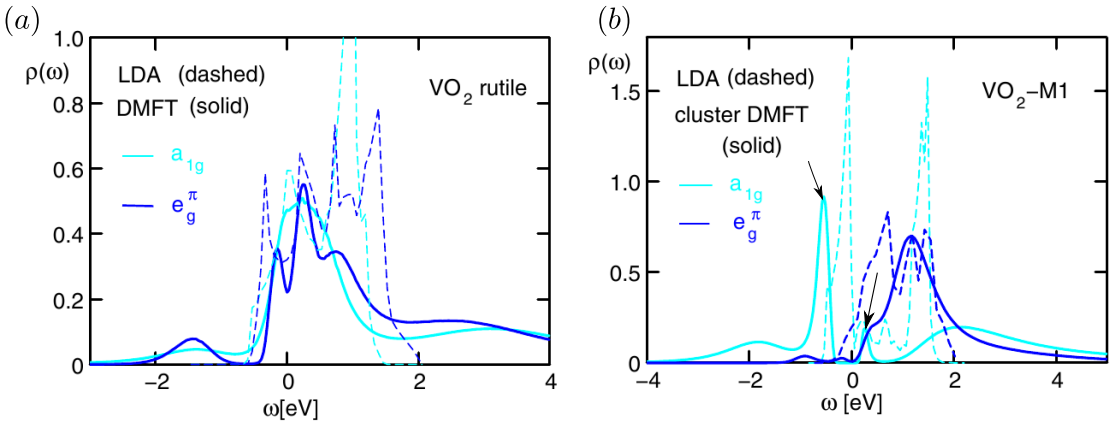

FIGURE 4.15: Density of states obtained by Biermann *et al.* for the (a) R and (b) M_1 phases of VO_2. DFT (LDA) and DFT+DMFT results are shown in dashed and solid lines, respectively. Figures taken from Ref. [226].

Furthermore, the authors found that electronic intersite correlations, within the vanadium dimers, renormalize down the a_{1g} bonding-antibonding splitting in comparison with DFT calculations. The corresponding a_{1g} bonding and antibonding peaks are marked by arrows in the density of states shown in figure 4.15(b). In their proposed mechanism for the gap opening, this renormalization combined with the upshift of the e^{π}_{g} states give rise to a gap between a_{1g} and e^{π}_{g} subbands. As can be noticed in figure 4.15(b) the bottom of the conduction band is composed by e^{π}_{g} and the a_{1g} antibonding states.

[7] In the cluster extension of DMFT the lattice problem is mapped into a cluster of sites embedded in an effective medium instead of a single-site.

Thus, according to the results obtained by Biermann and co-workers, the M_1 phase of VO_2 can be viewed as a renormalized Peierls insulator.

In contrast, by means of *ab initio* linear scaling DFT+cluster-DMFT calculations, Weber *et al.* [228] suggested a distinct mechanism for the gap opening in the M_1 phase. From their calculations, the M_1 phase was found to be insulating with gap of ~ 0.6 eV (see figure 4.16(a)) in agreement with the experimental value. In addition, the authors noticed the presence of a pole at the Fermi level in the imaginary part of the self-energy of M_1 phase (marked by an arrow in figure 4.16(b)) characteristic of a Mott insulator.[8] This finding suggested that the gap formation of the M_1 phase is mainly due to an orbital-selective Mott instability concerning the a_{1g} electronic states. Looking at the occupancy of the $3d$ shell, they obtained at around two electrons per vanadium, resulting in four electrons per vanadium dimer, suggesting that the M_1 phase is not a renormalized Peierls insulator [228].

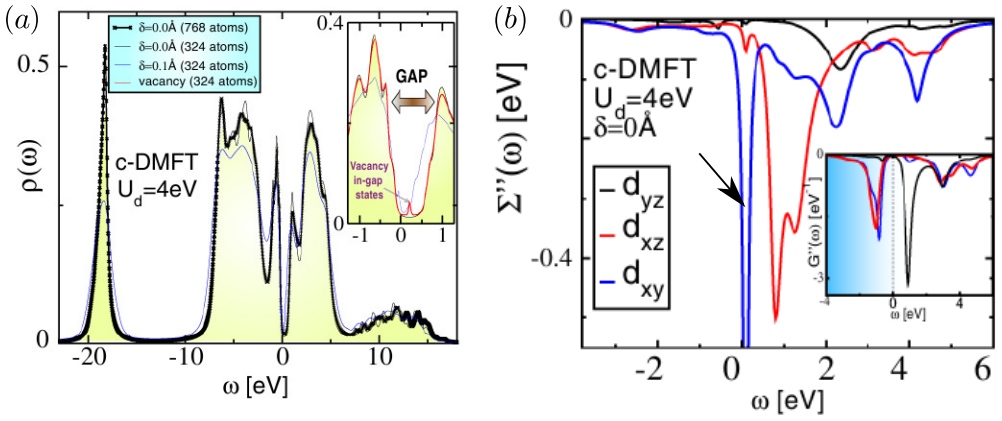

FIGURE 4.16: Density of states obtained by Weber *et al.* for (a) the M_1 phase of VO_2 and (b) the corresponding imaginary part of the self-energy. Figures taken from Ref. [228].

4.6 Final comments

In spite of the significant advances presented in the previous section, important fundamental challenges remain. As shown in figure 4.10 the close proximity of the M_1, M_2,

[8] As shown by Brinkman and Rice [229] the metal-insulator transition in the one-band Hubbard model is associated with the divergence of the effective mass renormalization as the system approaches the insulating phase. The corresponding insulating phase is characterized by the divergence of the imaginary part of the self-energy (pole) at the Fermi level (Mott instability) on the Matsubara frequency axis. We mention that the divergence $Z \to 0$, when the insulating phase is approached from the metallic side, was further supported by DMFT calculations [10].

and R phase in the phase diagram [187, 200] calls for an unified framework in which these phases can be simultaneously described. Another fundamental question is whether the MIT transitions take place if we fix the structure and change only the temperature.

We stress that it has not been possible to properly address the gap formation in the low-temperature phases of VO_2 as well as the physical mechanism behind the MIT in this material within an approach based on an effective model from which the oxygen degrees of freedom are eliminated and which contains only V-3d electrons electrons (Hubbard model presented in equation 4.1). Indeed, earlier DFT+DMFT works on the Hubbard model [226, 230, 231] showed that for a given set of Hubbard U and J parameters, the gap in the M_1 insulating phase is too robust, while the mass renormalization in the R phase is too small. For example, the insulating M_1 phase obtained by Biermann *et al.* [226] is gapped even at very high temperatures ($T = 770$ K), and the quasiparticle weight in the rutile phase is too large compared to experiment, *viz.* Biermann and co-workers obtained $Z \approx 0.6$ while Okazaki *et al.* [197] $Z \approx 0.33$. Both of these effects result from placing this material too far from the Mott transition boundary. Consequently, the M_2 phase was not described before with this approach, as half of V-atoms would not undergo Mott-Hubbard transition. In addition, the self-consistent evaluation of the charge-density in the DFT+DMFT implementation, not considered in Ref. [226], is of great importance to the appropriate description of the mechanism responsible for the gap opening in the monoclinic phases of VO_2. In this respect, we mention that the full charge self-consistency has been shown to be of crucial importance for the correct description of the metal-insulator transition in V_2O_3 [232]. Finally, we mention that our approach overcomes these problems as we explore in the next chapter.

Chapter 5

Metal-Insulator transitions in VO_2 and NbO_2: towards an unified description

In this chapter we present our theoretical investigation on the electronic structure of rutile (metallic) and insulating phases of VO_2 and NbO_2 employing DFT+DMFT calculations. In the following, we present our results in two sections: in section 5.1 we discuss our DFT calculations and in section 5.2 our DFT+DMFT calculations. Within our DFT+DMFT approach, we successfully describe the electronic structure of the metallic and insulating phases of both oxides. We show that Mott physics plays an essential role in all phases of VO_2, in particular the resulting transition from rutile to dimerized M_1 phase is adiabatically connected to Peierls-like transition, but is better characterized as the Mott transition in the presence of strong intersite exchange. For the NbO_2, we find that nonlocal dynamic correlations also play a role in the gap formation of the insulating phase (bct), by a similar physical mechanism as that for the M_1 phase of VO_2. Although the nonlocal dynamic correlations in bct phase play a less important role for the gap opening than in M_1 and M_2 phases of VO_2, it indicates that the bct phase of NbO_2 is not a pure Peierls-type insulator, as it was recently proposed.

The investigations on VO_2 presented in this chapter are under consideration for publication in Physical Review Letters. The preprint entitled "Metal-insulator Transition

in VO2: a DFT+DMFT perspective" by W. H. Brito, M. C. O. Aguiar, K. Haule and G. Kotliar is on arXiv:1509.02968.

5.1 DFT calculations

In this section we first present the DFT (GGA) electronic structure of the rutile phases. Next, we address the electronic structure of the insulating phases of both oxides. In appendix H.4 we detail the computational methodology employed in our DFT calculations.

5.1.1 Rutiles

As mentioned before the rutile is the high-temperature structure of both VO_2 and NbO_2. To investigate the electronic properties of the rutile phase of both oxides we used the experimental structural parameters from Refs. [183, 184], where $a = 4.5546$ (4.8483) Å, $c = 2.8514$ (3.0315) Å, $x = 0.3001$ (0.2924) for VO_2 (NbO_2). In figure 4.4(4.5)(a) the unit cell of rutile VO_2 (NbO_2) is illustrated. Structurally, the octahedron distortions in both structures can be compared by calculating the mean octahedral quadratic elongation which is defined as [233]

$$\langle\lambda\rangle = \sum_{i=1}^{6} \frac{1}{6}\Big(\frac{l_i}{l_0}\Big)^2, \tag{5.1}$$

where l_0 is the center-to-vertex distance for an octahedron whose volume is equal to that of the strained or distorted octahedron with bond lengths l_i. For our rutile structures, we obtained $\langle\lambda_{VO_2}\rangle = 1.0035$ and $\langle\lambda_{NbO_2}\rangle = 1.0019$, which indicates that octahedra in VO_2 is just a little bit more distorted than in NbO_2. As can be seen in our calculated density of states, shown in figures 5.1 and 5.2, this difference in the octahedron distortion enhances the lifting of degeneracy of the t_{2g} states in NbO_2.

From the total and projected density of states we also observe that both systems have semi-occupied levels and three different groups of bands. The densities of states reveal that the sixfold t_{2g} band (3 doubly denegerate levels) is formed by the $d_{x^2-y^2}$ (a_{1g}), d_{xz} and d_{yz} (e_g^π) bands. Further we find that the oxygen bands of VO_2 lie mainly between -8 and -1.7 eV below the Fermi level, and the e_g^σ bands formed by the d_{xy} and d_{xy} are at around 3.6 eV above the Fermi level. For the NbO_2 the oxygen bands lie

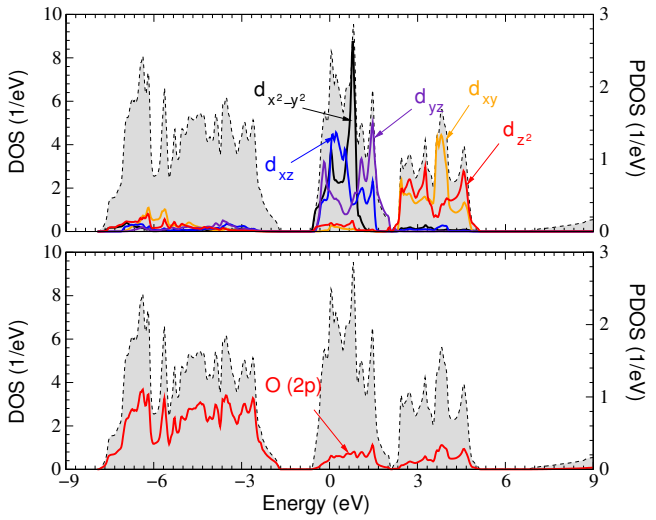

FIGURE 5.1: DFT (GGA) total (grey) and projected density of states of R phase of VO_2. The projections to $d_{x^2-y^2}$, d_{xz}, d_{yz}, d_{xy}, and d_{z^2} states are shown in black, blue, indigo, orange, and red, respectively. The projection to the O-2p states is shown in the bottom panel.

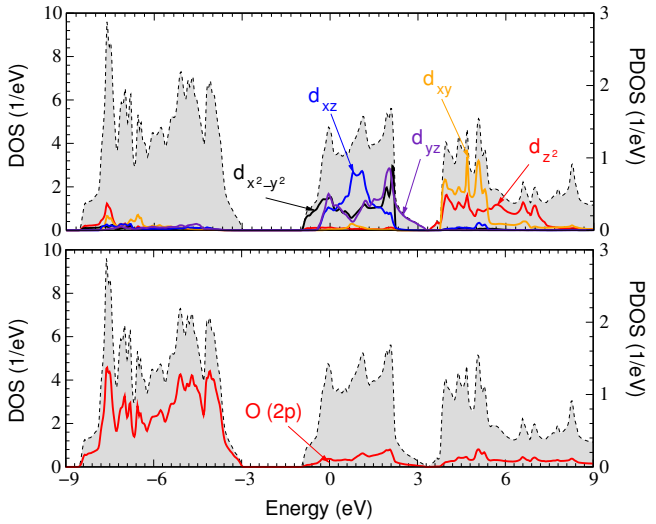

FIGURE 5.2: DFT (GGA) total (grey) and projected density of states of R phase of NbO_2. The projections to $d_{x^2-y^2}$, d_{xz}, d_{yz}, d_{xy}, and d_{z^2} states are shown in black, blue, indigo, orange, and red, respectively. The projection to the O-2p states is shown in the bottom panel.

mainly between -9 and -3 eV below the Fermi level and the e_g^σ bands are located at around 4.6 above the Fermi level.

From the band structures shown in figure 5.3, we obtain that the t_{2g} bandwidth of VO_2 is $W_{VO_2} = 2.80$ eV, in good agreement with calculations reported in Ref. [188], where the author found 2.60 eV. In relation to NbO_2 we find that the same band has a width of $W_{NbO_2} = 4.35$ eV, approximately 1 eV less than the bandwidth found in calculations of Ref. [234]. These findings lead to a ratio of $\frac{W_{NbO_2}}{W_{VO_2}} = 1.55$, which can be

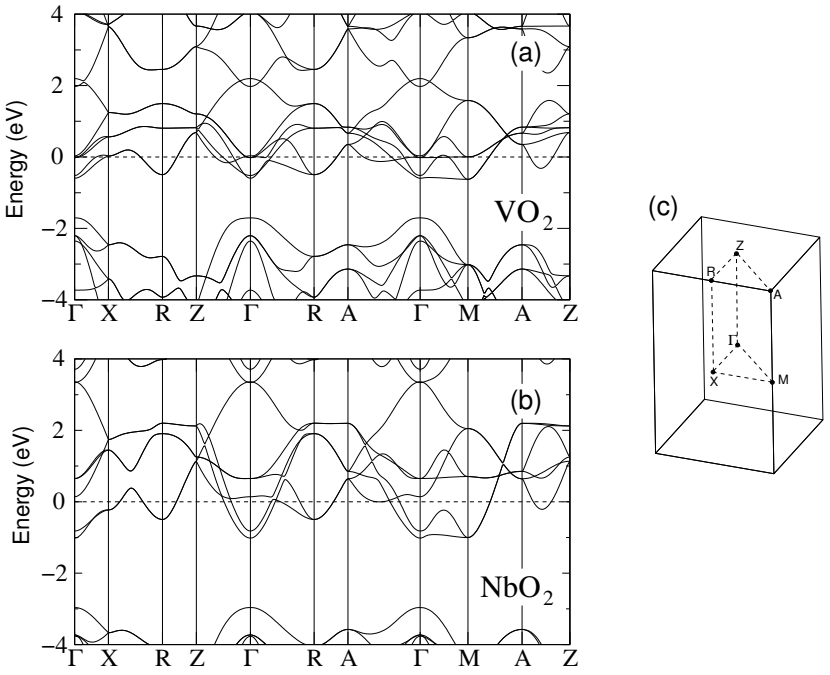

FIGURE 5.3: DFT (GGA) band structures of rutile phase of (a) VO_2 and (b) NbO_2. In (c) we present the high-symmetry points in the first Brillouin zone of rutile structure.

attributed to the more localized character of the $3d$ orbitals of V atoms in comparison to the $4d$ orbitals of Nb. In addition, we obtain a $p-d$ energy gap[1] of 1.12 eV in VO_2 and 1.97 eV in NbO_2, where the later is 2 eV less than the value found in Ref. [234]. Finally we notice that there is a small overlap between the t_{2g} and e_g^σ bands of VO_2, a fact related to the octahedron distortion. In the same context, our results do not show any energy gap between the t_{2g} and e_g^σ bands of NbO_2, in disagreement with previous theoretical results [219, 234].

5.1.2 M_1 and M_2 phases of VO_2

In our DFT calculations on the monoclinic phases of VO_2 we used the experimental lattice structures from Refs. [185, 235]. In particular, for the M_1 (M_2) phase the structural parameters are $a = 5.7527$ (9.0664), $b = 4.5378$ (5.7970), $c = 5.3825$ (4.5255) Å, and $\beta = 122.646$ (91.88)°. In our notation for the M_2 phase, a vanadium atom of the dimerized vanadium chain is denoted by V_1, whereas a vanadium atom of the zigzag chain is denoted by V_2.

[1]Energy difference between the maximum of the O-2p band and the minimum of the t_{2g} subband.

Motivated by the experimental findings [190, 202] concerning the antiferromagnetic ordering in the M_2 phase of VO_2, we considered in our DFT calculations an antiferromagnetic configuration for the vanadium atoms within each chain. From our calculations we find that the magnetic moments per vanadium atom in the dimerized chain (V_1) is negligible, that is, 0.05 μ_B/V, whereas in the zigzaig chain each vanadium atom (V_2) is found to has 0.7 μ_B. These findings are in agreement with the results reported by Eyert [188], where the author found 0.46 μ_B/V for the atoms within the zigzag chain, with negligibly small magnetic moments for the others.

In figures 5.4(a) and (b) we present the obtained band structures of M_1 and M_2 phases, respectively. At first, we observe that our DFT (GGA) calculations predict metallic monoclinic phases in total disagreement with the experimental results. For the M_1 phase the experimental results indicate the presence of an energy band gap of about 0.6 eV [199]. It is noteworthy that previous DFT calculations [188, 218], within LDA or GGA, reported the same disagreement with experiment. In comparison with the previous DFT calculations, we observe a good agreement; however in our results for the M_1 phase the bands around the Fermi level present a distinct dispersion along $\Gamma - A$, $A - E$, and $\Gamma - B$ directions. Likewise, we observe a different dispersion for the M_2 band structure along the $E - Z$ direction.

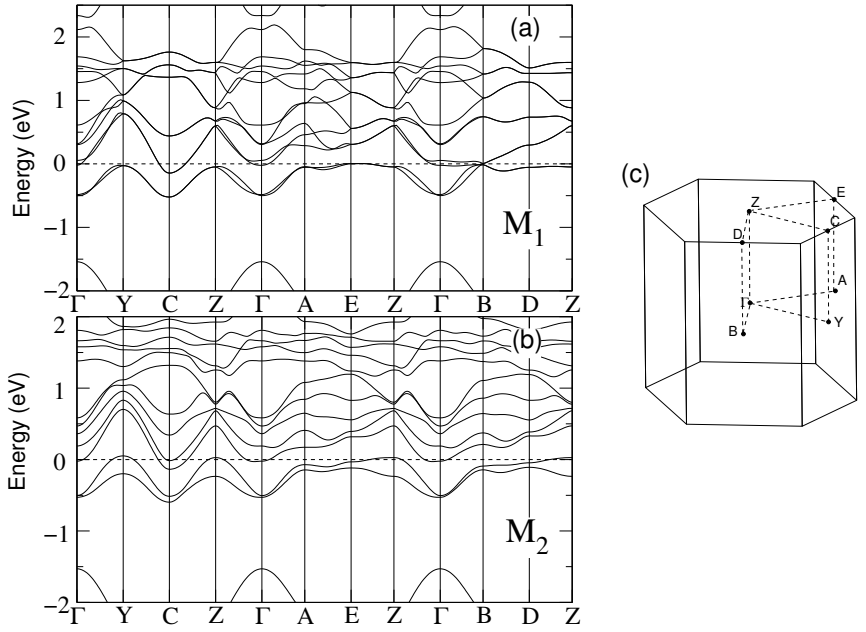

FIGURE 5.4: DFT (GGA) band structures of (a) M_1 and (b) M_2 phases of VO_2. In (c) we present the high-symmetry points in the first Brillouin zone of monoclinic structure.

From the M_1 density of states, shown in figure 5.5, we observe a strong effect on the a_{1g} subband due to the V^{4+}-V^{4+} dimerization. In particular, the a_{1g} subband splits into a bonding, at around -0.12 eV, and an antibonding subband, at around 1.45 eV. It leads to an energy gap of 1.54 eV between these subbands, in good agreement with Ref. [188], where the author found 1.7 eV. The e_g^π (d_{xz},d_{yz}) subband roughly upshits with respect to the R phase, while the e_g^σ manifold remains located $\approx$ 3.60 eV above the Fermi level. The O-2p bands lie between -7.64 and -1.53 eV below the Fermi level.

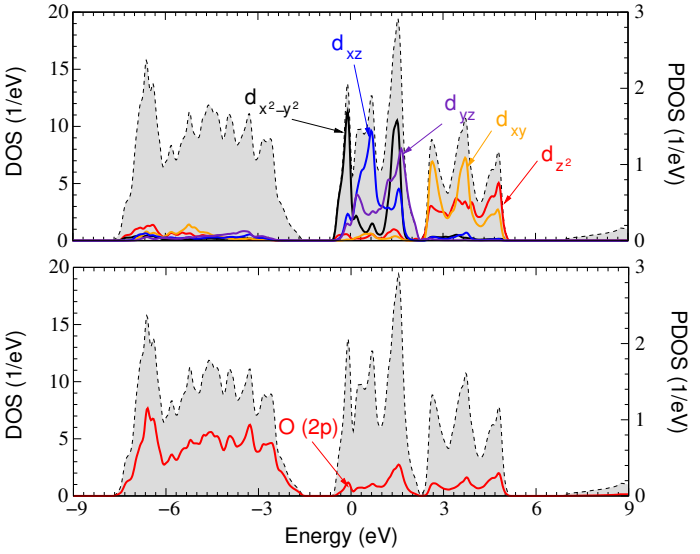

FIGURE 5.5: DFT (GGA) total and projected density of states of M_1 phase of VO_2. The projections to $d_{x^2-y^2}$, d_{xz}, d_{yz}, d_{xy}, and d_{z^2} states are shown in black, blue, indigo, orange, and red, respectively.

With respect to the M_2 phase, the density of states, shown in figure 5.6 present the same groups of states as observed in the M_1 phase; however in this case the two types of vanadium chains give rise to distinct contribution for the t_{2g} manifold. The density of states of a vanadium atom of the dimerized chain (V_1) shows a strong effect on the a_{1g} subband due to the dimerization, as observed in the M_1 phase. In particular, we notice that the a_{1g} subband splits into a bonding, at around -0.12 eV, and an antibonding branch, at around 1.76 eV. It leads to a split of 1.88 eV, 0.34 eV greater than in the M_1 phase. This can be understood by the fact that the distance between vanadium atoms in the dimer in the M_2 phase is 0.08 Å smaller than in the M_1 phase.

On the other hand, the density of states of an atom of the zigzag chain (V_2) shows a half-filled a_{1g} subband located at -0.21 eV and empty e_g^π subbands above the Fermi level. Thus, we notice that the magnetic moments originate mainly from the $d_{x^2-y^2}$ states of the vanadium atoms of the zigzag chain. Finally, the e_g^σ manifold is at 3.6 eV

above the Fermi level, while the oxygen band lies between -7.69 and -1.48 eV below the Fermi level.

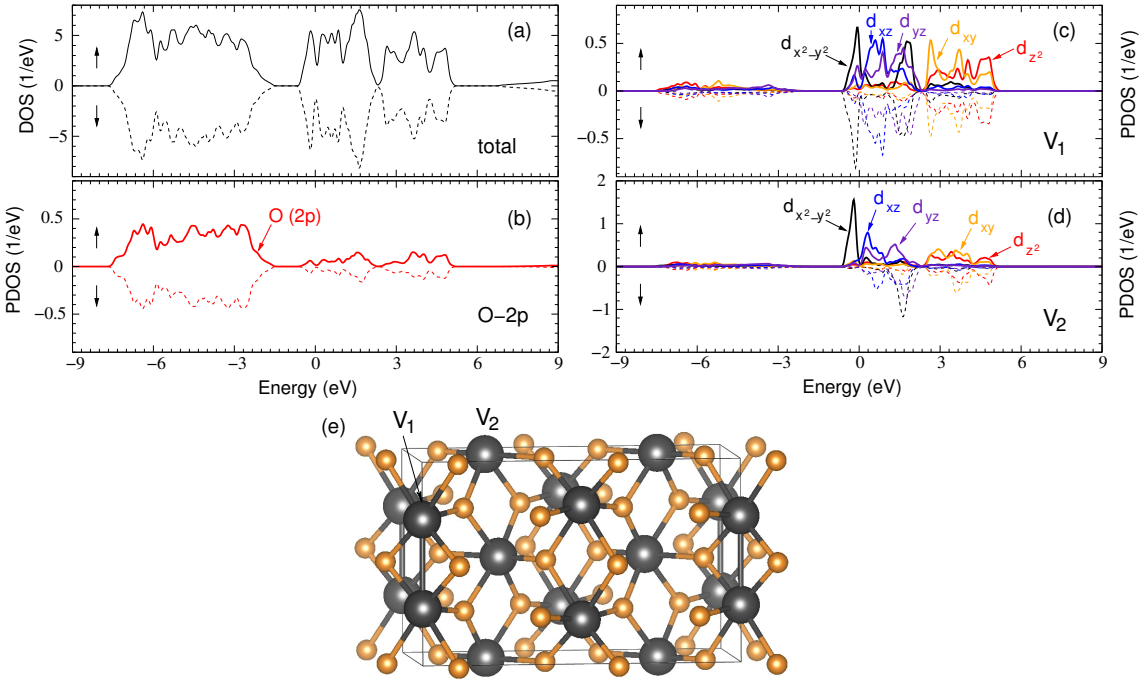

FIGURE 5.6: DFT (GGA) total and projected density of states of M_2 phase when antiferromagnetic order is allowed. In (b) we show the projection to the O$-2p$ states. In (c) and (d) the projected density of states of an vanadium atom of the dimerized chain (V_1) and of the zigzag chain (V_2) are presented, respectively. The projections to $d_{x^2-y^2}$, d_{xz}, d_{yz}, d_{xy}, and d_{z^2} states are shown in black, blue, indigo, orange, and red, respectively. In (e) the M_2 structure with the V_1 and V_2 atoms is illustrated.

5.1.3 bct phase of NbO_2

Finally, we address the electronic structure of the body-centered tetragonal phase of NbO_2. As in the M_1 phase of VO_2, in the bct phase the transition metal atoms dimerize and tilt with respect to the rutile c axis. As can be seen in our calculated band structure shown in figure 5.7, the structural distortion leads to the opening of a band gap of 0.24 eV, 0.14 eV greater than found by Eyert [219]. We mention that our obtained energy gap is underestimated in comparison with experimental findings, as is the previous DFT band gap reported by Eyert [219]. We remind that previous experimental works reported a minimum gap of 0.7 eV [215].

As similarly observed in the monoclinic phases of VO_2, the structural distortions have dramatic effects on the electronic states of bct phase. The calculated projected density of states, shown in figure 5.8, presents a a_{1g} splitting of 3.50 eV, as a result of

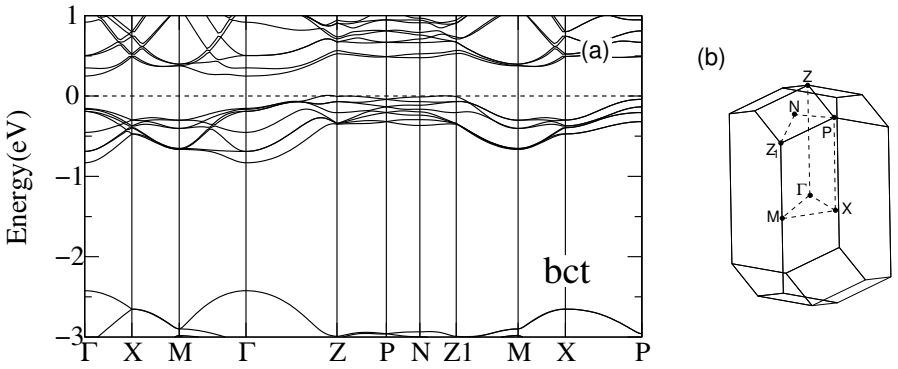

FIGURE 5.7: (a) DFT (GGA) band structure of bct phase of NbO_2. In (b) we present the high-symmetry points in the first Brillouin zone of the structure.

Nb^{4+}-Nb^{4+} dimerization. In addition, the e_g^π subband is upshifted to around 5.9 eV, while the e_g^σ manifold does not shift in comparison with rutile phase. Therefore, as a result of structural distortions there is a gap opening between the a_{1g} bonding subband and the e_g^π subband. We emphasize that this finding advocates in favor of a Peierls-type MIT in NbO_2, as proposed by Eyert [219]. Finally, we mention that the O-2p bands is a little bit upshifted in comparison with those in rutile, lying between -8 and -2.4 eV for this system.

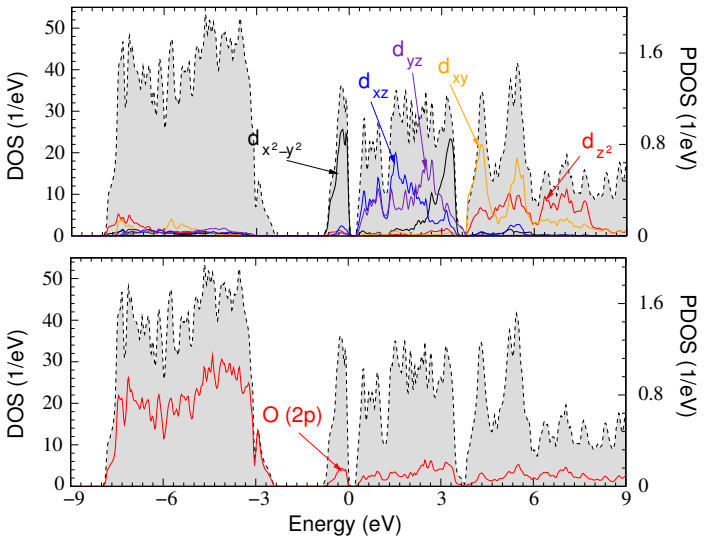

FIGURE 5.8: DFT (GGA) total and projected density of states of bct phase of NbO_2. The projections to $d_{x^2-y^2}$, d_{xz}, d_{yz}, d_{xy}, and d_{z^2} states are shown in black, blue, indigo, orange, and red, respectively. The projection to the O-2p states is shown in the bottom panel in red.

5.1.4 Summary of DFT calculations

In summary our DFT(GGA) calculations take into account only the metallic nature of the rutile structures. It is noteworthy that for the rutile phase of VO_2 our calculated density of states does not capture the features observed in the photoemission spectra reported by Koethe *et al.* [199], such as the shoulder located at -1.3 eV and the reduced t_{2g} bandwidth. Further, we find that structural distortions alone cannot give rise to an energy gap in the monoclinic phases of VO_2. This suggests that electronic correlations indeed play a role in the gap formation of VO_2. In respect to the NbO_2, DFT describes the MIT, although it underestimates the energy gap for the low-temperature bct phase in comparison with experiments.

5.2 MITs in VO_2 and NbO_2: a DFT+DMFT perspective

We now turn to the electronic structure of the high- and low-temperature phases of VO_2 and NbO_2 within a fully self-consistent combination of density functional theory and embedded real space dynamical mean field theory calculations. It is worth mentioning that previous DFT+DMFT works which used the downfolding procedure [226, 228] are less precise in comparison with our embedding DMFT technique. In particular, the Dyson equation in their method is solved for a Hubbard-like model, while in our method the Dyson equation is solved with all valence states of VO_2 and NbO_2 included (there is no construction of any low-energy model). Also in our method the O-2p states (ligand states) are considered and the charge-density is obtained self-consistently. As we mentioned in section 4.6 the full charge self-consistency has been shown to be of crucial importance for the correct description of the metal-insulator transition in V_2O_3 [232]. For the V-atoms in rutile and of the zigzag chain in the M_2 phase we applied the single-site DMFT to treat their corresponding t_{2g} states. As mentioned in Refs. [226, 230], the inclusion of nonlocal correlations for the description of the rutile phase did not lead to important effects, indicating that the rutile is well described within single-site DMFT.

5.2.1 Rutile phases

We first investigate the R phase of both oxides within our realistic DFT+DMFT calculations. In figure 5.9 we show the calculated DFT+DMFT-based total, t_{2g} and e_g^σ projected density of states of the rutile phase of both oxides, at temperatures close to their respective MITs.

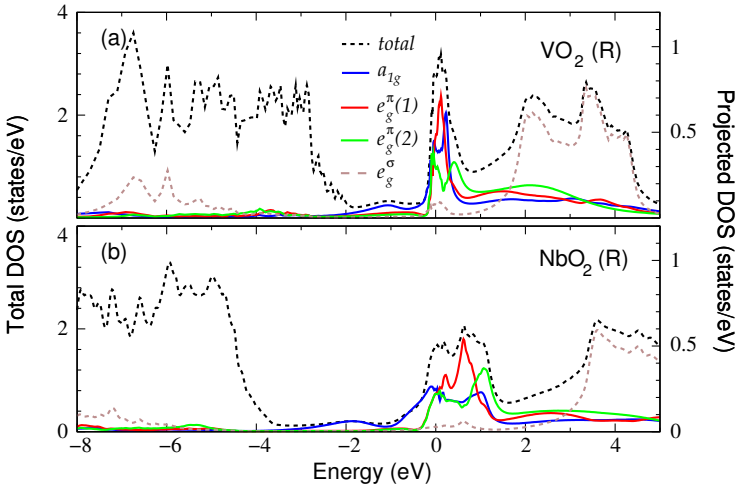

FIGURE 5.9: DFT+DMFT-based total (black dashed line) and projected density of states of R phases of (a) VO_2 and (b) NbO_2, at $T = 390$ K and $T = 1132$ K, respectively. The projections to a_{1g}, $e_g^\pi(1)$, $e_g^\pi(2)$, and e_g^σ states are shown in blue, red, green, and brown lines, respectively.

In comparison with our DFT-based density of states (see figures 5.1 and 5.2), we notice that the t_{2g} states are renormalized ("compressed") due to dynamic correlations, with stronger renormalization in VO_2. This renormalization can be explained by looking at the corresponding self-energies, which are depicted in figure 5.10.

As can be noticed on the right panel of figure 5.10, the imaginary part of the self-energies corresponding to the a_{1g}, $e_g^\pi(1)$, and $e_g^\pi(2)$ states vanishes at the Fermi level ($\omega = 0$). This allows us to discuss the t_{2g} renormalization within an effective band picture (correlated band structure) in the low-energy regime, in which the one-particle excitations are given by (see appendix J)

$$\omega_{\mathbf{k}} = \epsilon_{\mathbf{k}} + \Re\Sigma(\omega_{\mathbf{k}}) - \mu, \tag{5.2}$$

for each band. In this equation, μ is the chemical potential, $\epsilon_{\mathbf{k}}$ is the DFT band dispersion, and $\Re\Sigma(\omega_{\mathbf{k}})$ is the real part of the self-energy. The real part of the self-energies

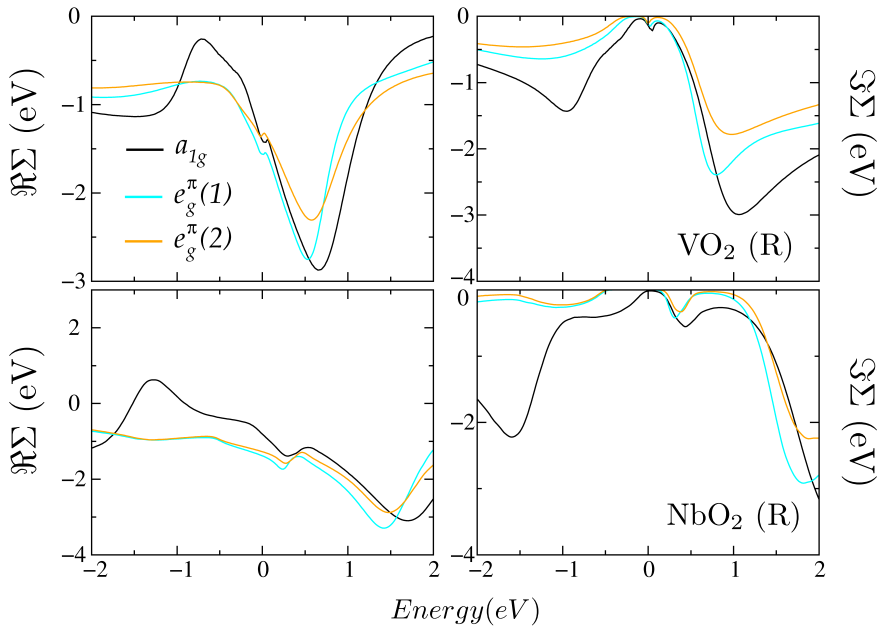

FIGURE 5.10: a_{1g} (black), $e_g^\pi(1)$ (cyan), and $e_g^\pi(2)$ (orange) self-energies, on real frequency axis, of rutile phase of VO_2 and NbO_2.

shown in figure 5.10 can be expanded to first order as it follows

$$\Re\Sigma(\omega_{\mathbf{k}}) = \Re\Sigma(0) + \frac{\partial\Re\Sigma(\omega)}{\partial\omega}\Big|_{\omega=0}\omega_{\mathbf{k}}. \tag{5.3}$$

Therefore, we obtain that

$$\begin{aligned}
\omega_{\mathbf{k}} &= \epsilon_{\mathbf{k}} + \Re\Sigma(0) + \frac{\partial\Re\Sigma(\omega)}{\partial\omega}\Big|_{\omega=0}\omega_{\mathbf{k}} - \mu \\
\omega_{\mathbf{k}}\Big(1 - \frac{\partial\Re\Sigma(\omega)}{\partial\omega}\Big|_{\omega=0}\Big) &= \epsilon_{\mathbf{k}} + \Re\Sigma(0) - \mu \\
\omega_{\mathbf{k}} &= Z(\Re\Sigma(0) - \mu) + Z\epsilon_{\mathbf{k}},
\end{aligned} \tag{5.4}$$

with Z defined by

$$Z = \frac{1}{\Big(1 - \frac{\partial\Re\Sigma(\omega)}{\partial\omega}\Big|_{\omega=0}\Big)}. \tag{5.5}$$

We mention that this Z is the quasiparticle weight mentioned in section 4.3 of the previous chapter. The first term in equation 5.4 can be interpreted as an energy shift; whereas the second term can be interpreted as a renormalized ("compressed") band, since $Z < 1$ as can be noticed from the slope of the real part of the self-energies shown in figure 5.10. Therefore, the energy band $\epsilon_{\mathbf{k}}$ is renormalized due to the correlation effects described by the self-energy.

In addition, these correlations also lead to the emergence of incoherent excitations (Hubbard bands) in the spectra of both oxides. For VO_2 a lower Hubbard band (LHB) is find at -1.09 eV, in agreement with photoemission measurements [199] and DMFT calculations for the Hubbard model [226]. The upper Hubbard band (UHB), by its turn, is observed at around 2.54 eV. For NbO_2 the LHB is found around -1.9 eV whereas the UHB is around 3 eV. We emphasize that the imaginary part of the self-energy becomes very enhanced in the energy near the incoherent peaks, signaling its incoherent character. We remind that in the case of R phase of NbO_2 there is not any experimental spectra reported which should be used for comparison with our findings. Overall, the LHBs come mainly from a_{1g} states while the UHBs come mainly from e_g^π states. Although the correlation effects are more pronounced in spectral properties of VO_2, our findings suggest that the electronic dynamic correlations in NbO_2 are still important.

To investigate the strength of correlations in both oxides we evaluated the quasiparticle weight Z_α for each dynamical orbital $\alpha = \{a_{1g}, e_g^\pi(1), e_g^\pi(2)\}$. Here Σ_α denotes the orbital-resolved self-energy. We remind that Z is the inverse of the bare band mass enhacement due to electronic correlations described by the self-energy Σ. In particular, Z is equal to unity for a noninteracting system while it goes to zero in a strongly correlated system. Our calculated quasiparticle weights for both oxides are listed in table 5.1.

TABLE 5.1: Quasiparticle weights (Z's) for each dynamical orbital $\alpha = \{a_{1g}, e_g^\pi(1), e_g^\pi(2)\}$ of rutile phases of VO_2 and NbO_2.

	VO_2	NbO_2
$Z_{a_{1g}}$	0.28	0.32
$Z_{e_g^\pi(1)}$	0.33	0.55
$Z_{e_g^\pi(2)}$	0.40	0.61
Z_{avg}	0.34	0.49

The obtained values of Z for each t_{2g} state indicate that the metallic phase of VO_2 is indeed more correlated (has smaller Z) than that of NbO_2. However, we stress that the Z values obtained for NbO_2 confirm that correlations are also important in this system. In particular, we observe that the a_{1g} subband is the most correlated, followed by the $e_g^\pi(1)$ and $e_g^\pi(2)$ subbands. The smaller values of Z obtained for VO_2 reveal that electrons in this system are closer to the Mott transition than electrons in NbO_2, which is in accordance with the more delocalized nature of $4d$ orbitals of niobium in comparison with the $3d$ ones of vanadium atoms.

5.2.2 M_1 phase

We next present the electronic structure of the M_1 phase. As observed in previous DFT+DMFT calculations on VO_2 [226, 236], the appropriate description of singlet pairs within DMFT calculations is essential to take into account the gap opening in the M_1 phase. Theoretically, this can be achieved by considering an extension of single-site DMFT, denoted as cluster-DMFT . Within this method the cluster degrees of freedom are treated exactly [237, 238], which in turn incorporates shortrange nonlocal correlations in our DMFT treatment. Within the V-dimer, treated as cluster in our DMFT calculations, it is useful to adopt the symmetric and antisymmetric combination of orbitals as performed in Ref. [231].[2] Hence, we have t_{2g} "molecular" states associated with the dimer. The associated self-energies are denoted as the bonding $\Sigma_{b,\alpha}$ and antibonding $\Sigma_{ab,\alpha}$ components, where $\alpha = \{a_{1g}, e_g^{\pi}(1), e_g^{\pi}(2)\}$.

In figure 5.11(a) the total, t_{2g}, and e_g^{σ} projected DOS are shown. In additon, we show in figure 5.11(b) the associated spectral function[3] which is defined in equation J.7 of appendix J. We mention that these calculations were performed at temperature of 332 K. At first, we notice the opening of a gap of 0.55 eV, between the a_{1g} and e_g^{π} subband, which is in good agreement with experimental and previous theoretical findings [199, 226, 228]. It is worth mentioning that in Ref. [226] the authours found a small contribution of the a_{1g} antibonding state to the bottom of the conduction band. As expected, upon dimerization and antiferroelectric distortion, the a_{1g} subband splits in bonding (solid blue) and antibonding (dashed blue) states, while the e_g^{π} subband upshifts in comparison with the R phase.

The a_{1g} bonding orbital has a coherent peak at around -0.30 eV, while the antibonding orbital has two incoherent peaks reminiscent of LHB and UHB located at -1.5 eV and 2.58 eV, respectively. The coherent peak and the satellite below it were also observed in previous theoretical [226, 231] and experimental [199] works. However, in our case there is not a weak coherent peak associated with the antibonding state in the bottom of the conduction band, as in Ref. [226]. The bonding-antibonding splitting (relative to the DFT and DFT + single-site DMFT calculations (not shown)) increases upon inclusion of intersite dynamic correlations within the dimer, in contrast to the result of Ref. [226].

[2] This basis also leads to a maximally diagonal hybridization matrix which reduces the sign error concerning the impurity solver.

[3] The density of states $\rho(\omega)$ can be obtained from the spectral function $A(\mathbf{k},\omega)$ as $\rho(\omega) = \sum_{\mathbf{k}} A(\mathbf{k},\omega)$.

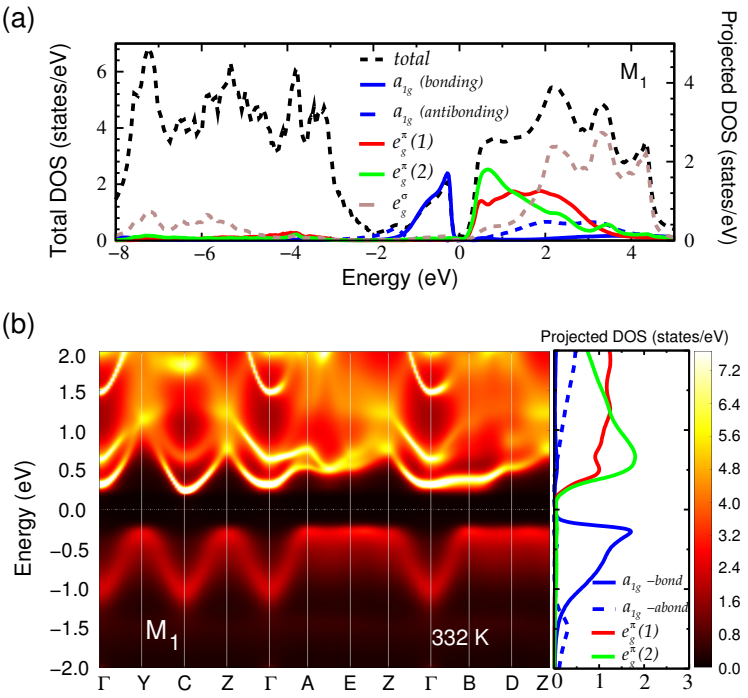

FIGURE 5.11: (a) DFT+DMFT-based total (black dashed line) and projected density of states of M_1 phase of VO_2. The projections to a_{1g}, $e_g^\pi(1)$, $e_g^\pi(2)$, and e_g^σ states are shown in blue, red, green, and brown lines, respectively. In particular, the solid (dashed) blue line corresponds to the projection on the bonding (antibonding) a_{1g} "molecular" state. (b) Spectral function with the projected density of states around the Fermi energy. In both panels the temperature is 332 K.

We next investigate how nonlocal dynamic correlations contribute to the opening of a gap between a_{1g} and e_g^π subbands in the M_1 phase. The inset in figure 5.12 shows the bonding and antibonding components of the imaginary part of the self-energy associated with the a_{1g} and $e_g^\pi(1)$ dimer electronic states.

We notice that once the dimerization is present in our calculation, the Mott instability is arrested, hence there is no pole in the imaginary part of the self-energy associated with the a_{1g} or e_g^π states. This excludes an orbital-selective Mott-Hubbard mechanism as the source of the gap of the M_1 phase, as proposed in Ref. [228]. Our results bear strong resemblance with the Mott transition of the Hubbard model in cluster-DMFT [239], where the local singlet state of the cluster dominates the low energy properties of the model. The energy gain to form the strong bonding state on the cluster is here not just due to increased hopping between the two V-atoms, but it is primarily due to the gain of the exchange energy, which is stronger than kinetic energy, as the latter is strongly reduced due to proximity to the Mott transition.

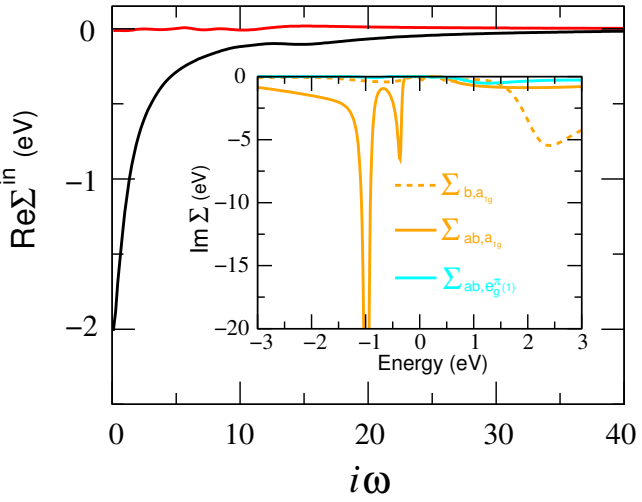

FIGURE 5.12: Real part of intersite self-energies, on imaginary frequency axis, of a_{1g}-a_{1g} (black) and $e_g^{\pi}(1)$-$e_g^{\pi}(1)$ (red) states of M_1 phase. Inset: Imaginary part, on real frequency axis, of bonding (dashed lines) and antibonding (solid lines) self-energies associated with the a_{1g} (orange) and $e_g^{\pi}(1)$ (cyan) dimer electronic states.

Now we define the local and intersite self-energies, which are related to the self-energies in the dimer basis as

$$\Sigma^{local} = \frac{1}{2}(\Sigma_b + \Sigma_{ab}), \tag{5.6}$$

and

$$\Sigma^{in(tersite)} = \frac{1}{2}(\Sigma_b - \Sigma_{ab}). \tag{5.7}$$

For more details see appendix K. In figure 5.12 (main panel) we also show the real part of the intersite components of self-energies associated with the same electronic states as those in the inset. We observe that the component of $e_g^{\pi}(1)$ is negligible, but, notably, one can see that $Re\Sigma^{in}_{a_{1g}-a_{1g}}$ depends strongly on the frequency in the low-energy part. This indicates the presence of strong intersite electronic correlations within the vanadium dimers, which in turn lower the a_{1g} bonding state. As a result, the bonding-antibonding splitting *increases* and a gap between the a_{1g} and e_g^{π} appears. We emphasize that in the work by Biermann *et al.*[226] this splitting was found to *decrease* upon inclusion of nonlocal correlations.

Since the imaginary part of self-energies associated with the bonding and antibonding states vanishes at the Fermi level (see figure 5.12), we can discuss the bonding-antibonding splitting within an effective band structure picture, in which the effects of electronic correlations are taken into account expanding the self-energies to first order.

In this case the bonding and antibonding bands are reshaped by the quantities

$$Z_b = \left(1 - \left.\frac{\partial \Re\Sigma_b}{\partial\omega}\right|_{\omega=0}\right)^{-1}, \tag{5.8}$$

and

$$Z_{ab} = \left(1 - \left.\frac{\partial \Re\Sigma_{ab}}{\partial\omega}\right|_{\omega=0}\right)^{-1}. \tag{5.9}$$

We emphasize that these quantities are not usual quasiparticle weights [240], although their definition are proper once there is no pole in the imaginary part of self-energies. As a result, we obtain the energies of renormalized bands as given by

$$E_b = Z_b(\epsilon_b + \Re\Sigma_b(\omega = 0)), \tag{5.10}$$

$$E_{ab} = Z_{ab}(\epsilon_{ab} + \Re\Sigma_{ab}(\omega = 0)), \tag{5.11}$$

where ϵ_b and ϵ_{ab} are the energies of noninteracting bonding and antibonding bands, respectively.

Therefore, the bonding-antibonding splitting energy, $\Delta = E_{ab} - E_b$, can be written as

$$\begin{aligned}\Delta =& Z_{ab}(\epsilon_{ab} + \Re\Sigma_{ab}(0)) - Z_b(\epsilon_b + \Re\Sigma_b(0)) \\ =& \frac{(Z_{ab} - Z_b)}{2}(\epsilon_{ab} + \Re\Sigma_{ab}(0) + \epsilon_b + \Re\Sigma_b(0)) \\ &+ \frac{(Z_{ab} + Z_b)}{2}(\epsilon_{ab} + \Re\Sigma_{ab}(0) - \epsilon_b - \Re\Sigma_b(0)).\end{aligned} \tag{5.12}$$

Taking the bonding and antibonding self-energies in terms of Σ_{11} and Σ_{12} (see appendix I) we obtain

$$Z_b = \frac{(1 - \frac{\partial \Re\Sigma_{11}}{\partial\omega}|_{\omega=0}) + (\frac{\partial \Re\Sigma_{12}}{\partial\omega}|_{\omega=0})}{(1 - \frac{\partial \Re\Sigma_{11}}{\partial\omega}|_{\omega=0})^2 - (\frac{\partial \Re\Sigma_{12}}{\partial\omega}|_{\omega=0})^2}, \tag{5.13}$$

$$Z_{ab} = \frac{(1 - \frac{\partial \Re\Sigma_{11}}{\partial\omega}|_{\omega=0}) - (\frac{\partial \Re\Sigma_{12}}{\partial\omega}|_{\omega=0})}{(1 - \frac{\partial \Re\Sigma_{11}}{\partial\omega}|_{\omega=0})^2 - (\frac{\partial \Re\Sigma_{12}}{\partial\omega}|_{\omega=0})^2}. \tag{5.14}$$

Notice that since Z_{ab}, Z_b, and $(1 - \frac{\partial \Re\Sigma_{11}}{\partial\omega}|_{\omega=0})$ are positive, it is the sign of $\frac{\partial \Re\Sigma_{12}}{\partial\omega}|_{\omega=0}$ that determines which orbital is more correlated.

Finally, on the basis of equations (5.13) and (5.14) the bonding-antibonding splitting energy is then given by

$$\begin{aligned}\Delta =& \frac{(1-\frac{\partial \Re\Sigma_{11}}{\partial\omega}|_{\omega=0})}{(1-\frac{\partial \Re\Sigma_{11}}{\partial\omega}|_{\omega=0})^2-(\frac{\partial \Re\Sigma_{12}}{\partial\omega}|_{\omega=0})^2} \\ & \times(\epsilon_{ab}-\epsilon_b-2\Re\Sigma_{12}(0)) \\ & -\frac{(\frac{\partial \Re\Sigma_{12}}{\partial\omega}|_{\omega=0})}{(1-\frac{\partial \Re\Sigma_{11}}{\partial\omega}|_{\omega=0})^2-(\frac{\partial \Re\Sigma_{12}}{\partial\omega}|_{\omega=0})^2} \\ & \times(\epsilon_{ab}+\epsilon_b+2\Re\Sigma_{11}(0)). \end{aligned} \tag{5.15}$$

The first term in the equation above is just the "local" Z_{local} multiplied by the bare splitting, enhanced by the intersite self-energy, while the second term arises from the asymmetry of the local crystal field levels corrected by local self-energy, and would vanish in the particle-hole symmetric limit.

Since according to figure 5.12 there exist strong intersite electronic correlations in the system, thus one can consider that these nonlocal correlations give rise to an effective $a_{1g}-a_{1g}$ frequency dependent hopping $t_{a_{1g}-a_{1g}}+Re\Sigma^{in}_{a_{1g}-a_{1g}}(i\omega)$, which properly takes into account the a_{1g} bonding-antibonding splitting. A similar observation was previously proposed for the low-temperature phase of Ti_2O_3 [241], but a strong intersite Coulomb interaction was required for opening the gap.

5.2.2.1 Metallization due to hot carriers

More recently, numerous experimental studies have reported the existence of monoclinic-like metallic phases of VO_2 [203–207]. This transition was also induced by the application of femtosecond laser pulses on VO_2 films. As pointed out by Wegkamp *et al.* [203], the photoexcitation gives rise to hot carriers, which have an associated temperature much higher than the lattice temperature. Motivated by this fact, we performed calculations considering a much higher temperature, *i.e.* $T = 900$ K, for electrons in the M_1 phase.

In figure 5.13(a) and (b) we show the calculated spectral function and the projected DOS of M_1 at 332 K (same results as those presented in figure 5.11(b)) and 900 K, respectively. From the spectral function at 900 K, one can see the closing of the gap suggesting that the collapse of the gap in photoexcited samples can be triggered by hot carriers. In particular, we observe that a_{1g} and $e^{\pi}_g(1)$ subbands shift towards the Fermi

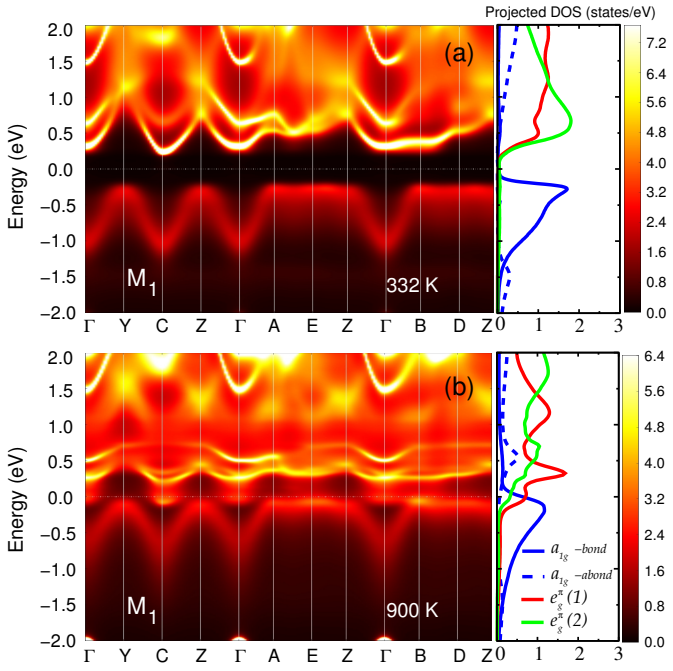

FIGURE 5.13: Spectral function and projected density of states of M_1 phase at (a) 332 and (b) 900 K (b). The projections to a_{1g}, $e_g^\pi(1)$, and $e_g^\pi(2)$ dimer states are shown in blue, red, and green lines, respectively. The solid (dashed) blue line corresponds to the projection to the bonding (antibonding) a_{1g} dimer state.

level, the latter shifting more than the a_{1g} subband. Also, there is a reduction in the intensity of the peak associated with the LHB at $T = 900$ K, and the appearance of a peak at 0.55 eV associated with the a_{1g} antibonding state.

To understand why the gap vanishes at 900 K, we examine the temperature dependence of the self-energies. In figure 5.14 we present the real part of intersite $\Sigma^{in}_{a_{1g}-a_{1g}}$, on the imaginary axis, for these two temperatures. In addition, in the inset we show the antibonding component of $Re\Sigma_{ab,a_{1g}}$ and the bonding component of $Re\Sigma_{b,e_g^\pi(1)}$, on the real frequency axis. Here, we observe that $Re\Sigma^{in}_{a_{1g}-a_{1g}}$, in the low-energy part, and $Re\Sigma_{ab,a_{1g}}$ are strongly suppressed with increasing temperature. Therefore at 900 K the renormalization of the a_{1g} subband decreases significantly in comparison to that at 332 K. Thus, this subband is shifted towards the Fermi level. In relation to the $e_g^\pi(1)$ subband, we note an enhancement of the $Re\Sigma_{b,e_g^\pi(1)}$ from -0.46 eV to 0.77 eV, leading to an downshift of this subband.

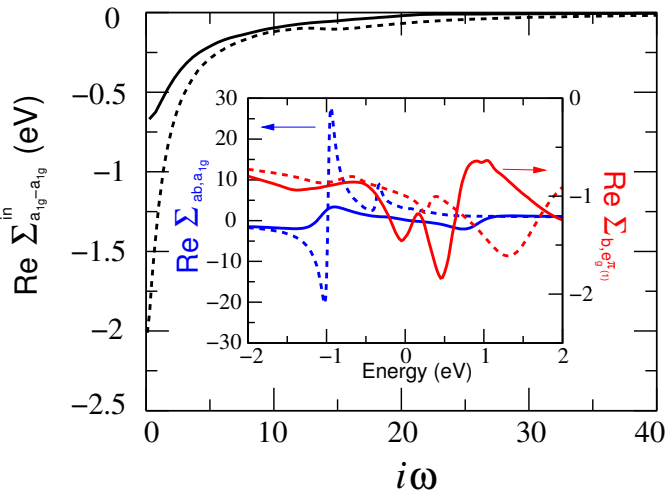

FIGURE 5.14: Real part of intersite $\Sigma^{in}_{a_{1g}-a_{1g}}$ on the imaginary axis at 332 (dashed lines) and 900 K (solid lines) of M_1 phase. Inset: Real parts of the antibonding $\Sigma_{ab,a_{1g}}$ (blue) and bonding $\Sigma_{b,e^{\pi}_{g}(1)}$ (red), on the real axis, at 332 (dashed lines) and 900 K (solid lines).

5.2.3 M_2 phase

We now turn to the M_2 phase of VO_2. In our calculations we considered a paramagnetic and antiferromagnetic state concerning the zigzag V-atoms. Our calculated spectral function and projected density of states of the M_2 phase, using the same values of U and J employed for the other phases, are shown in figure 5.15.

From our calculated spectral functions we observe that in both states the M_2 phase presents a gap. In particular, we obtain gaps of 0.55 and 0.61 eV for the antiferromagnetic and paramagnetic states, respectively. This indicates that the antiferromagnetic ordering related to the d electrons in the zigzag-like chains plays a minor role in the gap formation of this phase. In both situations the gap opens between the a_{1g} and e^{π}_{g} subband, although the a_{1g} states from the zigzag chains provide a small contribution to the bottom of the conduction band (see central and right panels of figure 5.15). The a_{1g} bonding subband presents a coherent peak at -0.34 eV (-0.31 eV) whereas the antibonding subband is centered at 2.5 eV (2.5 eV) for the paramagnetic (antiferromagnetic) state. The resulting bonding-antibonding splitting energy in this case is then $\approx$ 1 eV larger than the splitting energy obtained in our DFT calculations.

We also observe an increasing of the incoherence of the occupied levels close to the Fermi level going from the antiferromagnetic to the paramagnetic state, which indicates that antiferromagnetic ordering suppresses the electronic correlations. In fact, in the

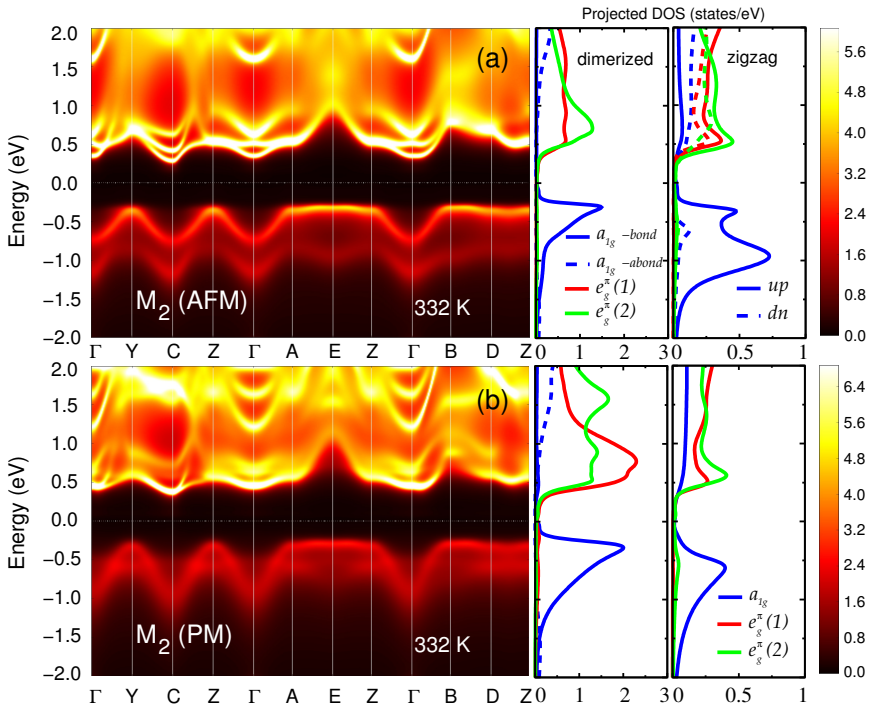

FIGURE 5.15: DFT+DMFT spectral function and projected density of states of M_2 phase at 332 K, considering (a) antiferromagnetic and (b) paramagnetic states. The projections to t_{2g} states associated with dimerized and zigzag-like chains of V-atoms are shown in the central and right panels, respectively. In respect to the dimerized atoms, projections to a_{1g}, $e_g^\pi(1)$, and $e_g^\pi(2)$ "molecular" states are shown in blue, red, and green, respectively. For the zigzag V-atoms, we use the same colors to indicate each t_{2g} state, where in particular the contributions of the *up* and *down*(dn) spins are shown in solid and dashed lines, respectively.

valence histograms shown in figure 5.16, we observe that the antiferromagnetic ordering suppresses the spin fluctuations of the zigzag V-atoms, while it does not affect the probabilities of states associated with the dimerized atoms. The histogram also shows that the singlet state associated with the dimerized atoms has the highest probability, followed by states with $N = 3$ (N is total number of electrons in atomic d state), which indicates that charge fluctuations are more important than spin fluctuations in this case.

Further, the a_{1g} states of zigzag atoms downshift and become less dispersive in the paramagnetic phase, similarly to a Hubbard subband. The a_{1g} states of dimerized V-atoms, by their turn, become broader but do not shift. Hence, the low-energy excitations in the paramagnetic phase are dominated by the a_{1g} states of the dimerized V-atoms, in contrast to the antiferromagnetic phase wherein both vanadium chains contribute to the top of the valence band.

To investigate the effects of electronic correlations in the M_2 phase we show in figure 5.17(a) the imaginary part of self-energies related to the dimerized and zigzag

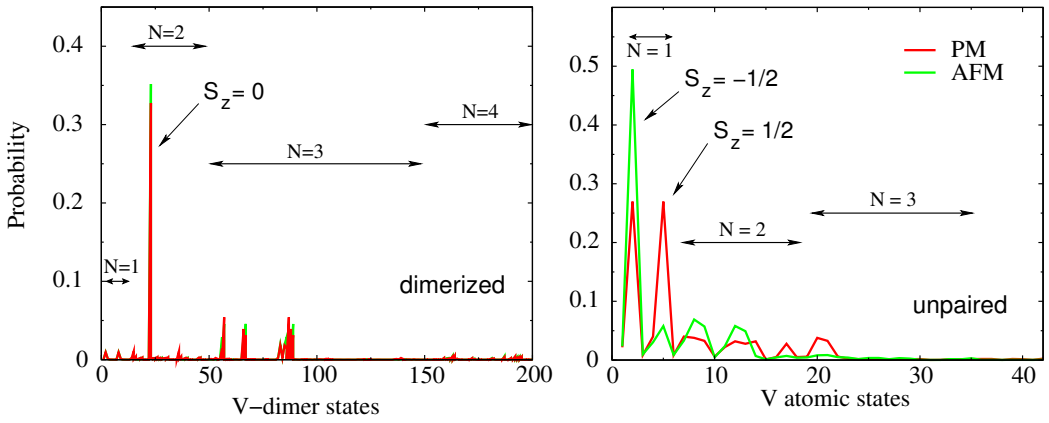

FIGURE 5.16: Valence histogram of vanadium dimer and atomic d states of dimerized and zigzag (unpaired) atoms, respectively.

V-atoms. In the paramagnetic phase, we notice that the t_{2g} states associated with the dimerized atoms do not present any pole in the imaginary part of self-energy, as similarly found in M_1 phase. In the antiferromagnetic phase, we find that even the t_{2g} states associated with the zigzag atoms do not present a Mott instability. In fact, the singularity of the self-energy is arrested once the antiferromagnetic ordered state is stabilized. Interestingly, as can be seen in figure 5.17(b), the real part of a_{1g} self-energy has a strong frequency dependence around the Fermi level, which indicates that the a_{1g} subband is renormalized by this component. On the other hand, in the paramagnetic phase (see figure 5.17(a)), the imaginary part of self-energy associated with a_{1g} states of zigzag V-atoms acquires a pole. As a result, the a_{1g} subband is splitted by a Mott instability, indicating that this subband undergoes an orbital-selective Mott-Hubbard transition. These findings suggest that the M_2 phase is best characterized as a Mott insulator.

5.2.4 bct phase

Finally we address the bct phase of NbO_2, presenting a comparison with the monoclinic phases of VO_2. In figure 5.18 we show our calculated projected DOS and spectral function of bct phase at 1000 K.

From the calculated spectral function we obtain an indirect gap of 0.73 eV, which is 0.49 eV higher than our DFT(GGA) band gap and is in good agreement with recent ellipsometric measurements reported by O'Hara *et al.* [215] (0.7 eV). It is worth mentioning, though, that our gap is underestimated in comparison with the gap of at least

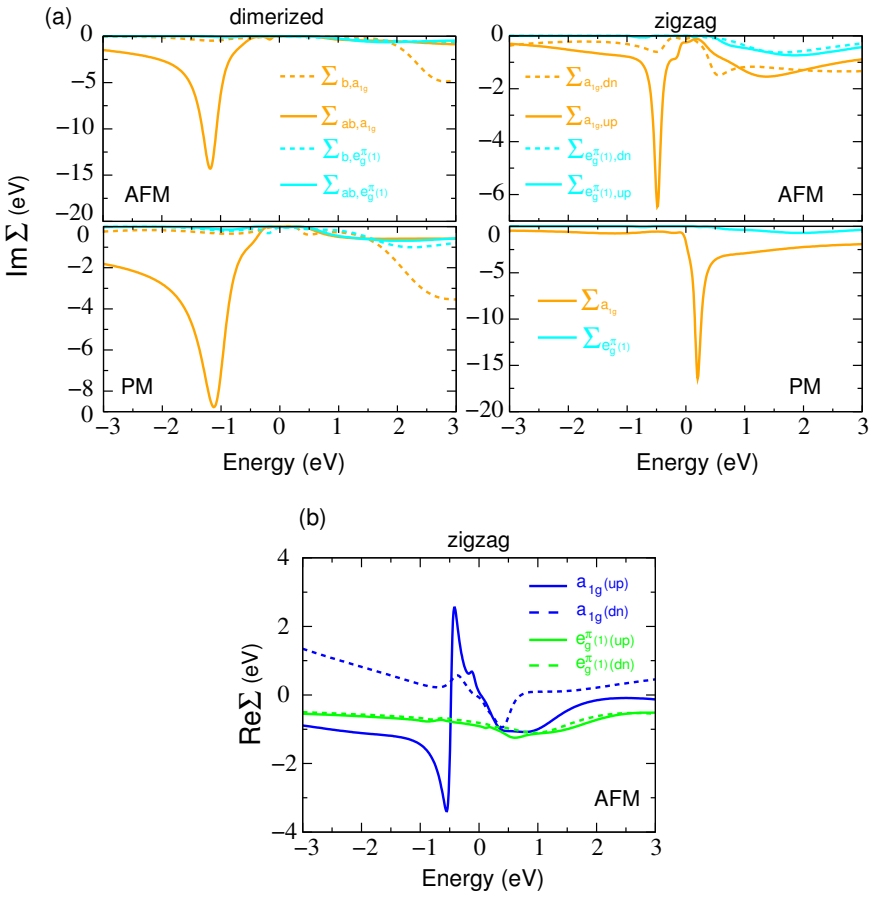

FIGURE 5.17: (a) Imaginary part, on real frequency axis, of bonding and antibonding self-energies of a_{1g} and $e_g^\pi(1)$ states of V-dimers, and a_{1g} and e_g^π states of zigzag vanadium atoms. (b) Real part of a_{1g} and e_g^π self-energies of zigzag (unpaired) vanadium atoms in the antiferromagnetic phase. Results are for the M_2 phase of VO_2.

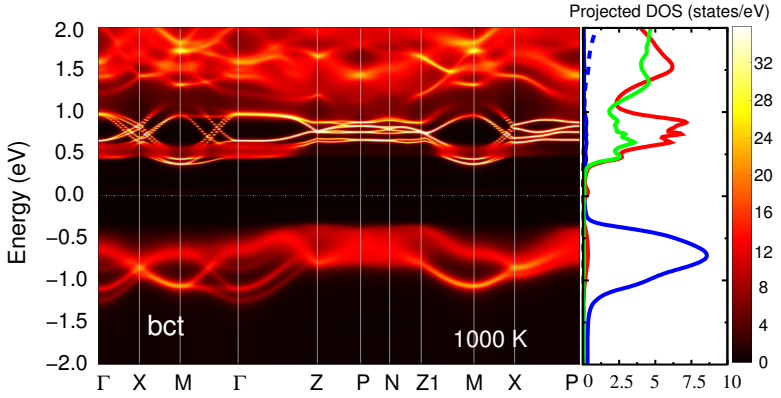

FIGURE 5.18: Spectral function and projected density of states of bct phase of NbO_2 at 1000 K. The projections to a_{1g}, $e_g^\pi(1)$, and $e_g^\pi(2)$ dimer states are shown in blue, red, and green lines, respectively. The solid (dashed) blue line corresponds to the projection on the bonding (antibonding) a_{1g} dimer state.

1.0 eV obtained by Posadas *et al.* [214] through x-ray photoelectron spectroscopic measurements of NbO_2 films. Further, the weak LHB associated with the a_{1g} antibonding state in M_1 phase of VO_2 is not seen in bct phase of NbO_2. The a_{1g} bonding subbands

present coherent peaks at around -0.30 and -0.70 eV in M_1 and bct phases, respectively. The respective antibonding subbands, by their turn, are centered around 2.58 and 3.54 eV. This indicates that the bonding-antibonding splitting energy increases 1.34 eV in M_1 phase and 0.74 eV in bct phase, in comparison with our DFT calculations.

Next we present in figure 5.19 the imaginary part of the self-energies associated with the a_{1g} dimer electronic states, for both M_1 (black) and bct (red) phases.

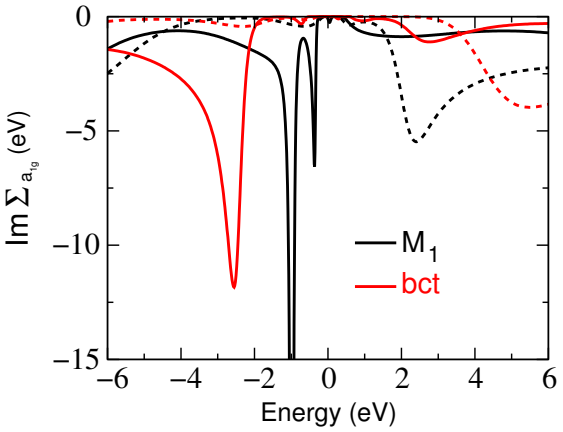

FIGURE 5.19: Imaginary part, on real frequency axis, of bonding (dashed lines) and antibonding (solid lines) self-energies associated with the a_{1g} dimer electronic states of M_1 phase of VO_2 (black) and bct phase of NbO_2 (red).

From these self-energies we notice a similar feature in both systems. The absence of poles in the imaginary part of the self-energies indicates that in M_1 phase as well as in the bct phase, once the dimerization occurs, the Mott instability is arrested. In particular, we notice that the peaks at -2.58 eV (bct) and -1.0 eV (M_1) associated with the a_{1g} antibonding states indicate that the electrons in M_1 phase are closer to a Mott transition than the ones in bct phase, suggesting that the structural distortions are more important in the gap opening of bct phase than in that of the M_1 phase.

5.2.5 Nonlocal dynamic correlations in M_1, M_2, and bct phases

As observed in the previous sections, the inclusion of nonlocal dynamic correlations increases the a_{1g} bonding-antibonding splitting energy in the low-temperature phases of VO_2 and NbO_2. As already discussed in section 5.2.2, within the transition metal dimers, treated as a cluster in our DMFT calculations, it is useful to look at the self-energies in the site representation, where we have the local self-energy, $\Sigma^{local} = \Sigma_{11}$, and the intersite self-energy, $\Sigma^{in} = \Sigma_{12}$. In order to compare the effects of nonlocal dynamic

correlations in M_1, M_2, and bct phases, we show in figure 5.20 the real part of intersite $a_{1g} - a_{1g}$ and $e_g^\pi(1) - e_g^\pi(1)$ self-energies of each insulating phase.

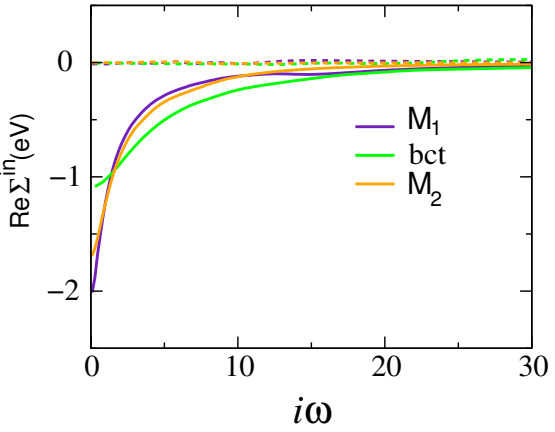

FIGURE 5.20: Real part of intersite self-energies, on imaginary frequency axis, of $a_{1g} - a_{1g}$ (solid lines) and $e_g^\pi(1) - e_g^\pi(1)$ (dashed lines) states of M_1 (indigo), M_2 (AFM) (orange) and bct (green) phases. For the monoclinic phases we considered $T = 332$ K and for the bct $T = 1000$ K.

First, we notice that the frequency dependence of the intersite self-energies associated with $e_g^\pi(1)$ states is negligible for all the insulating phases. In contrast, the intersite self-energies associated with a_{1g} states strongly depend on the frequency in the low-energy part. This indicates the presence of strong intersite correlations within the transition metal dimers. In particular, the intersite component is almost the same in the M_1 and M_2 phases of VO_2, with minor difference in the $i\omega \to 0$ limit, with $|\Sigma^{in}_{a_{1g}-a_{1g}}(0)|$ slightly larger in M_1 phase. Interestingly, the intersite a_{1g} self-energy in bct phase is frequency dependent as well, but with smaller intensity than in the insulating phases of VO_2, as noticeable when looking at the $i\omega \to 0$ limit. As discussed in section 5.2.2, within an effective band picture, the $\Sigma_{12}(\omega = 0)$ is responsible for the enhacement of the bare a_{1g} bonding-antibonding splitting as can be noticed from the term $\epsilon_{ab} - \epsilon_b - 2\Re\Sigma_{12}(0)$. These findings indicate a smaller enhacement of the bonding-antibonding splitting, due to nonlocal correlations, in bct phase of NbO_2 than in the monoclinic phases of VO_2, which in turn is in agreement with the obtained bonding-antibonding splitting energies of $\Delta_{bct} = 0.74$ eV and $\Delta_{M_1} = 1.34$ eV from our DFT+DMFT calculations. Therefore, our results suggest that the presence of strong nonlocal correlations within the transition-metal dimers leads to opening of a gap in all low-temperature phases of both oxides. However, these electronic correlations are more effective in the gap opening of the monoclinic phases of VO_2 than in the bct phase of NbO_2.

5.3 Summary

Concerning the MIT in VO_2 we present a comprehensive picture and an unified description of all the phases of VO_2 with the same values of the (U,J) parameters, including the mysterious M_2 phase which has not been considered previously in DMFT treatments. Mott physics is central for the proper description of all the phases, even though the Mott instability is arrested in the M_1 phase. We remind that the importance of Mott physics in all the phases of VO_2 was stressed early on in the comment of Pouget and Rice [15]. This physics now emerges from a quantitative first principles method.

Our theory leads to a different physical picture than that discussed previously for the gap opening in monoclinic phases of VO_2, and the possibility of the *collapse* of the M_1 insulating state by temperature. Our results indicate the presence of significant intersite correlations within the vanadium dimers, which in turn lower the a_{1g} subband in relation to the e_g^π. In particular, we notice that nonlocal dynamic correlations *enhance* the a_{1g} bonding-antibonding splitting, in contrast to what was reported by Biermann *et al.* [226]. The electrons in all phases of VO_2 are in the near vicinity of the Mott transition, but the pole in the self-energy, signaling the local moment formation, occurs only in the paramagnetic M_2 phase for undimerized V-atoms and its a_{1g} orbital. In the M_1 phase and in the antiferro-ordered M_2 phase, the singularity of the self-energy is arrested as the ordered states are adiabatically connected to Peierls and Slater insulators, respectively. The adiabatic connection between the weakly and the corresponding strongly interacting states makes the Mott mechanism hard to distinguish from alternative scenarios; nevertheless, collapsing a large insulating gap with raising electronic temperature is possible only in the Mott state in the presence of strong superexchange, as was found for example in the cluster-DMFT study of the 2D Hubbard model [242]. Hence, according to our results the M_1 phase is best characterized as the Mott phase in the presence of strong intersite superexchange[4] within the V-dimers, while the undimerized V-atoms in the M_2 phase undergo canonical Mott transition associated with local moment formation in the presence of weak superexchange. We mention that other consequence of Mott physics is the gap collapse of by sole increase of the electronic temperature.

[4]Strong antiferromagnetic interaction between spins of transition-metal elements.

With respect to the insulating phase of NbO_2, we find that nonlocal dynamic correlations play a role in the gap formation of the bct phase by a similar physical mechanism as that seen in the M_1 phase of VO_2. In particular, the nonlocal dynamic correlations in bct phase is less important for the gap opening than in M_1 and M_2 phases of VO_2. It indicates that the bct phase of NbO_2 is not a purely Peierls-type insulator, as it was recently proposed.

Conclusions

In this thesis by means of DFT and DFT+DMFT calculations we studied: (*i*) the structure, relative energetic stability, electronic and magnetic properties of graphene-like carbon nitride structures; (*ii*) the structural, energetics, electronic, and magnetic properties of polytetrafluoroethylene (Teflon) crystals with fluorine vacancies and oxygen substitutional impurities; and (*iii*) the metal-insulator transitions in VO_2 and NbO_2, focusing on the physical mechanisms responsible for the gap formation in their low-temperature structural phases. In the following we summarize our mainly findings.

(*i*) *Graphitic carbon nitrides:* From our simulated annealing calculations, we found a set of twenty eight structures with periodically distinct nanopores and different amounts of graphitic and pyridinic nitrogens. Our energetic analysis indicate that the energetic stability correlates with the relative concentration of pyridinic and graphitic nitrogens, with highest pyridinic concentrations leading to more stable structures. In particular, we found that the relative energetic stability, in some cases, is ruled by the energy cost associated with the doping due to the nitrogen impurities. In addition, the formation of pentagons with pyrrolic nitrogens was found to be energetically favorable in structures with large nanopores and carbon dangling bonds. The Fermi level of our set of structures was found to be controled, within an energy range of 2.65 eV, by variation of the relative concentration of graphitic and pyridinic nitrogens, which in turn indicates that carbon nitride materials are bipolar compounds. We also obtained that the band gap of some structures correlates with the increase of the nanopores. In particular, we obtained semiconductor structures with band gaps ranging from 0.11 eV to 1.69 eV. Based on these results, we suggested that, among the semiconducting structures, there are several possible new structures that may absorb in the visible light region and might be photo-catalyst candidates in the process of light-driven water-splitting. Also of interest are our results on the magnetic properties of the set of carbon nitride structures. Interestingly,

we obtained twelve structures with energetically favorable antiferromagnetic phase and nine with ferromagnetic properties. We concluded that this d^0 ferromagnetism is driven by Stoner-like instabilities of their corresponding nonmagnetic phases. Future perspectives of this work are the adsorption of transition-metal and hydrogen atoms as well as the inclusion of point defects on the graphene-like layers of carbon nitrides; and the electromechanical response of our carbon nitride structures upon charge doping. We mention that some of these perspectives are motivated by recent experiments reported on Refs. [243–245].

(*ii*) *Defects in polytetrafluoroethylene:* In this work we showed that fluorine vacancies and oxygen impurities in PTFE crystals lead to stable configurations without the breaking of the carbon backbone. From our energetic investigation we found that oxygen impurities are energetically more stable than fluorine vacancies and that by increasing the defects concentration we obtain more stable structures. Additional calculations also revealed that both point defects give rise to dispersionless levels and local magnetic moments. These dispersionless levels may give rise to defective bands which may explain the color and fluorescent properties of defective PTFE films. The magnetic moments, by their turn, were found to be suppressed under charge doping. From our total energy calculations, we did not find any defective structure with ferromagnetic coupling between the local moments, which rules out our investigated configurations as the source of the intrinsic ferromagnetism recently observed in experiments.

(*iii*) *MIT in VO_2 and NbO_2:* In this investigation we presented a comprehensive picture and a proper description of the electronic structure of all the phases of VO_2 and NbO_2 within our DFT+DMFT approximation. From our investigation we found that Mott physics is central for the proper description of all phases of VO_2, even though the Mott instability is arrested in the M_1 phase. Our theory suggested a new physical picture for the gap opening in the low-temperature phases of VO_2, and the collapse of this gap by increasing of temperature. In particular, in contrast with the previously proposed mechanisms in the literature, we find that nonlocal intersite correlations support the gap opening of the distorted low-temperature structures. For the VO_2, we find that electrons in all phases are in the near vicinity of the Mott transition, with the presence of orbital selective Mott- Hubbard instabilities in the case of undimerized V-atoms of the paramagnetic M_2 phase. In the M_1 phase and in the antiferromagnetically ordered M_2 phase, we found that this Mott-Hubbard instability is arrested as the ordered

states are adiabatically connected to Peierls and Slater insulators, respectively. This adiabatic connection between the weakly and the strongly interacting states makes the Mott mechanism hard to distinguish from alternative scenarios; nevertheless, collapsing a large insulating gap with raising electronic temperature, as we see in our results, is possible only in the Mott state in the presence of strong superexchange within the V-dimers. In respect to NbO_2, we showed that its low-temperature phase is not a purely Peierls-type insulator, due to the role played by nonlocal intersite correlations, as similarly found in M_1 phase of VO_2. We conclude by mentioning that the importance of nonlocal dynamic correlations for the gap opening of the bct phase of NbO_2 is smaller than in the case of the monoclinic phases of VO_2.

Overall, we investigated from a first principles perspective, different materials which exhibit emergent properties due to electron-electron interactions. By using different many-body approaches, we addressed their electronic structure as well as the corresponding mechanisms responsible for their physical properties. In my opinion, the theoretical methods used in this thesis, combined with the increasing of computational power over the years, encourage future applications of computational simulations to understand emergent phenonema in complex materials and to design new materials with new functionalities and desired properties. These subjects, by their turn, will stimulate very active research in condensed matter physics and materials science in the near future.

Appendix A

Path integral for the partition function

In this appendix we present a short derivation of the partition function of an interacting electron system using path integrals. A more detailed derivation of this equation can be found in Refs. [17, 18].

We start by considering a system of interacting electrons, described by the Hamiltonian H, at temperature $T = 1/\beta$. By definition the quantum partition function of this system is given by [246]

$$Z = \mathrm{Tr}\, e^{-\beta H} = \sum_n \langle n|e^{-\beta H}|n\rangle, \tag{A.1}$$

where $|n\rangle$ are Fock-space states.

Before rewriting the above equation in an integral form, we introduce the fermionic quantum states denoted as coherent states. Basically, these coherent states are the eigenstates of the annihilation operator a_i, $a_i|\psi\rangle = \psi_i|\psi\rangle$, with conjugate given by $\langle\psi|a_i^\dagger = \langle\psi|\psi_i^\dagger$, where $a_i^\dagger$ is the creator operator. Here the index i denotes the number of the state in the Fock-space $\{|n\rangle\}$,[1] while the quantities ψ_i, $\psi_i^\dagger$ are the Grassman variables. In particular, these Grassman variables form a characteristic algebra with anticommuting properties due to the anticommutativity of the operators $a_i^\dagger$ and a_i. We

[1] $|n_1, n_2, \ldots, n_i, \ldots\rangle = \ldots (a_i^\dagger)^{n_i} \ldots (a_2^\dagger)^{n_2} (a_1^\dagger)^{n_1}|0\rangle$, where $|0\rangle$ is the vaccum state and $n = 0, 1$.

stress that these variables lead to different sorts of algebric operations, in comparison with ordinary numbers.[2]

By definition the coherent states for fermions are given by

$$|\psi\rangle = e^{-\sum_i \psi_i a_i^\dagger}|0\rangle, \tag{A.2}$$

$$\langle\psi| = \langle 0|e^{-\sum_i a_i \psi_i^\dagger}. \tag{A.3}$$

Importantly, these states obey the following completeness relation [18]

$$\int d[\psi^\dagger\psi] e^{-\sum_i \psi_i^\dagger \psi_i}|\psi\rangle\langle\psi| = \mathbf{1}, \tag{A.4}$$

where $d[\psi^\dagger\psi] = \prod_{i=1}^{N} d\psi_i^\dagger d\psi_i$. As we shall see, N is the number of segments used to divide the time interval $[0, \beta)$ (number of time slices). From this relation one can rewrite the partition function, equation A.1, as it follows

$$Z = \int d[\psi^\dagger\psi] e^{-\sum_i \psi_i^\dagger \psi_i}\langle -\psi|e^{-\beta H}|\psi\rangle. \tag{A.5}$$

By partitioning the exponential in the equation above in N steps, we obtain that

$$Z = \int d[\psi^\dagger\psi] e^{-\sum_i \psi_i^\dagger \psi_i}\langle -\psi|(e^{-\Delta\tau H})^N|\psi\rangle, \tag{A.6}$$

where $\Delta\tau = \beta/N$.

We now consider that H has the general tight-binding form

$$H = \sum_{ij} h_{ij} a_i^\dagger a_j + \sum_{ijkl} V_{ijkl} a_i^\dagger a_j^\dagger a_k a_l, \tag{A.7}$$

where h_{ij} and V_{ijkl} are the one- and two-body operator matrices [18]. Hence, we obtain that

$$e^{-\Delta\tau H} = 1 + \Delta\tau \sum_{ij} h_{ij} a_i^\dagger a_j + \Delta\tau \sum_{ijkl} V_{ijkl} a_i^\dagger a_j^\dagger a_k a_l + O(\Delta\tau^2). \tag{A.8}$$

[2]For example, $(\psi_i^\dagger)^2 = (\psi_i)^2 = 0$ [17].

Inserting the completeness relation N times between each product of $e^{-\Delta\tau H}$ terms in equation A.6, one obtains

$$Z = \int \prod_{n=0}^{N} d[\psi_i^{n\dagger}\psi_i^n] e^{-\Delta\tau \sum_{n=0}^{N-1}[(\Delta\tau)^{-1}(\psi_i^{n\dagger}-\psi_i^{n+1\dagger})\psi_i^n + H(\psi_i^{n+1\dagger},\psi_i^n)]}, \tag{A.9}$$

where

$$H(\psi_i^{n+1\dagger},\psi_i^n) = \sum_{ij} h_{ij}\psi_i^{n+1\dagger}\psi_j^n + \sum_{ijkl} V_{ijkl}\psi_i^{n+1\dagger}\psi_j^{n+1\dagger}\psi_k^n\psi_l^n. \tag{A.10}$$

By taking the limit $N \to \infty$ ($\Delta\tau \to 0$, continuum limit), the partition function turns into

$$Z = \int D[\psi^\dagger\psi] e^{-S}, \tag{A.11}$$

with action given by

$$S = \int_0^\beta d\tau [\psi^\dagger \frac{\partial}{\partial\tau}\psi + H(\psi^\dagger,\psi)], \tag{A.12}$$

where $D[\psi^\dagger\psi] = \lim_{N\to\infty}\prod_{n=1}^{N} d(\psi_i^{n\dagger}\psi_i^n)$ and $\frac{\partial}{\partial\tau}\psi^\dagger \equiv \lim_{\Delta\tau\to 0}\frac{(\psi_i^{n+1\dagger}-\psi_i^{n\dagger})}{\Delta\tau}$.

Appendix B

Proofs of Hohenberg-Kohn Theorems

Proof of Theorem 1.2.1. Let us suppose two distinct external potentials $v(\mathbf{r})$ and $v'(\mathbf{r})$ which give rise to different Hamiltonians H and H', respectively. Their respective ground state wavefunctions are denoted by Ψ and Ψ'. Considering that both potentials are determined by the same ground state electron density ρ_o, it follows that

$$E = \langle \Psi | H | \Psi \rangle < \langle \Psi' | H | \Psi' \rangle, \tag{B.1}$$

$$E' = \langle \Psi' | H' | \Psi' \rangle < \langle \Psi | H' | \Psi \rangle. \tag{B.2}$$

One can rewrite these two equations by expressing the Hamiltonian as a sum of the potential energies,

$$E = \langle \Psi | \hat{T} + \hat{U} + \hat{V} | \Psi \rangle < \langle \Psi' | \hat{T} + \hat{U} + \hat{V} | \Psi' \rangle, \tag{B.3}$$

$$E' = \langle \Psi' | \hat{T} + \hat{U} + \hat{V}' | \Psi' \rangle < \langle \Psi | \hat{T} + \hat{U} + \hat{V}' | \Psi \rangle, \tag{B.4}$$

with $\hat{T}$ being the kinetic-energy operator, $\hat{U}$ the electron-electron potential energy operator, $\hat{V}(\hat{V}')$ the external potential energy operator. This external potential is given by

$$\hat{V} = \sum_{i=1}^{N} v(\mathbf{r}_i). \tag{B.5}$$

Using the many-body wavefunction and the external potential energy, the potential expectation value reads

$$\begin{aligned}\langle\Psi|\hat{V}|\Psi\rangle &= \sum_{i=1}^{N}\langle\Psi|v(\mathbf{r}_i)|\Psi\rangle \\ &= \sum_{i=1}^{N}\int d\mathbf{r}_1 \ldots \int d\mathbf{r}_N \Psi^*(\mathbf{r}_1,\ldots,\mathbf{r}_N)v(\mathbf{r}_i)\Psi(\mathbf{r}_1,\ldots,\mathbf{r}_N).\end{aligned} \tag{B.6}$$

Since $v(\mathbf{r}_i) = \int d\mathbf{r}\delta(\mathbf{r}-\mathbf{r}_i)v(\mathbf{r})$, one obtain

$$\begin{aligned}\langle\Psi|\hat{V}|\Psi\rangle &= \sum_{i=1}^{N}\int d\mathbf{r}_1 \ldots \int d\mathbf{r}_N \int d\mathbf{r}\delta(\mathbf{r}-\mathbf{r}_i)v(\mathbf{r})\Psi^*(\mathbf{r}_1,\ldots,\mathbf{r}_N)\Psi(\mathbf{r}_1,\ldots,\mathbf{r}_N) \\ &= \sum_{i=1}^{N}\int d\mathbf{r}\int d\mathbf{r}_1 \ldots \int d\mathbf{r}_i\delta(\mathbf{r}-\mathbf{r}_i)v(\mathbf{r})\ldots\int d\mathbf{r}_N\Psi^*\Psi.\end{aligned} \tag{B.7}$$

Further, the electron density is written as

$$\rho(\mathbf{r}) = \langle\Psi|\sum_{i=1}^{N}\delta(\mathbf{r}-\mathbf{r}_i)|\Psi\rangle, \tag{B.8}$$

which leads to

$$\langle\Psi|\hat{V}|\Psi\rangle = \int \rho(\mathbf{r})v(\mathbf{r})d\mathbf{r}. \tag{B.9}$$

On the other hand, one can rewrite the equation B.1 as the following

$$\langle\Psi|H|\Psi\rangle < \langle\Psi'|H'|\Psi'\rangle + \langle\Psi'|\hat{V}-\hat{V}'|\Psi'\rangle. \tag{B.10}$$

Thus from equation B.9 one obtain

$$\langle\Psi'|\hat{V}-\hat{V}'|\Psi'\rangle = \int \rho(\mathbf{r})[v(\mathbf{r})-v'(\mathbf{r})]d\mathbf{r}. \tag{B.11}$$

Likewise, from equation B.2 we have

$$\begin{aligned}\langle\Psi|H'|\Psi\rangle &= \langle\Psi|H|\Psi\rangle + \langle\Psi|H'-H|\Psi\rangle \\ &= \langle\Psi|H|\Psi\rangle + \langle\Psi|\hat{V}'-\hat{V}|\Psi\rangle,\end{aligned} \tag{B.12}$$

where

$$\langle \Psi | \hat{V}' - \hat{V} | \Psi \rangle = \int [v'(\mathbf{r}) - v(\mathbf{r})] \rho(\mathbf{r}) d\mathbf{r}. \tag{B.13}$$

Hence equations B.1 and B.2 turn into

$$E < E' + \int [v(\mathbf{r}) - v'(\mathbf{r})] \rho(\mathbf{r}) d\mathbf{r}, \tag{B.14}$$

$$E' < E + \int [v'(\mathbf{r}) - v(\mathbf{r})] \rho(\mathbf{r}) d\mathbf{r}. \tag{B.15}$$

By summing up equations B.14 and B.15 one obtain the following contradiction

$$E + E' < E' + E. \tag{B.16}$$

□

Therefore if the electron density ρ_o is unique then there cannot be two different external potentials. Accordingly since the Hamiltonian is fully determined by ρ_o the ground-state many-body wavefunctions are fully determined as well.

Proof of Theorem 1.2.2. From the first theorem one knows that the total energy of the many-body system reads

$$E = E[\rho] = \langle \Psi[\rho] | \hat{T} + \hat{U} + \hat{V} | \Psi[\rho] \rangle, \tag{B.17}$$

Moreoever one can split the energy functional as it follows

$$\begin{aligned} E[\rho] &= \langle \Psi[\rho] | \hat{T} + \hat{U} | \Psi[\rho] \rangle + \langle \Psi[\rho] | \hat{V} | \Psi[\rho] \rangle \\ &= F[\rho] + \langle \Psi[\rho] | \hat{V} | \Psi[\rho] \rangle, \end{aligned} \tag{B.18}$$

where $F[\rho]$ is an universal functional for any system of N interacting electrons. Then for the ground-state we obtain

$$E[\rho_o] = F[\rho_o] + \langle \Psi[\rho_o] | \hat{V} | \Psi[\rho_o] \rangle. \tag{B.19}$$

On the other hand, it is well known that the total energy of the ground-state is smaller than that of any electronic state with many-body wave function Ψ,

$$\begin{aligned} E[\Psi_o] &< E[\Psi], \\ \langle\Psi_o|\hat{T}+\hat{U}|\Psi_o\rangle + \langle\Psi_o|\hat{V}|\Psi_o\rangle &< \langle\Psi|\hat{T}+\hat{U}|\Psi\rangle + \langle\Psi|\hat{V}|\Psi\rangle. \end{aligned} \tag{B.20}$$

Since the electronic density $\rho_o(\rho)$ defines uniquely $\Psi_o(\Psi)$, from equation B.20 we obtain

$$\begin{aligned} F[\rho_o] + \langle\Psi[\rho_o]|\hat{V}|\Psi[\rho_o]\rangle &< F[\rho] + \langle\Psi[\rho]|\hat{V}|\Psi[\rho]\rangle, \\ E[\rho_o] &< E[\rho]. \end{aligned} \tag{B.21}$$

□

Therefore, the energy functional $E[\rho]$ is minimized for the exact ground-state electron density $\rho_o(\mathbf{r})$.

Appendix C

Constrained field in DFT

Let us consider a system of noninteracting electrons under an external potential $V_{ext}(\mathbf{r})$ described by the following model Hamiltonian

$$H_0 = \sum_{ij} c_i^\dagger t_{ij} c_j, \tag{C.1}$$

where $c_i^\dagger(c_j)$ creates (annihilates) an electron on the site i (j). The hopping amplitute is given by $t_{ij} = \langle \chi(\mathbf{r}-\mathbf{R}_i)| -\nabla^2 + V_{ext}(\mathbf{r})|\chi(\mathbf{r}-\mathbf{R}_j)\rangle$, where $\chi(\mathbf{r}-\mathbf{R}_j)$ is a nonorthogonal orbital centered at $\mathbf{R}_j$. The action associated with this noninteracting Hamiltonian reads [18]

$$S_0 = \int_0^\beta d\tau \Big[\sum_i c_i^\dagger(\tau)(\partial_\tau - \mu) c_i(\tau) + H_0[c_i^\dagger, c_i] \Big]. \tag{C.2}$$

We now turn to the action of this noninteracting system coupled to the constrained field $J_0(x)$ in similar way as in DFT (see equation 1.19)

$$S' = S_0 + \int dx J_0(x) \psi^\dagger(x) \psi(x). \tag{C.3}$$

By expressing the field operators in terms of the particle operators,

$$\psi^\dagger(x) = \sum_i \chi^*(\mathbf{r}-\mathbf{R}_i) c_i^\dagger(\tau), \tag{C.4}$$

$$\psi(x) = \sum_i \chi(\mathbf{r}-\mathbf{R}_i) c_i(\tau), \tag{C.5}$$

we obtain

$$S' = S_0 + \int dx \Big(\sum_i \chi^*(\mathbf{r} - \mathbf{R}_i) c_i^\dagger(\tau) \Big) J_0(x) \Big(\sum_j \chi(\mathbf{r} - \mathbf{R}_j) c_j(\tau) \Big). \tag{C.6}$$

Considering that J_0 does not depend on τ and using equation C.2, it results

$$\begin{aligned} S' &= S_0 + \int d\tau \sum_{ij} c_i^\dagger(\tau) \Big(\int d\mathbf{r} \chi^*(\mathbf{r} - \mathbf{R}_i) J_0(\mathbf{r}) \chi(\mathbf{r} - \mathbf{R}_j) \Big) c_j(\tau) \\ &= S_0 + \int d\tau \sum_{ij} c_i^\dagger(\tau) \langle \chi(\mathbf{r} - \mathbf{R}_i) | J_0(\mathbf{r}) | \chi(\mathbf{r} - \mathbf{R}_j) \rangle c_j(\tau) \qquad \text{(C.7)} \\ &= \int_0^\beta d\tau \sum_i c_i^\dagger(\tau) (\partial_\tau - \mu) c_i(\tau) \\ &+ \int_0^\beta d\tau \sum_{ij} c_i^\dagger(\tau) \langle \chi(\mathbf{r} - \mathbf{R}_i) | -\nabla^2 + V_{ext}(\mathbf{r}) + J_0(\mathbf{r}) | \chi(\mathbf{r} - \mathbf{R}_j) \rangle c_j(\tau) \qquad \text{(C.8)} \\ &= \int_0^\beta d\tau \sum_i c_i^\dagger(\tau) (\partial_\tau - \mu) c_i(\tau) + \int_0^\beta d\tau \sum_{ij} t'_{ij} c_i^\dagger(\tau) c_j(\tau), \qquad \text{(C.9)} \end{aligned}$$

where the new hopping amplitute is given by $t'_{ij} = \langle \chi(\mathbf{r} - \mathbf{R}_i) | -\nabla^2 + V_{ext}(\mathbf{r}) + J_0(\mathbf{r}) | \chi(\mathbf{r} - \mathbf{R}_j) \rangle$. Therefore, we see that $J_0(\mathbf{r})$ plays the role of an additional one-particle potential acting on the system of noninteracting electrons.

Appendix D

Nonorthogonal orbitals and Basis set

In this appendix we introduce a real space basis set used in our derivation of DMFT effective action [11] presented in section 1.4. We start by focusing on a basis set defined by nonorthogonal orbitals $\chi_\xi(\mathbf{r})$, in which ξ is a general index. Since these orbitals are nonorthogonal the overlap matrix yields

$$O_{\xi,\xi'} = \langle \chi_\xi | \chi_{\xi'} \rangle . \tag{D.1}$$

The field operators on this basis becomes [11]

$$\psi(x) = \sum_\xi c_\xi(\tau)\chi_\xi(\mathbf{r}), \tag{D.2}$$

$$\psi^\dagger(x) = \sum_\xi c^\dagger_\xi(\tau)\chi^*_\xi(\mathbf{r}), \tag{D.3}$$

where τ is the imaginary time and $c^\dagger_\xi$ (c_ξ) the creation (annihilation) operators. Many quantities such as the Green's function, self-energy, source fields, etc. are represented as

$$A(\mathbf{r},\mathbf{r}',\tau) = \sum_{\xi\xi'} \chi_\xi(\mathbf{r}) A_{\xi\xi'}(\tau)\chi_{\xi'}(\mathbf{r}'), \tag{D.4}$$

with coefficients $A_{\xi\xi'}$ on imaginary time or frequency axis.

Taking the ξ index as a combination of angular moment index lm and unit cell index R, one can rewrite the nonorthogonal orbitals such as $\chi_\alpha(\mathbf{r}-\mathbf{R})$. Within this general tight-binding basis set, the α index takes into account the angular moment lm, in case of one atom per unit cell, and R takes into account the unit cell index [11, 52]. In situations with more than one atom per unit cell, an additional index i is added such as $\chi_\alpha(\mathbf{r}-\mathbf{t}_i-\mathbf{R})$, where $\mathbf{t}_i$ denotes the position of the aditional atoms within the unit cell [52]. Hence, within this basis set, the atomic levels and generalized hopping matrix of a noninteracting tight-binding Hamiltonian $H=-\nabla^2+V_{ext}$ are given by

$$h_{\alpha\beta}=\left\langle\chi_\alpha\right|-\nabla^2+V_{ext}\left|\chi_\beta\right\rangle, \tag{D.5}$$

$$h_{\alpha R\beta R'}=\left\langle\chi_\alpha(\mathbf{r}-\mathbf{R})\right|-\nabla^2+V_{ext}\left|\chi_\beta(\mathbf{r}-\mathbf{R}')\right\rangle, \tag{D.6}$$

respectively.

Appendix E

Parametrization of Coulomb interactions

Let us consider a system of interacting electrons where the electron-electron potential depends on $1/|\mathbf{r}-\mathbf{r}'|$. We assume now that these electrons occupy atomic-like orbital levels denoted by $|L\rangle$ (L denotes a general angular momentum index lm), in such a way that the Coulomb interaction is given by [18]

$$\hat{U} = \sum_{L_a L_b L_c L_d \sigma\sigma'} U_{L_a L_b L_c L_d} f^{\dagger}_{L_a\sigma} f^{\dagger}_{L_b\sigma'} f_{L_d\sigma'} f_{L_c\sigma}, \tag{E.1}$$

where $U_{L_a L_b L_c L_d}$ are the Coulomb interaction matrix elements and $f^{\dagger}_{L\sigma}(f_{L\sigma})$ creates (annihilates) one electron in orbital L with spin σ. These Coulomb matrix elements can be written in terms of Slater integrals $F^k_{\{l\}}$ and complex spherical harmonics Y_L [247, 248],

$$U_{L_a L_b L_c L_d} = \sum_{k=0}^{2l} \sum_{q=-k}^{k} \frac{4\pi}{2k+1} F^k_{\{l\}} \langle Y_{L_a}|Y_{kq}|Y_{L_c}\rangle \langle Y_{L_b}|Y^*_{kq}|Y_{L_d}\rangle. \tag{E.2}$$

The Slater integrals $F^k_{\{l\}}$ are given by [12]

$$F^k_{\{l\}} = 2\int_0^{\infty} dr r^2 [\phi_l(r)]^2 \int_0^{\infty} dr' (r')^2 [\phi_l(r')]^2 \frac{r^k_<}{r^{k+1}_>}, \tag{E.3}$$

where $\phi_l(r)$ are the radial wavefunctions of l orbitals, and $r_< = r, r_> = r'$ if $r' > r$ and vice versa. The integral of the product of three spherical harmonics $\langle Y_{L_a}|Y_{kq}|Y_{L_c}\rangle$ is

given by [12]

$$\langle Y_{L_a}|Y_{kq}|Y_{L_c}\rangle = \int d\hat{r} Y_{L_a}(\hat{r}) Y^*_{kq}(\hat{r}) Y_{L_c}(\hat{r}). \tag{E.4}$$

Hence, from equations E.1 and E.2 one obtain the Coulomb interaction $\hat{U}$ presented in equation 1.98. In addition, within this formalism one can obtain the on-site Coulomb interaction U and the Hund's coupling J in terms of the Slater integrals as it follows [12, 37]

$$U = F^0, \tag{E.5}$$

$$J = \begin{cases} \frac{(F^2+F^4)}{14}, & \text{for } d \text{ orbitals,} \\ \frac{(286F^2+195F^4+250F^6)}{6435}, & \text{for } f \text{ orbitals.} \end{cases}$$

Appendix F

Continuous time quantum Monte Carlo

F.1 Introduction to Monte Carlo Method

The Monte Carlo[1] method can be viewed as a statistical approach to compute complex integrals, or solve different sorts of numerical problems, using random positions (samples) with a carefully chosen distribution over a space of configurations [249]. This method has a vast application in physics, ranging from the evaluation of the thermodynamic properties of materials or effective models, as well as alternative methods to solve quantum many-body problems [249]. In this section we give a brief introduction on the the basic ingredients of the Monte Carlo method, which will be used in our derivation of the CTQMC method presented in the next section.

Let us first consider a physical system for which we want to calculate the expectation value of a physical observable A, which is given by

$$\langle A \rangle = \frac{1}{Z} \int_C dx A(x) p(x). \tag{F.1}$$

In the equation above Z is the partition function, x the configuration in phase space C, and $p(x)$ the probability weight of configuration x. Instead of evaluating the integral

[1] Its name is in allusion to a district of the Principality of Monaco wherein a cassino is located.

above, one can aproximate the expectation value of A by

$$\langle A\rangle_{MC} = \frac{1}{M}\sum_{i=1}^{M} A(x_i). \tag{F.2}$$

In other words, one can approximate $\langle A\rangle$ by the average of it over the set of configurations $\{x_1, x_2, \ldots, x_i, x_M\}$ of the phase space.

To have a better sampling of $\langle A\rangle$ one can generate a set of configurations, denoted as a Markov chain, employing Markov processes obeying certain conditions. The Markov processes are characterized by a transition matrix with elements W_{xy} that specify the probability to go from state x to state y by application of one Markov process [250]. In addition, in order to satisfy ergodicity and the detailed balance condition, these matrix elements should obey the following condition

$$\frac{W_{xy}}{W_{yx}} = \frac{p(y)}{p(x)}. \tag{F.3}$$

The well known Metropolis algorithm [103] satisfies this detailed balance condition, in which the transition matrix is written as

$$W_{xy} = W_{xy}^{prop} W_{xy}^{acc}, \tag{F.4}$$

with

$$W_{xy}^{acc} = min\Big[1, \frac{p(y)W_{yx}^{prop}}{p(x)W_{xy}^{prop}}\Big]. \tag{F.5}$$

In these equations W_{xy}^{prop} denotes the probability that an update from a configuration x to a new configuration y is proposed, whereas W_{xy}^{acc} denotes the probability of acceptance of the respective update. Hence, starting from a random set of configurations over phase space C, one can obtain a stationary distribution of configurations (Markov chain) by applying the Metropolis algorithm. This Markov chain, by its turn, allow us to obtain a better sampling of $\langle A\rangle$.

If we assume that the probability weight of each configuration x is a Boltzmann weight $p(x) = e^{-\beta E(x)}$, one can obtain an acceptance transition matrix given by

$$W_{xy}^{acc} = min[1, e^{-\beta(E_y - E_x)}]. \tag{F.6}$$

From this equation, if the energy of the new configuration y is smaller than the energy of the previous configuration x, $E_y - E_x < 0$, $W_{xy}^{acc} = 1$. Otherwise, $W_{xy}^{acc} = e^{-\beta(E_y - E_x)}$. We mention that this procedure can be used as a basic algorithm to obtain energetic favorable configurations of a physical system by evulating the total energy of each configuration obtained during the Markov processes. Further, the concepts introduced here can be also used to study the Monte Carlo treatment of effective quantum impurity problems, as presented in the next section. For more details about Monte Carlo methods please see Refs. [249, 250].

F.2 Continuous time quantum Monte Carlo

In this section we derive the main equations of the continuous time quantum Monte Carlo (CTQMC) method [40, 41] within the hybridization expansion representation, which is used as an impurity solver in our calculations.

We start with the Hamiltonian of the quantum impurity model, that is, the single-orbital Anderson model

$$H = \sum_{\sigma} \epsilon_d d_\sigma^\dagger d_\sigma + U n_{d\uparrow} n_{d\downarrow} + \sum_{p\sigma} \epsilon_p c_{p\sigma}^\dagger c_{p\sigma} + \sum_{p\sigma} (V_{dp} d_\sigma^\dagger c_{p\sigma} + V_{dp}^* c_{p\sigma}^\dagger d_\sigma), \tag{F.7}$$

where $d_\sigma^\dagger$ (d_σ) creates (annihilates) an electron with spin σ on the impurity, $c_{p\sigma}^\dagger$ ($c_{p\sigma}$) creates (annihilates) a conduction electron with wave vector $\mathbf{p}$ and spin σ, ϵ_d is the impurity energy level, ϵ_p is the energy of conduction electrons, U is the on-site Coulomb interaction energy between impurity-electrons, $n_{d\sigma} = d_\sigma^\dagger d_\sigma$ is the number operator of the impurity-electrons, and V_{dp} is the hybridization between the impurity and conduction electrons.

For this model the partition function is given by

$$\begin{aligned} Z =& \int D[d^\dagger d] D[c_p^\dagger c_p] e^{-S} \\ =& Z_{bath} \int D[d^\dagger d] e^{-S_a - \int_0^\beta d\tau \int_0^\beta d\tau' \sum_\sigma d_\sigma^\dagger(\tau) \Delta(\tau - \tau') d_\sigma(\tau')} \qquad \text{(F.8)} \\ =& Z_{bath} Z_{imp} \qquad \text{(F.9)} \end{aligned}$$

where the bath partition function reads

$$Z_{bath} = det[(i\omega + \mu - \epsilon_p)^{-1}] \tag{F.10}$$

and the atomic action is defined by

$$S_a = \int_0^\beta d\tau \Big[\sum_\sigma d_\sigma^\dagger(\tau)\Big(\frac{\partial}{\partial\tau} - \mu\Big)d_\sigma(\tau) + \sum_\sigma \epsilon_d d_\sigma^\dagger(\tau)d_\sigma(\tau) + U d_\uparrow^\dagger(\tau)d_\uparrow(\tau)d_\downarrow^\dagger(\tau)d_\downarrow(\tau)\Big], \tag{F.11}$$

where τ is the imaginary time and ω the Matsubara frequencies.[2] The hybridization function $\Delta(\tau - \tau')$ by its turn is given by

$$\Delta(\tau - \tau') = \frac{1}{\beta}\sum_\omega \Big(\sum_p \frac{V_{dp}^* V_{dp}}{i\omega + \mu - \epsilon_p}\Big) e^{i\omega(\tau - \tau')}. \tag{F.12}$$

We now expand the partition function in orders of the hybridization function, resulting into [18]

$$\begin{aligned} Z_{imp} &= \int D[d^\dagger d] e^{-S_a} \sum_{k=0}^\infty \frac{1}{k!}\Big[\sum_\sigma \int_0^\beta d\tau \int_0^\beta d\tau' d_\sigma(\tau') d_\sigma^\dagger(\tau)\Delta(\tau - \tau')\Big]^k \\ &= \int D[d^\dagger d] e^{-S_a} \sum_{k=0}^\infty \frac{1}{k!} \sum_{\sigma_1 \dots \sigma_k} \int_0^\beta d\tau_1 \dots \int_0^\beta d\tau_k \int_0^\beta d\tau_1' \dots \int_0^\beta d\tau_k' \\ &\quad \times d_{\sigma_1}(\tau_1') d_{\sigma_1}^\dagger(\tau_1)\Delta(\tau_1 - \tau_1') d_{\sigma_2}(\tau_2') d_{\sigma_2}^\dagger(\tau_2)\Delta(\tau_2 - \tau_2') \dots \\ &\quad \dots d_{\sigma_k}(\tau_k') d_{\sigma_k}^\dagger(\tau_k)\Delta(\tau_k - \tau_k'). \end{aligned} \tag{F.13}$$

Using the functional average of a time-ordering operator T_τ [18], we can rewrite the integral over the impurity degrees of freedom as it follows

$$\int D[d^\dagger d] d_{\sigma_1}(\tau_1') d_{\sigma_1}^\dagger(\tau_1) \dots d_{\sigma_k}(\tau_k') d_{\sigma_k}^\dagger(\tau_k) = Z_a \langle T_\tau d_{\sigma_1}(\tau_1') d_{\sigma_1}^\dagger(\tau_1) \dots d_{\sigma_k}(\tau_k') d_{\sigma_k}^\dagger(\tau_k)\rangle_a, \tag{F.14}$$

where

$$Z_a = \int D[d^\dagger d] e^{-S_a}. \tag{F.15}$$

[2] In our notation in this appendix we omitted the subindex n of ω, but we emphasize that $\omega = \omega_n = (2n+1)\pi T$.

In equation F.14 the $\langle \ldots \rangle_a$ denotes the functional average of $(\ldots)$ weighted by S_a. Hence, the resulting impurity partition function is given by

$$Z_{imp} = Z_a \sum_{k=0}^{\infty} \sum_{\sigma_1 \ldots \sigma_k} \frac{1}{k!} \int_0^\beta d\tau_1 \ldots \int_0^\beta d\tau_k \int_0^\beta d\tau'_1 \ldots \int_0^\beta d\tau'_k \\ \times \langle T_\tau d_{\sigma_1}(\tau'_1) d^\dagger_{\sigma_1}(\tau_1) \ldots d_{\sigma_k}(\tau'_k) d^\dagger_{\sigma_k}(\tau_k) \rangle_a \Delta(\tau_1 - \tau'_1) \ldots \Delta(\tau_k - \tau'_k). \tag{F.16}$$

Notice that this partition function, as expressed in equation F.16, is a diagrammatic expansion of individual configurations $x = (k, (\sigma_1, \ldots, \sigma_k), (\tau_1, \tau'_1, \ldots, \tau_k, \tau'_k))$, where k denotes the diagram order [250]. For each configuration x in configuration space, the associated probability weight is given by [250]

$$p(x) = Z_a \langle T_\tau d_{\sigma_1}(\tau'_1) d^\dagger_{\sigma_1}(\tau_1) \ldots d_{\sigma_k}(\tau'_k) d^\dagger_{\sigma_k}(\tau_k) \rangle_a \Delta(\tau_1 - \tau'_1) \ldots \Delta(\tau_k - \tau'_k) \prod_{i=1}^{k} d\tau_i \prod_{i=1}^{k} d\tau'_i. \tag{F.17}$$

The mainly purpose of CTQMC is to evaluate the partition function of equation F.16 using Monte Carlo techniques. However, the configuration weights denoted by $p(x)$ would admit negative values for fermions.[3] In order to overcome this issue, it was suggested to group Δ functions of the same order k into determinants [40]. Thus, the partition function is rewritten as it follows

$$Z_{imp} = Z_a \sum_{k=0}^{\infty} \sum_{\sigma_1 \ldots \sigma_k} \frac{1}{k!} \int_0^\beta d\tau_1 \ldots \int_0^\beta d\tau_k \int_0^\beta d\tau'_1 \ldots \int_0^\beta d\tau'_k \\ \times \langle T_\tau d_{\sigma_1}(\tau'_1) d^\dagger_{\sigma_1}(\tau_1) \ldots d_{\sigma_k}(\tau'_k) d^\dagger_{\sigma_k}(\tau_k) \rangle_a \\ \times \frac{1}{k!} Det \begin{pmatrix} \Delta(\tau_1 - \tau'_1) & \cdots & \Delta(\tau_1 - \tau'_k) \\ \vdots & \ddots & \vdots \\ \Delta(\tau_k - \tau'_1) & \cdots & \Delta(\tau_k - \tau'_k) \end{pmatrix}. \tag{F.18a}$$

Considering the more general case of a multi-orbital atom with index α (this index can correspond to spin and orbital), the partition function turns into

$$Z = Z_{bath} \int D[d^\dagger d] e^{-S_a - \int_0^\beta d\tau \int_0^\beta d\tau' \sum_{\alpha\alpha'} d^\dagger_\alpha(\tau) \Delta_{\alpha\alpha'}(\tau - \tau') d_{\alpha'}(\tau')}, \tag{F.19}$$

[3] This issue is usually known as the negative sign problem [250].

where the resulting impurity partition function is written as

$$
\begin{aligned}
Z_{imp} = Z_a \sum_{k=0}^{\infty} \sum_{\alpha_1 \ldots \alpha_k} \sum_{\alpha'_1 \ldots \alpha'_k} \frac{1}{k!} \int_0^\beta d\tau_1 \ldots \int_0^\beta d\tau_k \int_0^\beta d\tau'_1 \ldots \int_0^\beta d\tau'_k \\
\times \langle T_\tau d_{\alpha'_1}(\tau'_1) d^\dagger_{\alpha_1}(\tau_1) \ldots d_{\alpha'_k}(\tau'_k) d^\dagger_{\alpha_k}(\tau_k) \rangle_a \\
\times \frac{1}{k!} Det \begin{pmatrix} \Delta_{\alpha_1\alpha'_1}(\tau_1 - \tau'_1) & \Delta_{\alpha_1\alpha'_2}(\tau_1 - \tau'_2) & \cdots & \Delta_{\alpha_1\alpha'_k}(\tau_1 - \tau'_k) \\ \vdots & \vdots & \ddots & \vdots \\ \Delta_{\alpha_k\alpha'_1}(\tau_k - \tau'_1) & \Delta_{\alpha_k\alpha'_2}(\tau_k - \tau'_2) & \cdots & \Delta_{\alpha_k\alpha'_k}(\tau_k - \tau'_k) \end{pmatrix}.
\end{aligned} \tag{F.20a}
$$

In the following we will denote the hybridization matrix by M^{-1}, with elements $M^{-1}_{ij} = \Delta_{\alpha_i\alpha'_j}(\tau_i - \tau'_j)$.

The Monte Carlo sampling of the partition function written above is performed by means of a stationary distribution of configurations x_i obtained from Markov processes (see section F.1). Hence, a Markov chain is obtained $\{x_1, x_2, \ldots, x_{MC}\}$ (MC corresponds to the number of configurations in the Markov chain), where each configuration $x_i = (k_i, (\alpha_1, \alpha'_1, \ldots, \alpha_{k_i}, \alpha'_{k_i}), (\tau_1, \tau'_1, \ldots, \tau_{k_i}, \tau'_{ki}))$ has a weight given by

$$
p(x_i) = Z_a \frac{1}{(k_i!)^2} \langle T_\tau d_{\alpha'_1}(\tau'_1) d^\dagger_{\alpha_1}(\tau_1) \ldots d_{\alpha'_{k_i}}(\tau'_{k_i}) d^\dagger_{\alpha_{k_i}}(\tau_{k_i}) \rangle_a Det M^{-1} \prod_{i=1}^{k_i} d\tau_i \prod_{i=1}^{k_i} d\tau'_i. \tag{F.21}
$$

In diagramatic sampling the configurations are generated by insertion and removal of pairs of creation and annihilation operators $(d^\dagger_{\alpha_{new}}(\tau_{new}), d_{\alpha'_{new}}(\tau'_{new}))$, at random times τ_{new} and τ'_{new} chosen uniformly between 0 and β [41]. These operators affect the impurity occupancy giving rise to "kinks" in the imaginary-time evolution of the impurity states. One can illustrate the imaginary-time evolution of the impurity using diagrams as shown in figure F.1, in which we make explicit the kinks. It is worth mentioning that additional improvements in sampling time can be achieved by other steps such as time displacements of operators $d^\dagger, d$ [41].

Hence, throughout the Markov process new configurations with distinct order k are obtained. In particular, if one starts with terms at order k, after an insertion or removal of a pair of kinks one obtains terms of order $k+1$ or $k-1$. Furthermore, within the Monte Carlo sampling the stationary distribution of configurations are obtained once the ergodicity and detailed balance condition are satisfied [250]. To fulfill these conditions the Metropolis algorithm is used, from which the probabilities to insert and remove a

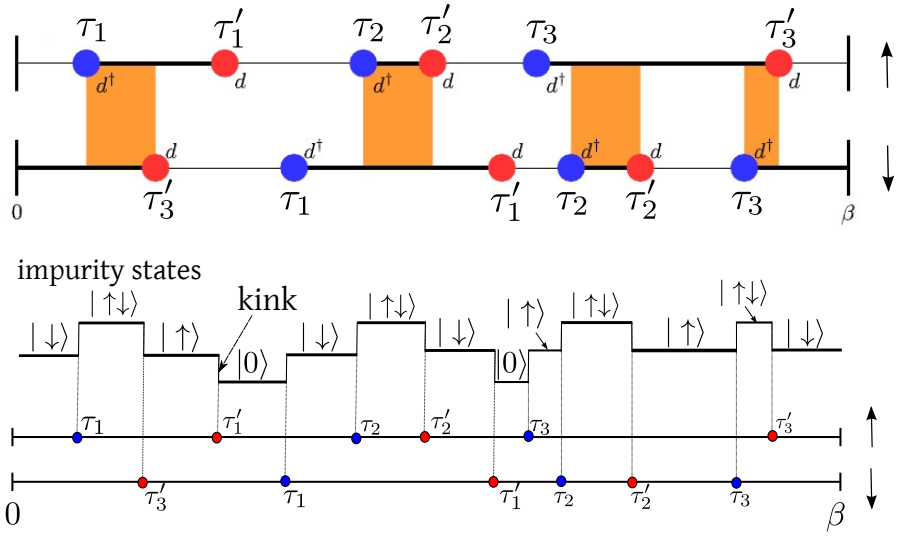

FIGURE F.1: Segment diagram showing the imaginary-time evolution of the impurity states. The two lines correpond to electrons of spin up and down, as represented by the up and down arrows. The areas in orange correspond to doubly occupied impurity states. The diagram on top is motivated by a similar diagram shown in Ref. [250]. The lower diagram presents the corresponding imaginary-time evolution of the impurity states in which the kinks are evident.

pair of kinks at random times τ_{new} and τ'_{new} ($\alpha = 1, \ldots, N_b$) are given by [41]

$$P_{add} = min\Big[\Big(\frac{\beta N_b}{k+1}\Big)^2 \frac{\mathcal{Z}_{new}}{\mathcal{Z}_{old}} \frac{\mathcal{D}_{new}}{\mathcal{D}_{old}}, 1\Big], \tag{F.22}$$

and

$$P_{remove} = min\Big[\Big(\frac{k}{\beta N_b}\Big)^2 \frac{\mathcal{Z}_{new}}{\mathcal{Z}_{old}} \frac{\mathcal{D}_{new}}{\mathcal{D}_{old}}, 1\Big], \tag{F.23}$$

respectively. $\mathcal{Z}_{new}$ and $\mathcal{Z}_{old}$ correspond to the local part of the weights of the old and new sampled configurations, which in case of insertion are given by

$$\mathcal{Z}_{new} = \langle T_\tau d_{\alpha'_{new}}(\tau_{new}) d^\dagger_{\alpha_{new}}(\tau_{new}) d_{\alpha'_1}(\tau'_1) d^\dagger_{\alpha_1}(\tau_1) \ldots d_{\alpha'_k}(\tau'_k) d^\dagger_{\alpha_k}(\tau_k)\rangle_a, \tag{F.24}$$

$$\mathcal{Z}_{old} = \langle T_\tau d_{\alpha'_1}(\tau'_1) d^\dagger_{\alpha_1}(\tau_1) \ldots d_{\alpha'_k}(\tau'_k) d^\dagger_{\alpha_k}(\tau_k)\rangle_a. \tag{F.25}$$

The terms D_{new} and D_{old} are the new and old determinants of the hybridization matrices.

The local part of the partition function $\mathcal{Z}$ can be rewritten using the eigenstates (eigenvalues) of the atomic Hamiltonian $|m\rangle$ (E_m) as it follows [41]

$$\begin{aligned}\mathcal{Z} = \sum_{\{m\}} [&e^{-E_{m_1}\tau_1'}(F^{\alpha_1})_{m_1 m_2} e^{-E_{m_2}(\tau_2-\tau_1')}(F^{\dagger\alpha_2})_{m_2 m_3}\cdots \\ &\times (F^{\alpha_{n-1}})_{m_{n-1}m_n} e^{-E_{m_n}(\tau_{n-1}'-\tau_n)}(F^{\dagger\alpha_n})_{m_n m_1} e^{-E_{m_1}(\beta-\tau_n)}],\end{aligned} \tag{F.26}$$

where $(F^{\dagger\alpha_i})_{nm} = \langle n|d_{\alpha_i}^{\dagger}|m\rangle$ and $(F^{\alpha_i})_{nm} = \langle n|d_{\alpha_i}|m\rangle$. A serious issue that appears in these calculations is the huge matrices involved due to the high number of atomic states, e.g. 2^{10} (2^{14}) states for d (f) shell. To reduce the calculations needed to evaluate $\mathcal{Z}$, superstates are introduced leading to block-diagonal matrices. These superstates are related to the atomic states and symmetries of the system, in such a way that a general impurity superstate is defined as $|N, S_z; \gamma>$, where N is the total number of electrons in the superstate, S_z the corresponding z component of the total spin, and γ the remaining quantum numbers. For more details about superstates see Ref. [41].

Finally, to sample the local Green's function the time set $\{\tau\}, \{\tau'\}$ and the inverse of the hybridization matrix are used [12, 41]

$$G_{loc}(i\omega; \{\tau\}, \{\tau'\}) = -\frac{1}{\beta}\sum_{i,j} e^{i\omega\tau_i} M_{ij}(\{\tau\}, \{\tau'\}) e^{-i\omega\tau_j}, \tag{F.27}$$

where the hybridization matrix is given by

$$M^{-1} = \begin{pmatrix} \Delta_\alpha(\tau_1^\alpha - \tau_1'^\alpha) & \Delta_\alpha(\tau_1^\alpha - \tau_2'^\alpha) & \cdots \\ \vdots & \ddots & \vdots \\ \Delta_\alpha(\tau_{k_\alpha}^\alpha - \tau_1'^\alpha) & \cdots & \Delta_\alpha(\tau_{k_\alpha}^\alpha - \tau_{k_\alpha}'^\alpha) \end{pmatrix}. \tag{F.28a}$$

For more details about the local Green's function sampling see Ref. [41].

Appendix G

Bond-counting model

G.1 Non-linear term in the bond-counting model

In this section we derive the expression for the additional term ΔE included in equation 2.2 of our bond-counting model. As previously mentioned, this term is included to take into account the effects introduced by the charge doping, induced by the different types of nitrogens, in the total energy of the $C_xN_yv_z$ structures. In particular, we postulate that this term is zero for the tri-s-triazine based g-C_3N_4, which is the most stable and experimentally synthesized structure [64, 109].

We start with the nitrogen-induced charge density, which we postulate as given by

$$\sigma = c\frac{(|2n_{C3N3} - n_{C3N2}|)}{\sum_{\alpha,\beta} n_{\alpha\beta}}, \tag{G.1}$$

where c is a constant and the term $|2n_{C3N3} - n_{C3N2}|$ is introduced to ensure that the tri-s-triazine based g-C_3N_4 is a fully compensated semiconductor. Next, we make the assumption that the additional energy ΔE can be obtained from nitrogen-doped graphene structures, namely C_xN_y, which we assume to have graphene-like density of states around the Fermi level, as shown in figure G.1.

We further assume that the density of states around the Fermi level is $g(E) = c'|E|$, where c' is a constant. From this density of states we can write the nitrogen-induced

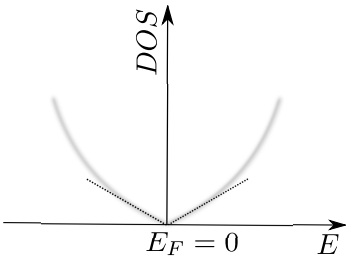

FIGURE G.1: Illustration of the graphene-like density of states (shown in gray) in the absence of dopants ($E_F = 0$) and our approximated density of states (shown in dotted lines).

charge density as it follows

$$\sigma = \int_0^{E_F} g(E)dE = \int_0^{E_F} c'|E|dE = c'\frac{E_F^2}{2}. \tag{G.2}$$

It is worthy mentioning that the nitrogen dopants shift the previous Fermi level (assumed at zero) to the new Fermi level, which we denote by E_F. Thus, the energy contribution to the total energy due to the occupation (nonoccupation) of the conduction (valence) band states yields

$$\Delta E = \int_0^{E_F} Eg(E)dE = c'\frac{E_F^3}{3} = \frac{2^{\frac{3}{2}}}{3}\frac{1}{\sqrt{c'}}\sigma^{\frac{3}{2}}, \tag{G.3}$$

where we used equation G.2. Since c' is proportional to $(\sum_{\alpha,\beta} n_{\alpha\beta})^{-2}$, using equation G.1 we finally obtain

$$\Delta E = k\frac{(|2n_{C3N3} - n_{C3N2}|)^{3/2}}{(\sum_{\alpha,\beta} n_{\alpha\beta})^{1/2}}, \tag{G.4}$$

where k is a constant. This ΔE is the non-linear term in the bond-couting model.

G.2 Parametrization of the bond-counting model

The total energy of the bond-counting model (see equation 2.2) depends on the bond energies of each $\alpha - \beta$ bond-type and the parameter k. To apply this total energy equation to our $C_xN_yv_z$ structures, we obtained these parameters from *ab initio* total energy calculations for the structures shown in figure G.2.

In particular, the ϵ_{C3C3} bond energy is obtained by considering the pristine graphene. The *ab initio* total energies of $C_6N_8v_4$, $C_8N_9v_1$, and $C_9N_9v_0$ and equation 2.2 were used to calculate ϵ_{C3N2}, ϵ_{C3N3}, and k. Similarly, from the $C_7N_8v_3$, $C_7N_9v_2$, $C_9N_8v_1$, and

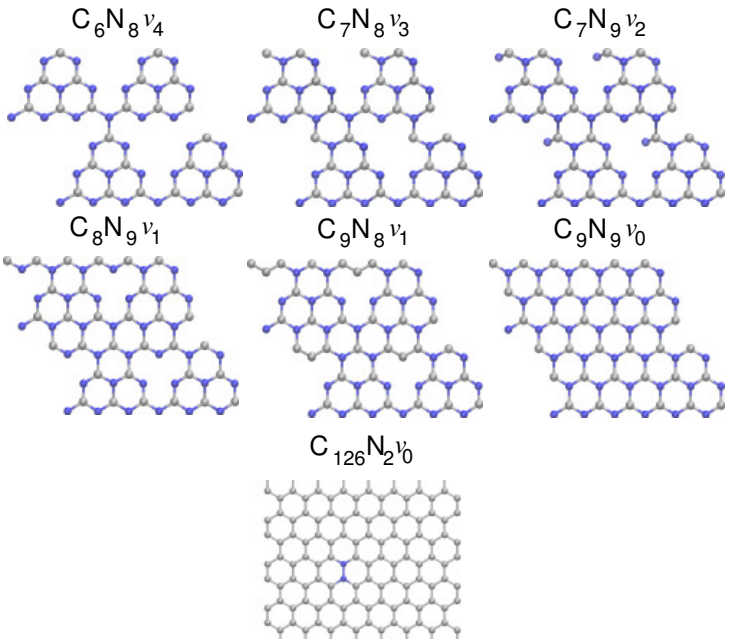

FIGURE G.2: Equilibrium geometries of the $C_xN_yv_z$ structures (shown in (2×2) unit cells) used to parametrize the bond-counting model, namely $C_6N_8v_4$, $C_7N_8v_3$, $C_7N_9v_2$, $C_8N_9v_1$, $C_9N_8v_1$, $C_9N_9v_0$, and $C_{126}N_2v_0$. C and N atoms are represented by silver and blue spheres, respectively.

$C_{126}N_2v_0$ we then obtain ϵ_{C2N3}, ϵ_{C3N1}, ϵ_{C3C2}, and ϵ_{N3N3}, respectively. In table G.1 we list the bond energies and the value of k parametrized from our calculations.

TABLE G.1: First-neighbor bond energies (in eV) and k parametrized from *ab initio* calculations.

ϵ_{C3C3}	-103.245
ϵ_{C3N3}	-141.670
ϵ_{C3N2}	-186.585
ϵ_{C2N3}	-166.611
ϵ_{C3N1}	-320.573
ϵ_{N3N3}	-178.100
ϵ_{C3C2}	-128.161
k	0.128

G.3 Formation energies within the bond-counting model

In this section we present the derivation of the formation energy per nitrogen atom of the graphitic and pyridinic N impurities. We start with the graphitic N impurities, where we write the formation energy using equations 2.2 and 2.5 as it follows

$$E_f = n_{C3C3}\epsilon_{C3C3} + n_{C3N3}\epsilon_{C3N3} + k\frac{(2n_{C3N3})^{3/2}}{\sqrt{n_{C3N3}+n_{C3C3}}} - x\mu_C - y\mu_N. \tag{G.5}$$

Since $\mu_C = \frac{3\epsilon_{C3C3}}{2}$[1], $n_{C3N3} = 3n_N = y$ and $c_N = y/(x+y)$ we obtain

$$\frac{E_f}{n_N} = 3\epsilon_{C3N3} - \mu_N + \Big[\frac{n_{C3C3}(1-c_N)}{c_N x} - \frac{3}{2}\frac{x(1-c_N)}{c_N x}\Big]\epsilon_{C3C3} + \frac{6^{3/2}k\sqrt{c_N x}}{\sqrt{3c_N x + n_{C3C3}(1-c_N)}}. \tag{G.6}$$

We now turn to the $C_{17}N_1$ structure which has one graphitic N impurity. As shown in figure G.3(a), this structure has $n_{C3C3} = 24$ (solid and dashed black lines) and $n_{C3N3} = 3$ (solid red lines). Hence, we obtain

$$\frac{E_f}{n_N} = 3\epsilon_{C3N3} - \mu_N - \frac{3}{2}\epsilon_{C3C3} + 12k\sqrt{c_N}, \tag{G.7}$$

which is equal to equation 2.6 with $A = 3\epsilon_{C3N3} - \frac{3}{2}\epsilon_{C3C3} - \mu_N$ and $B = 12k$.

For the pyridinic N impurities we apply the same procedure. From equations 2.2 and 2.5 we obtain

$$E_f = n_{C3C3}\epsilon_{C3C3} + n_{C3N2}\epsilon_{C3N2} - \frac{3x}{2}\epsilon_{C3C3} - y\mu_N + \frac{k n_{C3N2}^{3/2}}{\sqrt{n_{C3C3} + n_{C3N2}}}. \tag{G.8}$$

Considering now the $C_{14}N_3v_1$ structure (figure G.3(b)), which has one vacancy surrounded by pyridinic nitrogens, we obtain that $n_{C3C3} = 18$ (solid and dashed black lines) and $n_{C3N2} = 6$ (solid red lines). As a result, we find that for pyridinic N impurities

$$\frac{E_f}{n_N} = 2\epsilon_{C3N2} - \mu_N - \frac{81}{17}\epsilon_{C3C3} + \sqrt{\frac{17}{3}}k\sqrt{c_N}, \tag{G.9}$$

which is similar to equation 2.6 with $A = 2\epsilon_{C3N2} - \mu_N - \frac{81}{17}\epsilon_{C3C3}$ and $B = \sqrt{\frac{17}{3}}k$.

[1]Within the bond-counting model the total energy of graphene (2 atoms in the unit cell) is $E = 3\epsilon_{C3C3}$, while the carbon chemical potential is given by $\mu_C = \frac{E}{2}$ in this case.

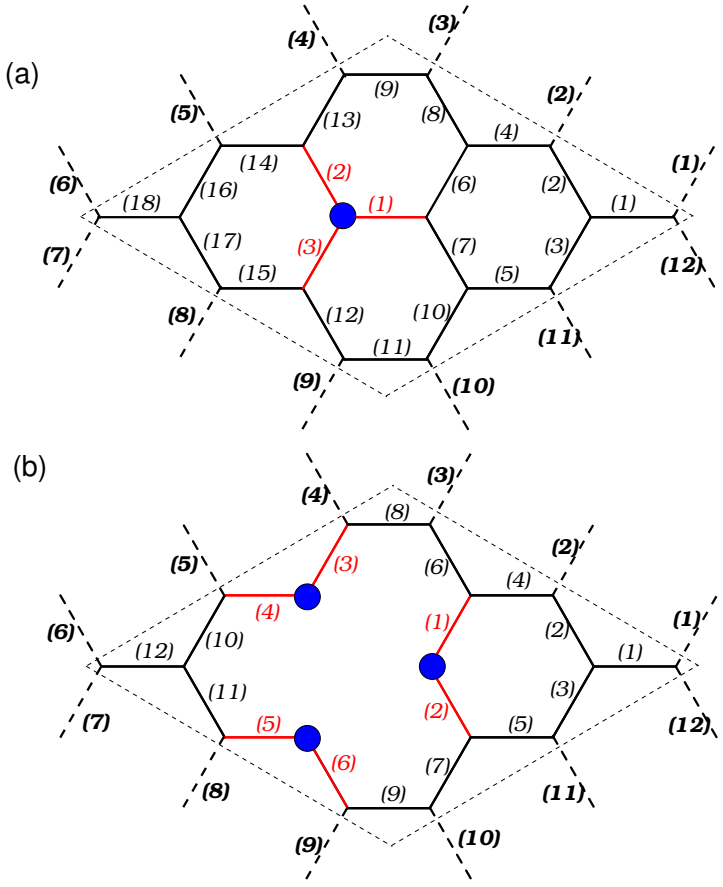

FIGURE G.3: (a) $C_{17}N_1$ and (b) $C_{14}N_3v_1$ structures showing the $C3-C3$ (solid and dashed black lines), $C3-N3$, and $C3-N2$ (red solid lines) bond-types. The numbers in parenthesis are counting index numbers of each type of bond in both structures. In (a) $n_{C3C3} = 18 + \frac{1}{2} \times 12 = 24$ and $n_{C3N3} = 3$ whereas in (b) $n_{C3C3} = 12 + \frac{1}{2} \times 12 = 18$ and $n_{C3N2} = 6$. Nitrogen atoms are represented by blue circles.

Appendix H

Ab initio calculations: technical details

In this appendix we present the technical details of each *ab initio* calculation performed in our investigations discussed in chapters 2, 3 and concerning the DFT part of calculations presented in chapter 5.

H.1 New graphene-like carbon nitride structures: energetic and electronic properties

In this investigation we performed *ab initio* calculations using the density functional theory (DFT) [21] within Perdew-Burke-Ernzerhof generalized gradient approximation (PBE-GGA) [46] as implemented in SIESTA code [51, 251, 252]. In particular, we used the spin-polarized formalism in the Fermi energy and band gap calculations. The Kohn-Sham wave functions [22] were expanded in a linear combination of numerical pseudoatomic orbitals using a double-ζ plus polarization (DZP) basis set, with an energy shift of 0.01 Ry [54]. Also, we have employed norm-conserving pseudopotentials [49] to describe the electron-ion interaction and 8 (36) special k-points in geometry (band gap) calculations to the Brillouin zone sampling [253]. All the atomic positions were fully relaxed by using the conjugated gradient scheme within a force convergence criterion of 0.02 eV/Å. All the systems were described by using periodic supercells and a vacuum space of 30 Å between the layers to avoid periodic image interactions.

H.2 Magnetic properties of graphitic carbon nitride structures

In this work we employed a similar methodology as that used in the section about the new graphene-like carbon nitride structures. However, the magnetic properties were investigated using a set of 36 special k-points and 2×2 supercells to avoid spurious effects on the magnetic properties. In addition, we investigate the stability of the ferromagnetic structures by means of first-principles molecular dynamics, by annealing the structures from 300 K to 273 K. For the distorted structures, further optimization using a conjugated gradient scheme was done. The finite temperature simulations of structures $C_8N_9v_1$, $C_9N_8v_1$, $C_9N_7v_2$, $C_6N_9v_3$, $C_6N_9v_3$, $C_{10}N_5v_3$, and $C_7N_7v_4$ only lead to out-of-plane atomic motions without any in-plane reconstruction, which resulted in structures with higher total energy than the ones previously considered. Therefore, our calculations indicate that the obtained structures are stable, and that finite temperature does not lead to any detectable effect on the net spin, the structures remaining magnetic. In contrast, for the $C_6N_{10}v_2$ structure the finite temperature simulations lead to a rupture of a N-N chemical bond, giving rise to in-plane reconstructions. For this new structure, we performed further relaxation using the conjugated gradient scheme, obtaining a more stable structure than the one previously obtained by us. For this new structure we obtained a nonmagnetic phase as the most stable one.

H.3 Point defects in Teflon crystals

Our DFT calculations were performed within PWscf code, which is part of Quantum Espresso package [254]. Within these calculations, the Kohn-Sham eigenstates are spanned in a plane-wave basis set, with an energy cutoff of 48 Ry. The structural optimizations were performed by using *van der Waals* functionals [255, 256] to treat the electron-electron interactions. The structures were relaxed until the residual forces become smaller than 0.025 eV/Å in each atom, with the usage of 2 k special points. To study the electronic and magnetic properties we employed the GGA functional as parametrized by Perdew-Burke-Ernzerhof [46]. To describe the electron-ion interaction

we used ultrasoft pseudopotentials [257], where we employed 24 k-points in our calculations.

H.4 Metal-Insulator transitions in VO_2 and NbO_2

We performed fully all-electron self-consistent DFT+DMFT calculations, with implementation described in Ref. [28]. We included dynamic correlations within single-site and cluster-DMFT approaches, for the R and monoclinic phases, respectively. Within our calculations, we obtain the electronic charge density, chemical potential, impurity levels, self-energy (Σ), and Green's function self-consistently. The all-electron DFT calculations were performed within Perdew-Burke-Ernzerhof generalized gradient approximation (PBE-GGA) [46], as implemented in Wien2K code [58]. The quantum impurity problem was solved by means of Continuous time quantum Monte Carlo (CTQMC) (see appendix F) calculations [41], at fixed distinct temperatures for R and monoclinic phases. To compute the self-energy on the real frequency axis we performed analytic continuation using the maximum entropy method as described in Ref. [28]. Throughout our calculations we employed the Coulomb interaction $U = 6.0$ eV and Hund's coupling $J = 1.0$ eV. We have also used the local axis system proposed by Eyert [188], wherein the $d_{x^2-y^2}$ orbitals mediate the σ-type $d-d$ overlap along the rutile c axis, while the remaining t_{2g} orbitals, *i. e.* d_{xz} and d_{yz}, mediate the π-type $d-d$ overlap. In our notation, the former is denoted as a_{1g} and the latter as the doubly degenerated e_g^π states. In particular, in our investigation $\{e_g^\pi(1), e_g^\pi(2)\}$ denotes the $\{d_{xz}, d_{yz}\}$ and $\{d_{yz}, d_{xz}\}$ orbitals in R and M_1 phase, respectively. Finally, in our calculations only the t_{2g} states were considered in the impurity model, while the remaining e_g^σ states were treated within DFT (GGA).

Appendix I

Peierls, Slater, and Mott-Hubbard insulators

In this appendix we introduce the different types of insulators discussed in chapters 4 and 5 of this thesis. We start by the Peierls and Slater insulators, which are band-type insulators, and then we present the so-called Mott-Hubbard insulator which appears due to strong electron-electron interactions.

Peierls and Slater insulators.– Let us suppose we have an one-dimensional system of equidistant atoms with a distance a. In addition, we consider that each atom has one single electron, i.e. they are monovalent atoms. Within a tight-binding approximation, the energy band of this system is given by

$$\epsilon(k) = -2t\cos(ka), \tag{I.1}$$

where t is the hopping amplitude between neighbouring atoms. For this system the Brillouin zone boundaries are $\pm\frac{\pi}{a}$, the Fermi wavevector is $k_F = \pm\frac{\pi}{2a}$ and we have a partly filled band (see figure I.1(a)), characteristic of an one-dimensional conductor.

We now suppose that the atoms dimerize in pairs in such a way that the lattice periodicity becomes $2a$, as illustrated in figure I.1(b). Due to this new periodicity, the Brillouin zone boundaries become $\pm\frac{\pi}{2a}$ which coincide with the Fermi wavevector. In this case, it can be shown [2, 258] that the periodic lattice potential leads to a gap opening at the Brillouin zone boundaries as shown in figure I.1(d). Therefore, as a result of

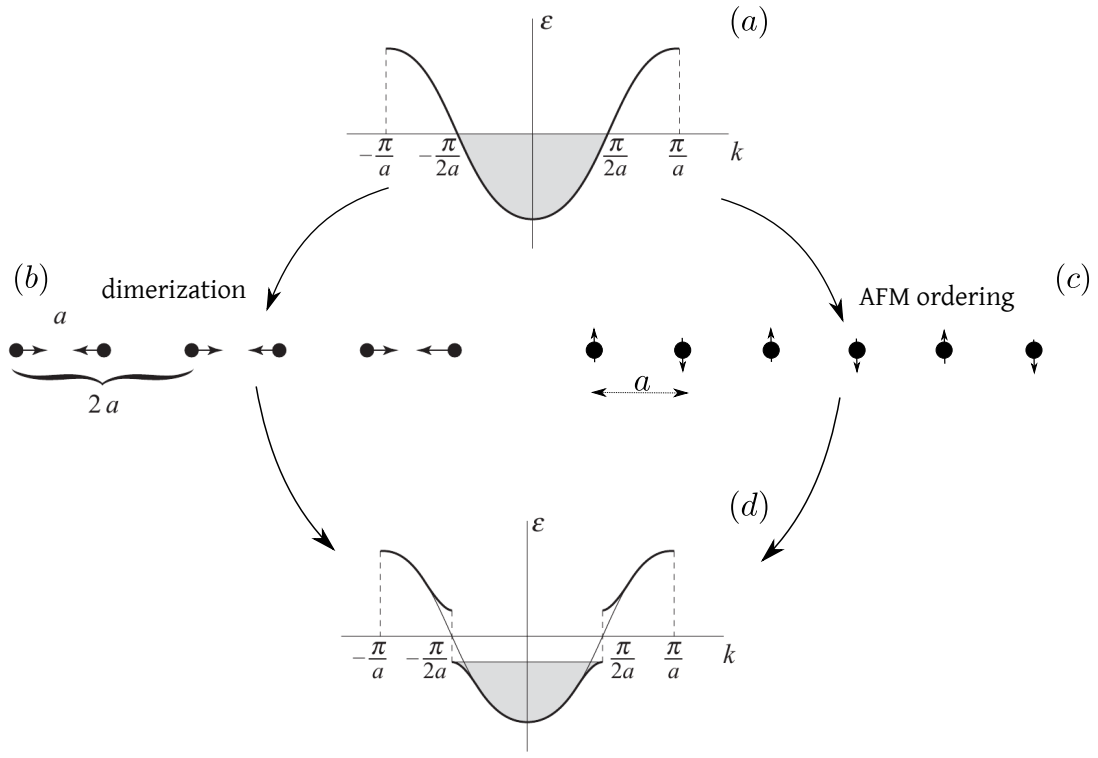

FIGURE I.1: (a) Energy band of an one-dimensional conductor, (b) pairing of monovalent atoms, (c) antiferromagnetic ordering of monovalent atoms, and (d) energy bands of a one-dimensional insulator. Figures (a), (b), and (c) were taken from Ref. [258].

the chain dimerization, the one-dimensional system of monovalent atoms turns into an one-dimensional insulator (Peierls insulator). Rudolf Peierls was the first to point out that the electronic energy gain due to the dimerization of the one-dimensional chain exceeds the associated increase of elastic energy [259]. This indicates that an equally spaced lattice of monovalent atoms is unstable with respect to dimerization (Peierls instability), that is, its dimerization (Peierls transition) is an energetically favourable process. For more details see Ref. [258].

We now suppose that instead of the lattice dimerization our one-dimensional system develops a magnetic ordering with antiparallel spins, as shown in figure I.1(c). As discussed by Slater in 1951 [260] this antiferromagentic ordering leads to a spin-dependent lattice potential of period $2a$, which accounts for the direct and exchange interactions between electrons, in addition to the Weiss molecular field interaction [261]. This new periodicity leads to a system with Brillouin zone boundaries at $\pm\frac{\pi}{2a}$, which coincide with the Fermi wavevector. As discussed above, this lattice potential leads to the appearance of a band gap at the Brillouin zone boundaries, as shown in figure I.1(d). Therefore,

the estabilishment of an antiferromagentic ordering leads to an insulating antiferromagnetic system (Slater insulator). We mention that both Peierls and Slater transitions are the result of instabilities of the Fermi liquid, in which there is perfect Fermi surface nesting [258][1]. It is also important to emphasize that the Peierls transition occurs due to electron-lattice interactions while the Slater transition due to electron-electron interactions.

Mott-Hubbard insulator.– The transitions discussed above, and schematically shown in figure I.1, are examples of metal-insulator transitions in weakly-correlated systems. On the other hand, strong electronic correlations can also give rise to insulating phases. Let us suppose a system described by the following Hamiltonian (Hubbard model)

$$H = -t \sum_{ij,\sigma} c^{\dagger}_{i\sigma} c_{j\sigma} + U \sum_{i} n_{i\uparrow} n_{i\downarrow}, \tag{I.2}$$

where t is the hopping amplitude between neighbouring sites while U is the on-site electron-electron Coulomb interaction. $c^{\dagger}_{i\sigma}$ ($c_{i\sigma}$) creates (annihilates) an electron with spin σ in the site i and $n_{i\sigma}$ is the corresponding occupation number. In addition, we consider that in our system there is one electron per site (half-filled band). The first term in equation I.2 describes the kinetic energy of the electrons whereas the second term the interaction energy between them.

In the weakly correlated regime, in which $t \gg U$, the electrons are highly itinerant and act like Bloch electrons with energy dispersion $\epsilon(k) = -2t(cosk_x + cosk_y + cosk_z)$ for a three-dimensional cubic lattice with lattice parameter $a = 1$. In this case, the band is half-filled accounting for a metallic system. However, once the interaction between electrons exceeds their kinetic energy, i.e $U \gg t$, the electrons localize in their own sites in order to minimize the Coulomb repulsion between them. As a result, the system becomes an insulator, the so-called Mott-Hubbard insulator. The energy gap (charge gap) in this system, considering $t \neq 0$, is then given by $U - W$, where W is half of the Hubbard bandwidth. We mention that metal-insulator transitions associated with the metallic and Mott insulating phases can be triggered by changes in $\frac{t}{U}$. In figure I.2 we illustrate the Mott-Hubbard transition and the band diagrams corresponding to a Mott-Hubbard insulator.

[1]The Fermi surface nesting is associated with the existence of wavevectors which connect parallel regions of the Fermi surface.

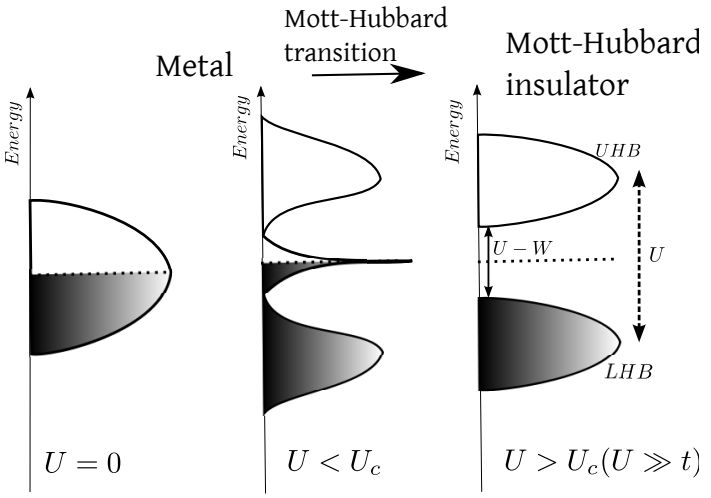

FIGURE I.2: Representation of the energy bands in a Mott-Hubbard transition within DMFT. In the left and center we show partly filled bands of a metallic system. In the right we present the band diagrams of a Mott-Hubbard insulator showing the lower Hubbard band (LHB) and the upper Hubbard band (UHB).

Appendix J

Effective band structure and Spectral Function

In this appendix we introduce the concepts of the an effective band structure and the spectral function used in chapter 5.

J.1 Effective band structure

The excitation spectrum of a solid is of great value to investigate its electronic structure and the electronic correlations between its electrons. In this respect, the excitation energies of numerous weakly correlated solids have been interpreted by using the Kohn-Sham eigenvalues, which in turn are not true excitation energies of the system [23]. In fact, the excitation energies of an interacting Fermi liquid can be obtained from the poles of the corresponding Green's function [17].

Let us suppose a Green's function of the following form

$$G_{loc}(\omega) = \sum_{\mathbf{k}} \frac{1}{\omega + \mu - H_{\mathbf{k}} - \Sigma(\omega)}, \tag{J.1}$$

where μ is the chemical potential, $H_{\mathbf{k}}$ is the noninteracting Hamiltonian, and $\Sigma(\omega)$ is the energy dependent self-energy.[1] Taking the limit $\Im\Sigma \approx 0$ (Fermi liquid behavior),

[1] The $\mathbf{k}$ dependence of the self-energy was neglected.

the **k**-resolved excitation energies are given by [240]

$$\det(\omega_{\mathbf{k}} + \mu - H_{\mathbf{k}} - \Re\Sigma(\omega_{\mathbf{k}})) = 0. \tag{J.2}$$

In one-band case this equation reduces to

$$\omega_{\mathbf{k}} + \mu - \epsilon_{\mathbf{k}} - \Re\Sigma(\omega_{\mathbf{k}}) = 0, \tag{J.3}$$

which is not an eigenvalue problem since $\Re\Sigma$ depends on $\omega_{\mathbf{k}}$.

As shown by Tomczak and Biermann [240], different approaches can be used to obtain the excitation energies $\omega_{\mathbf{k}}$, by solving equations J.2 or J.3. For instance, one can linearize the $\Re\Sigma(\omega_{\mathbf{k}})$ to first order

$$\Re\Sigma(\omega_{\mathbf{k}}) = \Re\Sigma(0) + \frac{\partial\Re\Sigma(\omega)}{\partial\omega}\Big|_{\omega=0}\omega_{\mathbf{k}}. \tag{J.4}$$

As a result, equation J.3 becomes

$$\omega_{\mathbf{k}} + Z(\mu - \epsilon_{\mathbf{k}} - \Re\Sigma(0)) = 0, \tag{J.5}$$

where we used $Z = \left(1 - \frac{\partial\Re\Sigma(\omega)}{\partial\omega}\Big|_{\omega=0}\right)^{-1}$. Likewise, the renormalized band structure (correlated band structure) is then given by

$$\det(\omega_{\mathbf{k}} + Z[\mu - H_{\mathbf{k}} - \Re\Sigma(0)]) = 0. \tag{J.6}$$

J.2 Spectral Function

The spectral function of a solid is of great value since it can be compaired to ARPES measurements [262, 263]. It is defined as

$$A(\mathbf{k},\omega) = -\frac{1}{\pi}\Im G(\mathbf{k},\omega), \tag{J.7}$$

where $G(\mathbf{k},\omega)$ is the one-electron Green's function.

Let us first consider a noninteracting system, for which $G(\mathbf{k},\omega) = 1/(\omega - \epsilon_{\mathbf{k}} \pm i\eta)$. The spectral function is then composed by delta functions, $A(\mathbf{k},\omega) = \delta(\omega - \epsilon_{\mathbf{k}})$, at each

band energy $\epsilon_{\mathbf{k}}$. If we now assume an interacting system, we can express the one-electron Green's function in terms of the self-energy $\Sigma(\mathbf{k},\omega)$ as follows

$$G(\mathbf{k},\omega) = \frac{1}{\omega - \epsilon_{\mathbf{k}} - \Sigma(\mathbf{k},\omega)}. \tag{J.8}$$

Therefore, for an interacting system the spectral function is given by

$$A(\mathbf{k},\omega) = -\frac{1}{\pi}\frac{\Im\Sigma(\mathbf{k},\omega)}{[\omega - \epsilon_{\mathbf{k}} - \Re\Sigma(\mathbf{k},\omega)]^2 + [\Im\Sigma(\mathbf{k},\omega)]^2}. \tag{J.9}$$

If we consider that the excitations of the interacting system are described by renormalized quasiparticles, one can show that the spectral function turns into [262]

$$A(\mathbf{k},\omega) = Z_{\mathbf{k}}\frac{\Gamma_{\mathbf{k}}}{(\omega - \epsilon^q_{\mathbf{k}})^2 + \Gamma^2_{\mathbf{k}}}, \tag{J.10}$$

in the proximity to the Fermi surface. The quasiparticle weight in equation J.10 is given by $Z_{\mathbf{k}} = \left(1 - \frac{\partial\Re\Sigma(\mathbf{k},\omega)}{\partial\omega}\big|_{\omega=\epsilon^q_{\mathbf{k}}}\right)^{-1}$, $\Gamma_{\mathbf{k}} = Z_{\mathbf{k}}|\Im\Sigma(\mathbf{k},\epsilon^q_{\mathbf{k}})|$, and the renormalized quasiparticle energy is $\epsilon^q_{\mathbf{k}} = Z_{\mathbf{k}}(\epsilon_{\mathbf{k}} - \Re\Sigma(\mathbf{k},\epsilon^q_{\mathbf{k}}))$. The finite lifetime of excitations can be defined by $\tau_{\mathbf{k}} = 1/\Gamma_{\mathbf{k}}$. It is worthy mentioning that the many-body effective mass (m^*) is given by [264]

$$m^* = \frac{m_{band}}{Z_{\mathbf{k}}\left(1 + \frac{m_{band}}{k_F}\frac{\partial\Re\Sigma(\mathbf{k},\epsilon^q_{\mathbf{k}})}{\partial k}\Big|_{k=k_F}\right)}, \tag{J.11}$$

where m_{band} is the bare band mass of noninteracting Bloch electrons.

By comparing the spectral function J.10 with that of a noninteracting system ($A(\mathbf{k},\omega) = \delta(\omega - \epsilon_{\mathbf{k}})$) we observe that electron-electron interactions have important effects on the spectral function. In particular, one can notice that sharp excitations represented by delta functions turn into Lorentzians centered at $\epsilon^q_{\mathbf{k}}$ with width given by $2\Gamma_{\mathbf{k}}$ (see figure J.1). Therefore, the electronic correlations lead to a renormalization of the bare band energy as well as a broadening of excitations due to finite lifetime effects.

Finally, we mention that besides the coherent form of the spectral function expressed in equation J.10, there are also contributions which come from the part without poles of the full Green's function. By taking to account this incoherent part the spectral function turns into $A(\mathbf{k},\omega) = Z_{\mathbf{k}}\frac{\Gamma_{\mathbf{k}}}{(\omega-\epsilon^q_{\mathbf{k}})^2+\Gamma^2_{\mathbf{k}}} + A_{incoh.}$. We emphasize that this incoherent part does not depend on $\mathbf{k}$ and in strongly correlated systems is associated with the presence

of Hubbard bands in the spectrum. In figure J.1 we schematically illustrate the spectral functions of a noninteracting and of an interacting system.

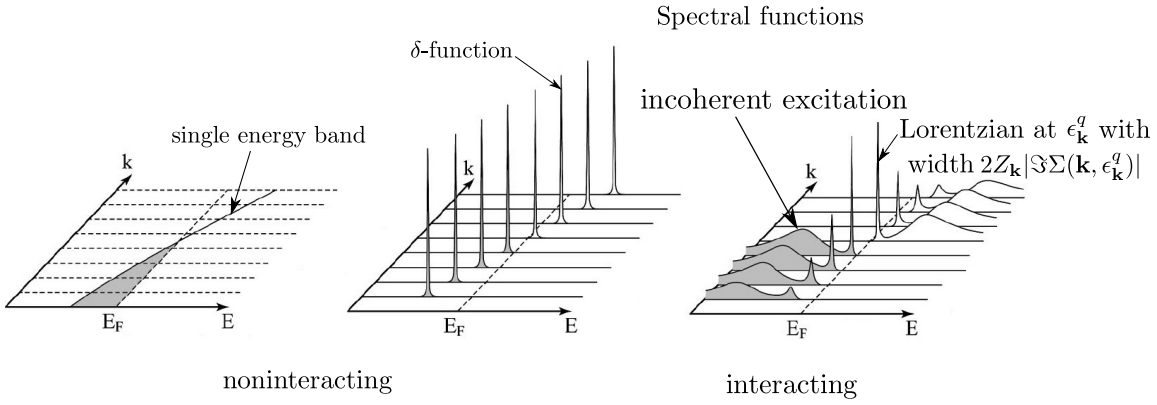

FIGURE J.1: Scheme showing the spectral function of noninteracting and interacting systems. Adapted from Ref. [263].

Appendix K

Local and intersite self-energies

Within our approach the cluster self-energy is diagonal in the momentum basis, with (diagonal) elements given by $\Sigma_{K=0}$ and $\Sigma_{K=\pi}$, due to the neglect of intercluster self-energies. The cluster self-energy in the site representation contains, on the other hand, the local and intersite self-energies in the following form

$$\Sigma_c = \begin{pmatrix} \Sigma_{11} & \Sigma_{12} \\ \Sigma_{21} & \Sigma_{22} \end{pmatrix}.$$

Using the cluster symmetry one can notice that $\Sigma_{11} = \Sigma_{22}$ and $\Sigma_{12} = \Sigma_{21}$, where the former is the local self-energy and the latter the intersite self-energy. By means of a Fourier transform one can obtain the self-energy in the momentum basis from the local and intersite self-energies [238],

$$\Sigma_K = \frac{1}{N_c} \sum_{i,j} \Sigma_{ij} e^{iK(R_i - R_j)}, \tag{K.1}$$

where N_c is the number of sites within the cluster, K is the cluster momentum, and $R_{i,j}$ denote the sites within the cluster. In our cluster we have $R = 0, 1$ and $K = 0, \pi$. Thus, one obtain that

$$\Sigma_{K=0} = \Sigma_{11} + \Sigma_{12}, \tag{K.2}$$

and

$$\Sigma_{K=\pi} = \Sigma_{11} - \Sigma_{12}. \tag{K.3}$$

Based on the molecular scenario with bonding and antibonding orbitals, we change the names of $\Sigma_{K=0}$ and $\Sigma_{K=\pi}$ to bonding (Σ_b) and antibonding (Σ_{ab}) self-energies, respectively. Therefore, the two previous equations lead to the following linear relations:

$$\Sigma_{11} = \frac{1}{2}(\Sigma_b + \Sigma_{ab}), \tag{K.4}$$

$$\Sigma_{12} = \frac{1}{2}(\Sigma_b - \Sigma_{ab}), \tag{K.5}$$

which are used in our investigation.

Bibliography

[1] A. Rockett. *The Materials Science of Semiconductors.* Springer, 2008.

[2] C. Kittel. *Introduction to Solid State Physics.* John Wiley & Sons, 1996.

[3] J. M. Ziman. *Principles Of The Theory of Solids.* Cambridge University Press, 1999.

[4] D. L. Cox and D. Pines. Complex Adaptive Matter: Emergent Phenomena in Materials. *MRS Bulletin*, 30:425–432, 2005.

[5] M. L. Cohen. The Theory of Real Materials. *Annu. Rev. Mater. Sci.*, 30:1–26, 2000.

[6] J. M. D. Coey. d^0 ferromagnetism. *Solid State Sci.*, 7:660–667, 2005.

[7] T. L. Makarova and F. Palacio. *Carbon-based Magnetism: An overview of Metal Free Carbon-based Compounds and Materials.* Elsevier, 2006.

[8] S. A. Khatipov, R. N. Nurmukhametov, D. I. Seliverstov, and A. M. Sergeev. Spectrophotometric and luminescent analysis of polytetrafluoroethylene treated by γ-irradiation near the melting point. *Polymer Science Series A*, 48:153–158, 2006.

[9] A. Georges. Strongly Correlated Electron Materials: Dynamical Mean-Field Theory and Electronic Structure. In A. Avella and F. Mancini, editors, *Lectures on the Physics of Highly Correlated Electron Systems VIII.* AIP Conference Proceedings, 2004.

[10] A. Georges, G. Kotliar, W. Krauth, and M. J. Rozenberg. Dynamical mean-field theory of strongly correlated fermion systems and the limit of infinite dimensions. *Rev. Mod. Phys.*, 68:13–125, 1996.

[11] G. Kotliar, S. Y. Savrasov, K. Haule, V. S. Oudovenko, O. Parcollet, and C. A. Marianetti. Electronic structure calculations with dynamical mean-field theory. *Rev. Mod. Phys.*, 78:865–951, 2006.

[12] V. Anisimov and Y. Yzyumov. *Electronic Structure of Strongly Correlated Materials.* Springer-Verlag, 2010.

[13] J. B. Goodenough. The two components of the crystallographic transition in VO_2. *Journal of Solid State Chemistry*, 3:490–500, 1971.

[14] A. Zylbersztejn and N. F. Mott. Metal-insulator transition in vanadium dioxide. *Phys. Rev. B*, 11:4383–4395, 1975.

[15] T. M. Rice, H. Launois, and J. P. Pouget. Comment on "VO_2: Peierls or Mott-Hubbard? A View from Band Theory". *Phys. Rev. Lett.*, 73:3042–3042, 1994.

[16] A. Tsvelik. *Quantum Field Theory in Condensed Matter Physics.* Cambridge, 2003.

[17] P. Coleman. *Introduction to Many Body Physics.* Cambridge, 2015.

[18] A. Altland and B. Simons. *Condensed Matter Field Theory.* Cambridge, 2006.

[19] C.-H. Yee. *Towards an ab initio description of correlated materials.* PhD thesis, Rutgers University, 2012.

[20] J. R. Chelikowsky and S. G. Louie. *Quantum Theory of Real Materials.* Kluwer Academic Publishers, 1996.

[21] P. Hohenberg and W. Kohn. Inhomogeneous Electron gas. *Phys. Rev.*, 136:B864, 1964.

[22] W. Kohn and L. J. Sham. Self-consistent equations including exchange and correlation effects. *Phys. Rev.*, 140:A1133, 1965.

[23] R. M. Martin. *Electronic Structure: Basic Theory and Practical Methods.* Cambridge University Press, 2008.

[24] K. Capelle. A Bird's-Eye View of Density-Functional Theory. *Braz. J. Phys.*, 36: 1318, 2006.

[25] G. Kotliar and S. Y. Savrasov. *New Theoretical Approaches to Strongly Correlated Systems*, chapter 10, pages 259–301. Kluwer Academic, 2001.

[26] V. Anisimov, A. Poteryaev, M. Korotin, A. Anokhin, and G. Kotliar. First-principles calculations of the electronic structure and spectra of strongly correlated systems: dynamical mean-field theory. *J. Phys.: Condens. Matter*, 9:7359, 1997.

[27] V. Anisimov, J. Zaanen, and O. K. Andersen. Band Theory and Mott insulators: Hubbard U instead of Stoner I. *Phys. Rev. B*, 44:943, 1991.

[28] K. Haule, C.-H. Yee, and K. Kim. Dynamical mean-field theory within the full-potential methods: Electronic structure of $CeIrIn_5$, $CeCoIn_5$, and $CeRhIn_5$. *Phys. Rev. B*, 81:195107, 2010.

[29] P. Phillips. *Advanced Solid State Physics.* Westview Press, 2003.

[30] A. C. Hewson. *The Kondo Problem to Heavy Fermions.* Cambridge, 2003.

[31] V. I. Anisimov, I. V. Solovyev, M. A. Korotin, M. T. Czyżuk, and G. A. Sawatzky. Density-functional theory and NiO photoemission spectra. *Phys. Rev. B*, 48:16929, 1993.

[32] G. A. Sawatzky and J. W. Allen. Magnitude and Origin of the Band gap in NiO. *Phys. Rev. Lett.*, 53:2339, 1984.

[33] D. van der Marel. *The electronic structure of embedded transition metal atoms.* PhD thesis, Rijksuniversiteit Groningen, 1985.

[34] J. K. Lang, Y. Baer, and P. A. Cox. Study of the 4f and valence band density of states in rare-earth metals: II. Experiment and results. *J. Phys. F: Metal Phys.*, 11:121, 1981.

[35] A. Kutepov, K. Haule, S. Y. Savrasov, and G. Kotliar. Self-consistent *GW* determination of the interaction strenght: Application to the iron arsenide superconductors. *Phys. Rev. B*, 82:045105, 2010.

[36] L. Vaugier, H. Jiang, and S. Biermann. Hubbard U and Hund exchange J in transition metal oxides: Screening versus localization trends from constrained random phase approximation. *Phys. Rev. B*, 86:165105, 2012.

[37] V. I. Anisimov and O. Gunnarsson. Density-functional calculation of effective Coulomb interactions in metals. *Phys. Rev. B*, 43:7570, 1991.

[38] M. T. Czyżuk and G. A. Sawatzky. Local-density functional and on-site correlations: The electronic structure of La_2CuO_4 and $LaCuO_3$. *Phys. Rev. B*, 49:14211, 1994.

[39] K. Haule. Exact Double Counting in Combining the Dynamical Mean Field Theory and the Density Functional Theory. *Phys. Rev. Lett.*, 115:196403, 2015.

[40] P. Werner, A. Comanac, L. de' Medici, M. Troyer, and A. Millis. Continuous-Time Solver for Quantum Impurity Models. *Phys. Rev. Lett.*, 97:076405, 2006.

[41] K. Haule. Quantum Monte Carlo impurity solver for cluster dynamical mean-field theory and electronic structure calculations with adjustable cluster base. *Phys. Rev. B*, 75:155113, 2007.

[42] R. G. Parr and W. Yang. *Density-Functional Theory of atoms and Molecules.* Oxford University Press, 1989.

[43] D. M. Ceperley and J. Alder. Ground State of the Electron Gas by a Stochastic Method. *Phys. Rev. Lett.*, 45:566, 1980.

[44] J. P. Perdew and A. Zunger. Self-interaction correction to density-functional approximations for many-electron systems. *Phys. Rev. B*, 23:5048, 1981.

[45] J. Kohanoff. *Electronic Structure Calculations for Solids and Molecules: Theory and Computational Methods.* Cambridge University Press, 2006.

[46] J. P. Perdew, K. Burke, and M. Ernzerhof. Generalized Gradient Approximation Made Simple. *Phys. Rev. Lett.*, 77:3865, 1996.

[47] M. C. Payne, M. P. Teter, D. C. Allan, T. A. Arias, and J. D. Joannopoulos. Iterative minimization techniques for ab initio total-energy calculations: molecular dynamics and conjugate gradients. *Rev. Mod. Phys.*, 64:1045, 1992.

[48] G. B. Bachelet, D. R. Hamann, and M. Schluter. Pseudopotentials that work: From H to Pu. *Phys. Rev. B*, 26:4199, 1982.

[49] N. Troullier and J. L. Martins. Efficient pseudopotentials for plane-wave calculations. *Phys. Rev. B*, 43:1993, 1991.

[50] D. Vanderbilt. Soft self-consistent pseudopotentials in a generalized eigenvalue formalism. *Phys. Rev. B*, 41:7892, 1990.

[51] J. M. Soler, E. Artacho, J. D. Gale, A. García, J. Junquera, P. Ordejón, and D. Sánchez-Portal. The SIESTA method for ab-initio order-N materials simulation. *J. Phys.: Condens. Matter*, 14:2745, 2002.

[52] E. Kaxiras. *Atomic and Electronic Structure of Solids.* Cambridge University Press, 2003.

[53] A. Fazzio, J. D. Vianna, and S. Canuto. *Teoria Quântica de Moléculas e Sólidos: Simulação Computacional.* Livraria da Física, 2004.

[54] J. Junquera, Ó. Paz, D. Sánchez-Portal, and E. Artacho. Numerical atomic orbitals for linear-scaling calculations. *Phys. Rev. B*, 64:235111, 2001.

[55] E. Artacho, D. Sánchez-Portal, P. Ordejón, A. García, and J. M. Soler. Linear-Scaling ab-initio Calculations for Large and Complex Systems. *Phys. Stat. Sol. B*, 215:809, 1999.

[56] N. A. W. Holzwarth, G. E. Matthews, R. B. Dunning, A. R. Tackett, and Y. Zeng. Comparison of the projector augmented-wave, pseudopotential, and linearized augmented-plave-wave formalism from density-functional calculations of solids. *Phys. Rev. B*, 55:2005, 1997.

[57] D. J. Singh and L. Nordström. *Planewaves, Pseudopotentials and the LAPW Method.* Springer, 2006.

[58] P. Blaha, K. Scwarz, G. Madsen, D. Krasnicka, and J. Luitz. *WIEN2K, An Augmented Plane Wave + Local Orbitals Program for Calculating Crystal Properties*, 2012.

[59] G. K. Madsen, P. Blaha, K. Schwarz, E. Sjöstedt, and L. Nordström. Efficient linearization of the augmented plane-wave method. *Phys. Rev. B*, 64:195134, 2001.

[60] A. Y. Liu and M. L. Cohen. Prediction of New Low Compressibility Solids. *Science*, 245:841–842, 1989.

[61] Y. Guo and W. A. Goddard III. Is carbon nitride harder than diamond? No, but its girth increases when stretched (negative Poisson ratio). *Chem. Phys. Lett.*, 237:72–76, 1995.

[62] A. Y. Liu and R. M. Wentzcovitch. Stability of carbon nitride solids. *Phys. Rev. B*, 50:10362, 1994.

[63] D. M. Teter and R. J. Hemley. Low-Compressibility Carbon Nitrides. *Science*, 271:53–55, 1996.

[64] E. Kroke and M. Schwarz. Novel Group 14 nitrides. *Coord. Chem. Rev.*, 248: 493–532, 2004.

[65] M. L. Cohen. Structural, Electronic and Optical Properties of Carbon Nitride. *Mater. Sci. Eng. A*, 209:1–4, 1996.

[66] Y. F. Lu, Z. M. Ren, W. D. Song, and D. S. H. Chan. Electronic and Optical Properties of Carbon Nitride Thin Films Synthesized by Laser Ablation Under Ion Beam Bombardment. *J. Appl. Phys.*, 84:2133–2137, 1998.

[67] G. Goglio, D. Foy, and G. Demazeau. State of Art and recent trends in bulk carbon nitrides synthesis. *Mater. Sci. Eng., B*, 58:195–227, 2008.

[68] S. Matsumoto, E. Q. Xie, and F. Izumi. On the validity of the formation of crystalline carbon nitrides, C_3N_4. *Diamond and Related Materials*, 8:1175–1182, 1999.

[69] T. Malkow. Critical observations in the research of carbon nitride. *Materials Science and Engineering: A*, 292:112–124, 2000.

[70] Z.-M. Ren, Y.-C. Du, Y. Qiu, J.-D. Wu, Z.-F. Ying, X.-X. Xiong, and F.-M. Li. Carbon nitride films synthesized by combined ion-beam and laser-ablation processing. *Phys. Rev. B*, 51:5274–5277, 1995.

[71] X. W. Su, H. W. Song, F. Z. Cui, and W. Z. Li. Observations of Laue pattern and stability of beta-C_3N_4 grains. *J. Phys.: Condens. Matter*, 7:L517, 1995.

[72] Y. Zhang, H. Gao, and Y. Gu. Structure studies of C_3N_4 thin films prepared by microwave plasma chemical vapour deposition. *J. Phys. D: Appl. Phys.*, 34: 299–302, 2001.

[73] D. G. Liu, J. P. Tu, R. Chen, and C. D. Gu. Microstructure, corrosion resistance and biocompatibility of titanium incorporated amorphous carbon nitride films. *Surface and Coatings Technology*, 206:165–171, 2011.

[74] J. Kouvetakis, R. B. Kaner, M. L. Sattler, and N. Bartlett. A Novel Graphite-like Material of Composition BC_3, and Nitrogen-Carbon Graphites. *J. Chem. Soc., Chem. Commun.*, pages 1758–1759, 1986.

[75] T. Sekine, H. Kanda, Y. Bando, M. Yokoyama, and K. Hojou. A graphitic carbon nitride. *J. Mater. Sci. Lett.*, 9:1376–1378, 1990.

[76] J. Kouvetakis, M. Todd, B. Wilkens, A. Bandari, and N. Cave. Novel Synthetic Routes to Carbon-Nitrogen Thin Films. *Chemistry of Materials*, 6:811–814, 1994.

[77] G. Algara-Siller, N. Severin, S. Y. Chong, T. Björkman, R. G. Palgrave, A. Laybourn, M. Antonietti, Y. Z. Khimyak, A. V. Krasheninnikov, J. P. Rabe, U. Kaiser, A. I. Cooper, A. Thomas, and M. J. Bojdys. Triazine-Based Graphitic Carbon Nitride: a Two-Dimensional Semiconductor. *Angewandte Chemie International Edition*, 53:7450–7455, 2014.

[78] Y. Wang, X. Wang, and M. Antonietti. Polymeric Graphitic Carbon Nitride as a Heterogeneous Organocatalyst: From Photochemistry to Multipurpose Catalysis to Sustainable Chemistry. *Angewandte Chemie International Edition*, 51:68–89, 2012.

[79] Q. Guo, Q. Yang, C. Yi, L. Zhu, and Y. Xie. Synthesis of carbon nitrides with graphite-like or onion-like lamellar structures via a solvent-free route at low temperatures. *Carbon*, 43:1386–1391, 2005.

[80] J. S. Lee, X. Wang, H. Luo, and S. Dai. Fluidic Carbon Precursors for Formation of Functional Carbon under Ambient Pressure Based on Ionic Liquids. *Advanced Materials*, 22:1004–1007, 2010.

[81] Y. Gu, L. Chen, L. Shi, J. Ma, Z. Yang, and Y. Qian. Synthesis of C_3N_4 and graphite by reacting cyanuric chloride with calcium cyanamide. *Carbon*, 41:2674–2676, 2003.

[82] F. Goettmann, A. Fischer, M. Antonietti, and A. Thomas. Chemical Synthesis of Mesoporous Carbon Nitrides Using Hard Templates and Their Use as a Metal-Free Catalyst for FriedelCrafts Reaction of Benzene. *Angewandte Chemie International Edition*, 45:4467–4471, 2006.

[83] S. C. Yan, Z. S. Li, and Z. G. Zou. Photodegradation Performance of g-C_3N_4 Fabricated by Directly Heating Melamine. *Langmuir*, 25:10397–10401, 2009.

[84] J. Oh, S. Lee, K. Zhang, J. O. Hwang, J. Han, G. Park, S. O. Kim, J. H. Park, and S. Park. Graphene oxide-assisted production of carbon nitrides using a solution process and their photocatalytic activity. *Carbon*, 66:119–125, 2014.

[85] L. Qu, Y. Liu, J.-B. Baek, and L. Dai. Nitrogen-Doped Graphene as Efficient Metal-Free Electrocatalyst for Oxygen Reduction in Fuel Cells. *ACS Nano*, 4: 1321–1326, 2010.

[86] Z. Luo, S. Lim, Z. Tian, J. Shang, L. Lai, B. MacDonald, C. Fu, Z. Shen, T. Yu, and J. Lin. Pyridinic N doped graphene: synthesis, electronic structure, and electrocatalytic property. *J. Mater. Chem.*, 21:8038–8044, 2011.

[87] H. M. Jeong, J. W. Lee, W. H. Shin, Y. J. Choi, H. J. Shin, J. K. Kang, and J. W. Choi. Nitrogen-Doped Graphene for High-Performance Ultracapacitors and the Importance of Nitrogen-Doped Sites at Basal Planes. *Nano Letters*, 11:2472–2477, 2011.

[88] H. Wang, T. Maiyalagan, and X. Wang. Review on Recent Progress in Nitrogen-Doped Graphene: Synthesis, Characterization, and Its Potential Applications. *ACS Catalysis*, 2:781–794, 2012.

[89] T. Schiros, D. Nordlund, L. Pálová, D. Prezzi, L. Zhao, K. S. Kim, U. Wurstbauer, C. Gutiérrez, D. Delongchamp, C. Jaye, D. Fischer, H. Ogasawara, L. G. M. Pettersson, D. R. Reichman, P. Kim, M. S. Hybertsen, and A. N. Pasupathy. Connecting Dopant Bond Type with Electronic Structure in N-Doped Graphene. *Nano Letters*, 12(8):4025–4031, 2012.

[90] J. Jin, X. Fu, Q. Liu, Y. Liu, Z. Wei, K. Niu, and J. Zhang. Identifying the Active Site in Nitrogen-Doped Graphene for the VO^{2+}/VO_2^+ Redox Reaction. *ACS Nano*, 7:4764–4773, 2013.

[91] L. Lai, J. R. Potts, D. Zhan, L. Wang, C. K. Poh, C. Tang, H. Gong, Z. Shen, J. Lin, and R. S. Ruoff. Exploration of the active center structure of nitrogen-doped graphene-based catalysts for oxygen reduction reaction. *Energy Environ. Sci.*, 5:7936–7942, 2012.

[92] M. Hankel, D. Ye, L. Wang, and D. J. Searles. Lithium and Sodium Storage on Graphitic Carbon Nitride. *The Journal of Physical Chemistry C*, 119:21921–21927, 2015.

[93] X. Wang, K. Maeda, A. Thomas, K. Takanabe, G. Xin, J. M. Carlsson, K. Domen, and M. Antonietti. A metal-free polymeric photocatalyst for hydrogen production from water under visible light. *Nat. Mater.*, 8:76–80, 2009.

[94] Q. Xiang, J. Yu, and M. Jaroniec. Preparation and Enhanced Visible-Light Photocatalytic H_2-Production Activity of Graphene/C_3N_4 Composites. *The Journal of Physical Chemistry C*, 115:7355–7363, 2011.

[95] A. B. Jorge, D. J. Martin, M. T. S. Dhanoa, A. S. Rahman, N. Makwana, J. Tang, A. Sella, F. Corà, S. Firth, J. A. Darr, and P. F. McMillan. H_2 and O_2 Evolution from Water Half-Splitting Reactions by Graphitic Carbon Nitride Materials. *The Journal of Physical Chemistry C*, 117:7178–7185, 2013.

[96] J. Liu, Y. Liu, N. Liu, Y. Han, X. Zhang, H. Huang, Y. Lifshitz, S.-T. Lee, J. Zhong, and Z. Kang. Metal-free efficient photocatalyst for stable visible water splitting via a two-electron pathway. *Science*, 347:970–974, 2015.

[97] G. Xie, K. Zhang, B. Guo, Q. Liu, L. Fang, and J. R. Gong. Graphene-Based Materials for Hydrogen Generation from Light-Driven Water Splitting. *Advanced Materials*, 25:3820–3839, 2013.

[98] J. Mahmood, E. K. Lee, M. Jung, D. Shin I.-Y. Jeon, S.-M. Jung, H.-J. Choi, J.-M. Seo, S.-Y. Bae, S.-D. Sohn, N. Park, J. H. Oh, H.-J. Shin, and J.-B. Baek. Nitrogenated holey two-dimensional structures. *Nat. Commun.*, 6:6468, 2015.

[99] X. Zhang, X. Xie, H. Wang, J. Zhang, B. Pan, and Y. Xie. Enhanced Photoresponsive Ultrathin Graphitic-Phase C_3N_4 Nanosheets for Bioimaging. *Journal of the American Chemical Society*, 135:18–21, 2013.

[100] E. Kroke, M. Schwarz, E. H.-Bordon, P. Kroll, B. Noll, and A. D. Norman. Tri-s-triazine derivatives. Part I. From trichloro-tri-s-triazine to graphitic C_3N_4 structures. *New J. Chem.*, 26:508, 2002.

[101] H. Zhao, H. Yu, X. Quan, S. Chen, H. Zhao, and H. Wang. Atomic single layer graphitic-C_3N_4: fabrication and its high photocatalytic performance under visible light irradiation. *RSC Adv.*, 4:624–628, 2014.

[102] S. Kirkpatrick, C. D. Gelatt Jr, and M. P. Vecchi. Optimization by Simulated Annealing. *Science*, 220:671–680, 1983.

[103] N. Metropolis, A. W. Rosenbluth, M. N. Rosenbluth, A. H. Teller, and E. Teller. Equation of State Calculations by Fast Computing Machines. *J. Chem. Phys.*, 21: 1087–1092, 1953.

[104] J. R. Martins and H. Chacham. Disorder and Segregation in BCN Graphene-Type Layers and Nanotubes: Tuning the Band Gap. *ACS Nano*, 5:385–393, 2011.

[105] D. F. Styer, M. K. Phani, and J. L. Lebowitz. Multiatom interactions in the fcc Ising binary alloy: Low-temperature behavior and Monte Carlo simulations. *Phys. Rev. B*, 34:3361–3370, 1986.

[106] L. G. Ferreira, A. A. Mbaye, and Alex Zunger. Chemical and elastic effects on isostructural phase diagrams: The ε-G approach. *Phys. Rev. B*, 37:10547–10570, 1988.

[107] L. G. Ferreira, A. Zunger, S.-H. Wei, and Z. W. Lu. *5th Brazilian School on Semiconductor Physics*, chapter Stability and Metastability of semiconductor alloys, pages 42–60. World Scientific, 1992.

[108] J. R. Martins and H. Chacham. N-rich B-C-N layers: From segregated alloy to solid solution. *Phys. Rev. B*, 86:075421, 2012.

[109] A. Thomas, A. Fischer, F. Goettmann, M. Antonietti, J.-O. Muller, R. Schlogl, and J. M. Carlsson. Graphitic carbon nitride materials: variation of structure and morphology and their use as metal-free catalysts. *J. Mater. Chem.*, 18:4893–4908, 2008.

[110] F. Joucken, Y. Tison, P. L. Fèvre, A. Tejeda, A. T.-Ibrahimi, E. Conrad, V. Repain, C. Chacon, A. Bellec, Y. Girard, S. Rousset, J. Ghijsen, R. Sporken, H. Amara, F. Ducastelle, and J. Lagoute. Charge transfer and electronic doping in nitrogen-doped graphene. *Sci. Rep.*, 5:14564, 2015.

[111] M. S. C. Mazzoni, R. W. Nunes, S. Azevedo, and H. Chacham. Electronic structure and energetics of $B_xC_yN_z$ layered structures. *Phys. Rev. B*, 73:073108, 2006.

[112] Y. Sun, C. Li, Y. Xu, H. Bai, Z. Yao, and G. Shi. Chemically converted graphene as substrate for immobilizing and enhancing the activity of a polymeric catalyst. *Chem. Commun.*, 46:4740–4742, 2010.

[113] Y. Xu and S.-P. Gao. Band gap of C_3N_4 in the GW approximation. *International Journal of Hydrogen Energy*, 37:11072–11080, 2012.

[114] Y. Wang, Y. Shao, D. W. Matson, J. Li, and Y. Lin. Nitrogen-Doped Graphene and Its Application in Electrochemical Biosensing. *ACS Nano*, 4:1790–1798, 2010.

[115] Y. Li, Y. Zhao, H. Cheng, Y. Hu, G. Shi, L. Dai, and L. Qu. Nitrogen-Doped Graphene Quantum Dots with Oxygen-Rich Functional Groups. *Journal of the American Chemical Society*, 134:15–18, 2012.

[116] O. V. Yazyev and L. Helm. Defect-induced magnetism in graphene. *Phys. Rev. B*, 75:125408, 2007.

[117] O. V. Yazyev. Emergence of magnetism in graphene materials and nanostructures. *Reports on Progress in Physics*, 73:056501, 2010.

[118] S. S. Alexandre, M. S. C. Mazzoni, and H. Chacham. Edge States and Magnetism in Carbon Nanotubes with Line Defects. *Phys. Rev. Lett.*, 100:146801, 2008.

[119] D. Gao, Q. Xu, J. Zhang, Z. Yang, M. Si, Z. Yan, and D. Xue. Defect-related ferromagnetism in ultrathin metal-free g-C_3N_4 nanosheets. *Nanoscale*, 6:2577–2581, 2014.

[120] D. Pesin and A. H. MacDonald. Spintronics and pseudospintronics in graphene and topological insulators. *Nat. Mater.*, 11:409–416, 2012.

[121] W. Han, R. K. Kawakami, M. Gmitra, and J. Fabian. Graphene spintronics. *Nat. Nanotechnol.*, 9:794–807, 2014.

[122] K. S. Novoselov, A. K. Geim, S. V. Morozov, D. Jiang, Y. Zhang, S. V. Dubonos, I. V. Grigorieva, and A. A. Firsov. Electric Field Effect in Atomically Thin Carbon Films. *Science*, 306:666–669, 2004.

[123] A. H. Castro Neto, F. Guinea, N. M. R. Peres, K. S. Novoselov, and A. K. Geim. The electronic properties of graphene. *Rev. Mod. Phys.*, 81:109–162, 2009.

[124] M. Drögeler, F. Volmer, M. Wolter, B. Terrés, K. Watanabe, T. Taniguchi, G. Güntherodt, C. Stampfer, and B. Beschoten. Nanosecond Spin Lifetimes in Single- and Few-Layer Graphene–hBN Heterostructures at Room Temperature. *Nano Letters*, 14:6050–6055, 2014.

[125] S. Roche, J. Åkerman, B. Beschoten, J.-C. Charlier, M. Chshiev, S. P. Dash, B. Dlubak, J. Fabian, A. Fert, M. Guimarães, F. Guinea, I. Grigorieva, C. Schönenberger, P. Seneor, C. Stampfer, S. O. Valenzuela, X. Waintal, and B. van Wees. Graphene spintronics: the European Flagship perspective. *2D Materials*, 2:030202, 2015.

[126] S. Z. Butler, S. M. Hollen, L. Cao, Y. Cui, J. A. Gupta, H. R. Gutiérrez, T. F. Heinz, S. S. Hong, J. Huang, A. F. Ismach, E. J.-Halperin, M. Kuno, V. V. Plashnitsa, R. D. Robinson, R. S. Ruoff, S. Salahuddin, J. Shan, L. Shi, M. G. Spencer, M. Terrones, W. Windl, and J. E. Goldberger. Progress, Challenges, and Opportunities in Two-Dimensional Materials Beyond Graphene. *ACS Nano*, 7:2898–2926, 2013.

[127] N. Zibouche, A. Kuc, J. Musfeldt, and T. Heine. Transition-metal dichalcogenides for spintronic applications. *Annalen der Physik*, 526:395–401, 2014.

[128] A. Du, S. Sanvito, and S. C. Smith. First-Principles Prediction of Metal-Free Magnetism and Intrinsic Half-Metallicity in Graphitic Carbon Nitride. *Phys. Rev. Lett.*, 108:197207, 2012.

[129] A. Wang and M. Zhao. Intrinsic half-metallicity in fractal carbon nitride honeycomb lattices. *Phys. Chem. Chem. Phys.*, 17:21837–21844, 2015.

[130] H. Qiu, Z. Wang, and X. Sheng. First-principles prediction of an intrinsic half-metallic graphitic hydrogenated carbon nitride. *Physics Letters A*, 377:347–350, 2013.

[131] H. Qiu, Z. Wang, and X. Sheng. Ferromagnetism and antiferromagnetism in hydrogenated g-C_3N_4: A first-principles study. *Physica B: Condensed Matter*, 421: 46–49, 2013.

[132] X. Li, J. Zhou, Q. Wang, Y. Kawazoe, and P. Jena. Patterning Graphitic C–N Sheets into a Kagome Lattice for Magnetic Materials. *The Journal of Physical Chemistry Letters*, 4:259–263, 2013.

[133] X. Zhang, A. Wang, and M. Zhao. Spin-gapless semiconducting graphitic carbon nitrides: A theoretical design from first principles. *Carbon*, 84:1–8, 2015.

[134] X. Zhang, M. Zhao, A. Wang, X. Wang, and A. Du. Spin-polarization and ferromagnetism of graphitic carbon nitride materials. *J. Mater. Chem. C*, 1:6265–6270, 2013.

[135] X. Li, S. Zhang, and Q. Wang. Stability and physical properties of a tri-ring based porous g-C_4N_3 sheet. *Phys. Chem. Chem. Phys.*, 15:7142–7146, 2013.

[136] Y. Ito, C. Christodoulou, M. V. Nardi, N. Koch, M. Kläui, H. Sachdev, and K. Müllen. Tuning the Magnetic Properties of Carbon by Nitrogen Doping of Its Graphene Domains. *Journal of the American Chemical Society*, 137:7678–7685, 2015.

[137] Y. W. Ma, Y. H. Lu, J. B. Yi, Y. P. Feng, T. S. Herng, X. Liu, D. Q. Gao, D. S. Xue, J. M. Xue, J. Y. Ouyang, and J. Ding. Room temperature ferromagnetism in Teflon due to carbon dangling bonds. *Nature Communications*, 3:727, 2012.

[138] J. S. Braithwaite and P. Rez. The Effect of Impurities on Grain Boundaries in Iron. *Microscopy and Microanalysis*, 9:590–591, 2003.

[139] A. V. Krasheninnikov and F. Banhart. Engineering of nanostructured carbon materials with electron or ion beams. *Nat. Materials*, 6:723 – 733, 2007.

[140] L. Seixas, L. B. Abdalla, T. M. Schmidt, A. Fazzio, and R. H. Miwa. Topological states ruled by stacking faults in Bi_2Se_3 and Bi_2Te_3. *Journal of Applied Physics*, 113:023705, 2013.

[141] H. Aramberri, J. I. Cerdá, and M. C. Muñoz. Tunable Dirac Electron and Hole Self-Doping of Topological Insulators Induced by Stacking Defects. *Nano Letters*, 15:3840–3844, 2015.

[142] P. Dev, Y. Xue, and P. Zhang. Defect-Induced Intrinsic Magnetism in Wide-Gap III Nitrides. *Phys. Rev. Lett.*, 100:117204, 2008.

[143] G. Rahman, V. M. García-Suárez, and J. M. Morbec. Intrinsic magnetism in nanosheets of SnO_2: A first-principles study. *Journal of Magnetism and Magnetic Materials*, 328:104–108, 2013.

[144] B. Song, J. C. Han, J. K. Jian, H. Li, Y. C. Wang, H. Q. Bao, W. Y. Wang, H. B. Zuo, X. H. Zhang, S. H. Meng, and X. L. Chen. Experimental observation of defect-induced intrinsic ferromagnetism in III-V nitrides: The case of BN. *Phys. Rev. B*, 80:153203, 2009.

[145] L. Kilanski, F. Tuomisto, R. Szymczak, and R. Kruszka. Magnetically active vacancy related defects in irradiated GaN layers. *Applied Physics Letters*, 101: 072102, 2012.

[146] Y. Liu, G. Wang, S. Wang, J. Yang, L. Chen, X. Qin, B. Song, B. Wang, and X. Chen. Defect-Induced Magnetism in Neutron Irradiated 6H-SiC Single Crystals. *Phys. Rev. Lett.*, 106:087205, 2011.

[147] R.-W. Zhou, X.-C. Liu, H.-J. Wang, W.-B. Chen, F. Li, S.-Y. Zhuo, and E.-W. Shi. Ferromagnetism in proton irradiated 4H-SiC single crystal. *AIP Advances*, 5: 047146, 2015.

[148] Q. Y. Xie, M. Q. Gu, L. Huang, F. M. Zhang, and X. S. Wu. Defect-induced room temperature ferromagnetism in un-doped InN film. *AIP Advances*, 2:012185, 2012.

[149] P. Esquinazi, D. Spemann, R. Höhne, A. Setzer, K.-H. Han, and T. Butz. Induced Magnetic Ordering by Proton Irradiation in Graphite. *Phys. Rev. Lett.*, 91:227201, 2003.

[150] Y. Wang, Y. Huang, Y. Song, X. Zhang, Y. Ma, J. Liang, and Y. Chen. Room-Temperature Ferromagnetism of Graphene. *Nano Letters*, 9:220–224, 2009.

[151] R. K. Eby, E. S. Clark, B. L. Farmer, G. J. Piermarini, and S. Block. Crystal structure of poly(tetrafluoroethylene) homo- and copolymers in the high pressure phase. *Polymer*, 31:2227–2237, 1990.

[152] E. S. Clark. The molecular conformations of polytetrafluoroethylene: forms II and IV. *Polymer*, 40:4659–4665, 1999.

[153] C. Quarti, A. Milani, and C. Castiglioni. Ab Initio Calculation of the IR Spectrum of PTFE: Helical Symmetry and Defects. *The Journal of Physical Chemistry B*, 117:706–718, 2013.

[154] A. Oshima, S. Ikeda, T. Seguchi, and Y. Tabata. Improvement of radiation resistance for polytetrafluoroethylene (PTFE) by radiation crosslinking. *Radiation Physics and Chemistry*, 49:279–284, 1997.

[155] Y. E. Sakhno, V. G. Klimenko, D. I. Seliverstov, T. V. Sakhno, and S. A. Khatipov. The nature of color centers in γ-irradiated poly(tetrafluoroethylene). *Polymer Science Series B*, 50:117–119, 2008.

[156] S. Khatipov, R. Nurmukhametov, Y. Sakhno, V. Klimenko, D. Seliverstov, and T. Sakhno. Fluorescent analysis of polytetrafluoroethylene treated by γ-irradiation near the melting point. *Radiation Physics and Chemistry*, 80:522–528, 2011.

[157] S. A. Khatipov, R. N. Nurmukhametov, Y. E. Sakhno, V. G. Klimenko, D. I. Seliverstov, S. T. Sychkova, and T. V. Sakhno. Color and fluorescence of polytetrafluoroethylene treated by γ-irradiation near the melting point. *Nuclear Instruments and Methods in Physics Research Section B: Beam Interactions with Materials and Atoms*, 269:2600–2604, 2011.

[158] L. Ignatieva, V. Kuryaviy, A. Tsvetnikov, S. Polyshchuk, and V. Bouznik. The structures of new forms of polytetrafluoroethylene obtained by modification of commercial PTFE using different methods. *Journal of Physics and Chemistry of Solids*, 68:1106–1111, 2007.

[159] A. Calzolari, A. Ruini, C. Cavazzoni, and M. J. Caldas. Substitutional Impurities in PPV Crystals: An Intrinsic DonorAcceptor System for High VOC Photovoltaic Devices. *The Journal of Physical Chemistry C*, 114:19535–19539, 2010.

[160] C. G. Van de Walle and J. Neugebauer. First-principles calculations for defects and impurities: Applications to III-nitrides. *Journal of Applied Physics*, 95:3851–3879, 2004.

[161] C. G. Van de Walle and A. Janotti. *Advanced Calculations for Defects in Materials: Electronic Structure Methods*, chapter Advances in Electronic Structure Methods for Defects and Impurities in Solids, pages 1–16. Wiley, 2011.

[162] C. N. R. Rao and G. V. S. Rao. Transition metal oxides: Crystal chemistry, phase transition and related aspects. `http://www.nist.gov/data/nsrds/NSRDS-NBS-49.pdf`, 1974. Online; accessed 15 December 2015.

[163] J. M. Rondinelli and N. A. Spaldin. Structure and Properties of Functional Oxide Thin Films: Insights From Electronic-Structure Calculations. *Advanced Materials*, 23:3363–3381, 2011.

[164] L. Gao, Y. Y. Xue, F. Chen, Q. Xiong, R. L. Meng, D. Ramirez, C. W. Chu, J. H. Eggert, and H. K. Mao. Superconductivity up to 164 K in $HgBa_2Ca_{m-1}Cu_mO_{2m+2+\delta}$ (m =1, 2, and 3) under quasihydrostatic pressures. *Phys. Rev. B*, 50:4260–4263, 1994.

[165] A. A. Kordyuk. Iron-based superconductors: Magnetism, superconductivity, and electronic structure (Review Article). *Low Temperature Physics*, 38:888–899, 2012.

[166] A. P. Drozdov, M. I. Eremets, I. A. Troyan, V. Ksenofontov, and S. I. Shylin. Conventional superconductivity at 203 kelvin at high pressures in the sulfur hydride system. *Nature*, 525:7376, 2015.

[167] B. Raveau, A. Maignan, C. Martin, and M. Hervieu. Colossal Magnetoresistance Manganite Perovskites: Relations between Crystal Chemistry and Properties. *Chemistry of Materials*, 10:2641–2652, 1998.

[168] T. Hotta and E. Dagotto. Orbital ordering in manganites and ruthenates. *Physica B: Condensed Matter*, 312–313:700–702, 2002. The International Conference on Strongly Correlated Electron Systems.

[169] Y. T. Wang, C. W. Luo, and T. Kobayashi. Understanding Multiferroic Hexagonal Manganites by Static and Ultrafast Optical Spectroscopy. *Advances in Condensed Matter Physics*, 2013:104806, 2013.

[170] S. Fujitsu, S. Matsuishi, and H. Hosono. Iron based superconductors processing and properties. *International Materials Reviews*, 57:311–327, 2012.

[171] L. H. Chen, T. H. Tiefel, S. Jin, T. T. M. Palstra, R. Ramesh, and C. Kwon. Colossal magnetoresistance in La-Y-Ca-Mn-O films. *Magnetics, IEEE Transactions on*, 32(5):4692–4694, 1996.

[172] M. Foëx and J. Loriers. Changes in expansion and electrical conductivity of titanium sesquioxide near 200. *Coinpt. Reiidus.*

[173] M. Foëx, J. Jaffray, S. Goldstamb, R. Lyanol, R. Wey, and J. Wucker. The changes in some properties of vanadium sesquioxide near its transformation points. *J. des Rech. du C. N. R. S.*

[174] F. J. Morin. Oxides of the 3d transition metals. *Bell System Tech.*, 37:1047, 1958.

[175] F. J. Morin. Oxides which show a metal-insulator transition at the Neel temperature. *Phys. Rev. Lett.*, 3:34, 1959.

[176] M. D. Pickett and R. S. Williams. Sub-100 fJ and sub-nanosecond thermally driven threshold switching in niobium oxide crosspoint nanodevices. *Nanotechnology*, 23: 215202, 2012.

[177] M. D. Pickett, G. Medeiros-Ribeiro, and R. S. Williams. A scalable neuristor built with Mott memristors. *Nature Materials*, 12:114117, 2013.

[178] Z. Yang, C. Ko, and S. Ramanathan. Oxide Electronics Utilizing Ultrafast Metal-Insulator Transitions. *Annual Review of Materials Research*, 41:337–367, 2011.

[179] N. F. Mott. *Metal-Insulator transitions.* Taylor and Francis, 1990.

[180] R. F. Jannick and D. H. Whitmore. Electrical conductivity and thermoelectric power of niobium dioxide. *J. Phys. Chem. Solids*, 27:1183, 1966.

[181] K. Seta and K. Naito. Calorimetric study of the phase transition in NbO_2. *J. Chem. Thermodynamics*, 14:921, 1982.

[182] Y. Sakai, N. Tsuda, and T. Sakata. Electrical properties of semiconducting NbO_2. *J. Phys. Soc. Jpn.*, 54:1514, 1985.

[183] D. B. McWhan, M. Marezio, J. P. Remeika, and P. D. Dernier. X-ray diffraction study of metallic VO_2. *Phys. Rev. B*, 10:490–495, 1974.

[184] A. A. Bolzan, C. Fong, B. J. Kennedy, and C. J. Howard. A Powder Neutron Diffraction Study of Semiconducting and Metallic Niobium Dioxide. *Journal of Solid State Chemistry*, 113:9–14, 1994.

[185] J. M. Long and P. Kierkegaard. A refinement of the structure of VO_2. *Acta Chem. Scand.*, 24:420, 1970.

[186] J. P. Pouget, H. Launois, J. P. D'Haenens, P. Merenda, and T. M. . Electron Localization Induced by Uniaxial Stress in Pure VO_2. *Phys. Rev. Lett.*, 35:873–875, 1975.

[187] E. Strelcov, A. Tselev, I. Ivanov, J. D. Budai, J. Zhang, J. Z. Tischler, I. Kravchenko, S. V. Kalinin, and A. Kolmakov. Doping-Based Stabilization of the M2 Phase in Free-Standing VO_2 Nanostructures at Room Temperature. *Nano Letters*, 12:6198–6205, 2012.

[188] V. Eyert. The metal-insulator transitions of VO_2: A band theoretical approach. *Annalen der Physik*, 11:650–704, 2002.

[189] J. B. Goodenough. Direct Cation-Cation Interactions in Several Oxides. *Phys. Rev.*, 117:1442–1451, 1960.

[190] J. P. Pouget, H. Launois, T. M. Rice, P. Dernier, A. Gossard, G. Villeneuve, and P. Hagenmuller. Dimerization of a linear Heisenberg chain in the insulating phases of $V_{1-x}Cr_xO_2$. *Phys. Rev. B*, 10:1801–1815, 1974.

[191] J. P. D'Haenens, D. Kaplan, and P. Merenda. Electron spin resonance in $V_{1-x}Cr_xO_2$. *Journal of Physics C: Solid State Physics*, 8:2267, 1975.

[192] Budai J. D., Hong J., Manley M. E., Specht E. D., Li C. W., Tischler J. Z., Abernathy D. L., Said A. H., Leu B. M., Boatner L. A., McQueeney R. J., and Delaire O. Metallization of vanadium dioxide driven by large phonon entropy. *Nature*, 515:535–539, 2014.

[193] H. Terauchi and J. B. Cohen. Diffuse x-ray scattering due to the lattice instability near the metal-semiconductor transition in VO_2. *Phys. Rev. B*, 17:2494–2496, 1978.

[194] F. Gervais and W. Kress. Lattice dynamics of oxides with rutile structure and instabilities at the metal-semiconductor phase transitions of NbO_2 and VO_2. *Phys. Rev. B*, 31:4809–4814, 1985.

[195] J. P. Pouget, P. Lederer, D. S. Schreiber, H. Launois, D. Wohlleben, A. Casalot, and G. Villeneuve. Contribution to the study of the metal-insulator transition in the $V_{1-x}Nb_xO_2$ system-II magnetic properties. *Journal of Physics and Chemistry of Solids*, 33:1961–1967, 1972.

[196] D. Okuyama, K. Shibuya, R. Kumai, T. Suzuki, Y. Yamasaki, H. Nakao, Y. Murakami, M. Kawasaki, Y. Taguchi, Y. Tokura, and T. Arima. X-ray study of metal-insulator transitions induced by W doping and photoirradiation in VO_2 films. *Phys. Rev. B*, 91:064101, 2015.

[197] K. Okazaki, H. Wadati, A. Fujimori, M. Onoda, Y. Muraoka, and Z. Hiroi. Photoemission study of the metal-insulator transition in $VO_2/TiO_2(001)$: Evidence for strong electron-electron and electron-phonon interaction. *Phys. Rev. B*, 69: 165104, 2004.

[198] M. W. Haverkort, Z. Hu, A. Tanaka, W. Reichelt, S. V. Streltsov, M. A. Korotin, V. I. Anisimov, H. H. Hsieh, H.-J. Lin, C. T. Chen, D. I. Khomskii, and L. H. Tjeng. Orbital-Assisted Metal-Insulator Transition in VO_2. *Phys. Rev. Lett.*, 95: 196404, 2005.

[199] T. C. Koethe, Z. Hu, M. W. Haverkort, C. Schüßler-Langeheine, F. Venturini, N. B. Brookes, O. Tjernberg, W. Reichelt, H. H. Hsieh, H.-J. Lin, C. T. Chen, and L. H. Tjeng. Transfer of Spectral Weight and Symmetry across the Metal-Insulator Transition in VO_2. *Phys. Rev. Lett.*, 97:116402, 2006.

[200] J. H. Park, J. M. Coy, T. S. Kasirga, C. Huang, Z. Fei, S. Hunter, and D. H. Cobden. Measurement of a solid-state triple point at the metal-insulator transition in VO_2. *Nature*, 500:431, 2013.

[201] M. M. Qazilbash, M. Brehm, B.-G. Chae, P.-C. Ho, G. O. Andreev, B.-J. Kim, S. J. Yun, A. V. Balatsky, M. B. Maple, F. Keilmann, H.-T. Kim, and D. N. Basov. Mott Transition in VO_2 Revealed by Infrared Spectroscopy and Nano-Imaging. *Science*, 318:750, 2007.

[202] J. Park, I. H. Oh, E. Lee, K. W. Lee, C. E. Lee, K. Song, and Y.-J. Kim. Structure and magnetism in VO_2 nanorods. *Applied Physics Letters*, 91:153112, 2007.

[203] D. Wegkamp, M. Herzog, L. Xian, M. Gatti, P. Cudazzo, C. L. McGahan, R. E. Marvel, R. F. Haglund, A. Rubio, M. Wolf, and J. Stähler. Instantaneous Band Gap Collapse in Photoexcited Monoclinic VO_2 due to Photocarrier Doping. *Phys. Rev. Lett.*, 113:216401, 2014.

[204] H.-T. Kim, Y. W. Lee, B.-J. Kim, B.-G. Chae, S. J. Yun, K.-Y. Kang, K.-J. Han, K.-J. Yee, and Y.-S. Lim. Monoclinic and Correlated Metal Phase in VO_2 as

Evidence of the Mott Transition: Coherent Phonon Analysis. *Phys. Rev. Lett.*, 97: 266401, 2006.

[205] E. Arcangeletti, L. Baldassarre, D. Di Castro, S. Lupi, L. Malavasi, C. Marini, A. Perucchi, and P. Postorino. Evidence of a Pressure-Induced Metallization Process in Monoclinic VO_2. *Phys. Rev. Lett.*, 98:196406, 2007.

[206] J. Laverock, S. Kittiwatanakul, A. A. Zakharov, Y. R. Niu, B. Chen, S. A. Wolf, J. W. Lu, and K. E. Smith. Direct Observation of Decoupled Structural and Electronic Transitions and an Ambient Pressure Monocliniclike Metallic Phase of VO_2. *Phys. Rev. Lett.*, 113:216402, 2014.

[207] Z. Tao, T.-R. T. Han, S. D. Mahanti, P. M. Duxbury, F. Yuan, C.-Y. Ruan, K. Wang, and J. Wu. Decoupling of Structural and Electronic Phase Transitions in VO_2. *Phys. Rev. Lett.*, 109:166406, 2012.

[208] K. Seta and K. Naito. Calorimetric study of the phase transition in NbO_2. *The Journal of Chemical Thermodynamics*, 14:921–935, 1982. doi: 10.1016/0021-9614(82)90002-7.

[209] M. Posternak, A. J. Freeman, and D. E. Ellis. Electronic band structure, optical properties, and generalized susceptibility of NbO_2. *Phys. Rev. B*, 19:6555–6563, 1979.

[210] S. M. Shapiro, J. D. Axe, G. Shirane, and P. M. Raccah. Neutron scattering study of the structural phase transition in NbO_2. *Solid State Communications*, 15:377–381, 1974.

[211] R. Pynn, J. D. Axe, and P. M. Raccah. Structural fluctuations in NbO_2 at high temperatures. *Phys. Rev. B*, 17:2196–2205, 1978.

[212] A. O'Hara and A. A. Demkov. Nature of the metal-insulator transition in NbO_2. *Phys. Rev. B*, 91:094305, 2015.

[213] D. Adler. Mechanisms for Metal-Nonmental Transitions in Transition-Metal Oxides and Sulfides. *Rev. Mod. Phys.*, 40:714–736, 1968.

[214] A. B. Posadas, A. O'Hara, S. Rangan, R. A. Bartynski, and A. A. Demkov. Band gap of epitaxial in-plane-dimerized single-phase NbO_2 films. *Applied Physics Letters*, 104:092901, 2014.

[215] A. O'Hara, T. N. Nunley, A. B. Posadas, S. Zollner, and A. A. Demkov. Electronic and optical properties of NbO_2. *Journal of Applied Physics*, 116:213705, 2014.

[216] P. B. Allen, R. M. Wentzcovitch, W. W. Schulz, and P. C. Canfield. Resistivity of the high-temperature metallic phase of VO_2. *Phys. Rev. B*, 48:4359–4363, 1993.

[217] R. M. Wentzcovitch, W. W. Schulz, and P. B. Allen. VO_2: Peierls or Mott-Hubbard? A view from band theory. *Phys. Rev. Lett.*, 72:3389–3392, 1994.

[218] V. Eyert. VO_2: A Novel View from Band Theory. *Phys. Rev. Lett.*, 107:016401, 2011.

[219] V. Eyert. The metal-insulator transition of NbO_2: An embedded Peierls instability. *EPL (Europhysics Letters)*, 58:851, 2002.

[220] R. Grau-Crespo, H. Wang, and U. Schwingenschlögl. Why the Heyd-Scuseria-Ernzerhof hybrid functional description of VO_2 phases is not correct. *Phys. Rev. B*, 86:081101, 2012.

[221] Z. Zhu and U. Schwingenschlögl. Comprehensive picture of VO_2 from band theory. *Phys. Rev. B*, 86:075149, 2012.

[222] A. Continenza, S. Massidda, and M. Posternak. Self-energy corrections in VO_2 within a model GW scheme. *Phys. Rev. B*, 60:15699–15704, 1999.

[223] R. Sakuma, T. Miyake, and F. Aryasetiawan. First-principles study of correlation effects in VO_2. *Phys. Rev. B*, 78:075106, 2008.

[224] Huihuo Zheng and Lucas K. Wagner. Computation of the Correlated Metal-Insulator Transition in Vanadium Dioxide from First Principles. *Phys. Rev. Lett.*, 114:176401, 2015.

[225] Z. Weibin, W. Weidong, W. Xueming, C. Xinlu, Y. Dawei, S. Changle, P. Liping, W. Yuying, and B. Li. The investigation of NbO_2 and Nb_2O_5 electronic structure by XPS, UPS and first principles methods. *Surface and Interface Analysis*, 45: 1206–1210, 2013.

[226] S. Biermann, A. Poteryaev, A. I. Lichtenstein, and A. Georges. Dynamical Singlets and Correlation-Assisted Peierls Transition in VO_2. *Phys. Rev. Lett.*, 94:026404, 2005.

[227] E. Pavarini, S. Biermann, A. Poteryaev, A. I. Lichtenstein, A. Georges, and O. K. Andersen. Mott Transition and Suppression of Orbital Fluctuations in Orthorhombic $3d^1$ Perovskites. *Phys. Rev. Lett.*, 92:176403, 2004.

[228] C. Weber, D. D. O'Regan, N. D. M. Hine, M. C. Payne, G. Kotliar, and P. B. Littlewood. Vanadium Dioxide: A Peierls-Mott Insulator Stable against Disorder. *Phys. Rev. Lett.*, 108:256402, 2012.

[229] W. F. Brinkman and T. M. Rice. Application of Gutzwiller's Variational Method to the Metal-Insulator Transition. *Phys. Rev. B*, 2:4302–4304, 1970.

[230] J. M. Tomczak, F. Aryasetiawan, and S. Biermann. Effective bandstructure in the insulating phase versus strong dynamical correlations in metallic VO_2. *Phys. Rev. B*, 78:115103, 2008.

[231] B. Lazarovits, K. Kim, K. Haule, and G. Kotliar. Effects of strain on the electronic structure of VO_2. *Phys. Rev. B*, 81:115117, 2010.

[232] I. Leonov, V. I. Anisimov, and D. Vollhardt. Metal-insulator transition and lattice instability of paramagnetic V_2O_3. *Phys. Rev. B*, 91:195115, 2015.

[233] K. Robinson, G. V. Gibbs, and P. H. Ribbe. Quadratic Elongation: A Quantitative Measure of Distortion in Coordination Polyhedra. *Science*, 172:567–570, 1971.

[234] J. H. Xu, T. Jarlborg, and A. J. Freeman. Self-consistent band structure of the rutile dioxides NbO_2, RuO_2, and IrO_2. *Phys. Rev. B*, 40:7939–7947, 1989.

[235] M. Marezio, D. B. McWhan, J. P. Remeika, and P. D. Dernier. Structural Aspects of the Metal-Insulator Transitions in Cr-Doped VO_2. *Phys. Rev. B*, 5:2541–2551, 1972.

[236] M. S. Laad, L. Craco, and E. Müller-Hartmann. Metal-insulator transition in rutile-based VO_2. *Phys. Rev. B*, 73:195120, 2006.

[237] G. Kotliar, S. Y. Savrasov, G. Pálsson, and G. Biroli. Cellular Dynamical Mean Field Approach to Strongly Correlated Systems. *Phys. Rev. Lett.*, 87:186401, 2001.

[238] T. Maier, M. Jarrell, T. Pruschke, and M. H. Hettler. Quantum cluster theories. *Rev. Mod. Phys.*, 77:1027–1080, 2005.

[239] K. Haule and G. Kotliar. Strongly correlated superconductivity: A plaquette dynamical mean-field theory study. *Phys. Rev. B*, 76:104509, 2007.

[240] J. M. Tomczak and S. Biermann. Effective band structure of correlated materials: the case of VO_2. *Journal of Physics: Condensed Matter*, 19:365206, 2007.

[241] A. I. Poteryaev, A. I. Lichtenstein, and G. Kotliar. Nonlocal Coulomb Interactions and Metal-Insulator Transition in Ti_2O_3: A Cluster LDA + DMFT Approach. *Phys. Rev. Lett.*, 93:086401, 2004.

[242] H. Park, K. Haule, and G. Kotliar. Cluster Dynamical Mean Field Theory of the Mott Transition. *Phys. Rev. Lett.*, 101:186403, 2008.

[243] Y.-C. Lin, P.-Y. Teng, P.-W. Chiu, and K. Suenaga. Exploring the Single Atom Spin State by Electron Spectroscopy. *Phys. Rev. Lett.*, 115:206803, 2015.

[244] Y.-C. Lin, P.-Y. Teng, C.-H. Yeh, M. Koshino, P.-W. Chiu, and K. Suenaga. Structural and Chemical Dynamics of Pyridinic-Nitrogen Defects in Graphene. *Nano Letters*, 15:7408–7413, 2015.

[245] G. Wu, Y. Hu, Y. Liu, J. Zhao, X. Chen, V. Whoehling, C. Plesse, G. T. M. Nguyen, F. Vidal, and W. Chen. Graphitic carbon nitride nanosheet electrode-based high-performance ionic actuator. *Nature Communications*, 6:7258, 2015.

[246] M. Kardar. *Statistical Physics of Particles.* Cambridge University Press, 2007.

[247] B. R. Judd. *Operator Techniques in Atomic Spectroscopy.* Princeton University Press, 1998.

[248] V. Anisimov, F. Aryasetiawan, and A. I. Lichtenstein. First-principles calculations of the electronic structure and spectra of strongly correlated systems: the LDA+U method. *J. Phys.: Condens. Matter*, 9:767, 1997.

[249] W. Krauth. *Statistical Mechanics: Algorithms and Computations.* Oxford University Press, 2006.

[250] E. Gull, A. J. Millis, A. I. Lichtenstein, A. N. Rubtsov, M. Troyer, and P. Werner. Continuous-time Monte Carlo methods for quantum impurity models. *Rev. Mod. Phys.*, 83:349, 2011.

[251] P. Ordejón, E. Artacho, and J. M. Soler. Self-Consistent Order-N Density-Functional Calculations for Very Large Systems. *Phys. Rev. B*, 53:R10441, 1996.

[252] D. Sánchez-Portal, P. Ordejón, E. Artacho, and J. M. Soler. Density-Functional Method for Very Large Systems with LCAO Basis sets. *Int. J. Quantum Chem.*, 65:453–461, 1997.

[253] H. J. Monkhorst and J. P. Pack. Special Points for Brillouin-Zone integrations. *Phys. Rev. B*, 13:5188–5192, 1976.

[254] P. Giannozzi, S. Baroni, N. Bonini, M. Calandra, R. Car, C. Cavazzoni, D. Ceresoli, G. L. Chiarotti, M. Cococcioni, I. Dabo, A. Dal Corso, S. de Gironcoli, S. Fabris, G. Fratesi, R. Gebauer, U. Gerstmann, C. Gougoussis, A. Kokalj, M. Lazzeri, L. Martin-Samos, N. Marzari, F. Mauri, R. Mazzarello, S. Paolini, A. Pasquarello, L. Paulatto, C. Sbraccia, S. Scandolo, G. Sclauzero, A. P. Seitsonen, A. Smogunov, P. Umari, and R. M. Wentzcovitch. QUANTUM ESPRESSO: a modular and open-source software project for quantum simulations of materials. *Journal of Physics: Condensed Matter*, 21:395502, 2009.

[255] M. Dion, H. Rydberg, E. Schröder, D. C. Langreth, and B. I. Lundqvist. Van der Waals Density Functional for General Geometries. *Phys. Rev. Lett.*, 92:246401, 2004.

[256] T. Thonhauser, V. R. Cooper, S. Li, A. Puzder, P. Hyldgaard, and D. C. Langreth. Van der Waals density functional: Self-consistent potential and the nature of the van der Waals bond. *Phys. Rev. B*, 76:125112, 2007.

[257] D. Vanderbilt. Soft self-consistent pseudopotentials in a generalized eigenvalue formalism. *Phys. Rev. B*, 41:7892–7895, 1990.

[258] D. I. Khomskii. *Basic Aspects of the Quantum Theory of Solids: Order and Elementary excitations.* Cambridge University Press, 2010.

[259] R. E. Peierls. *Quantum Theory of Solids.* Oxford, 1955.

[260] J. C. Slater. Magnetic Effects and the Hartree-Fock Equation. *Phys. Rev.*, 82: 538–541, 1951.

[261] A. M. Graaf and R. Luzzi. On the split-band model of antiferromagnetism in insulators. *Il Nuovo Cimento B Series 10*, 61:449–461.

[262] R. Comin and A. Damascelli. ARPES: A probe of electronic correlations. 2013. preprint arXiv:1303.1438.

[263] A. Damascelli, Z. Hussain, and Z.-X. Shen. Angle-resolved photoemission studies of the cuprate superconductors. *Rev. Mod. Phys.*, 75:473–541, 2003.

[264] H. Bruus and K. Flensberg. *Introduction to Quantum Many body Theory in Condensed Matter physics*. Oxford, 2002.